Durham University

Durham E-Theses

Structural studies into AM(_2)O(_7) framework materials and parametric Rietveld refinement

Graham William Stinton

How to cite:

Stinton, Graham William (2006) Structural studies into AM(_2)O(_7) framework materials and parametric Rietveld refinement. Doctoral thesis, Durham University.

Use policy

The full-text may be used and/or reproduced, and given to third parties in any format or medium, without prior permission or charge, for personal research or study, educational, or not-for-profit purposes provided that:

- a full bibliographic reference is made to the original source
- a https://etheses.durham.ac.uk/id/eprint/2436/ is made to the metadata record in Durham E-Theses
- the full-text is not changed in any way

The full-text must not be sold in any format or medium without the formal permission of the copyright holders.

Please consult the full Durham E-Theses policy for further details.

Academic Support Office, The Palatine Centre, Durham University, Stockton Road, Durham, DH1 3LE
e-mail: e-theses.admin@durham.ac.uk Tel: +44 0191 334 6107
https://etheses.durham.ac.uk

Structural Studies into AM_2O_7 framework materials and Parametric Rietveld Refinement

Graham William Stinton M.Chem. (Dunelm)

University of Durham

A thesis submitted in partial fulfilment of the requirements

for the degree of Doctor of Philosophy

The copyright of this thesis rests with the author or the university to which it was submitted. No quotation from it, or information derived from it may be published without the prior written consent of the author or university, and any information derived from it should be acknowledged.

Supervisor: Dr John S. O. Evans

Department of Chemistry, University of Durham

2006

- 7 AUG 2007

Abstract

Structural Studies into AM_2O_7 framework materials and Parametric Rietveld Refinement

Graham William Stinton Ph.D. Thesis

2006

This thesis investigates the structural properties of the AM_2O_7 family of materials, many of which show interesting thermal expansion properties and remarkably complex structures. It also develops Parametric Rietveld refinement, a method of extracting more information from multi-condition powder diffraction data.

Chapter 1 reviews the relevant literature.

Chapter 2 describes the equipment and analytic techniques used in the work.

Chapter 3 describes Parametric Rietveld refinement, which aims to fit a single, evolving structural model to a series of diffraction data collected as a function of time, temperature, pressure or other external variable. This can lead to a number of benefits over conventional, sequential Rietveld refinement: it can increase the precision of refined parameters; allow physically realistic models to be applied during data analysis; and allow 'non-crystallographic' quantities, such as temperature or rate constants, to be refined directly from diffraction data.

Chapter 4 presents a full structure solution of ZrP_2O_7 at room temperature from powder diffraction data. This involved developing a method for combining Rietveld refinement, restraints and simulated annealing. Despite 136 unique atoms and close-to metrically cubic symmetry, the true structure of this orthorhombic material can be refined to a high degree of precision.

Chapter 5 is an investigation into the structures and thermal expansion of two AM_2O_7 species, pseudo-cubic SnP_2O_7 and GeP_2O_7. A full structure solution of the room temperature phase of SnP_2O_7 is presented. Two higher temperature phases of SnP_2O_7 and the low temperature phase of GeP_2O_7 are also analysed. Variable temperature data for both materials are presented.

Chapter 6 describes the synthesis and characterisation *via* powder diffraction of solid-state solutions of the general formula $Zr_xSn_{1-x}P_2O_7$. The variation of properties across the series is investigated both at room temperature and upon heating.

Acknowledgements

I would like to thank the following people for their help during the course of my Ph.D.

Firstly, John Evans, my supervisor, for providing inspiration and support throughout this work. For always finding time to answer the thousands of questions I have plagued him with during it course. For teaching me chemistry, crystallography, practical diffraction skills, presentation skills, English and a little Latin *inter alia*. Thank you John for always believing in me.

To those who have directly assisted to the science in this thesis. Richard Gover for the SnP_2O_7 synthesis and data. Pat Woodward for collecting the X-ray data on ZrP_2O_7. Franck Fayon for synthesizing GeP_2O_7. Anne Soleilhavoup for carrying out NMR on the $Zr_xSn_{1-x}P_2O_7$ series and Simon Allen for collecting data on $ZrWMoO_8$.

To all my fellow research group member/ inmates of CY31. Neil for making me feel at home when I first started and showing me how to use the equipment. Dr. Hampson for sympathy when things didn't work and encouragement when they did. Dr. Hampson for musical enlightenment and crazy road trips. Lue for the discussions of football, cricket and sandwiches. Sarah for always listening, always caring and tea. Loc for the cheerful attitude that made the group a much more pleasant place to work and generally being the lab guru. Lars for imparting a large amount of crystallographific knowledge in a short space of time.

All the project students that have toiled in the office/lab. Thanks to Pete, Sarah (again), Martin, Laura, Charlie, David, May, Tom, Hannah, Rosie and Matt C. for the banter, tea-making and occasional science.

To all those who have made the last 3 (and a bit) years a much better time in a non-chemistry capacity. To my housemates, especially Si, Greig, Tony and Owen, cheers for putting up with living with me. To all the members of DUSAGG, sorry that there is too many of you for individual thanks, it has been really great to be a member. To all those who have played football for either Ustinov AFC or the Dukes of Hazzard five-a-side. Thanks to Nicky, Em, Paul and Rach for being generally wonderful and providing some brilliant holidays.

Finally, a massive thank you to my family, Mum, Dad, Bro, Susie, Grandma Stinton and Grandma Meyrick. Thank you for all your love and support, I could not have done this without your help. Thank you mum and dad for putting up with me squatting at home for 3 months. Don't worry, I'm not going to make you read any further than this.

List of Abbreviations Used in this Thesis

NTE	-	Negative Thermal Expansion
TCHz	-	Thompson-Cox-Hastings pseudo-Voigt

NMR Terminology

2Q	-	double quantum
C7	-	Seven-fold symmetry phase shift scheme
COSY	-	Correlation Spectroscopy
INADEQUATE	-	Incredible Natural Abundance Double Quantum Transfer Experiment
MAS	-	Magic Angle Spinning
POST	-	Permutationally Offset Stabilised
TOBSY	-	Through Bond Correlation Spectroscopy

Declaration and Statement of Copyright

The work described in this thesis is entirely my own work, except where I have acknowledged help from a named person or given a reference to a published source or a thesis.

The research presented was performed in the Department of Chemistry, Durham University between October 2003 and September 2006, the results of which have not been submitted for a degree in this or any other university.

This thesis conforms to the word limit set out in the Degree Regulations. It contains 42,831 words including appendices but excluding references, or experimental data included on the CD_R located at the rear of the thesis.

The copyright of this thesis rests with author. No quotation from it should be published without their prior consent and information derived from it should be acknowledged in the form of a reference.

Date: 22/05/2007 Signature:

List of Contents

1. Negative Thermal Expansion in the Pseudo-Cubic AM_2O_7 Family

1.1. Negative Thermal Expansion

It is well known that the overwhelming majority of materials expand upon heating. This causes a variety of problems in every-day & high-tech situations; doors jamming due to expansion causing contact with the frame, materials which are repeatedly heated and cooled developing stress fractures; and the reflected wavelength of fibre optics varying with temperature. These types of problems have caused considerable interest in the few materials which demonstrate the opposing property, that of negative thermal expansion (NTE). Such materials could compensate for the expansion of other components or one could combine NTE materials with positive thermal expansion (PTE) materials in order to produce composites with no thermal expansion.

An ideal NTE material should be cubic to give equal thermal contraction in all directions. It is also desirable that the NTE remains at a constant rate over a large temperature range and that the material undergoes no phase transitions in the temperature range of the application. These properties make it easier to match the thermal contraction with the thermal expansion of other materials.

The linear thermal expansion coefficient (α_l) is formally defined by Equation 1-1, where a is the length of the material (or a unit cell parameter). The volume thermal expansion (α_v) is defined by Equation 1-2, were v is volume. For a cubic material $\alpha_l = \frac{1}{3}\alpha_v$.

$$\alpha_l = \left(\frac{1}{a}\right)\left(\frac{\partial a}{\partial T}\right)_P \qquad \text{Equation 1-1}$$

$$\alpha_v = \left(\frac{1}{v}\right)\left(\frac{\partial v}{\partial T}\right)_P \qquad \text{Equation 1-2}$$

It is more common to quote the mean thermal expansion over a range, as shown in Equation 1-3, where a and a_0 are cell lengths at T and T_0 respectively.

$$\alpha_l = \frac{[(a - a_0)/a_0]}{T - T_0} \qquad \text{Equation 1-3}$$

1.2. Structural Phenomena leading to NTE

A typical diatomic bond has an asymmetric interatomic potential well as shown in Figure 1-1. As higher energy vibrational levels become populated, the average bond length also increases. This expansion is the reason for why most materials show PTE. For a few NTE

materials, over limited temperature ranges, a decrease in average bond lengths with heating may occur. It is far more common however, for some additional structural effect to cause contraction. Five main effects have so far been discovered.

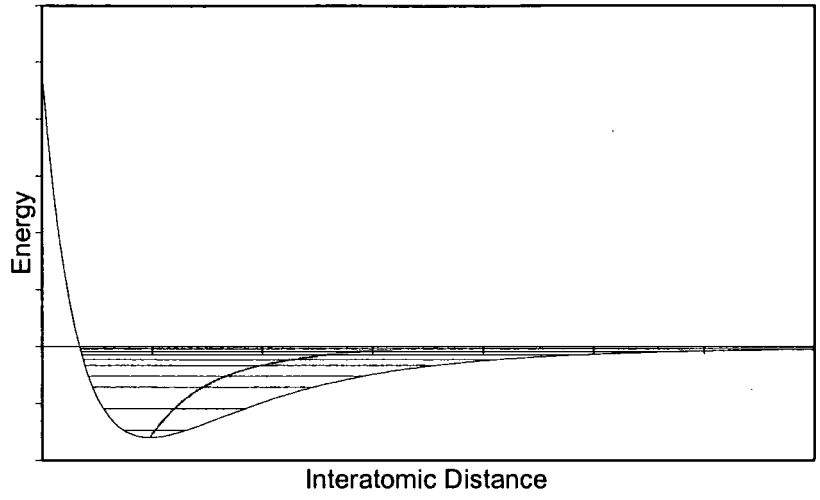

Figure 1-1: Plot showing the general shape of the potential energy well for a typical bond. The energy of the vibration is quantised, with horizontal lines showing possible energy levels. The grey line shows the average length of the bond with varying energy.

1.2.1. Phase Transitions

Phase transitions can cause a contraction of the unit cell. It was demonstrated by Brown[1] that the contribution of a given bond to an atom's total valence can be approximated by Equation 1-4, were v is the valence, r the interatomic distance and r_0 a constant for a given pair of atoms.

$$\upsilon = \exp(r_0 - r)/0.37 \qquad \text{Equation 1-4}$$

This shows that distorted polyhedra will have a greater average bond length than regular polyhedra. This is illustrated by Figure 1-2, for example, where two bonds with a valence contribution of 1 would have a length of 1.95 Å. Distorting to give valence contribution of 1.5 and 0.5, from the two bonds would lead to lengths of 1.8 and 2.2 Å respectively, an average increase of 0.05 Å.

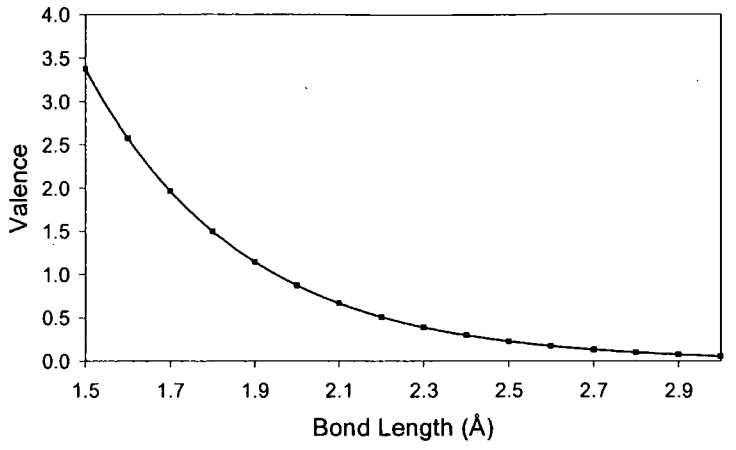

Figure 1-2: A plot of bond valence to bond length for a typical bond.

An example of this occurs below the ferromagnetic-paramagnetic phase transition at 490°C in $PbTiO_3$. At room temperature the Ti-O distances are 1.766, 4 x 1.979 and 2.390 Å, giving an average length of 2.012 Å. After the phase transition, all lengths are 1.983 Å. As the polyhedra slowly become less distorted between room temperature and 490°C, there is a steady contraction in the average cell length ($(a^2c)^{1/3}$). This is shown in Figure 1-3.

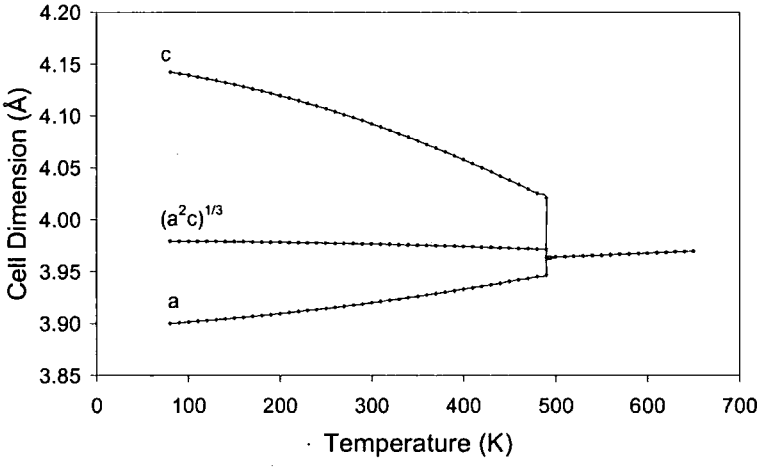

Figure 1-3: Thermal expansion data for $PbTiO_3$ by Rossetti *et al.*[2]

1.2.2. Magnetic Effects

The second phenomena potentially causing NTE is caused by changing magnetic structure with temperature. As a material changes from a ferromagnetic phase to a paramagnetic phase, electrons move from anti-bonding to bonding bands. These magnetostrictive effects cause a contraction in bond length of a similar magnitude to the expansion caused by phonons. The most widely studied material showing this property is the alloy Invar ($Fe_{0.65}Ni_{0.35}$) which has the very low thermal expansion of 0.02 x 10^{-6} K^{-1}.[3] Lu_2Fe_{17} and Y_2Fe_{17} have been shown to demonstrate NTE below 400 K.[4]

1.2.3. Electronic Effects

Certain rare-earth ions can have more than one available electronic configuration, e.g. the outer orbitals of Yb^{2+} can have two configurations, either $(4f)^{14}$ or $(4f)^{13}(5d)^{1}$, with the latter giving a smaller ion. On heating, electrons transfer from the 4f to the 5d band, meaning the average ion size decreases, causing NTE in some Yb^{2+} and Sm^{2+} materials.[5]

A related effect is found for the near-zero expansion material of YbGaGe.[6] On heating electrons transfer from the Yb (4f) band to the Ga (4p) band. This causes a contraction of the Yb ions, which is greater than the expansion of the Ga ions. By controlling the Ga to Ge ratio, zero thermal expansion can be achieved between 100 and 300 K. A similar effect occurs in $Sm_{2.75}C_{60}$.[7] This shows a very large thermal contraction of -1.13×10^{-4} between 4 and 32 K. Samarium ions are located in 1.12 Å wide tetrahedra holes in the fulleride framework. Sm^{2+} ions (1.14 Å) expand the fulleride framework, but as electron density is transferred to fullerides on heating, the smaller Sm^{3+} ions (0.96 Å) no longer cause this to occur. The size of the fullerides is largely unaffected by the additional electron density.

1.2.4. Phonons

The fourth main effect causing NTE is the properties of certain phonons in a solid lattice. As discussed in section 1.1, vibrations in the same direction as the bond (longitudinal) will cause thermal expansion. Other vibrational modes are also present. For example, where there is an atom bonded to only two other atoms, the centre atom can also vibrate perpendicularly to the other two atoms (a transverse vibration). Assuming the bond lengths remain approximately constant, the two adjoining atoms will be pulled closer together as this motion is activated, as shown in Figure 1-4.

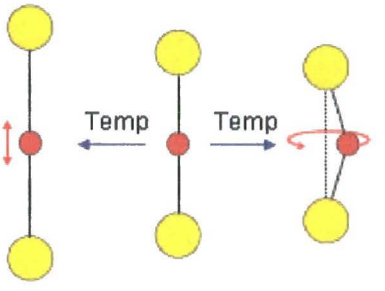

Figure 1-4: Schematic of different types of vibrational mode. Longitudinal vibrations (left) cause positive thermal expansion, transverse vibrations (right) can cause negative thermal expansion.

For this type of phonon to be significant, a relatively open structure is required, such as the zinc-blende structure. Transverse modes tend to be lower in energy than those of longitudinal vibrations. At low temperatures, excited transverse modes can become populated, leading to negative thermal expansion. As the temperature increases, sufficient energy is available to start populating higher energy longitudinal vibrational modes, leading to positive thermal

expansion. The effect of this on the unit cell is shown in Figure 1-5. This pattern of thermal expansion is seen in materials such as Si, Ga, GaAs, CuCl, $CuFeS_2$ and ice.

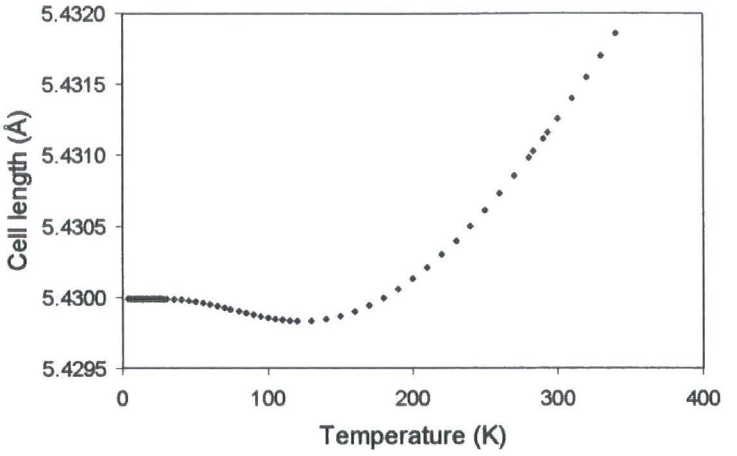

Figure 1-5: Thermal expansion of silicon derived from dilatometry measurements by Lyon *et al.*[8]

1.2.5. Rigid Unit Modes

Whilst the phonons discussed in section 1.2.4 cause NTE at very low temperatures, these generally don't lead to useful NTE materials. Some framework materials with particularly open structures demonstrate the related property of simultaneous rotation of polyhedra, leading to translational motion of the bridging atoms. These are known are rigid unit modes (RUMs). This is demonstrated in Figure 1-6.

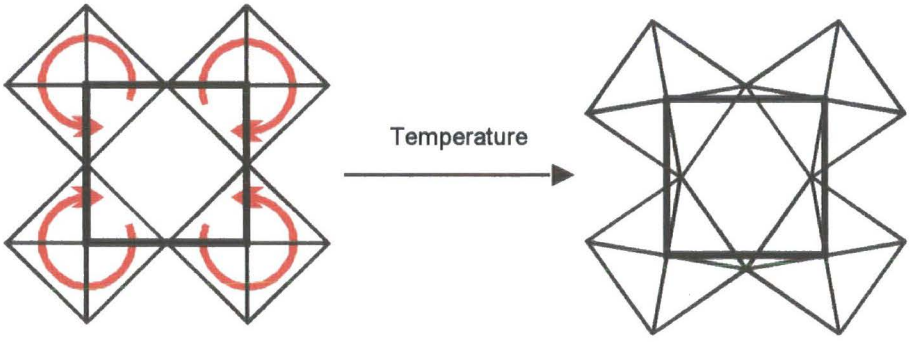

Figure 1-6: 2D schematic of the effect of rigid unit modes, shown for 4 octahedra.

In order for RUMs to cause significant contraction, the structure must be able to bend at the atoms joining the polyhedra, but the polyhedra themselves must be relatively rigid. This property is therefore usually found in oxide frameworks where one of the other elements is capable of forming very strong covalent bonds, typically Si, P, Zr, V, W or Mo. Where small distortions of the polyhedra occur, these phonons are known as quasi-Rigid Unit Modes (qRUMs).

The effect of these RUMs on the size of the unit cell was characterised by Welche *et al.*[9] For Figure 1-6 ,the area of the 2D unit cell is given by Equation 1-5, where $A(\theta)$ is the unit cell

area for a tilt angle of θ, A_0 is the cell area at $\theta = 0$ and η_A is a constant for a given sets of RUMs.

$$A(\theta) = A_0 \cos^2 \theta \approx A_0(1 - \eta_A \theta^2) \qquad \text{Equation 1-5}$$

If the tilt angle at a certain temperature ($<\theta^2>_T$) is treated as an average distortion away from the unrotated model, then Equation 1-5 is modified to give Equation 1-6.

$$A(T) \approx A_0(1 - \eta_A <\theta^2>_T) \qquad \text{Equation 1-6}$$

If $<\theta^2>_T$ is modelled as a simple harmonic motion, then the cell area can be defined by Equation 1-7, where k_b is the Boltzmann constant, I the moment of inertia, ν the vibrational frequency and T temperature. Thus the size of the unit cell will decrease with increasing temperature.

$$A(T) \approx A_0\left(1 - \eta_A \frac{k_b T}{I\nu^2}\right) \qquad \text{Equation 1-7}$$

The number of RUMs (also known as floppy modes) in a system is equal to F – C,[10,11,12] where F is the number of degrees of freedom and C is the number of constraints. The number of degrees of freedom for polyhedron is typically 6 (3 possible rotations and 3 possible translations in space). Polyhedra are constrained by the corner atoms being shared with other groups. For tetrahedra there will be 4 bridging atoms, each restrained in 3 directions. Those 12 constraints are each shared between the 2 polyhedra they are part of, giving a theoretical total of six constraints. The fact that F = C = 6 initially seems to imply the number of RUMs (F - C) will be zero. However, it was shown by Dove and co-workers[13,14] that symmetry means some of the constraints are not independent, effectively lowering their number. This means RUMs are more likely to be present where there is a high symmetry around tetrahedra.

1.3. Framework Materials Demonstrating NTE

The majority of work presented in this thesis focuses on the AM_2O_7 family of materials, in which the thermal expansion expected due to longitudinal vibrations can be counteracted by RUMs/qRUMs. This family is discussed in detail in section 1.4. There has also been significant work on 2 related families which demonstrate NTE due to RUMs/qRUMs, AM_2O_8 and $A_2M_3O_{12}$ materials.

1.3.1. AM_2O_8 Materials

AM_2O_8 materials form an infinite framework, consisting of corner-sharing AO_6 and MO_4 polyhedra. AO_6 octahedra are connected to 6 different MO_4 tetrahedra, but each tetrahedron is only connected to 3 octahedra, with one oxygen atom only connected to the central M

atom. The most widely studied material in this group is ZrW_2O_8.[15,16,17,18,19] The room temperature structure was solved independently by Mary *et al.*[15] and Auray *et al.*[19] and is shown in Figure 1-7. The significant interest in this material is due to the two large regions over which the NTE is negative and linear, as shown in Figure 1-8, and its cubic symmetry giving isotropic thermal expansion.

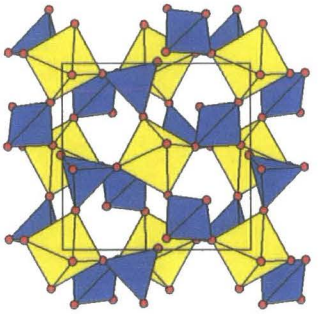

Figure 1-7: Room temperature structure of ZrW_2O_8. WO_4 tetrahedra are in blue, ZrO_6 octahedra in yellow and oxygen atoms in red.[15]

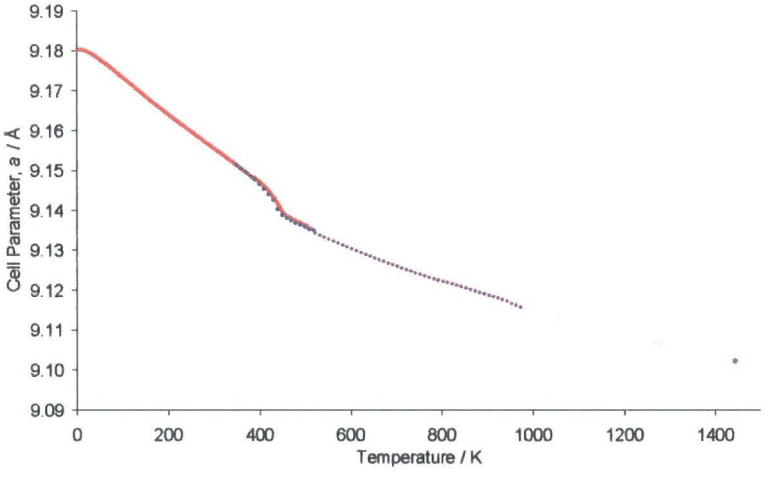

Figure 1-8: Thermal expansion of ZrW_2O_8. The red and blue points show results from neutron diffraction on warming and cooling respectively.[16] Purple points show the results of dilatometry measurements.[20] A single neutron diffraction measurement was taken at 1443 K,[21] with the dashed line an extrapolation of the cell parameter into the unstable region.

At room temperature ZrW_2O_8 has $P2_13$ symmetry. Above 448 K oxygen migration occurs, and the symmetry changes to $Pa\bar{3}$. This could cause problems in some applications. Therefore structural modifications based on substitution at the Zr site (with Hf, Sn, Sc, In or Y) or at the W site (with Mo) have been investigated. All of the substituted materials have the same basic structure and still demonstrate the order-disorder phase transition & NTE.

Yamamuri *et al.*[22] measured the order-disorder phase transition in HfW_2O_8 at 463 K using calorimetry. This increase in temperature of the transition was ascribed to the greater strength of Hf-O bonds compared to Zr-O bonds. The substitution of Sn for Zr lowered the transition to 400 K, due to the weaker Sn-O bonds.[23] Doping with lanthanide ions produced a contraction of the unit cell due to the 3+ ions causing oxygen vacancies. This was also found to lower the

phase transition despite only small amounts of doping (less than 4%). This is possibly due to the vacancies making it easier for oxygen migration to occur.

$ZrMo_2O_8$ shows a similar pattern of thermal contraction to ZrW_2O_8, only with a transition from static to dynamic disorder at 200 K,[24] significantly lower than ZrW_2O_8 and usefully below room temperature. The order-disorder phase transition for $ZrMoWO_8$ was found to begin at ~ 270 K on slow cooling. As shown in Figure 1-9, if the material is quench-cooled after formation, the disordered phase is kinetically stable at low temperature and reversion to the ordered phase is unfavourable below ~ 205 K. There is only a small temperature range where the disordered form is neither kinetically or thermodynamically stable, where the "hump" in the unit cell parameter occurs on warming. Chapter 3 uses the kinetics of this process as a test example of the parametric Rietveld refinement methods developed there; further discussion of the order-disorder transition is given in that chapter.

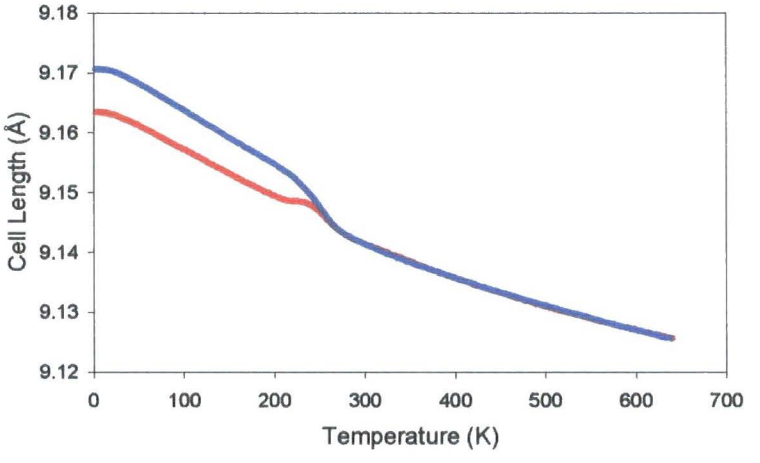

Figure 1-9: Plot of the thermal expansion of $ZrMoWO_8$. The red data are from warming a quench-cooled sample, the blue data are on subsequent cooling.

1.3.2. $A_2M_3O_{12}$

The orthorhombic phases of the $A_2M_3O_{12}$ family (where A^{3+} = Sc, Zr, Fe, Lu and others; M^{6+} = Mo and W) also demonstrate NTE. Due to the structure, thermal contraction only occurs along the a and c axes, with expansion in b, but the overall effect is a contraction of volume. This anisotropic thermal contraction makes it more difficult to make useful materials from them compared to the AM_2O_8 family. The basic structure is shown in Figure 1-10; it again consists of AO_6 octahedra corner sharing with MO_4 tetrahedra; in contrast to ZrW_2O_8, both octahedra and tetrahedra share all corners.

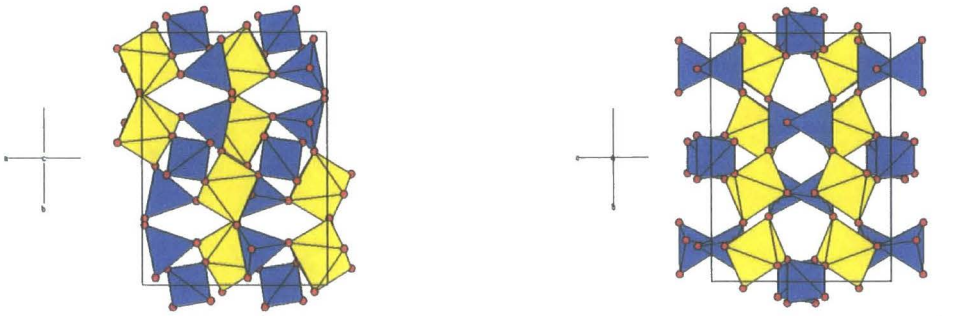

Figure 1-10: Structure of $Sc_2(WO_4)_3$ by Evans *et al.*[25] ScO_6 octahedra are shown in yellow, WO_4 tetrahedra in blue and oxygen atoms in red.

1.3.3. Other NTE materials

In addition to the framework materials described above, a large number of zeolites also demonstrate NTE.[26] For most zeolites this is believed to be primarily due to RUMs, although other types of transverse vibration have been suggested as a cause.[27] A range of other materials also show NTE, from certain polymers,[28] foams,[29] metal oxides such as Ag_2O and gold-nanoparticles.

1.4. Introduction to AM_2O_7 Materials

The AM_2O_7 family of materials (where A is a 4+ metal ions, either Si, Ge, Sn, Pb, Ti, Zr, Hf, Mo, W, Re, Sb, Ce, Th, Pa, Np, U or Pu; M is either P^{+5}, V^{+5} or As^{5+}) show interesting thermal properties, with several members showing either low or negative thermal expansion. This has led to significant interest in their structure and they form one of the main areas of research in this thesis. Details of previous research into this field are given in this section.

The first structural model for this family was produced by Levi and Peyronel[30] in 1935. This described ZrP_2O_7 using $Pa\bar{3}$ symmetry with the structure shown in Figure 1-11. The unit cell length was given as 8.2 Å. Further work described PbP_2O_7[31] and ZrV_2O_7[32] as having similar structures. Most AM_2O_7 materials have at least one polymorph approximately isostructural to these, which are henceforth referred to as pseudo-cubic phases; some members of the family also show polymorphs with radically different structures.

The structure consists of an infinite network of AO_6 octahedra and M_2O_7 groups consisting of two, corner-linked MO_4 tetrahedra. The structure can be thought of as analogous to that of NaCl, with the AO_6 centred on the Na sites and the central oxygen of M_2O_7 on the Cl site. The presence of the M_2O_7 group lowers the symmetry from $Fm\bar{3}m$ to $Pa\bar{3}$. The AO_6 octahedra share an oxygen atom with six different M_2O_7 groups, which likewise share their six external oxygen atoms with six different AO_6 groups. The oxygen atoms bonded to two M atoms are referred to as $O_{bridging}$ and those bonded to one M and one A atom as O_{AM} from here onwards.

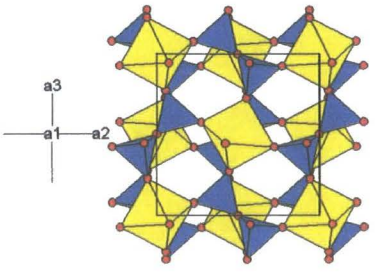

Figure 1-11: Structure of ZrP_2O_7 as described Levi and Peyronel. AO_6 octahedra are in green, PO_4 tetrahedra are in blue and oxygen atoms are in red.

It was noted by several researchers that, due to the M_2O_7 groups lying on the $\bar{3}$ axis, there were energetically unfavourable linear M-O-M groups. Typical P-O-P bond angles are between 130° and 160°. These structures would also require unusually short M-O bond lengths.

The first study to provide insight into this problem was by Vollenkle *et al.*[33] The improvement in diffraction techniques by 1963 enabled the detection of additional, very weak peaks in the diffraction pattern of GeP_2O_7. These could be fitted by a 3 x 3 x 3 supercell of the original model. Vollenkle *et al.* suggested that the symmetry of the supercell remained $Pa\bar{3}$. Changing from the subcell model to the supercell model removes 26/27 of the translational symmetry elements and 2/3 of the $\bar{3}$ axes. This enables 4 of the 6 crystallographically unique P_2O_7 groups to distort away from the linearity; due to differing multiplicities, 96 of the 108 groups in the unit cell can bend. This distortion of P-O-P angles is the main energetic driving force in the formation of the supercell.

Superstructure peaks have now been detected for almost all AM_2O_7 compounds at room temperature and a number have been shown to have lower symmetry than $Pa\bar{3}$ (for example ZrP_2O_7,[34] GeP_2O_7 and SnP_2O_7.[35] For some of these materials supercell to subcell phase transitions have been detected, for example ZrP_2O_7 shows this at 293°C. This is due to the P-O-P groups changing from being statically disordered from linearity to being vibrationally disordered. The time-averaged position of the oxygen is directly between the two phosphorus atoms in these high temperature phases, but it vibrates around this position, thus maintaining non-linearity. A schematic of this is shown in Figure 1-12. The thermal expansion, which is low before the phase transition for all of these compounds (e.g. $\alpha_v = 3.3 \times 10^{-5}\ K^{-1}$ for GeP_2O_7[36]), decreases even further after it. In some cases, such as ZrV_2O_7, it becomes negative. This is due to the presence of quasi-rigid unit modes, which are discussed in section 1.2.5.

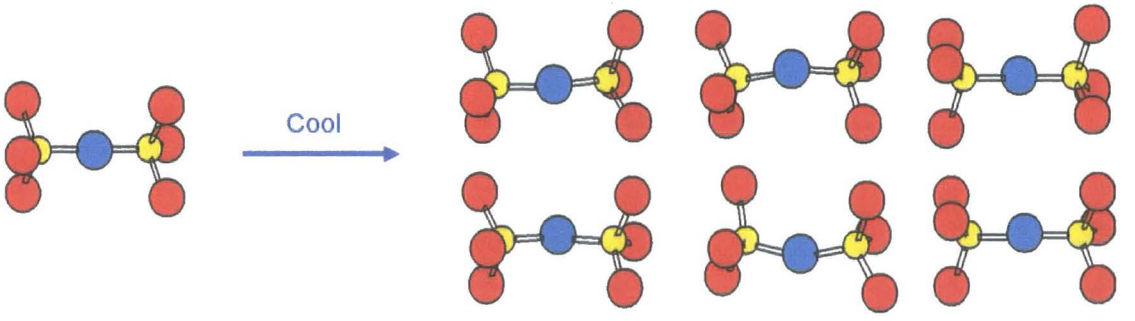

Figure 1-12: The changes in P_2O_7 groups in ZrV_2O_7 at the subcell to supercell phase transition.

A few members of the group, such as SnP_2O_7, do not show this supercell to subcell transition. In the case of SnP_2O_7, it shows a series of different 3 x 3 x 3 supercells on heating. It can be hypothesised at sufficiently high temperatures that this phase transition would occur, but the compound breaks down before this.

All of the space groups detected for this series of compounds are non-isomorphic subgroups of $Pa\bar{3}$. These are shown in Figure 1-13. Individual members of the AM_2O_7 family are discussed in sections 1.5 to 1.8.

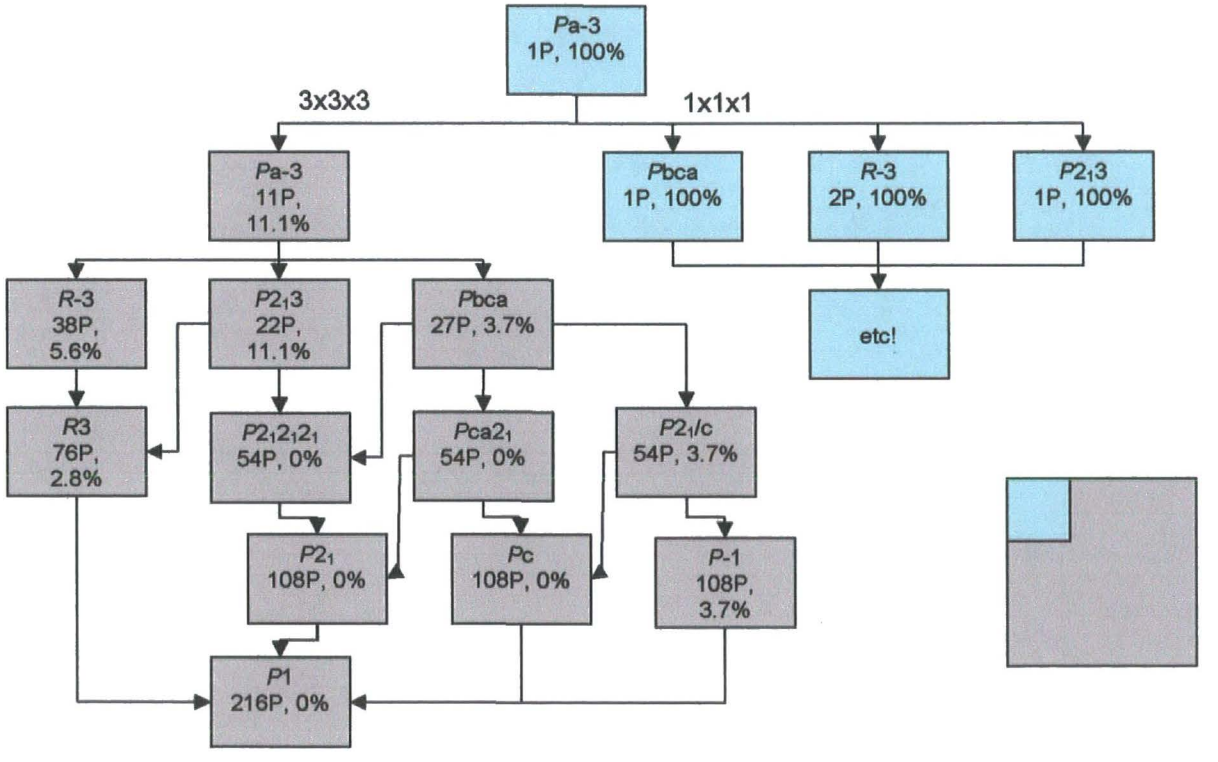

Figure 1-13: Allowed space groups for pseudo-cubic AM_2O_7 materials. The number of phosphorus environments and percentage of linear P-O-P groups is also shown for each space group.

1.5. AM_2O_7 Material where A is a Group 14 element

1.5.1. SiP_2O_7

A number of different polymorphs of SiP_2O_7 exist. These include materials with monoclinic, hexagonal, tetragonal and cubic symmetries, with the latter being of particular interest here.[37,38,39,40] An overview of the various phases reported in the ICSD is given in Table 1-1.

Name	Crystal System	a (Å)	b (Å)	c (Å)	β (°)	Reference
AI	Cubic	22.418	—	—	—	33
AIII	Monoclinc	4.73	6.33	14.71	90.1	37
AIV*	Monoclinic	4.733	12.019	7.654	91.03	37,38
BI	Hexagonal	8.18	—	11.85	—	37
Form I	Hexagonal	4.72	—	11.82	—	38
Form III	Tetragonal	14.20	—	7.39	—	38

Table 1-1: Reported phases of SiP_2O_7. All unit cell parameters quoted are at room temperature. *Form AIV is also known as form II.

All these phases contain silicon octahedra, instead of the more usual tetrahedral coordination. This can be related to the high electronegativity of the other element (phosphorus) in the material.[41] The structure of the monoclinic phase AIII has been solved by Bissert *et al.*[39] in space group $P2_1/c$ and can be described in terms of corner sharing SiO_6 octahedra and P_2O_7 pyrophosphate groups. The structure is shown in Figure 1-14 a. It contains only one type of P_2O_7 group which is bent with a P-O-P angle of 139.2°. The monoclinic form AIV was solved by Leibau & Makart[37] and is closely related but Tillmanns *et al.*[42] proved using connectivity analysis that the two monoclinic forms of silicon phosphate, AIII and AIV, were not lower symmetry distortions of the cubic form and were also structurally different to one other.

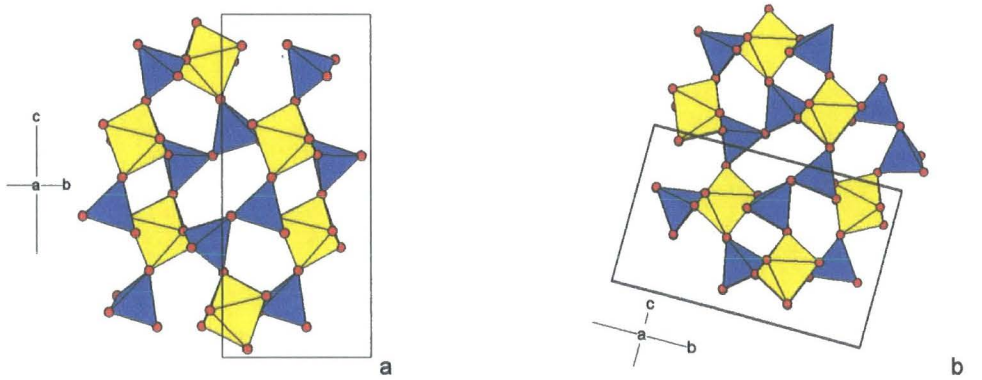

Figure 1-14: (a) shows Phase AIII,[39] (b) phase AIV.[41] SiO_6 octahedra are shown in yellow, PO_4 tetrahedra in blue and oxygen atoms are in red here and in the remainder of this section.

Poojary *et al.*[40] determined the structure of hexagonal SiP_2O_7, known as Form I. This is shown in Figure 1-15. Form I contains layers of silicon octahedra joined by linear P-O-P links. The P-O-P links in the structure are quite unusual for several reasons. Firstly the bond angle is 180°, normally an unfavourable situation. Secondly, as can be seem from the picture in the ab plane, the two PO_3 groups are nearly eclipsed with a torsion angle of 14.7°. The R_{Bragg} of the refinement was 16%, suggesting the model may not entirely correct, probably due to some additional distortion of the P-O-P bonds away from linearity.

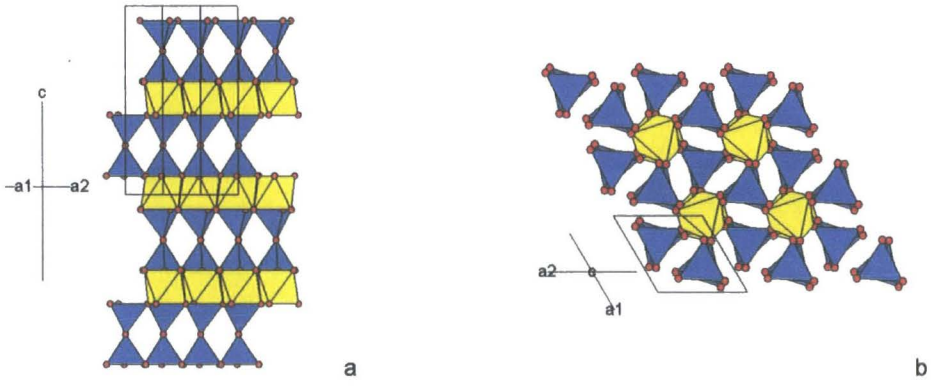

Figure 1-15: Proposed structure of the hexagonal form I of SiP_2O_7,.

The most relevant phase to the work of this thesis is polymorph AI. It was initially described using a unit cell with 4 formula units and $Pa\bar{3}$ symmetry by Levi *et al.*[30] Vollenkle *et al.*[33] discovered additional low intensity, high angle peaks which could not be fitted with this model. These could be only be explained by using a 3 x 3 x 3 supercell. The two models are shown in Figure 1-16.

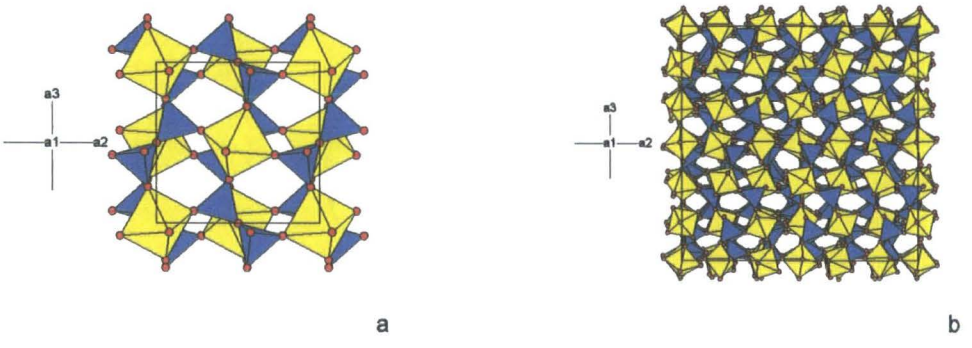

Figure 1-16: The structure of the cubic phase AI. (a) is the subcell, with the supercell shown in (b).

SiP_2O_7 was the first cubic AM_2O_7 material to have the full structure of the supercell determined. This was perform by Tillmann *et al.*[42] in 1973 using a combination of distance least-squares (DLS) calculations and single crystal X-ray diffraction data. In DLS calculations, ideal values for interatomic angles and bond lengths are set, together with a series of

penalties for the angles and lengths distorting from these values. The structural model is then refined to minimise these penalties, whilst simultaneously fitting the experimental diffraction pattern. This is analogous to the method developed in section 4 which uses DLS calculations alongside Rietveld refinement of powder diffraction data. There are 6 unique P_2O_7 groups in this structure. 4 groups are in general positions (m=24) and have bent P-O-P bonds. The other two types of P_2O_7 groups lie on a 3 fold axis and therefore contain linear P-O-P linkages. The theoretical model using a $Pa\bar{3}$ supercell was also supported by ^{31}P MAS and 2D exchange NMR by Hartmann *et al.*[43] Ten separate peaks were observed, thus giving the minimum number of phosphorus environments. A $Pa\bar{3}$ supercell contains 11 environments, thus the NMR signals of two types of phosphorus are assumed to overlap. While it is possible that the space group could be lower symmetry, with more phosphorus environments, it seems unlikely given that the next lowest number of phosphorus environments is 22, for space group $P2_13$ (see Figure 1-13) which would require a very high degree of overlap in the NMR data.

Three alternate models were suggested by Iuliucci and Meier[44] to account for the linear groups in the model proposed by Tillmann *et al.* The first of these was a statistically disordered arrangement of locally bent P_2O_7 groups - i.e. the diphosphate groups that appeared linear were on average linear but actually distorted. The rationale for this model was that the difference in the diffraction pattern caused by having 12 of the 108 diphosphate groups in the unit cell modelled as linear rather than bent would be minimal. In the work of Tillmann *et al.* it is possible that these subtle distortions could not be resolved. The second possibility is a dynamically disordered system, where P_2O_7 units interconvert at a much slower rate than the vibrational frequency. This would have a similar effect on the diffraction pattern to theory one. The third option is that the structure contains truly linear diphosphates group, with the bridging oxygen possibly having unusually large thermal motion.

Iuliucci and Meier used 2D TOBSY NMR to distinguish between these three possibilities. The method was based on measuring the chemical shift anisotropies (CSA) of the atoms relative to the molecular frame. It gave similar results to those produced by diffraction, with two types of linear P_2O_7 groups and four types of bent P_2O_7 groups. They concluded that this ruled out a statistically disordered arrangement of locally bent P_2O_7 groups, meaning that either theory two or three applied to this material. One of the linear groups contained only a single phosphorus environment; this signified an inversion centre and therefore the P-O-P angle must be truly linear. For the second P_2O_7 unit either theory could be correct, but no averaging of the CSA tensor was observed, which would be expected for dynamic disordering. This was used to conclude that these groups were truly linear and therefore theory 3 was correct.

1.5.2. GeP_2O_7

Three polymorphs of GeP_2O_7 are well established in the literature. The alpha form was

synthesised *via* the dehydration of α-$Ge(HPO_4)_2 \cdot H_2O$.[36] On heating to 950°C the alpha form converts to the beta form. If the alpha phase is rapidly heated to around 1020°C, then the pseudo-cubic gamma phase is formed instead. Near to 1160°C the gamma form decomposes with loss of P_2O_5 to form $GeO(PO_4)_6$.

The alpha form of germanium phosphate has low crystallinity and its unit cell has not been reported. It is believed to be layered due to the relative peak intensities, and it has been hypothesised that the structure is related to form I of SiP_2O_7. β-GeP_2O_7 is triclinic with a space group of $P\bar{1}$ and has cell dimensions of a = 7.730(1) Å; b = 6.724(1) Å; c = 4.6543(8) Å; α = 105.39(1)°; β = 92.81(1)°; γ = 91.49(1)° at room temperature.[45] It contains corner sharing GeO_6 octahedra and PO_4 tetrahedra. It contains a single unique P_2O_7 group, which contains two crystallographically independent phosphorus atoms. The P-O-P bond angle is 127°. This structure is shown in Figure 1-17.

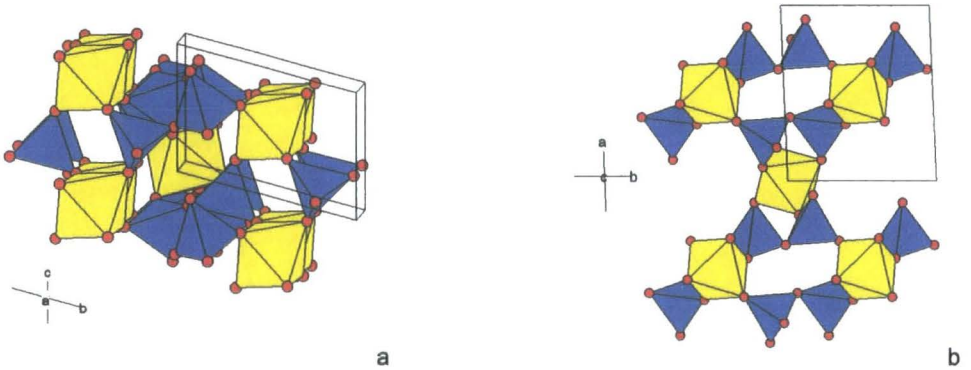

Figure 1-17: Two views of the structure of triclinic β-GeP_2O_7.

The gamma form has a structure related to cubic SiP_2O_7 and, like the silicon containing compound, was initially believed to have a simple cubic $Pa\bar{3}$ 1 x 1 x 1 structure. This assumption has been shown to be incorrect by Losilla *et al.*[36] using both X-ray diffraction and ^{31}P MAS-NMR. The diffraction pattern gave a peak splitting which could not be modelled by a cubic unit cell. It was fitted using a Le Bail fit in $P2_1/c$ using a tripled monoclinic cell of a = 22.8647(4) Å, b = 22.8783(4) Å, c = 22.9429(4) Å and β = 90.328(1)°.

1D ^{31}P NMR data showed at least 35 ^{31}P peaks, giving the minimum number of phosphorus environments present. Three monoclinic space groups, $P2_1/c$, $P2_1$ and Pc, can be formed by removing symmetry elements from a tripled superstructure; these have 54, 108 and 108 independent phosphorus sites respectively. No full structural description of this phase has been reported. Losilla *et al.* investigated the thermal expansion of γ-GeP_2O_7 up to 750°C. This gave near-linear thermal expansion with $\alpha_v = 3.3 \times 10^{-5}$ K^{-1} and no evidence of phase transitions. The structural chemistry of GeP_2O_7 is discussed in more detail in section 5.

1.5.3. SnP_2O_7

Huang *et al.*[46] described two pseudo-cubic room temperature polymorphs of tin phosphate. Both are modifications of the general structure shown in Figure 1-11. The first was synthesised at low temperature and the linear P_2O_7 groups of the Levi and Peyronel model are replaced by bent P_2O_7 groups. Huang *et al.* suggested that the values of these angles varied throughout the structure.

This form could be converted irreversibly by heating to Type II. Type II has a 3 x 3 x 3 superstructure, analogous to the SiP_2O_7 superstructure discussion in section 1.5.1. Both structures were initially believed to be cubic.

As part of a wider study on these materials, Gover *et al.*[35] examined the structural properties of type II tin phosphate using X-ray, electron and neutron diffraction. From the X-ray data shown in Figure 1-18, they deduced that two phase transitions occur upon heating: one at 550 K and a second at 850 K. The unit cell parameters showed strong hysteresis with the reverse phase transitions occurring at ~300K and ~750 K on cooling. Preliminary experiments suggested that this was independent of the cooling rate. All three phases are pseudo cubic.

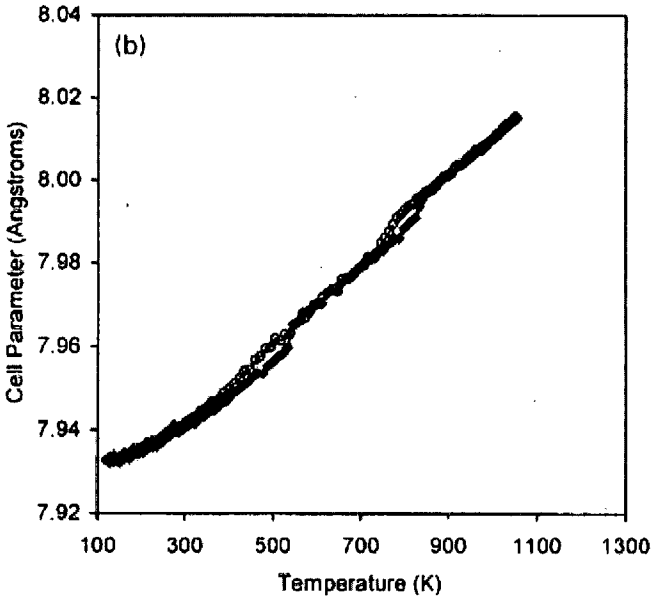

Figure 1-18: Subcell parameters of SnP_2O_7 derived using a cubic model by Gover *et al.*,[35] on both warming (filled points) and cooling (open points).

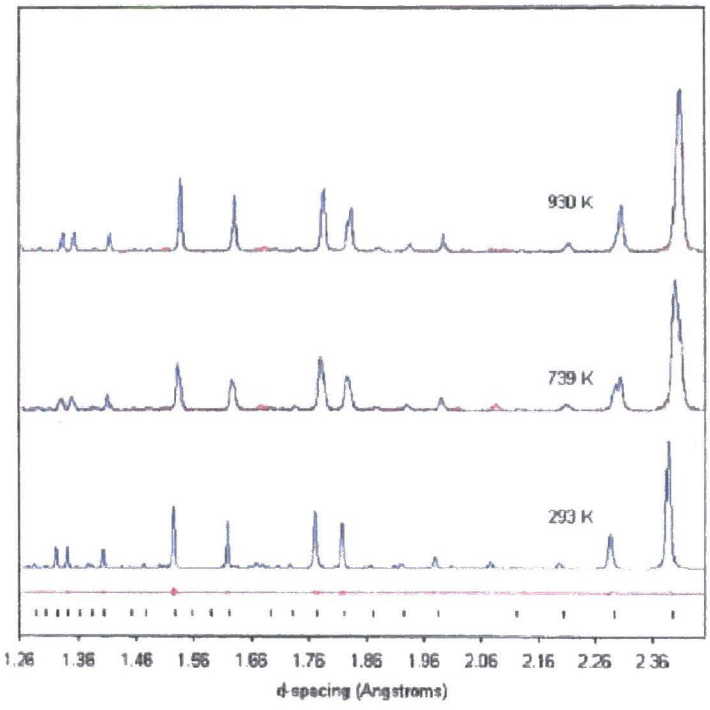

Figure 1-19: Pawley fits to X-ray diffraction data by Gover *et al.*,[35] with observed data shown as red and the calculated pattern in blue. For the 293 K data, the difference between the observed and the calculated patterns is shown below the data and the position of reflections predicted by a $Pa\bar{3}$ subcell model are shown as tick marks.

The strong reflections of the room temperature phase can be fitted by a cubic subcell model with a unit cell length of 7.944 Å at room temperature. Between 550 K and 850 K it was reported that a triclinic cell was required to fit the splitting pattern of the subcell reflections. The data was fitted with a unit cell of a = 7.9804 Å, b = 7.9708 Å, c = 8.003 Å, α = 90.08°, β = 90.38° and γ = 90.10° at 739 K. Above 850 K the subcell could be described using a rhombohedral cell with a = 8.0132 Å and α = 90.18° at 1073 K.

Electron diffraction of the room temperature structure by Gover *et al.* suggested that there was no extinction condition on the <hk0>* reflections. Therefore the a-glide expected for $Pa\bar{3}$ is not present, ruling out this space group. This suggests the space group is either $P2_13$, $P2_12_12_1$ or a even lower symmetry isomorphic subgroup of $Pa\bar{3}$. Electron diffraction patterns showing the supercell reflections are shown in Figure 1-20.

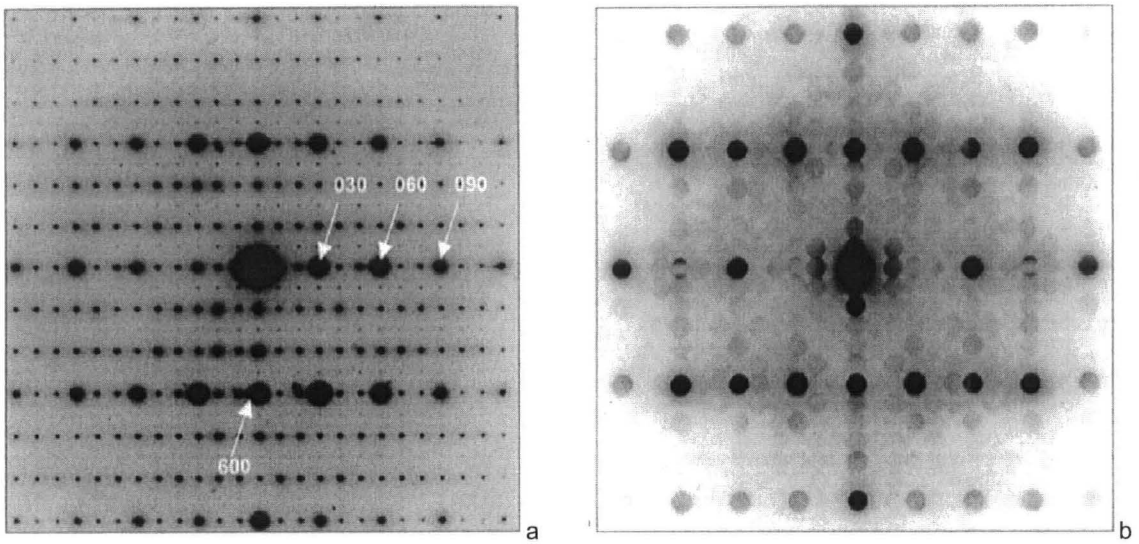

Figure 1-20: (a) and (b) show the electron diffraction and the micro-diffraction patterns respectively, by Gover *et al.*[35] Both are viewed down the 001 axis with 100 down the page and 010 across the page. There is no extinction condition on the hk0* reflections meaning that the a-glide expected for $Pa\bar{3}$ is not present.

Fayon *et al.*,[47] probed the symmetry of the supercell at room temperature by analysis of the coupling of the phosphorus atoms using 2D refocused INADEQUATE ^{31}P NMR experiments. This work showed the presence of at least 96 symmetry independent phosphorus atoms in the unit cell. The two space groups consistent with these results are $P2_1$ or Pc, each with 108 phosphorus environments in the unit cell, but it could not be determined which of these was correct. A slightly better fit of the data could be achieved by using 216 independent phosphate groups, rather than 108. This suggests $P\bar{1}$ or P1 symmetry, however this would require a greater amount of peak overlap and given small improvement in fitting the authors still favoured $P2_1$ or Pc as the space group. Of these two space groups, $P2_1$ seems the more likely given the 2_1 axis shown in the electron diffraction pattern. This compound is investigated further in section 5.

1.5.4. PbP_2O_7

There has been less interest in PbP_2O_7 than other members of this family. It was initially synthesised by Peyronel[31] in 1939 by heating PbO_2 and H_3PO_4 in a 1:3 ratio to 300°C for 3 hours. It was described as having $Pa\bar{3}$ symmetry with a unit cell length of 8.01 Å.

Electron diffraction work by Brindley[48] showed that the structure was actually incommensurate at room temperature, which prevented a full structure solution. The electron diffraction pattern is shown in Figure 1-21. The large subcell peaks are clearly visible (-1 0 1 and -1 1 0 are labelled in Figure 1-21). If the structure was a commensurate 3 x 3 x 3 superstructure then the small supercell peaks highlighted by the yellow circles would appear on the intersection of the dotted and continuous yellow lines.

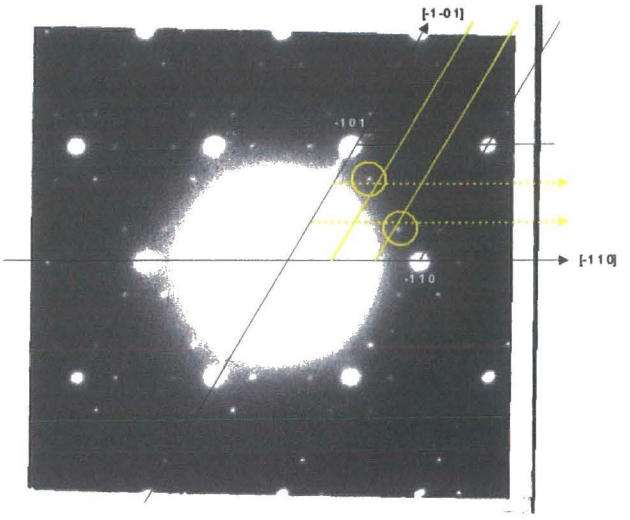

Figure 1-21: Electron diffraction image of PbP_2O_7 down the [111] axis by Brindley.[48]

This was supported by ^{31}P NMR, which showed one large, broad peak. This suggests a large number of subtly different crystallographic environments. This could have been produced by a poorly crystalline material, but this option was ruled out by ^{31}P 2D 2Q POST C7 NMR,[49] which showed no cross-coupling peaks.

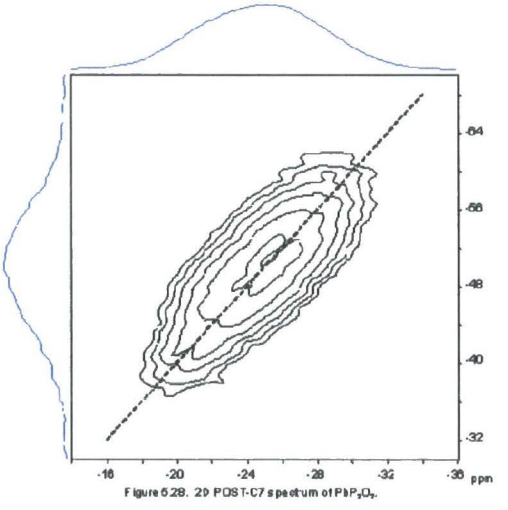

Figure 6.28. 2D POST-C7 spectrum of PbP_2O_7.

Figure 1-22: ^{31}P 2D 2Q POST C7 NMR[49] of PbP_2O_7.

PbP_2O_7 is believed to be the only incommensurate structure of this family of materials at room temperature. Variable temperature X-ray diffraction[48] showed no obvious phase transitions between 100 K and 700 K.

1.6. AM_2O_7 Materials where A is a group IV metal

1.6.1. TiP_2O_7

Cubic titanium pyrophosphate has been studied by a number of techniques including X-ray

diffraction, neutron diffraction and ^{31}P NMR.[50,51,52,53] Soria *et al.*[52] synthesised TiP_2O_7 by heating $Ti(HPO_4)_2.H_2O$, with the product starting to form around 573 K. By 973 K, pure cubic titanium phosphate had been formed. 1D NMR of the TiP_2O_7 at room temperature gave 9 peaks. Two of the peaks were of significantly higher intensity than the other seven. This suggested 11 phosphorus environments, with two pairs of peaks overlapping to form the two larger peaks. This would be consistent with a 3 x 3 x 3 superstructure with $Pa\bar{3}$ symmetry.

X-ray diffraction measurements were carried out by Sanz *et al.*[50] Distance least-squares calculations were used to obtain a reasonable starting point for Rietveld refinement of the data using space group $Pa\bar{3}$. The final structural model produced gave significant distortion in the PO_4 tetrahedra, with O-P-O bond angles in between 101° and 117°. The lengths of $P\text{-}O_{AM}$ bonds was between 1.50 and 1.53 Å

Helluy *et al.* [51] carried out a more detailed NMR analysis. The initial 1D NMR was consistent with that published by Soria *et al.* but contained 8 peaks. Three of the peaks were significantly larger than the others, suggesting they each contained two overlapping peaks. These data were consistent with $Pa\bar{3}$ symmetry but lower symmetry space groups are also possible if there was significant overlap of peaks. The most likely of these was $P2_13$ with 22 phosphorus environments. In order to distinguish between these two, a 2D NMR TOBSY experiment was preformed. This type of experiment shows $^2J_{iso}$ couplings clearly, but suppresses through space homonuclear dipole interactions. This shows which phosphorus atoms are in the same P_2O_7 group by giving an off-diagonal signal. A $Pa\bar{3}$ superstructure would have six different P_2O_7 environments, of which five contain two different phosphorus atoms. Therefore five off-diagonal signals would be expected. Four of these signals were clearly present. One of the peaks present on the diagonal was possibly two signals with similar shift values, these two were possibly coupled, with the off-diagonal signal naturally very close to both peaks. This would account for the fifth off-diagonal peak. Therefore the symmetry was confirmed as $Pa\bar{3}$.

Norberg *et al.*[53] carried out single crystal X-ray diffraction measurements. From these they derived the superstructure shown in Figure 1-23. The structure was solved in $Pa\bar{3}$ with a unit cell length of 23.5340 Å. The results of this were compared to those for ZrV_2O_7[54]. TiP_2O_7 gave much larger supercell peaks, the largest being 30 % of the size of the largest subcell peak, rather than the 1 % found for ZrV_2O_7. This means TiP_2O_7 is more heavily distorted from the ideal subcell model than ZrV_2O_7.

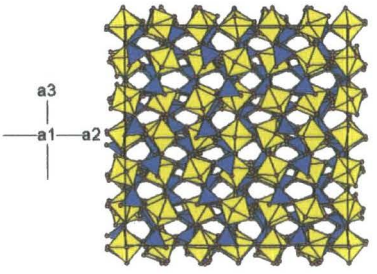

Figure 1-23: Superstructure of TiP_2O_7 by Norberg *et al.* [53]

Carlson *et al.*[55] studied the properties of TiP_2O_7 at high pressure, but discovered no phase changes with increasing pressure with measurements up to 40 GPa. The volume compressibility was 1.6×10^{-2} GPa^{-1} over the range of 0 to 5 GPa, smaller than the 2.2×10^{-2} and 2.8×10^{-2} GPa^{-1} found for ZrP_2O_7 and ZrV_2O_7 in the same work. The greater compressibility of the latter frameworks is due to the greater size of the cations. This leads to a more open framework which can be more easily distorted by increased pressure. The more open framework also leads to the lower thermal expansion of the later materials, with very open framework of ZrV_2O_7 showing NTE above the phase transition.

Lipinska-Kalita *et al.*[56] carried out infra-red and Raman spectroscopy on TiP_2O_7 with increasing pressure. This showed a discontinuity between 6 and 7 GPa. Peaks from the low pressure material either became very broad or disappeared entirely. It was hypothesised that this was either due to true amorphisation of the material or the beginning of the formation of a high-pressure phase. If this phase nucleated throughout the sample, but lacked the thermal energy to form large crystallites, a huge number of tiny crystallites would form, giving an effectively amorphous material.

Lipinska-Kalita *et al.* also calculated the Grünesien parameters for each of the vibrational modes from their shift in frequency with pressure. Two symmetric stretching models of the PO_4 groups gave negative parameters, suggesting these contribute to the low thermal expansion found in the material. It should be noted however, that the calculated Grünesien parameters are within one ESD of zero.

1.6.2. ZrP_2O_7

ZrP_2O_7 is one of the most widely studied materials of the AM_2O_7 family.[57,30, 33, 34, 55, 58-66] Two room-temperature polymorphs have been discovered. Both contain corner-sharing PO_4 tetrahedra and ZrO_6 octahedra. Beta-phase zirconium pyrophosphate was synthesised by Andersen and Norby[57] by heating $Zr(HPO_4)_2$ to 688 K. This had Pnnm symmetry with unit cell parameters of a = 8.3127 Å, b = 6.6389 Å and c = 5.3407 Å. The structure is shown in Figure

1-24.

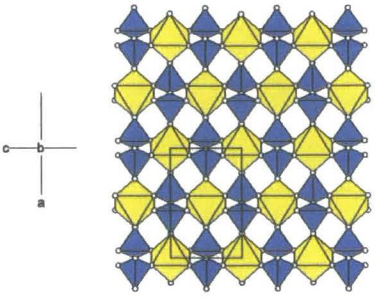

Figure 1-24: Beta zirconium phosphate by Andersen and Norby.[57] PO_4 tetrahedra are shown in blue with ZrO_6 octahedra in yellow.

Above 973 K beta zirconium phosphate transforms to the pseudo-cubic alpha form. The first model for its structure was proposed by Levi and Peyronel[30] as discussed in section 1.4. Additional supercell peaks were found by Vollenkle *et al.*[33] This gave a 3 x 3 x 3 superstructure with a cell length of 24.72 Å but was still modelled using $Pa\bar{3}$ symmetry. This was supported by studies by Chaunac[58] and Hagman & Kierkega.[59] A full structural model for the supercell was produced by Khosrovani *et al.*[65] using $Pa\bar{3}$ symmetry.

^{31}P NMR measurements have also been carried out to help determine the correct space group. Korthius *et al.*[66] fitted the heavily overlapping ^{31}P NMR spectrum using 12 peaks, with eleven of these believed to be caused by the eleven phosphorus environments in $Pa\bar{3}$ together with one impurity peak. Doubt was cast over this explanation by Anderson and Norby,[57] whose work showed the same peaks, despite the fact no impurity peaks appeared in the diffraction patterns before the formation of the alpha form. This was investigated by King *et al.*[34] 1-D NMR gave 13 resonances, meaning either alpha zirconium phosphate has lower symmetry than $Pa\bar{3}$ or impurities were present. ^{31}P 2-D exchange MAS NMR with an exchange time of 40 ms, showed cross-correlation between all of the peaks. This proved all the peaks were due to the same phase with no impurity present. ^{31}P 2-D double quantum NMR was used to show which phosphorus signals were from the same P_2O_7 groups. The data were consistent with the 27 phosphorus peaks produced by Pbca symmetry. This space group was also used to obtain excellent fits of both the previous NMR and diffraction data. A full structure solution in space group Pbca using powder diffraction data is presented in section 4, together with a comparison of a recent single crystal solution by Birkedal *et al.*[67]

Withers *et al.* [64] showed that at 294°C α-ZrP_2O_7 undergoes a transition from a 3 x 3 x 3 superstructure to the subcell. This phase transition can also be seen in the cell parameter data of Figure 1-25. Studies of the related material, ZrV_2O_7, showed this transition occurred *via* an incommensurate phase.[68] Withers *et al.* carried out electron diffraction measurements at 294°C, which showed intensity at positions that could only be produced by an

incommensurate structure. This raises the possibility that all supercell to subcell phase transitions in this series of material occur *via* an incommensurate structure. The incommensurate phases may only exist for a very small temperature range, thus hampering their detection. X-ray diffraction based evidence for this incommensurate structure is given in section 3.

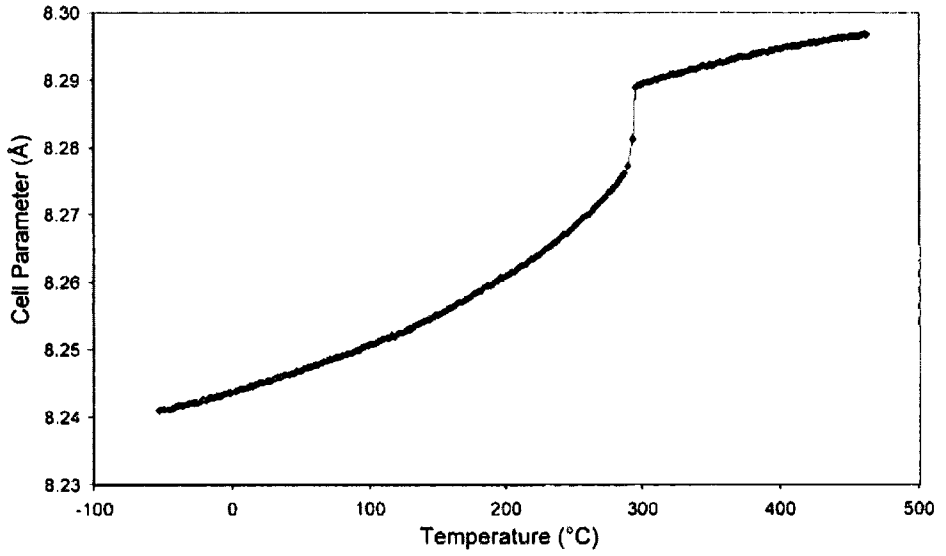

Figure 1-25: Thermal expansion of α-ZrP_2O_7 as a function of temperature by Withers *et al.*[64] Below 294°C the cell length is shown for the subcell.

High pressure studies of ZrP_2O_7 were carried out by Carlson *et al.*[55] No phase transitions were found up to 20 GPa. The rate of contraction was significantly greater for ZrP_2O_7 than for TiP_2O_7, as discussed in section 1.6.1.

1.6.3. ZrV_2O_7

Although there have been a number of studies into ZrV_2O_7, certain details of its structural chemistry remain unclear. It can be synthesised either by grinding $ZrOCl_2.8H_2O$ and NH_4VO_3 together and heating, or by mixing solutions of the two reagents. The material was first reported in 1939 by Peyronel[31] as a simple cubic phase. Work by Craig and Hummel[69] in the early 1970's revealed that it had the 3 x 3 x 3 superstructure common to these materials at room temperature and showed a series of phase transitions as a function of temperature. Perhaps the definitive thermal expansion data are those reported by Withers *et al.* which are shown in Figure 1-26. These data showed 2 phase transitions on warming at 350 K and 375 K

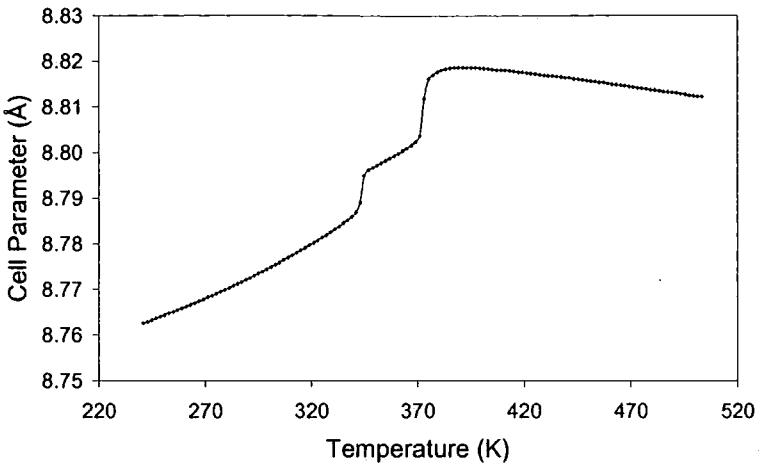

Figure 1-26: Thermal expansion of ZrV_2O_7 as a function of temperature.[68] Below 375 K the cell parameter has been divided by 3 to enable comparison with the cell parameters above the second phase transition. Note the negative thermal expansion above 375 K.

There have been a number of studies into the structure of ZrV_2O_7. Withers *et al.* took a series of electron diffraction measurements from room temperature to above the 2nd phase transition. At RT, a series of strong, subcell reflections existed with weak superstructure peaks in between them, with both sets of reflections having cubic symmetry. This supported the 3 x 3 x 3 superstructure model. At 365 K, ZrP_2O_7 showed incommensurate superstructure reflections. Although the subcell structure remained cubic, the supercell structure was not and the exact symmetry was not determined. Measurements above 375 K showed no supercell reflections.

Zirconium vanadate was studied by ^{51}V NMR between 298 K and 413 K by Korthius *et al.*[66] Below 353 K numerous ^{51}V environments were present in the NMR pattern, supporting the theory that ZrV_2O_7 has a superstructure at room temperature. Between 353 K and 403 K, only one broad peak was present. This supports the theory of an incommensurate structure with a large number of very similar vanadium environments. At 403 K two clear peaks were present, Korthius *et al.* explained this splitting as being due to quadrupolar coupling. Doubt was cast on this explanation by Hodgkinson *et al.*[70] as there was no change in the frequency difference between the two peaks when measurements were carried out on NMR spectrometers with different operating frequencies. It was therefore suggested that the splitting was due to slight distortion in symmetry which causes the two ^{51}V sites to be inequivalent and leads to dipolar coupling between them.

The superstructure for ZrV_2O_7 at RT was solved using single crystal diffraction by Evans *et al.*[54] The solution is shown in Figure 1-27. Systematic absences were found for 0kl, k = 2n. This suggested the structure had $Pa\bar{3}$ symmetry. The cell length was determined as 26.296 Å. Some weak violations of the symmetry conditions were found but the intensity of the strongest of these was only 1.3 % of the strongest supercell peak and 0.02 % of the strongest subcell

peak. These peaks were explained as being due to multiple diffraction effects.

The model of rigid polyhedra with flexible Zr-O-V links appears to be correct. Zr-O-V bond angles vary between 145° and 174°, with the variation in the internal polyhedra angles being much smaller. All the O-Zr-O angles lie between 88.0° and 92.0° and the O-V-O angles lie between 108.3° and 110.0°. The Zr-O distances are between 2.055 Å and 2.086 Å, with V-O bonds in Zr-O-V links between 1.665 Å and 1.682 Å. Small distortions of the polyhedra occur to facilitate the formation of non linear V-O-V groups.

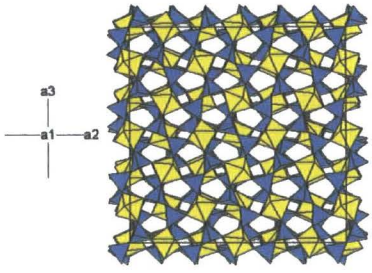

Figure 1-27: Full structure of ZrV_2O_7 from single crystal data by Evans *et al.*[54]

There are 11 crystallographically unique vanadium sites in 6 different V_2O_7 groups. Two of these groups lie on 3-fold axes, both are therefore constrained by symmetry to have bridging V-O-V angles of 180°. One of these two groups is on the centre of inversion and therefore has only one unique V environment. The other four groups each have two crystallographically independent vanadium sites. These groups have bridging angles of 159.3°, 162.9°, 166.2° and 167.6°. The incommensurate phase has not been fully characterised.

Carlson *et al.*[55] discovered a second ZrV_2O_7 phase above 1.5 GPa. This high-pressure phase, labelled β-ZrV_2O_7, is described with a tetragonal subcell with unit-cell parameters at 2.97 GPa of a = 8.3075 Å and c = 8.4029 Å. It has a 2 x 3 x 3 orthorhombic supercell but the symmetry of this could not be determined as each peak can be indexed using several close indices due to the very large unit cell. At 4 GPa β-ZrV_2O_7 undergoes amorphization.

1.6.4. $ZrV_{2-x}P_xO_7$

Korthius *et al.*[66] measured the thermal expansion of zirconium phosphate and zirconium vanadate solid solutions using dilatometry. The results of this are reproduced in Figure 1-28. ZrV_2O_7 converts from the superstructure to the subcell structure at a lower temperature than ZrP_2O_7. This is believed to be due to the low lying 3d orbital of vanadium being available for π bonding.[66] This stabilises the linear V-O-V groups, meaning the subcell structure can be formed at lower temperature.

ZrV_2O_7 has two phase transitions on heating, at 77°C and 102°C. As the phosphate content of

the material increases, these phase transitions occur at lower temperatures. For x = 0.1, the phase transitions occur at 66 and 89°C, for x = 0.2 the phase transitions occur at 48 and 67°C. For x = 0.3 only one phase transition occurred at 53°C, a direct 3 x 3 x 3 supercell to subcell transition. This composition still showed NTE above the phase transition. This transition occurs at lower temperature in $ZrV_{2-x}P_xO_7$ than for either ZrV_2O_7 or ZrP_2O_7. It was suggested by Korthius *et al.* that this may be due to the relative stability of linear P-O-V links compared to P-O-P and V-O-V links.

For the materials with a composition between $ZrV_{1.7}P_{0.3}O_7$ and $ZrVPO_7$, there is a single phase transition occurs around 60°C, with NTE above the phase transition. The scale of the NTE decreases with increasing phosphorus content. There appears to be a second phase transition at high temperature for all of these compositions, though this may be due to sintering of the pellets. $ZrV_{0.8}P_{1.2}O_7$ has no obvious phase transition until 650°C, with thermal expansion from RT to approximately 300°C, near zero thermal expansion until 400°C followed by weak NTE. Compositions between $ZrV_{0.6}P_{1.4}O_7$ and $ZrV_{0.2}P_{1.8}O_7$ show no obvious phase transitions, with low positive thermal expansion over the measured range.

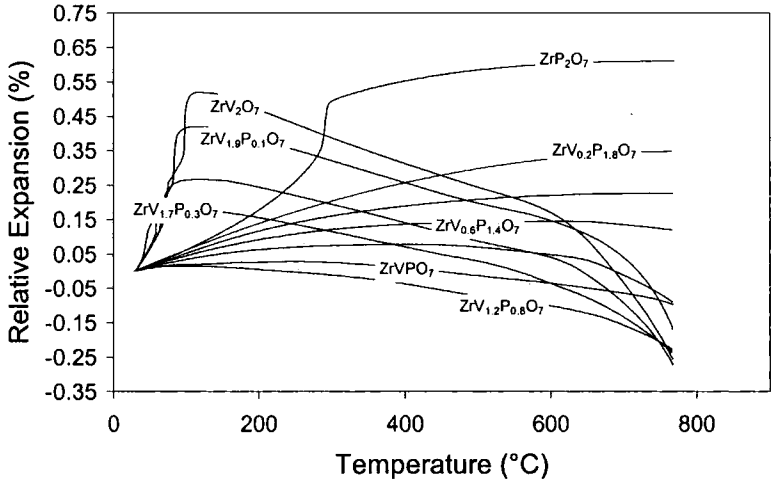

Figure 1-28: Relative thermal expansion of $ZrV_{2-x}P_xO_7$ series by Korthius *et al.* [66]

Korthius *et al.* also carried out ^{31}P NMR measurements on this series of compounds. Phosphorus atoms in VPO_7 groups have a lower chemical shift than those in P_2O_7 groups. By comparison of the intensities of the two peaks it was possible to determine the ratio of the two groups. It was determined that a mix of P_2O_7 and V_2O_7 was favoured over VPO_7 group for x = 1.6, but VPO_7 groups were favoured at x = 1.0. At x = 0.3, no P_2O_7 groups were detected. No conclusive reasons for this pattern were drawn.

1.6.5. HfP_2O_7

HfP_2O_7 was shown to contain 27 phosphorus sites by King,[49] using 2D refocused INADEQUATE NMR. This suggested it shared the same space group as ZrP_2O_7, having a

3 x 3 x 3 supercell with Pbca symmetry. The structure was determined from powder data by co-workers[71] using the same method as described in section 4 for ZrP_2O_7. The distortions of the pseudo-cubic unit cell for HfP_2O_7 and ZrP_2O_7 are similar as shown in Table 1-2. The average shift of the atomic positions between HfP_2O_7 and ZrP_2O_7 was 0.0693 Å. This showed that the two materials were essentially isostructural. This is unsurprising given their similar ionic radii, 0.71 and 0.72 Å[72] for Hf and Zr respectively for a 4+ ion surrounded by oxygen in octahedral geometry.

Cell length	ZrP_2O_7 cell lengths (Å)[67]	Distortion from the mean value for ZrP_2O_7 (%)	HfP_2O_7 cell lengths (Å)[71]	Distortion from the mean value for HfP_2O_7 (%)
a	24.7390(2)	0.022	24.652(2)	0.032
b	24.7184(2)	-0.061	24.6296(6)	-0.060
c	24.7431(2)	0.039	24.651(1)	0.028
mean	24.7335		24.6441	

Table 1-2: Comparison of absolute cell length and their relative shifts from metrically cubic symmetry between ZrP_2O_7 and HfP_2O_7.

Thermal expansion data were reported by Tait,[73] and are shown in Figure 1-29. On heating there was a phase transition from a 3 x 3 x 3 supercell to a subcell phase at ~580 K. On cooling, an incommensurate phase could be clearly detected between the two other phases. This was indexed with a modulation of 0.312.

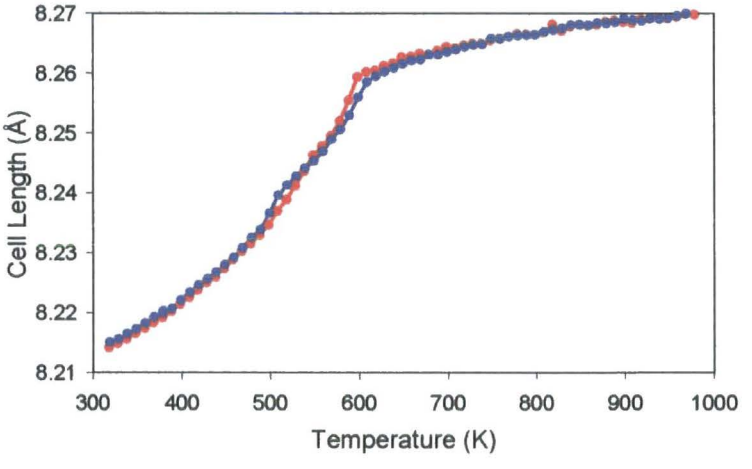

Figure 1-29: Thermal expansion data of HfP_2O_7 by Tait, with the heating cycle shown in red and cooling in blue.

1.6.6. HfV_2O_7 and $HfV_{2-x}P_xO_7$

The first structure model of HfV_2O_7 was by Baran.[74] This unit cell was cubic with a 26.3 Å cell edge. The full structure at room temperature was described by Turquat *et al.*[75] as being very

similar to ZrV_2O_7 with a 3 x 3 x 3 superstructure, with $Pa\bar{3}$ symmetry derived from electron diffraction. Some forbidden subcell reflections are present in the HfV_2O_7 diffraction pattern, e.g. the (030) reflection. Turquat *et al.* explained this as being caused by double diffraction. There were also weak supercell reflections which were forbidden if the HfV_2O_7 was isostructural with ZrV_2O_7, e.g. the (050). These could not be explained by double diffraction as the reflections were present even when the diffraction pattern was taken along an axis for which no double diffraction should be detected, due to the two possible double diffraction paths being completely out of phase. This suggests there may be minor differences between the structures.

Two phase transitions were found at 340±2 K and 369±2 K on heating by DSC. On cooling the two transitions occur at 326±2 K and 368±2 K. For the higher temperature transition these values are within the margin of error, but the lower temperature transition appears to show significant hysteresis. The cell parameters were measured by neutron diffraction, as shown in Figure 1-30. The first transition is from the superstructure to what is believed to be, by analogy to ZrV_2O_7, an incommensurate phase. Above the second phase transition, the $Pa\bar{3}$ 1 x 1 x 1 cubic structure exists. The structure of all these phases is very similar to the three phases of ZrV_2O_7. Above the second phase transition, negative thermal expansion is observed.

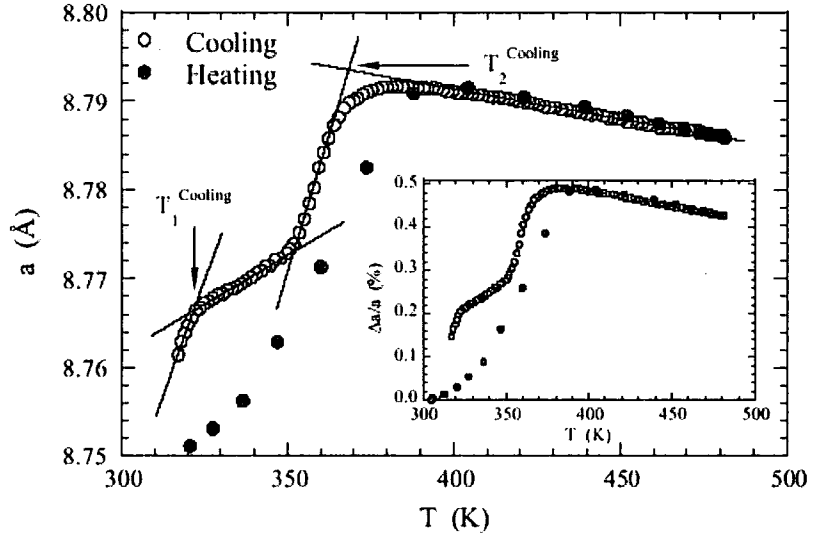

Figure 1-30: Cell parameters of HfV_2O_7 determined by neutron diffraction by Turquat *et al.*[75] A very rapid heating rate was chosen (200 K/h), the authors suggested that because of this the cell parameters obtained on cooling were more accurate.

The only study of $HfV_xP_{2-x}O_7$ was by Korthius *et al.*[66] No clear details were given but the materials were stated to follow the same pattern as the zirconium based materials (see Figure 1-28). Given the similarity of the room temperature structures and thermal expansion between ZrP_2O_7 and HfP_2O_7, and between ZrV_2O_7 and HfV_2O_7, this seems probable.

1.7. AM_2O_7 where A is a non-group IV transition metal

1.7.1. NbP_2O_7

Niobium pyrophosphates are potentially more complicated than the pyrophosphates described previous as they may contain either Nb(IV) or Nb(V). This leads to either $Nb(IV)P_2O_7$, $Nb(V)_2P_4O_{15}$ or $Nb_{1-x}P_{2-y}O_{7+z}$. The pseudo-cubic material was first described by Haider[76,77] as $NbP_2O_{7.5}$ with a cubic unit cell with an edge of 8.073 Å. Fukuoka *et al.*[78] carried out a more complete structural investigation. Several modifications of the compound were produced with different mixes of oxidation states for the niobium. The lowest average oxidation state found was +4.66. Electron diffraction showed this compound possessed $Pa\bar{3}$ symmetry, with powder diffraction showing that a 3 x 3 x 3 supercell was present. The increase of oxidation state of the niobium was thought to be compensated by absences on phosphorus sites.

1.7.2. MoP_2O_7

The first characterisation of MoP_2O_7 was preformed by Leclaire *et al.*[79] using single crystal data. This gave a subcell model in $Pa\bar{3}$ with cell lengths of 7.944 Å. The ADPs were unusually high, suggesting a supercell, but no structure was given for this. Haushalter *et al.*[80] showed the existence of weak supercell reflections, again using single crystal data. The supercell reflections appeared to show orthorhombic symmetry, rather than cubic. Lezama *et al.*[81] found asymmetric stretching in the P_2O_7 group using IR spectroscopy. This meant that not all the P_2O_7 groups are linear; therefore the symmetry must be lower than that suggested by Leclaire *et al.*

1.7.3. WP_2O_7

WP_2O_7 was characterised with a similar structure to MoP_2O_7 by Teweldemedlin *et al.*[82] No supercell reflections were found and a unit cell length of 7.947 Å was reported. Lezama *et al.*[83] used IR to show that an asymmetric stretch existed for the $P\text{-}O_{bridging}$ bond. This means that the P-O-P group cannot lie on an inversion centre and therefore the structure is more complicated than the model produced by Teweldemedlin *et al.*

1.7.4. ReP_2O_7

Rhenium pyrophosphate was characterised in space group $Pa\bar{3}$ with cell edges of 7.94 Å by Banks and Sacks.[84] The authors also attempted to synthesis MnP_2O_7 but this proved unsuccessful.

1.7.5. PtP_2O_7

Wellman and Leibau[85] produced a full structural solution of PtP_2O_7, using the space group

$P2_1/n$, with cell parameters of a = 7.095, b = 7.883, c = 9.032 Å and β = 111.37°. The connectivity is different from other AM_2O_7 materials; of the two crystallographically independent PtO_6 groups, one is bonded to 6 different P_2O_7 groups as normal but the second is bonded only to 4.

1.8. AM_2O_7 materials where A is a Lanthanide or Actinide

1.8.1. CeP_2O_7

Cerium pyrophosphate is the sole lanthanide pyrophosphate with the AM_2O_7 formula. This is unsurprising given the tendency of the lanthanides to form +3 ions. It has been characterised with a cubic subcell of 8.5648 Å; no supercell peaks could be detected.[73] 1D MAS ^{31}P NMR by King[49] showed only a single broad peak, of a similar breadth to the whole spectrum from ZrP_2O_7 and HfP_2O_7. This suggested either low crystallinity, a very large number of overlapping resonances or an incommensurate structure.

1.8.2. ThP_2O_7 and UP_2O_7

Actinide pyrophosphates have attracted attention as a potential storage material for the bi-products of the nuclear power industry. Thorium and uranium pyrophosphates both have two isomers. The alpha phase is isostructural with the other pseudo-cubic AM_2O_7 phases. The beta phase is more accurately formulated $A_2(PO_4)(P_3O_{10})$. It was characterised by Podor *et al.*[86] for the uranium compound. This orthorhombic form has $Pn2_1a$ symmetry, cell lengths of a = 11.526, b = 7.048 and c = 12.807 Å, and consists of chains of UO_8 groups linked to individual PO_4 tetrahedra and P_3O_{10} groups, as shown in Figure 1-31. Brandel *et al.*[87] suggested that $Th_2(PO_4)(P_3O_{10})$ is isostructural with $U_2(PO_4)(P_3O_{10})$ with unit cell parameters of a = 11.678, b = 7.171 and c = 12.925 Å.

Alpha uranium pyrophosphate was first described by Peyronel[88] using a $Pa\bar{3}$ subcell model with a cell length of 8.61 Å. A second structural solution was produced by Cabeza *et al.*[89] this used the same $Pa\bar{3}$ symmetry, but the bridging oxygen was delocalised over several sites, as shown in Figure 1-31. The cell length was given as 8.6311 Å. The authors suggested that this disordering was only an approximation, but with the quality of the available diffraction data, there were no clear superstructure peaks and therefore this oxygen disorder could not be determined. The cell length of the isostructural alpha phase of ThP_2O_7 was given as 8.721 Å by Burdese and Borlera.[90]

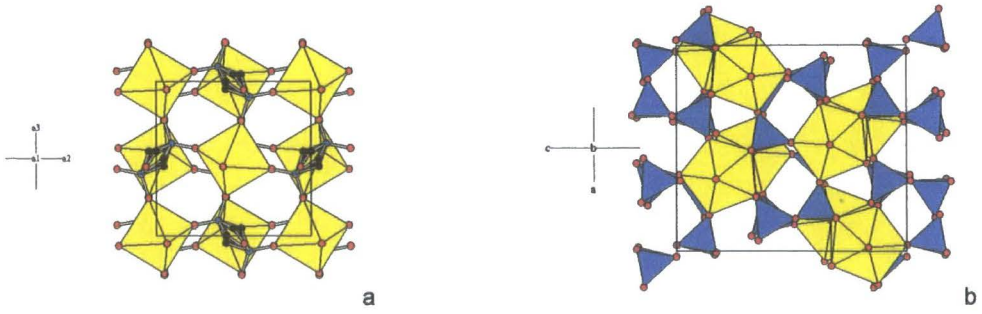

Figure 1-31: Pictures of structure of alpha (a) and beta (b) uranium pyrophosphate. In (a), UO_6 octahedra are yellow, P_2O_7 groups are shown as individual atoms due to the delocalised bridging oxygen. P atoms are green, O_{OA} atoms are red and the sites for $O_{bridging}$ are black. In b, UO_8 groups are shown in yellow, PO_4 groups in blue and oxygen atoms in red.

1.8.3. Other Actinide Pyrophosphates

Three other actinide pyrophosphates have been characterised using the $Pa\bar{3}$ subcell model. These are PaP_2O_7,[91] NpP_2O_7[92] and PuP_2O_7,[93] which have cell lengths of 8.65, 8.593 and 8.560 Å respectively.

1.9. Mixed Valence AM_2O_7 Materials

1.9.1. $Sb_{0.5}^{III}Sb_{0.5}^{V}P_2O_7$

Antimony pyrophosphate exists in two phases, both consisting of an infinite lattice of SbO_6 and P_2O_7 units. Verbaere *et al.*[94] synthesised both by heating $(NH_4)H_2PO_4$ and $Sb_2O_5 \cdot nH_2O$ to either 650°C (for the alpha form) or 500°C (for the beta form). Both structures were solved by single crystal diffraction and are shown in Figure 1-32. The beta form is the more closely related to the pseudo-cubic AM_2O_7 materials, sharing the same connectivity. In the alpha form each SbO_6 is linked to 10 of its 12 nearest neighbours in the same manner as the cubic phase, but to 1 of the neighbours by two single PO_4 groups and to the final one by two P_2O_7 groups. The structures are shown in Figure 1-32.

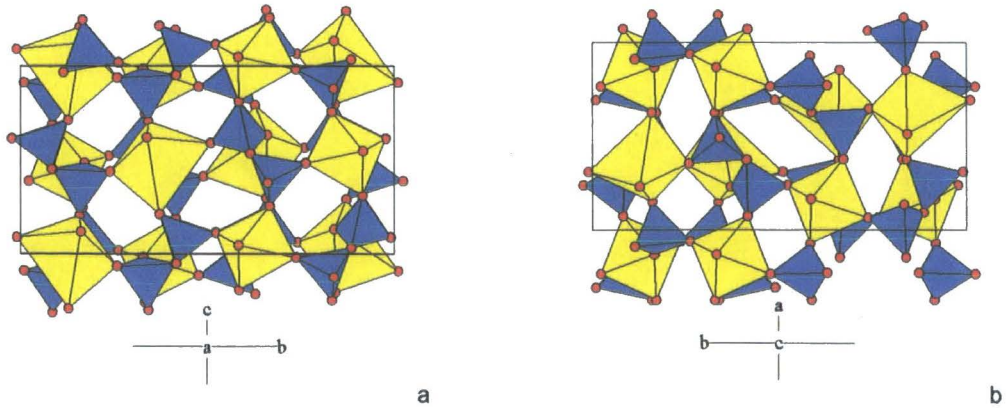

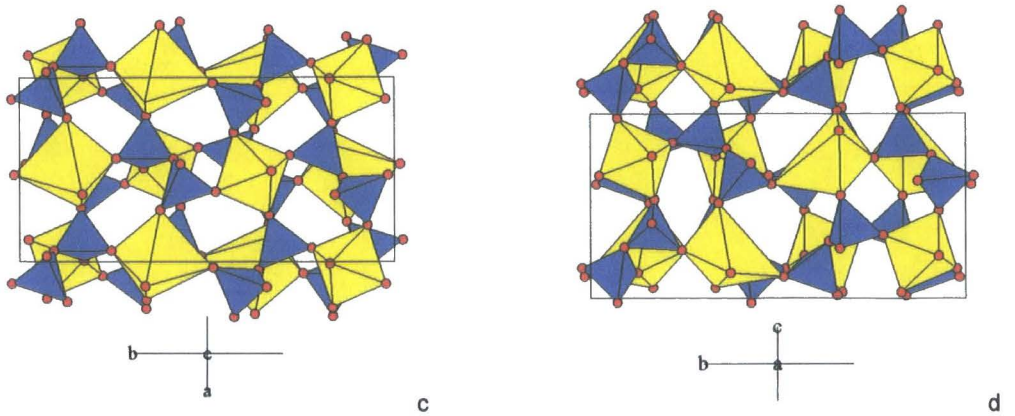

c d

Figure 1-32: Structure of alpha and beta SbP_2O_7, shown in (a) + (b) and (c) + (d) respectively. Note the similarities between (a) and (c), together with the difference in connectivity shown in (b) and (d).

The alpha phase is monoclinic, with $P2_1/c$ symmetry and cell dimensions of a = 8.088(1) Å, b = 16.015(3) Å, c = 8.135(5) Å and β = 90.17(2)°. The beta phase is orthorhombic with $Pna2_1$ symmetry and cell dimensions of a = 8.018(1) Å, b = 16.134(3) Å and c = 8.029(5) Å. Both phases show virtually no distortion of the $Sb^{(V)}O_6$ octahedra, with bond lengths between 1.91(2) and 2.00(2) Å. There is heavy distortion of the $Sb^{(III)}O_6$ octahedra which has a stereochemically active lone pair, with four Sb-O distances with an average of 2.15 Å and two significantly larger distances in both the alpha (2.49 and 2.50 Å) and the beta (2.41 and 2.74 Å) forms.

1.9.2. Mixed Cation AM_2O_7 Materials

A large number of materials with the general formula $A'(III)_{0.5}A''(V)_{0.5}M_2O_7$ have been synthesised and the dimensions of the subcell characterised. A summary is shown in Table 1-3. Note there are differences in the cell parameters between the two cell parameters listed for both $Nb_{0.5}Ta_{0.5}P_2O_7$ and $Bi_{0.5}Ta_{0.5}P_2O_7$. Varga *et al.*[95] suggested that their synthesis produced purer material than that of Oyetola *et al.*[96] and that their cell parameters are therefore more accurate.

A'(III)	A''(V)	Cation Size (Å)[Shannon R. D., 1976 #204			Cubic cell length (Å)	Authors
		A'	A''	Average		
Al	Ta	0.675	0.78	0.728	7.8863 (5)	Varga *et al.*[95]
Ga	Ta	0.76	0.78	0.770	7.923 (1)	Varga *et al.*[95]
Fe	Ta	0.785	0.78	0.782	7.9807 (3)	Varga *et al.*[95]
In	Nb	0.94	0.78	0.860	8.0896 (1)	Varga *et al.*[95]
Y	Nb	1.04	0.78	0.910	8.2617 (2)	Varga *et al.*[95]
Nd	Ta	1.123	0.78	0.952	8.3047 (3)	Varga *et al.*[95]
Bi	Ta	1.17	0.78	0.975	8.2334 (3)	Varga *et al.*[95]
Sb	Ta	0.90	0.78	0.84	8.171 (1)	Oyetola *et al.*[96]
Bi	Nb	1.17	0.78	0.98	8.236 (1)	Oyetola *et al.*[96]
Bi	Ta*	1.17	0.78	0.975	8.253 (2)	Oyetola *et al.*[96]
Nd	Ta	1.123	0.78	0.952	8.269 (1)	Oyetola *et al.*[96]
Eu	Nb	1.087	0.78	0.934	~ 8.26**	Oyetola *et al.*[96]
Eu	Ta	1.087	0.78	0.934	8.297 (1)	Oyetola *et al.*[96]
Bi	Sb	1.17	0.74	0.96	8.125****	Oyetola *et al.*[96]
Bi	Ta***	1.17	0.78	0.98	8.293*****	Oyetola *et al.*[96]

Table 1-3: Properties of the mixed cation AM_2O_7 materials. *Two phases of $Bi_{0.5}Ta_{0.5}P_2O_7$ were found, this phase is the pseudo-cubic phase. **Listed as pseudo-cubic by the authors. ***The second phase of $Bi_{0.5}Ta_{0.5}P_2O_7$, isostructural with the alpha phase of SbP_2O_7. ****This phase has $Pna2_1$ symmetry (a = 8.061, b = 16.398 & c = 8.117), the value given is $(V/2)^{1/3}$ for comparison purposes. ***** This phase has $P2_1/c$ symmetry (a = 8.276, b = 16.376, c = 8.417 & β = 90.02°).

1.10. Conclusion

A large number of AM_2O_7 materials have been synthesised and characterised using the $Pa\bar{3}$ subcell model. A summary of the cell parameter sizes versus ionic radii is given in Figure 1-33. Two roughly linear trends appear, one for the group 14 metals and one for the other metals. The group 14 pyrophosphates have smaller unit cells than would be expected when compared to the transition metal /lanthanide/actinide pyrophosphates. The increase in size with respect to cation size is also smaller. This suggests there are differences in the structures of the two sets of materials. There is a possible trend for the mixed-cation materials

(where the average radii of the two metals is used) but this is less clear, especially as the available data is from mixes of main group, transition and lanthanide metals.

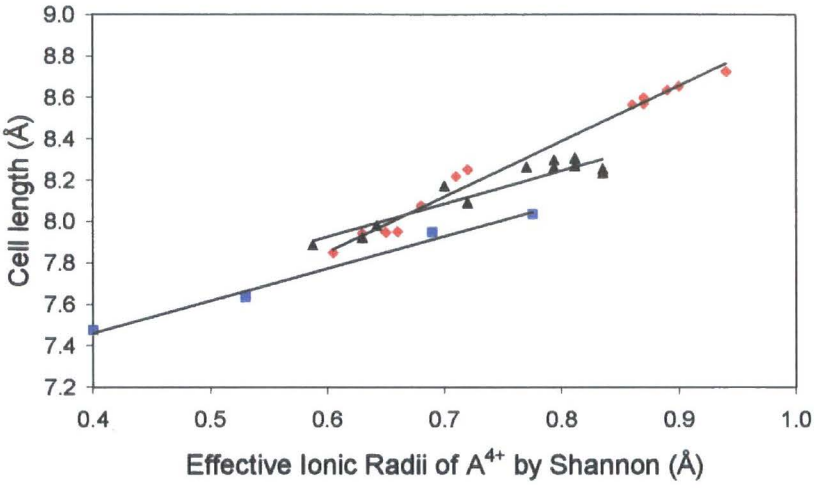

Figure 1-33: Cell parameter of the subcell versus the ionic radii of A. Ionic radii are from Shannon.[97] A = main group, points are blue squares, black triangles show materials with mixed cations; red diamonds those with transition, lanthanide or actinide cations.

1.11. Work in This Thesis

Chapter 2 contains a guide to the X-ray and neutron diffraction techniques used within this thesis. Chapter 3 explores parametric Rietveld refinement, a new method of refining multiple diffraction data sets. This can be used to obtain more accurate results and determine non-crystallographic quantities directly from Rietveld refinement. Chapter 4 contains a method for combining distance least-squares calculations with Rietveld refinement. This process is used for determining the structure of ZrP_2O_7 at room temperature. Chapter 5 investigates the changes in structure of both pseudo-cubic SnP_2O_7 and GeP_2O_7 with temperature. Chapter 6 explores the sold-state solutions of $Zr_xSn_{(1-x)}P_2O_7$, investigating the changes caused both at room temperature and upon heating.

1.12. References

1 Brown I. D. and Altermatt D., *Acta Crystallogr., Sect. B: Struct. Sci.*, 1985, **B41**, 245.

2 Rossetti G. A., Cline J. P., and Navrotsky A., *J. Mater Res.*, 1998, **31**, 3197.

3 Schlosser W. F., Graham G. M., and Meincke P. P. M., *J. Phys. Chem. Solids*, 1971, **32**, 927.

4 Gignoux D., Givord D., Givord F., and Lemaire R, *J. Magn. Magn. Mater.*, 1979, **10**, 288.

5 Sleight A., *Nature*, 2003, **425**, 674.

6 Salvador J. R., Guo F., Hogan T., and Kanatzidis M. G., *Nature*, 2003, **425**, 702.

7 Arvanitidis J., Papagelis K., Margadonna S., Prassides K., and Fitch A., *Nature*, 2003, **425**, 599.

8 Lyon K. G., Salinger G. L., Swenson C. A., and White G. K., *J. Appl. Phys.*, 1977, **48**,

865.

[9] Welche P.R.L., Heine V., and Dove M. T., *Phys. Chem. Mater.*, 1998, **26**, 63.

[10] Marians C. S. and Hobbs L. W., *J. Non-Cryst. Solids*, 1990, **124**, 242.

[11] Marians C. S. and Burdett J. K., *J. Non-Cryst. Solids*, 1990, **124**, 1.

[12] Marians C. S. and Hobbs L. W., *J. Non-Cryst. Solids*, 1990, **119**, 269.

[13] Giddy A. P., Dove M. T., Pawley G. S., and Heine V., *Acta Crystallogr., Sect. A: Found. Crystallogr.*, 1993, **A49**, 697.

[14] Dove M. T., Cool T., Palmer D. C., Putnis A., Salje E. K. H., and Winkler B., *Amer. Min.*, 1993, **78**, 486.

[15] Mary T. A., Evans J. S. O., Vogt T., and Sleight A. W., *Science*, 1996, **272**, 90.

[16] Evans J. S. O., David W. I. F., and S. A. W., *Acta Crystallogr., Sect. B: Struct. Sci.*, 1999, **B55**, 1.

[17] Evans J. S. O., Hu Z., Jorgensen J.D., Argyriou D.N., Short S., and S. A. W., *Science*, 1997, **275**, 61.

[18] Pryde A. K. A., Hammonds K. D., Dove M. T., Heine V., Gale J. D., and W. M. C., *Phase Transitions*, 1997, **61**, 141.

[19] Auray M., Quarton M., and Leblanc M., *Acta Crystallogr., Sect. C: Cryst. Struct. Commun.*, 1995, **C51**, 2210.

[20] Evans J. S. O., Mary T. A., Vogt T., Subramanian M. A., and Sleight A. W., *Chem. Mat.*, 1996, **8**, 2809.

[21] Duan N., Kameswari U., and S. A. W., *J. Am. Chem. Soc.*, 1999, **121**, 10432.

[22] Yamamura Y., Tsuji T., Yamaguchi T., and Hisashige T., *J. Ceram. Soc. Jpn.*, 2006, **114**, 607.

[23] De Meyer C., Bouree F., Evans J. S. O., De Buysser K., Bruneel I., Van Driessche I., and Hoste S., *J. Mater. Chem.*, 2004, **14**, 2988.

[24] Allen S. and Evans J. S. O., *Phys. Rev. B: Condens. Matter Mater. Phys.*, 2003, **B 68**, 134101.

[25] Evans J. S. O., Mary T. A., and Sleight A. W., *J. Solid State Chem.*, 1998, **137**, 148.

[26] Attfield M. P. and Sleight A. W., *Chem. Commun.*, 1998, **5**, 601.

[27] Tao J. Z. and Sleight A. W., *J. Solid State Chem.*, 2003, **173**, 442.

[28] Grima J. N. and Evans K. E., *J. Am. Chem. Soc.*, 2000, **220**, 130.

[29] Grima J. N., Alderson A., and Evans K. E., *J. Phys. Soc. Jpn.*, 2005, **74**, 1341.

[30] Levi G. R. and Peyronel G., *Z. Kristallogr*, 1935, **92**, 190.

[31] Peyronel G., *Gazz. Chim. Ital.*, 1939, **69**, 254.

[32] Peyronel G., *Gazz. Chim. Ital.*, 1942, **72**, 83.

[33] Vollenkle H., Nowotny H., and Wittman A., *Mon. Chem.*, 1963, **94**, 956.

[34] King I. J., Fayon F., Massiot D., Harris R. K., and Evans J. S. O., *Chem.Commun.*, 2001, 1766.

[35] Gover R. K. B., Withers N. D., Allen S., Withers R. L., and Evans J. S. O., *J. Solid State Chem.*, 2002, **166**, 42.

[36] Losilla E. R., Cabeza A., Bruque S., Aranda M. A. G., Sanz J., Iglesias J. E., and Alonso J. A., *J. Solid State Chem.*, 2001, **156**, 213.

[37] Liebau F., Koppen N., and Bissert G., *Z. Anorg. Allg. Chem.*, 1968, **359**, 113.

[38] Makart H., *Helv. Chim. Acta*, 1967, **50**, 399.

[39] Bissert G. and Liebau F., *Acta Crystallogr., Sect. B: Struct. Sci.*, 1970, **B 26**, 229.

[40] Poojary D. M., Borade R. B., Campbell F. L., and Clearfield A., *J. Solid State Chem.*, 1994, **112**, 106.

[41] Liebau F., *Bull. Soc. Fran. Minéralogie,*, 1971, **94**, 239.

[42] Tillmanns E., Gebert W., and Baur W. H., *J. Solid State Chem.*, 1973, **7**, 69.

[43] Hartmann P., Jana C., Vogel J., and Jager C., *Chem. Phys. Lett.*, 1996, **258**, 107.

[44] Iuliucci R. J. and Meier B. H., *J. Am. Chem. Soc.*, 1998, **120**, 9059.

[45] Kaiser U. and Glaum R., *Z. Anorg. Allg. Chem.*, 1994, **620**, 1755.

[46] Huang C. H., Knop O., Othen D. A., Woodhams F. W., and Howie R. A., *Can. J. Chem.-Rev. Can. Chim.*, 1975, **53**, 79.

[47] Fayon F., King I. J., Harris R. K., Gover R. K. B., Evans J. S. O., and Massiot D., *Chem. Mat.*, 2003, **15**, 2234.

[48] Brindley J., 'Negative thermal expansion and AM_2O_7 materials', Durham University, Durham, 2001.

[49] King I. J., 'Combined Use of Powder Diffraction and Magic-Angle Spinning NMR to Structural Chemistry', Durham University, Durham, 2003.

[50] Sanz J., Iglesias J. E., Soria J., Losilla E. R., Aranda M. A. G., and Bruque S., *Chem. Mat.*, 1997, **9**, 996.

[51] Helluy X., Marichal C., and Sebald A., *J. Phys. Chem. B*, 2000, **104**, 2836.

[52] Soria J., Iglesias J. E., and Sanz J., *J. Chem. Soc.-Faraday Trans.*, 1993, **89**, 2515.

[53] Norberg S. T., Svensson G., and Albertsson J., *Acta Crystallogr. Sect. C-Cryst. Struct. Commun.*, 2001, **57**, 225.

[54] Evans J. S. O., Hanson J. C., and Sleight A. W., *Acta Crystallogr., Sect. B: Struct. Sci.*, 1998, **54**, 705.

[55] Carlson S. and Andersen A. M. K., *J. Appl. Crystallogr.*, 2001, **34**, 7.

[56] Lipinska-Kalita K. E., Kruger M. B., Carlson S., and Andersen A. M. K., *Physica B*, 2003, **337**, 221.

[57] Andersen A. M. K. and Norby P., *Acta Crystallogr., Sect. B: Struct. Sci.*, 2000, **56**, 618.

[58] Chaunac M., *Bull. Soc. Chim. Fr.*, 1971, 424.

[59] Hagman L. O. and Kierkega P., *Acta Chem. Scan.*, 1969, **23**, 327.

[60] Inomata Y., Inomata T., and Moriwaki T., *Spectroc. Acta Pt. A-Molec. Biomolec. Spectr.*, 1980, **36**, 839.

[61] Kim C. H. and Yim H. S., *Solid State Commun.*, 1999, **110**, 137.

[62] Ota T. and Yamai I., *J. Mater. Sci.*, 1987, **22**, 3762.

[63] Seo D. K. and Whangbo M. H., *J. Solid State Chem.*, 1997, **129**, 160.

[64] Withers R. L., Tabira Y., Evans J. S. O., King I. J., and Sleight A. W., *J. Solid State Chem.*, 2001, **157**, 186.

[65] Khosrovani N., Korthuis V., Sleight A. W., and Vogt T., *Inorg. Chem.*, 1996, **35**, 485.

[66] Korthuis V., Khosrovani N., Sleight A. W., Roberts N., Dupree R., and Warren W. W.,

Chem. Mat., 1995, **7**, 412.

[67] Birkedal H., Andersen A. M. K., Arakcheeva A., Chapius G., Norby P., and Pattison P., *Inorg. Chem.*, 2006, **45**, 4346.

[68] Withers R. L., Evans J. S. O., Hanson J., and Sleight A. W., *J. Solid State Chem.*, 1998, **137**, 161.

[69] Craig D. F. and Hummel F. A., *J. Am. Ceram. Soc.*, 1972, **55**, 532.

[70] Hodgkinson P. H., Evans J. S. O., and Hampson M. R., *Unpublished work*, 2003.

[71] Stinton G. W., Hampson M. R., and Evans J. S. O., *Inorgan. Chem.*, 2006, **45**, 4352.

[72] Shannon R. D. and Prewitt C. T., *Acta Crystallogr., Sect. B: Struct. Sci.*, 1969, **B25**, 925.

[73] Tait M., 'The structure and Properties of AM_2O_7 materials', 4th year report, Durham University, Durham, 2002.

[74] Baran E. J., *J. Less-Com. Met.*, 1976, **46**, 343.

[75] Turquat C., Muller C., Nigrelli E., Leroux C., Soubeyroux J. L., and Nihoul G., *Eur. Phys. J.-Appl. Phys*, 2000, **10**, 15.

[76] Haider S. Z., *Anal. Chim. Acta*, 1961, **24**, 250.

[77] Haider S. Z., *Proc. Pak. Acad. Sci*, 1964, **1**, 19.

[78] Fukuoka H., Imoto H., and Saito T., *J. Solid State Chem.*, 1995, **119**, 98.

[79] Leclaire A., Borel M. M., Grandin A., and Raveau B., *Eur. J. Solid State Inorg. Chem.*, 1988, **25**, 323.

[80] Haushalter R. C. and Mundi L. A., *Chem. Mat.*, 1992, **4**, 31.

[81] Lezama L., Rojo J. M., Pizarro J. L., Arriortua M. I., and Rojo T., *Solid State Ion.*, 1993, **63-5**, 657.

[82] Teweldemedhin Z. S., Ramanujachary K. V., and Greenblatt M., *Mater. Res. Bull.*, 1993, **28**, 427.

[83] Lezama L., Rojo J. M., Mesa J. L, and Rojo T., *J. Solid State Chem.*, 1995, **115**, 146.

[84] Banks E. and Sacks R., *Mater. Res. Bull.*, 1982, **17**, 1053.

[85] Wellmann B. and Liebau F., *Journal of the Less-Common Metals*, 1981, **77**, P31.

[86] Podor R., Francois M., and Dacheux N., *J. Solid State Chem.*, 2003, **172**, 66.

[87] Brandel V. and Dacheux N., *J. Solid State Chem.*, 2004, **177**, 4743.

[88] Peyronel G., *Z. Kristallogr*, 1936, **94**, 311.

[89] Cabeza A., Aranda M. A. G., Cantero F. M., Lozano D., Martinez-Lara M., and Bruque S., *J. Solid State Chem.*, 1996, **121**, 181.

[90] Burdese A. and Borlera M. L., *Ann. Chim. Roma*, 1963, **53**, 344.

[91] Lecloarec M. F. and Cazaussus A., *J. Inorgan. Nuc. Chem.*, 1978, **40**, 1680.

[92] Bamberger C. E., Haire R. G., Begun G. M., and Hellwege H. E., *J. Less-Com. Met.*, 1984, **102**, 179.

[93] Bjorklund C. W., *J. Am. Chem. Soc.*, 1958, **79**, 6347.

[94] Verbaere A., Oyetola S., Guyomard D., and Piffard Y., *J. Solid State Chem.*, 1988, **75**, 217.

[95] Varga T., Wilkinson A.P., Haluska M.S., and Payzant E.A., *Journal of Solid State Chemistry*, 2005, **178**, 3565.

[96] Oyetola S., Verbaere A., Guyomard D., Crosnier M. P., Piffard Y., and Tournoux M., *Eur. J. Solid State Inorg. Chem.*, 1991, **28**, 23.

[97] Shannon R. D., *Acta Crystallogr., Sect. A: Found. Crystallogr.*, 1976, **A32**, 751.

2. Characterisation Methods

2.1. Powder X-ray Diffraction (XRD)

Powder X-ray diffraction is a powerful technique for determining the phase composition and crystal structure of polycrystalline materials. It is primarily used for materials (or certain polymorphs of a material) for which sufficiently large crystals can't be grown for single crystal measurements. It is also used to analyse naturally occurring materials where re-crystallisation could result in a change of polymorph. Powders are also generally more robust than single crystals. This allows diffraction measurements to be carried out under a wide range of experimental conditions. These can include heating and cooling across phase transitions, high pressure experiments and even following *in situ* solid-state reactions. It is the primary analytical technique in this thesis.

X-rays are scattered in all directions upon hitting atoms. For a regular crystal structure, the X-rays scattered by electrons from different atoms will form an interference pattern, meaning diffracted intensity is only detected in certain places. The angle at which constructive interference occurs is described by the Bragg equation, shown in Equation 2-1, where λ is the wavelength and θ is the angle shown in Figure 2-1. The term d_{hkl} is the spacing between theoretical crystallographic planes, described by Miller indices h, k & l. The angle at which diffraction peaks occur is determined by the size and shape of the unit cell. The relative intensities of peaks is determined by the position of atoms within the unit cell.

$$\lambda = 2d_{hkl}(\sin\theta) \qquad \text{Equation 2-1}$$

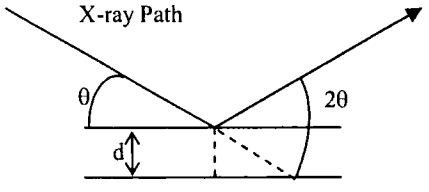

Figure 2-1: Angle of reflections from parallel crystallographic planes.

2.2. Determining the Crystal Structure from Powder X-ray Diffraction Data

Most single crystal diffraction patterns give easily integratable, isolated peaks for each hkl reflection. In powder diffraction, the polycrystalline sample means that each peak is transformed in a cone of intensity. As the source and detector are moved around the sample, the measured area of intensity is effectively a thin strip across all these cones. The 3D nature of the single crystal pattern is thus compressed in 1D. This leads to much greater overlap of hkl reflections, making determination of the crystal structure more difficult. Structural determination can be divided into two parts, structural solution (where a rough model is

formed) and structural refinement (where the model is improved). For the majority of structural work performed on powders, an approximate starting model is known and structure determination is largely a process of refinement, typically using the Rietveld method (section 2.2.2).

2.2.1. Structure Solution

If no structural model is available as a starting point then the first stage of deducing a crystal structure from powder data is indexing the pattern to determine the unit cell. Theoretical hkl reflections from a huge number of possible unit cells of differing size and symmetry are compared to reflections in the data automatically. This method works best where there is limited peak overlap.

The second stage is to determine the space group from systematic absences, or (as performed in this work) by bringing in additional information from NMR or electron diffraction. The third stage is to produce an approximate model of the unit cell contents using either direct methods, Patterson syntheses or real space methods.

Direct methods are based on combining chemical knowledge about the distribution of electrons in a unit cell (discrete atoms must be formed, no negative electron density etc.) with a series of relationships between the phases of different reflections. Large numbers of starting values for a few phases are randomly generated. The phase relationships are then used to generate other phases, leading to a series of possible structures. These structures are then automatically analysed to determine which is the most probable. Patterson syntheses are based upon Fourier transforming the squares of the peak amplitudes. This produces a map of vectors between pairs of atoms. From these vectors it is possible to calculate the position of atoms in the unit cell. This method is most effective were there are a few heavy atoms and a large number of light atoms, e.g. organometallic compounds. Real space methods are designed to work with molecular structures were the connectivity is known but the position and orientation of the molecule and any internal degrees of freedom are not. Possible structures are generated, at random initially, and their theoretical diffraction patterns compared to the experimental ones. Further possible models are then generated using either Monte Carlo methods, simulated annealing or genetic algorithms, until a good model is found.

2.2.2. Structure Refinement *via* the Rietveld Method

Early attempts at structure refinement from powder diffraction data focused on determining individual peak intensities before fitting these intensities with a structural model. This is equivalent to producing a theoretical single crystal pattern from powder data before structure refinement. This works well where the diffraction pattern has no overlapping peaks but producing the correct intensities is dependent on having a good idea of the type of unit cell at this stage.

As most powder data sets will have some form of peak overlap, these early method were generally unsatisfactory. The main method now used is Rietveld refinement.[1] This is based on producing a theoretical diffraction pattern from a starting model over the whole data range and comparing to the experimental pattern. The model is then adjusted by least-squares so the theoretical data fits the experimental pattern. The model typically contains structural information (unit cell parameters, atomic coordinates, atomic displacement parameters etc.); instrumental effects (wavelength, zero, a peak shape description) and a function to model background.

2.2.3. Quality of Fit

The quality of fit of a model produced by Rietveld refinement can be measured by a selection of R-factors, with lower numbers suggesting a better fit of the data. The most commonly quoted R-factor is the weighted R-factor (Rwp or wRp), shown in Equation 2-2. $Y_{o,m}$ and $Y_{c,m}$ are the observed and calculated intensities at data point m. w_m is the weighting of point m, equal to $1/\sigma Y_{o,m}$ where $\sigma Y_{o,m}$ is the error of $Y_{o,m}$.

$$R_{wp} = \sqrt{\frac{\sum w_m \left(Y_{o,m} - Y_{c,m}\right)^2}{\sum w_m {Y_{o,m}}^2}}$$ Equation 2-2

The statistically expected quality of fit is given by R_{exp} (Equation 2-3). M is the number of data points; P is the number of parameters. The number of parameters should never be greater than the number of data points, therefore M - P should never be negative.

$$R_{\exp} = \sqrt{\frac{\sum M - P}{\sum w_m {Y_{o,m}}^2}}$$ Equation 2-3

The quality of the model can be judged by the ratio of R_{wp} (actual fit quality) to R_{exp} (expected fit quality) as shown in Equation 2-4. Values of between 1 and 1.5 are indicative of a good fit; values below 1 suggest that too many parameters have been refined for the data available.

$$GOF = \chi^2 = \frac{R_{wp}}{R_{\exp}} = \sqrt{\frac{\sum w_m (Y_{o,m} - Y_{c,m})^2}{M - P}}$$ Equation 2-4

The other main R value used is the R_{Bragg}, shown in Equation 2-5. $I_{o,k}$ and $I_{c,k}$ are the observed and calculated intensities of the kth reflections. $I_{o,k}$ is biased by the model used and therefore R_{Bragg} can give a false impression if an incorrect model is used. For example, if one reflection is missing entirely then R_{Bragg} could still be low, if the predicted reflections fitted the local data well. R_{wp} would be high in this case. R_{wp} can be biased by correlations with the background fitting but R_{Bragg} is free of this type of correlation. Therefore for a structural model

to be accepted both R_{wp} and R_{Bragg} must be low and the theoretical data pattern also be visibly correct. R_{Bragg} is equivalent to R_F^2, the most commonly reported R value in single crystal refinements.

$$R_{Bragg} = \frac{\sum \left| I_{"o",k} - I_{c,k} \right|}{\sum I_{"o",k}}$$ Equation 2-5

2.2.4. TOPAS Academic

All Rietveld refinement in this thesis was carried out using TOPAS (TOtal Pattern Analysis System) Academic.[2] This enables simple routine analysis of data whilst providing a powerful platform to develop non-standard methods of refinement. It is controlled *via* a text input file, which was normally edited with Jedit,[3] which is designed to interface with TOPAS. The input file contains a series of commands in TOPAS's specific scripting language. It also allows additional information on the refinement to be easily added, such as constraints and/or restraints for bond angles and lengths. This ability to add large numbers of restraints or constraints proved very useful for work on the AM_2O_7 materials, where the underlying network of polyhedra is known but not the atomic locations.

The refinement of large amounts of variable temperature diffraction data is also simplified by TOPAS Academic. A standard refinement is carried out using the most appropriate starting data set (typically the first). A batch file can be used to sequentially refine each data set, using the structural model(s) of the previous data set as a starting point. This batch file is generated using the FORTRAN routine, *multitopas*. After each refinement any chosen parameters can be output, together with the full results file for each refinement if desired. This method can also be used for any series of data where there is progression between individual data sets, e.g. time-dependent kinetic studies. A new method, designed to improve the quality of information that can be extracted from these types of data sets, is described in chapter 3.

One of the major problems with the Rietveld refinement is that the starting model can prejudice the solution obtained. Structure models can become stuck in false minima, in which slight shifts in the model lead to worse fitting of the data, and the required large shift to achieve the true minima never occurs.

In order to prevent this, a modified version of simulated annealing was used. Rietveld refinement was carried out as normal until convergence. Rather than randomly shifting all parameters based on a temperature régime, certain parameters were then randomized within user defined boundaries to shift the model and the model was re-refined. Many cycles of this randomization and refinement process were used to try to find the true minima. Control of which parameters were refined was critical, these typically included unit cell parameters as these had a significant affect on the entire model, thus theoretically enabling large areas of

parameter space to be explored. The result with the lowest Rwp was retained at the end of the annealing process. Care must be taken to ensure that simulated annealing does not produce chemically implausible models. This is done using minimum and maximum limits on any parameters likely to reach implausible values during the early stages of annealing. Bond distance and angle restraints were also used where appropriate.

TOPAS Academic also enables a variety of different peak shapes to model data. For all X-ray data in this thesis, a pseudo-Voigt TCHz peak shape was used. This provided the most accurate fit of the various preset peak shapes for a variety of data. It is based on a convolution of Gaussian broadening (FWHM calculated by Equation 2-6) and Lorentzian (Equation 2-7), where u, v, w, x, y and z are freely refining terms. A simpler model was used for the peak broadening from neutron data with a single value for Lorentzian FWHM and one for Gaussian.

$$Gaussian\_FWHM = \sqrt{u(Tan\theta)^2 + vTan\theta + w + \frac{z}{(\cos\theta)^2}} \qquad \text{Equation 2-6}$$

$$Lorentzian\_FWHM = xTan\theta + \frac{y}{\cos\theta} \qquad \text{Equation 2-7}$$

2.3. X-ray Diffraction Equipment

Three lab-based diffractometers were used, a Siemens d5000 and two Bruker AXS d8 Advance X-ray powder diffractometers. All were used in reflection mode. Two X-ray synchrotron sources were also used, and are described in section 2.3.4.

2.3.1. Siemens D5000

The groups Siemens d5000 with automatic sample changer was used for most of the basic diffraction work, predominately checking the composition and purity of syntheses. This initially used CuKα radiation, a graphite (001) monochromator (average λ = 1.54195 Å) and a scintillation counter as a detector. The diffractometer was controlled using the Bruker Diffrac+ v4.0 suite. The beam passes through Soller slits and a divergence slit before diffraction from the sample and second Soller slit, a graphite (001) monochromator & a 0.2 mm receiving slit before the detector. The monochromater and detector were later replaced by a Baltic Instruments SolX energy dispersive detector. The divergence slit could be set to use a v6, v20 or 1 degree fixed slits. The first two setting mean that the slit varies with 2θ angle to constantly illuminate 6 mm or 20 mm at all 2θ angles. Samples could be mounted in either bulk holders, on glass or silicon plates.

2.3.2. Bruker D8

The group laboratory contains two Bruker d8 AXS powder diffractometers, referred to as the

'd8' and the 'd9'. The 'd8' used a CuKα_1 source (λ = 1.540598 Å) selected using a Ge (111) monochromator. The detector was initially a Braun PSD-50M linear Position Sensitive Detector, before being replaced by a Bruker Vantec-1 single photon counting detector. The monochromated X-rays pass through a 6mm aperture slit, an anti-scatter slit, a fixed Soller slit and a 1° divergence slit before hitting the sample. After diffracting the X-rays pass through a radial soller before hitting the detector. The samples were typically mounted on quartz discs using vaccum grease. The d8 was generally fitted with the HTK furnace (see section 2.3.3).

The 'd9' used a CuKα source. The detector was initially a SolX, before being replaced by a Bruker LynxEye detector. The LynxEye uses a series of 192 silicon strip detectors, each effectively a point detector to provide very high resolution. The unmonochromated X-rays passed through divergence slits and anti-scatter slits before hitting the sample. The d9 was used for either room temperature measurements with a sample changer or for low temperature measurements using the Phenix (section 2.3.3). Room temperature samples were mounted on either silicon or glass plates; samples for low temperature measurements were mounted on quartz discs using Vaseline.

2.3.3. Controlling the Sample Environment

Both d8 diffractometers could be fitted with any of three sample temperature control systems available in the laboratory, or a sample changer. The three system were the HTK1200 furnace (above RT), the PheniX (below RT) and the TTK cryofurnace (around RT). The latter was not used for thesis and so isn't discussed any further. An Oxford Cryosystems "PheniX" Closed Circuit Refrigerator enabled the collection of diffraction data between 15 and 300 K. The sample was contained in a vacuum chamber and data were collected continuously as the sample was cooled or heated. The PheniX was controlled using the software Cryopad.

The Bruker HTK1200 furnace enabled the sample to be heated from room temperature to 1473 K and was set-up to allow gas flow across the sample. The furnace was controlled using Bruker *Diffrac+ v4.0* software. Here data collection was not continuous; the correct temperature was achieved and stabilized before each data collection.

2.3.4. Synchrotron Sources

While laboratory X-ray sources are easily available and used for most analysis, for some work better quality data from synchrotron sources was required. These central facilities are particularly useful for pseudo-cubic AM_2O_7 materials, as the much higher resolution can allow the observation of either split peaks or clearly visible shoulders where laboratory-based facilities would give a single, unresolved peak. Data from two synchrotrons was used; the National Synchrotron Light Source at Brookhaven National Laboratory and the European Synchrotron Radiation Facility (ESRF).

In both of these synchrotron facilities, pulses of electrons are generated using a triode gun, then accelerated using a pulsed electric field, at first through a linear accelerator (Linac), then around a booster ring. After reaching the required speed, they are then passed into the main storage ring. This hollow ring is actually a polygon, with magnets to bend the pulse of electrons at each corner. As the path of the electron pulse is bent, radiation is emitted; this radiation is highly synchronised and very intense, making it very useful for diffraction. On straight sections of the storage ring there are also additional sets of magnets, which force the electron to follow a sinusoidal pattern, emitting more radiation. To replace energy lost *via* radiation there are accelerators in the ring based on the same principle as the initial accelerators.

SnP_2O_7 was studied at the ESRF using the High-Resolution Powder-diffraction Beamline, located on an Insertion Device 31 (ID31). Pulses of electrons are fed into the storage ring at 6 GeV, producing a beam intensity of 200 mA at the stations.[4] It can be operated at energies between 5 KeV and 60 KeV (0.21 to 2.5 Å); a wavelength of 0.495754 Å was used for this work.

ZrP_2O_7 was studied at X7A (powder diffraction station) of the National Synchrotron Light Source at Brookhaven National Laboratory. This uses energies between 8 and 35 KeV (0.35 to 1.55 Å) and gives a resolution of 2×10^{-4} $\Delta d/d$.[5] A wavelength of 0.8019 Å was used for this work.

2.4. Neutron Diffraction

2.4.1. Introduction to Neutron Diffraction

As X-rays are scattered by electrons, X-ray diffraction is highly sensitive to the position of high atomic number atoms with large numbers of electrons. The contribution to the intensity of peak from these atoms (such as tin in this work) is much greater than from light atoms such as oxygen. It therefore becomes difficult to accurately determine the location of the latter.

The de Broglie wavelength of neutrons with energies between 1 and 100 MeV is similar in length to the interatomic distances in crystals, enabling diffraction. As neutrons are scattered by the nucleus of an atom, the scattering power is unique for each element and there is no linear relationship between scattering power and atomic mass. This means that neutron diffraction can be a much more effective technique for finding light atom positions when heavy atoms are present. The combination of X-ray and neutron diffraction is particularly effective, potentially enabling all atomic positions to be accurately determined.

2.4.2. HRPD at ISIS

All neutron data in this thesis was collected using the High Resolution Powder Diffractometer (HRPD) at the ISIS pulsed neutron source of the Rutherford Appleton Laboratory. Protons are

accelerated using a synchrotron, before leaving the ring at high speed and hitting a tantalum target. White neutrons are produced *via* a process of spallation. This produces very high energy neutrons. The energy of the neutrons is then moderated by cold methane to between 0.5 and 330 MeV, before passing down a beam guide to the HRPD station, where they are diffracted by the sample and hit three fixed banks of detectors.

This station works on a time of flight principle; the detector measures the time it takes for the neutron to arrive, giving data as intensity against time. If the time is known for a given peak, the speed and therefore the de Broglie wavelength of the neutron can be calculated. Each bank of detectors is at a fixed angle, enabling the solution of the Bragg equation (Equation 2-1). HRPD has very high resolution for a neutron source, 4×10^{-4} $\Delta d/d$ for the backscattering bank of detectors.[6] This is due to the very long distance (100m) between the tantalum target and the ZnS scintillation detector, which reduces the error in determining the overall distance travelled by the neutron and hence the determination of its wavelength (as the ratio of the overall flight length to the uncertainty in exact generation position of the neutron is high). This bank of detectors allows routine measurements between 0.6 and 4.6 Å, with d-spacings as low as 0.3 Å having been recorded.

2.5. References

1 Rietveld H. M., *J. Appl. Crystallogr.*, 1969, 2, 65.

2 Coelho A. A., 'Topas - Academic', Karlsruhe, 2004.

3 Pestov S., 'jEdit', Ottawa, 1998.

4 European Synchrotron Radiation Facility website, 'http://www.esrf.eu'.

5 Brookhaven National Laboratory website, 'http://www.bnl.gov/world/'.

6 ISIS website, 'http://www.isis.rl.ac.uk/Crystallography/HRPD/'.

3. Parametric Rietveld Refinement

3.1 Introduction

Whilst performing a single diffraction measurement may provide some understanding of a material, more information can be obtained by carrying out a series of measurements as a function of an external variable. These variables can include temperature, time, pressure or chemical environment. Such series of diffraction experiments are often referred to as "parametric" studies.

In recent years this style of application of diffraction techniques has increased due to improving equipment. These enable the collection of good quality diffraction patterns in minutes, or even seconds at synchrotron sources. This makes the collection of a large number of data sets, each at subtly different conditions, feasible.

The conventional method of carrying out Rietveld refinement on such data is to independently refine each set. One of the problems with sequential refinement of parametric data is its poor treatment of parameters which either remain constant or are known to vary smoothly throughout the range of an experiment. Either they are allowed to refine freely, resulting in different, potentially unrelated values for different scans, or the parameter is fixed at one value, which may be sub-optimal if it has been determined from only one scan.

In order to prevent this, a method of simultaneously refining all of the data ranges of a parametric powder diffraction experiment has been developed in TOPAS Academic.[1] This process is called 'parametric fitting' hereafter, as one parametrically fits a surface of diffraction data with variables 2θ, T (for example) and I on the x, y and z axis. This enables control over whether a given parameter is refined independently for each data set (i.e. for cell parameters where a phase transition occurs), as a single refining parameter for all of the data sets (for instrumental parameters etc.) or using a simple function based on the external variable.

Where a single parameter is refined across all of the data sets, this value can be calculated with greater accuracy. For example, an axial model for peak asymmetry calculated from a single 2 minute data set may contain large errors. By calculating the same value from 100 2 minute data sets, a significantly more accurate value may be obtained. A parallel can be drawn with using several data sets from different banks of detectors in a neutron source to obtain a better model.

Structural parameters tend to vary smoothly with changing external factors, unless a phase transition occurs. This means that not only must a value of a variable fit the diffraction pattern at T; it should also be related to the value of that variable at $T\pm\Delta T$. By describing the parameter as a function of the external variable a more realistic model can be obtained and the chances of a structural model for the individual data sets finding a false minimum is

reduced.

This method must be used with care. An incorrect function applied to a given parameter, or a single value applied to a varying parameter will cause problems. An analogy can be drawn with the use of constraints and restraints in refinement, if used correctly they aid the finding of the solution, if not they force the model to a false minimum.

In this chapter the structure of parametric input files is described, together with the method of creating them. Three examples of this approach are also given, variable temperature work on ZrP_2O_7, background fitting of a variable temperature study of FePt nanoparticles and time-dependent kinetic studies on $ZrWMoO_8$. In all of these examples the sequential refinement is carried out to compare with the results of surface fitting. This helps decide whether the assumptions made in the surface fitting are correct.

3.1.1 Format and Creation of Parametric Fitting Input Files

All refinements were carried out using TOPAS Academic, which provides a flexible platform for performing this type of refinement. The input file for simultaneous refinement in TOPAS contains different sections as shown by the schematic in Figure 3-1. The file consists of two overall sections, followed by one section for each data set. The first overall part contains any information required by the whole refinement. This could include any known instrument factors. The second part contains any parameters which are refined for all of the data sets. An example would include any instrumental parameters which had not already been determined. The separation of these two parts is to help the user keep track of which variables are refined. Information from parts 1 & 2 is input into the sections for each data set. These also contain details such as background parameters and the structure model.

Creating the input file required making only a single example of the latter sections. All variables were given parameter names ******_t_0000, where ****** is the desired name eg. cell_a_t_0000 for the first cell length parameter. This file, together with a second file which contained a list of values of the external parameter, was used by a Fortran 77 program called 'substitute' to automatically produce section 3 of the main input file. It replicated the refinement details for each external variable, replacing the zeroes in each parameter labelled ******_t_0000 with the actual value of the variable (eg. cell_a_t_0318 for a cell at 318 K). Parts 1 & 2 where then added manually.

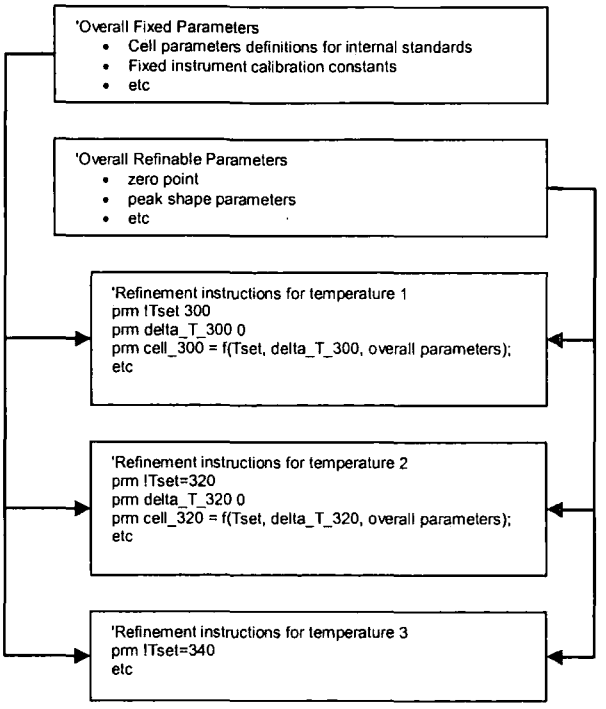

Figure 3-1: Schematic of surface fitting TOPAS input file. This example is for the variable temperature experiment shown in section 3.2.

3.2 Surface Rietveld Refinement Example 1: Variable Temperature Study of ZrP_2O_7

3.2.1 Introduction

The aim of this work was to demonstrate the application of surface fitting on VT powder diffraction data of ZrP_2O_7 and in particular to obtain an accurate temperature for the 3 x 3 x 3 supercell to 1 x 1 x 1 subcell phase transition as discussed in section 1.6.2.

Unit cell parameters are determined from X-ray diffraction data using the position of the Bragg peaks, with the change in peak position with temperature giving the thermal expansion. Unfortunately many other factors in addition to thermal expansion can also affect the peak position in a VT experiment and can lead to an inaccurate, though precise, determination of the unit cell. The first of these is the position of the sample with respect to the beam. As the temperature increases, the sample holder expands, moving the sample upwards through the beam. This causes the peaks to shift to higher angles. There can also be slight errors in the calibration of the instrument, including zero point, motor errors and psd calibration, which can lead to inaccurate 2θ values.

There are several factors, either due to the sample or the instrument, which broaden the Bragg peaks. Many of these, such as crystallite size and strain, the emission profile and broadening due to certain slit widths are symmetric, so have no effect on the position of the

centre of the peak. There are two main factors which cause asymmetric peak broadening. The first is axial divergence. The diffracted X-rays from the sample form a cone of intensity for each angle which meets the Bragg equation. The detector measures a strip of space which cuts across all of these cones. As the sample is not infinitely narrow, axial divergence of the diffracted beam means that the curvature of cones from different parts of the sample will lead to an asymmetric build-up of intensity at lower 2θ values than the maximum.

The second main factor is absorption, where instead of the all the X-rays diffracting from the surface layers of a sample, some will penetrate it and diffract from internal atomic planes. This leads to diffraction at a lower height, giving X-ray intensity at a lower angle. As X-rays diffracting from the surface have the highest 2θ, the effect of this is a tail on the low angle side of the peak. This is a more significant problem with large, weakly absorbing organic samples.

In order to prevent the above effects leading to inaccurate determination of the unit cell, it is usual to mix the subject material with an internal standard to obtain the highest quality cell parameters. These standards have had their unit cell determined to a high level of accuracy. Most are highly symmetric systems, as these produce simpler diffraction patterns, which means there is less chance of overlap between the peaks of the standard and sample. The known unit cell of the standard can then be used to calibrate the shift in 2θ values caused by other factors. This can then be taken into account in the determination of the unknown unit cell.

If the thermal expansion of the standard material were known, it could be used to determine the temperature of the system for VT work. Unfortunately the many temperature dependent factors affecting peak position normally prevent this approach from being accurate. If however, two standards are mixed with the sample, then the systematic errors in peak position for the two will be the same. This means that an accurate temperature can be obtained from the difference in the thermal expansion between the two, regardless of absolute errors.

For this experiment Si and Al_2O_3 were chosen as standards. Both are reasonably well characterised. For Al_2O_3 the most comprehensive thermal expansion data available are from Taylor.[2] Taylor fitted this literature thermal expansion data to the polynomial shown in Equation 3-1, with the coefficients summarised in Table 3-1. The National Institute of Standards and Technology (NIST)[3] have produced a more recent RT measurement of the cell parameters, on Standard Reference Material 676. For the current work, the x0 terms of a, c and volume from Taylor's equation were adjusted so that Equation 3-1 gives the NIST cell values at 298 K. Note that T in Equation 3-1 is parameterised in °C.

$$y = x_o(1 + x_1T + x_2T^2)$$ Equation 3-1

	Taylor x0 (Å)	NIST x_0 (Å)	x_1 (K^{-1})	x_2 (K^{-2})	Taylor cell at 298 K (Å)	NIST cell at 298 K (Å)
a	4.7568	4.7584	6.55E-06	1.82E-09	4.75758	4.75918
c	12.9886	12.9897	6.54E-06	2.60E-09	12.99073	12.99183
volume	254.53	254.71	1.96E-05	6.54E-09	254.65500	254.83970

Table 3-1: Thermal expansion coefficients by Taylor.

Two sets of data were used to model the thermal expansion of silicon. The first, Okada and Tokumaru[4] gave cell parameters from 300 to 1500 K. The second, by Lyon *et al.*[5] gave the relative thermal expansion between 6 and 340 K. Both data sets were normalised to fit with the NIST 640 C value of 5.4311946 Å[6] at 295.65 K. To make use of these data in the later stages of this work, the raw data were fitted to the expression shown in Equation 3-2 using TOPAS. This gave the parameters shown in Table 3-2.

The errors in all the fitted parameters, with the exception of a_0, are significant, as shown below. This is due to the strong correlation between the parameters which means a similar quality of fit to the data can be obtained even if a significant shift of one of the parameters occurs, providing the other parameters are adjusted to compensate. The expression does, however, provide a good parameterisation of the overall thermal expansion with a maximum deviation of the function from the measured cell length of $< 5 \times 10^{-5}$ Å at 1500 K. This is shown in Figure 3-2.

$$cell\_length = Exp\left[\ln(a_0) + \left(\frac{C_1 \times 10^{-6} \times \theta_1}{Exp(\theta_1 / T - 1)}\right) + \left(\frac{C_2 \times 10^{-6} \times \theta_2}{Exp(\theta_2 / T - 1)}\right) + \left(\frac{C_3 \times 10^{-6} \times \theta_3}{Exp(\theta_3 / T - 1)}\right)\right]$$

Equation 3-2

	C_n (K^{-1})	E.S.D. (K^{-1})	Θ_n (K)	E.S.D. (K)	a_0 (Å)	E.S.D. (Å)
1	-1.272	0.015	217	37	5.42999	0.00001
2	4.819	0.027	571	43		
3	1.016	0.017	1500	147		

Table 3-2: Coefficients of Equation 3-2 used to fit the silicon thermal expansion data of Okada and Tokumaru, and Lyon *et al.*

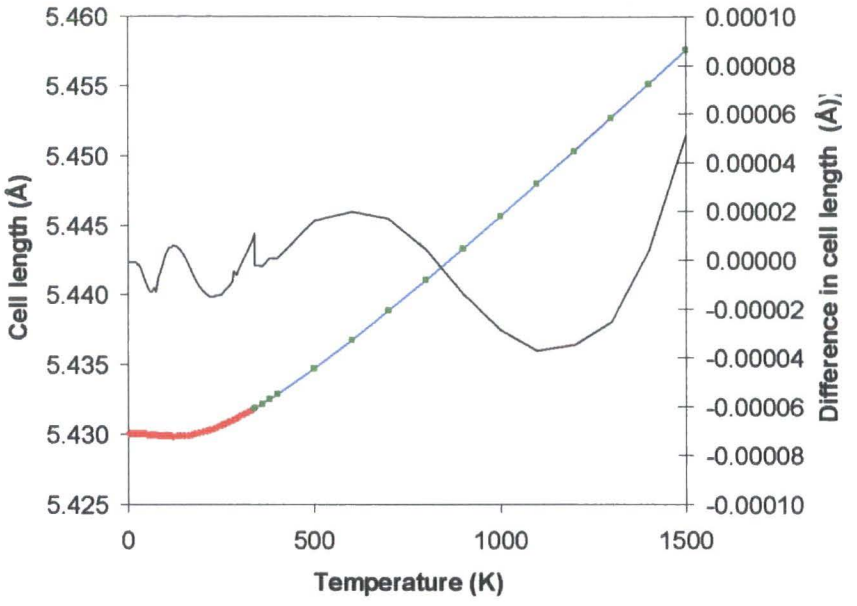

Figure 3-2: Silicon thermal expansion data from Okada and Tokumaru is shown as red diamonds, Lyon *et al.* as green squares, with the expression from Equation 3-2 shown in blue. The difference between the expression and the data points are shown by the black line, which uses the right-hand axis.

3.2.2 Synthesis of ZrP_2O_7

The zirconium phosphate used in this work was synthesised by JSO Evans as sample JSOE 370, later relabelled JSOE 439. This sample was used as many other measurements have been performed on it. 23.038g of $ZrOCl_2.(7.14)H_2O$ (0.075 moles) was ground for 10 minutes and added to 17.3913g of 85% H_3PO_4 (0.15 moles). The mixture was ground for a further 15 minutes until it was a thick, white paste. The paste was heated at 5°C a minute to 350°C, where it was held for one hour. The resultant powder was centrifuged 4 times in 75 cm^3 of distilled water for 10 minutes at 2000 rpm. After the fourth cycle, the water was clear. The resultant paste was placed in a Pt crucible and dried at 180°C for 30 minutes. It was then heated to 750°C at 3°C per minute and held for 7 hours. The final annealing of the sample was for 12 hours at 1000°C, after a heating rate of 10°C per minute to that temperature.

0.2g of this ZrP_2O_7 sample was mixed with 0.2g of silicon (-325 mesh, 99.5% Alfa) and 0.2g of aluminium oxide (-100 mesh, 99%, Aldrich). These were ground together for 10 minutes to ensure sample homogeneity before VT X-ray studies.

3.2.3 X-ray Diffraction Measurement

A Bruker AXS d8 Advance X-ray powder diffractometer was used to collect X-ray diffraction data, see sections 2.3.2 and 2.3.3 for details. For the purpose of this experiment the sample was heated in an HTK 1200 furnace which allows temperatures from 298 K to 1473 K to be accessed.

The sample was mounted on an amorphous silica plate then scanned on the d8. 51 data sets

were recorded, the first a 16 hour scan at 30°C (scan d8_02967), with subsequent measurements over 30 minutes every 15°C from 30°C up to 390°C then down to 30°C (scan d8_02968, ranges 1 to 50). The heating and cooling rates between data sets were 0.2 Ks^{-1}. Data points were measured every 0.017° from 5° to 139.9° and the whole data range was used for all refinements. A slow flow of nitrogen was passed across the sample to prevent the silicon oxidising.

3.2.4 Sequential Rietveld Refinement

The first stage of analysis after acquiring the data was to use the TOPAS Academic package for Rietveld refinement. The different temperature ranges were refined sequentially with the structural model resulting from one refinement being used as the starting model for the next refinement.

The silicon and aluminium oxide cell parameters were allowed to refine freely at this stage. To allow a reasonable speed of refinement a subcell model with $Pa\bar{3}$ symmetry was used for zirconium phosphate throughout this work. This meant there were large ADPs in the ZrP_2O_7 model, particularly for the oxygen atoms. 53 parameters were refined for each scan, 18 terms of a Chebychev polynomial to describe the background, 1 sample height parameter, 1 parameter to describe axial divergence, 4 cell parameters (1 ZrP_2O_7, 1 silicon, 2 aluminium oxide), 7 atomic displacement parameters (1 Zr, 1 P, 2 O for ZrP_2O_7; 1 for Si; 1 Al and 1 O for Al_2O_3), 18 peak shape parameters (6 terms for a TCHz pseudo-Voigt model of each compound), 3 scale factors and one fractional coordinate of the phosphorus in ZrP_2O_7. This gave 2650 parameters for all 50 VT data sets.

This produced Rwps between 18.1 and 19.9%, with an average of 18.9%. Assuming the set temperature of the instrument to be the true sample temperature, the most important results are plotted in Figure 3-3.

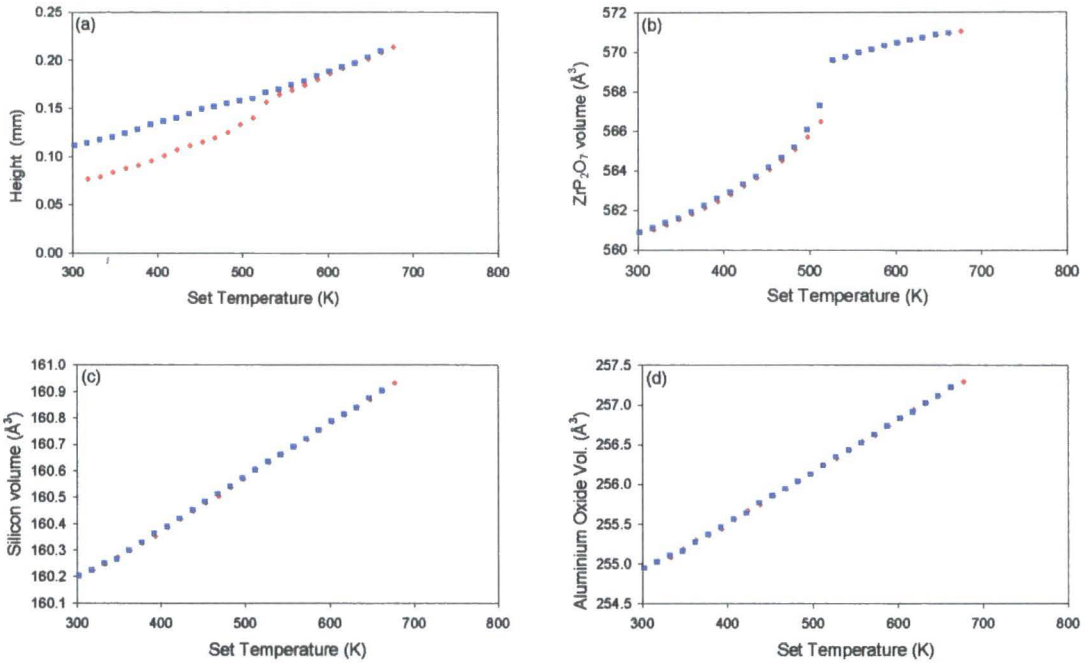

Figure 3-3: Key parameters from sequential Rietveld refinement. All data points on warming are shown as red diamonds, cooling as blue squares. (a) shows the height displacement in millimetres from the optimum position. (b), (c) and (d) show the volume with respect to temperature of ZrP_2O_7, Si and Al_2O_3 respectively.

From Figure 3-3b the 3x3x3 to 1x1x1 phase transition occurred between 239 and 254°C. This temperature is significantly lower than the 293°C determined by DSC. Around 240°C, just before the phase transition, a small irreversible change in sample height occurred. This causes no discontinuity in either the silicon or aluminium oxide cell parameters.

3.2.5 Sequential Rietveld Refinement with an Applied 2θ Correction and Predetermined Temperature Calibration

As shown in Figure 3-3(c) the silicon cell volume at 302 K is 160.2092 $Å^3$, which corresponds to a cell parameter of 5.43120 Å. This value compares to an expected value for NIST silicon of 5.43129 Å from Equation 3-2. Therefore a 2θ calibration curve of the form shown in Equation 3-3 was applied. 'X_0' is the original 2θ value, with '2θ_offset' the correction applied. For this work 'data_middle' is set to 75 as the approximate midpoint of the refined data range; 'square', 'step_error' and 'zero' are parameters to be refined.

$$2\theta\_offset = (X_0 - data\_middle)\text{^}2 \times (square/1000) + (X_0 - data\_middle) \times (step\_error/1000) + zero$$

Equation 3-3

A 2θ calibration of this form will always show strong correlation with the height correction, therefore the two cannot be refined simultaneously. As the height of the sample varies with temperature, it cannot be fixed during the refinement of VT data, therefore the 'zero' term was fixed at 0.

The parameters for the 2θ correction were fixed by refining the initial 16 hour scan (d8_02967). The silicon cell length was fixed at the NIST value (5.43129 at 303 K), step_error, square, height, a0 and c0 were all refined. The 'step_error' and 'square' refined to values of 0.14854 (384) and 0.00309 (8) respectively. The effect of this correction is shown in Figure 3-4. This 2θ correction was then applied during the refinement of the variable temperature data, with the parameters fixed at the values stated above. The magnitude of the correction is relatively small compared to the step size of 0.017°.

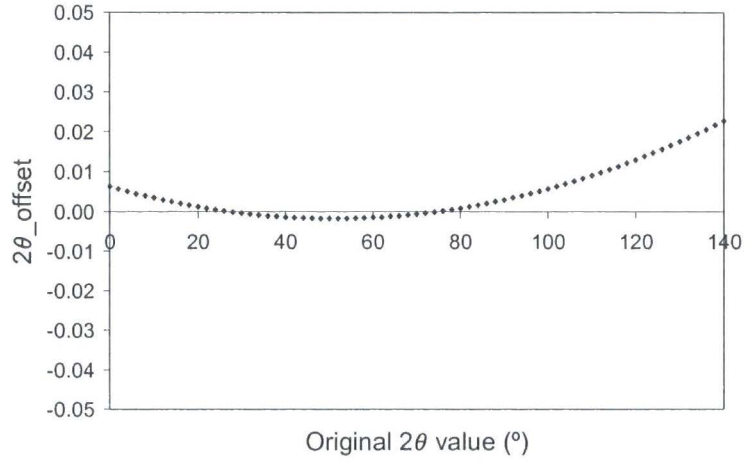

Figure 3-4: Magnitude of the 2θ correction applied.

The cell parameters of aluminium oxide were allowed to refine freely. This gave values of a = 4.75987 (6) Å and c = 12.99361(30) Å, slightly larger than the NIST 676 values of a = 4.75937(1) Å and c = 12.99227(2) Å at room temperature. It was decided to use the former values as the basis for the thermal expansion. This was done as the Al_2O_3 sample used was not from NIST and there can be subtle variations in cell parameter between samples. The x_0 values for a & c (a_0, c_0) in Equation 3-1 were therefore modified to 4.75892 Å and 12.99103 Å respectively. Using these cell parameters at 25°C gives the experimental observed values at room temperature.

Assuming Taylor's formula (Equation 3-1), one can then calculate the experimental temperature from the expression shown in Equation 3-4 where Vol_0 = 254.7885 $Å^3$ and x_1 & x_2 have the values shown in Table 3-1. The resultant difference between this experimentally derived T and the set T ($T_{actual} - T_{set}$) is shown in Figure 3-5(e).

$$T = \frac{-x_1 + \sqrt{x_1^{\,2} - 4 \times x_2 \times \left(1 - vol / vol_0\right)}}{2 \times x_2} + 273.15$$

Equation 3-4

The results of refinement after applying the temperature correction are shown in Figure 3-5 with the temperatures given as the corrected values. The most noticeable result of this is the shifting of the phase transition to between 265 and 283°C, much closer to the value obtained by DSC.

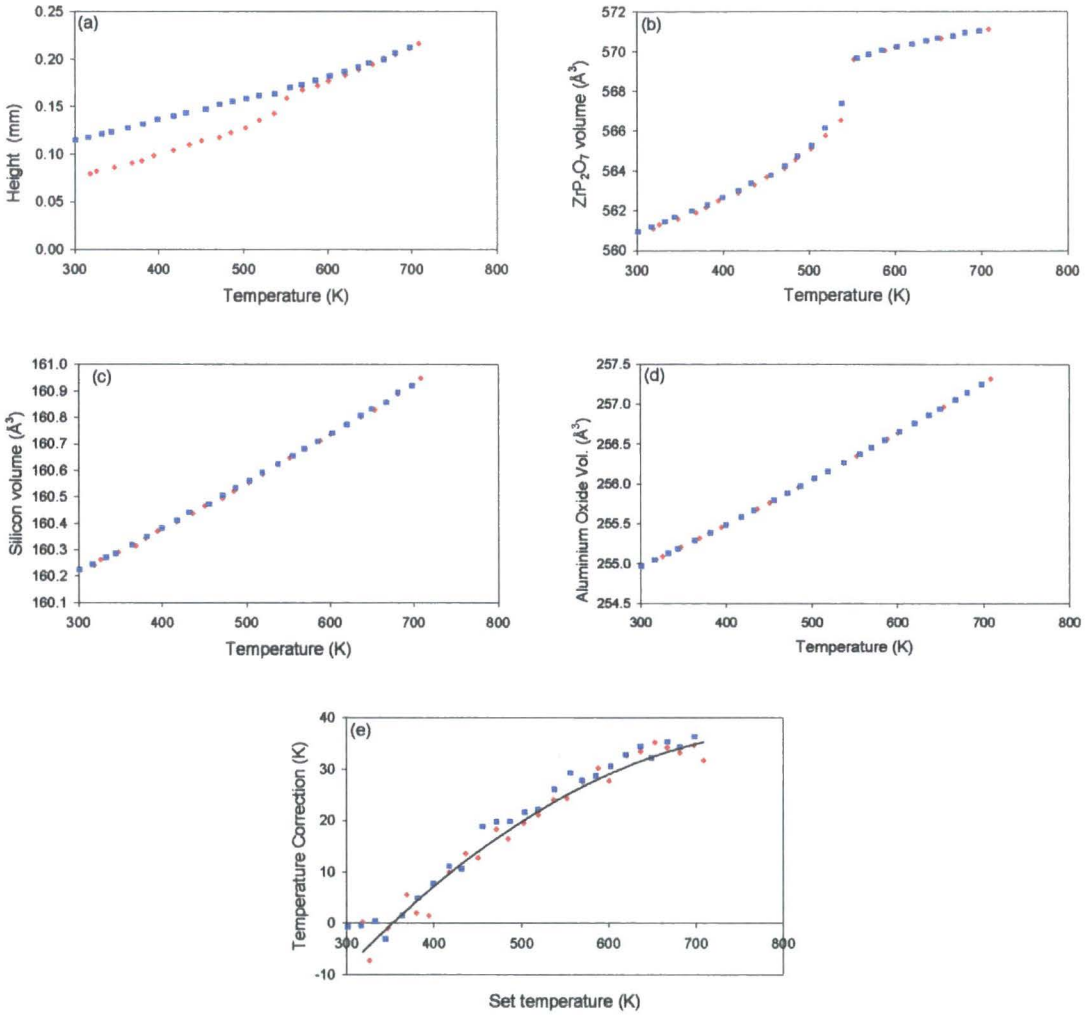

Figure 3-5: Results of sequential Rietveld refinement with a temperature correction and a 2θ correction applied. All data points during heating are shown as red diamonds, those during cooling as blue squares. (a) shows the height displacement in millimetres from the optimum position. (b), (c) and (d) show the volume with respect to temperature of ZrP_2O_7, Si and Al_2O_3 respectively. (e) shows the shift in temperature between the set temperature and the corrected temperature. The black line is a polynomial fitted through the data with the form delta T = - 0.00015 T^2 + 0.25158 T – 69.17337.

3.2.6 Simultaneous Refinement of VT Data

The next stage was to see if parametric Rietveld refinement could be used to improve the quality of the temperature calibration. The method of determining the temperature was also improved. It was shown in section 3.2.5 that it is possible to use an internal standard to help with temperature calibration; to minimise systematic errors it is best to use the difference in thermal expansion of two standards. The method used in previous sections, consisting of determining the cell parameters *via* Rietveld refinement then using these to calculate the sample temperature, can lead to different temperatures being derived from the two standards. Given that the thermal expansion of the standards is well known, it ought to be possible to express them in terms of the experimental temperature and then to refine this directly from the diffraction data along with the other parameters of a Rietveld refinement. In essence one

is using the difference between experimentally observed peak positions at any set temperature and the theoretical positions to determine the actual temperature. To achieve this, a new variable of temperature is introduced which is then refined for each of the individual data ranges. The cell parameters of the internal standards are then derived from this temperature using Equation 3-1 and Equation 3-2.

The input file used the same format as shown in Figure 3-1. The overall fixed parameter section contained the constants which are used to calculate the silicon and aluminium oxide unit cells, and the 2θ calibration values. Initially the only overall parameter allowed to refine in part 1c was an axial divergence term, although more variables were added in subsequent refinements. The actual input file is in appendix 3.2.6.

In total 2501 parameters were refined, 1 overall axial model and 50 sets of 50 parameters for each individual temperature. For each range there were 18 background terms, 1 height, 1 ZrP_2O_7 cell parameter, 1 temperature, 7 atomic displacement parameters (1 Zr, 1 P, 2 O for ZrP_2O_7; 1 Si and 1 Al & 1 O for Al_2O_3), 18 peak shape (6 terms for a TCHZ model for each compound), 3 scale factors and 1 parameter for the position of the phosphorus atom in ZrP_2O_7.

The final results are shown in Figure 3-6, with all data plotted against refined experimental temperature. The temperature correction is similar to that produced in section 3.2.5. This set of refinements gave the phase transition between 279 and 293°C; (DSC measurements showed the transition at 293°). The overall Rwp was 18.9 %, which was the same to 1 decimal place as the average value produced by the sequential refinement. The Rietveld plot for the parametric refinement is shown in Figure 3-7.

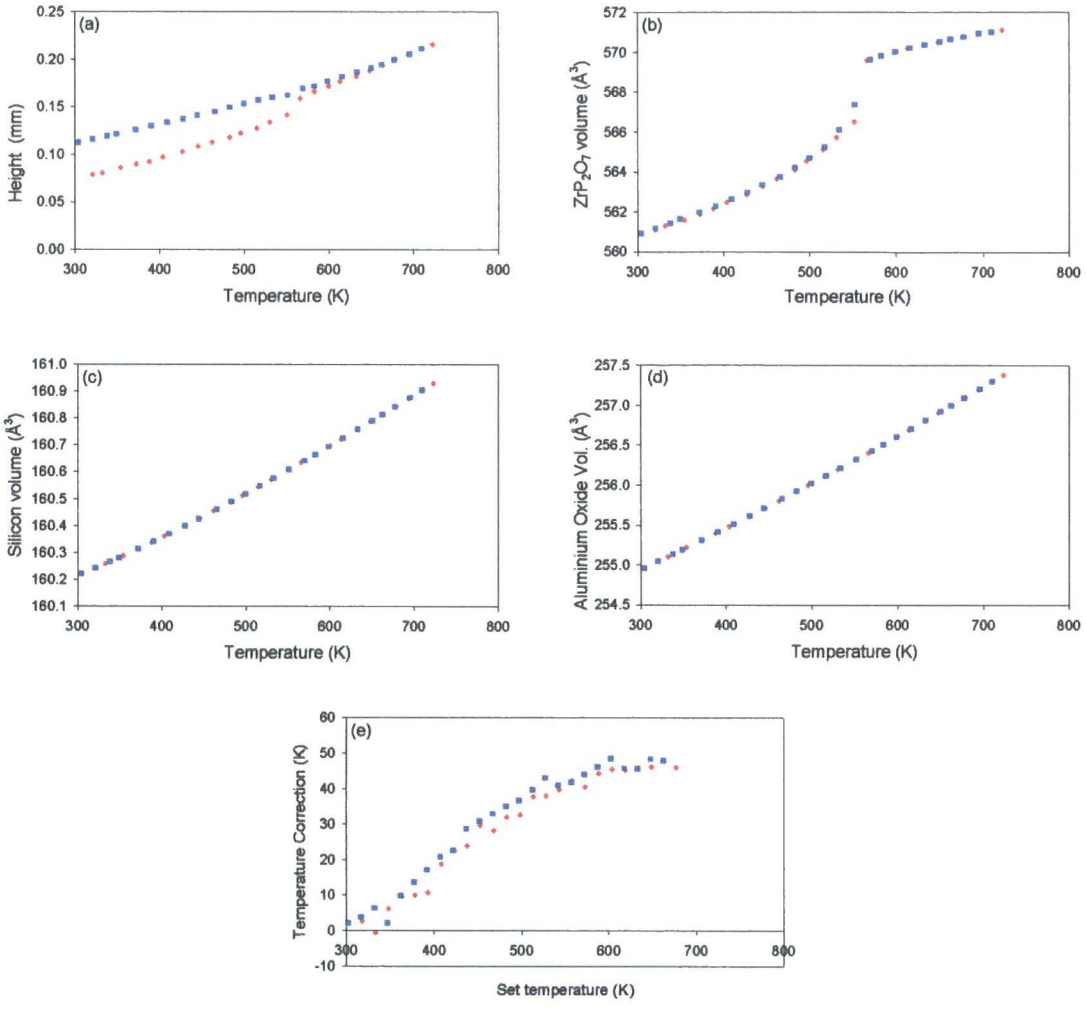

Figure 3-6: Results of simultaneous Rietveld refinement with a temperature correction and a 2θ correction applied. All data points taken during heating are shown as red diamonds, those during cooling as blue squares. (a) shows the height displacement in millimetres from the optimum position. (b), (c) and (d) show the volume with respect to temperature of ZrP_2O_7, Si and Al_2O_3 respectively. (e) shows the difference in temperature between the set temperature and the actual temperature determined from the silicon and aluminium oxide cell parameters.

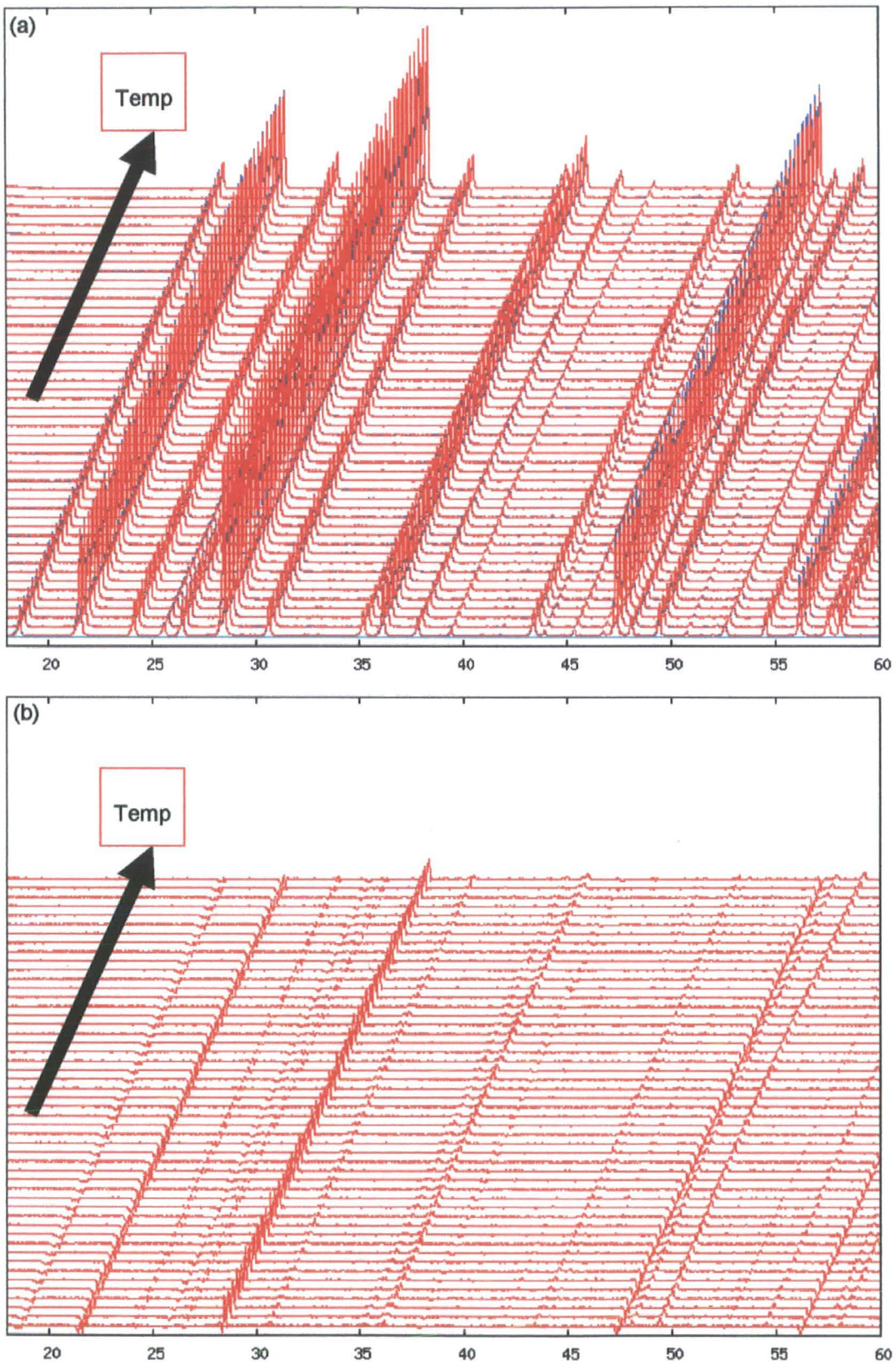

Figure 3-7: Rietveld plot of the parametric fit. 2θ theta angle is on the x axis, temperature is on the y axis and intensity is on the z axis. (a) shows the experimental data in blue and the theoretical fit in red. (b) shows the difference between the experimental data and the theoretical fit.

3.2.7 Fitting the Temperature Calibration to a Polynomial Function

The series of individual temperature corrections produced in section 3.2.6 provided a good fit of the data and a temperature calibration with the expected functional form, which gave a phase transition T in agreement with calorimetry. It is unlikely that the error between the set temperature of the HTK1200 and the real temperature varies erratically with changing set temperature. Therefore the individual temperature refinements were replaced by a polynomial of the form shown in Equation 3-5. The parameters a to d were refined in the overall refinable parameters block (part 2).

$$real\_T = T_{set} + a + b*\left(\frac{T_{set}}{200}\right) + c*\left(\frac{T_{set}}{200}\right)^2 + d*\left(\frac{T_{set}}{200}\right)^3$$

Equation 3-5

The refinements were found to be more stable in practice and converged more easily if the parameters were expressed in terms of T_{set}-$T_{average}$. This results in the equation shown in Equation 3-6. The differences in convergence between the two methods are shown in Figure 3-8.

$$real\_T = T_{set} + a + b*\left(\frac{T_{set} - T_{av.}}{200}\right) + c*\left(\frac{T_{set} - T_{av.}}{200}\right)^2 + d*\left(\frac{T_{set} - T_{av.}}{200}\right)^3$$

Equation 3-6

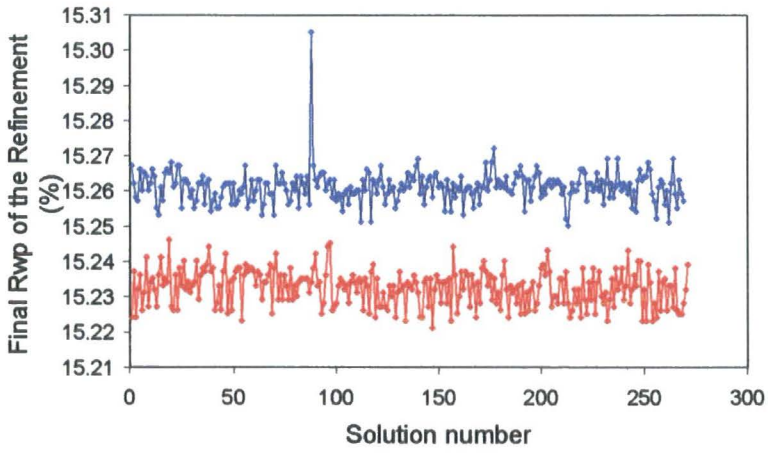

Figure 3-8: Graph showing the Rwp of different solutions produced for a polynomial fitting of the temperature. The quality of fit for the original model (Equation 3-5) is shown in blue, with the later model (Equation 3-6) shown in red. This experiment was carried out with a rebinning of data to increase speed. This rebinning was not used in later refinements.

The variables a, b, c, and d were set as overall parameters for the refinement. Upon refinement these produced values of 35.19015, 30.18364, -14.32588 and -7.34908 respectively. This process resulted in a fit of similar quality to that of the free refinement, with an Rwp 18.889 of compared to 18.874 % in the free refinement. The refined temperature of the phase transition was between 277 and 293°C. The refined parameters are shown in

Figure 3-9. Figure 3-9e shows the key result. The smooth parametrically fitted temperature correction is in excellent agreement with values refined from individual data sets.

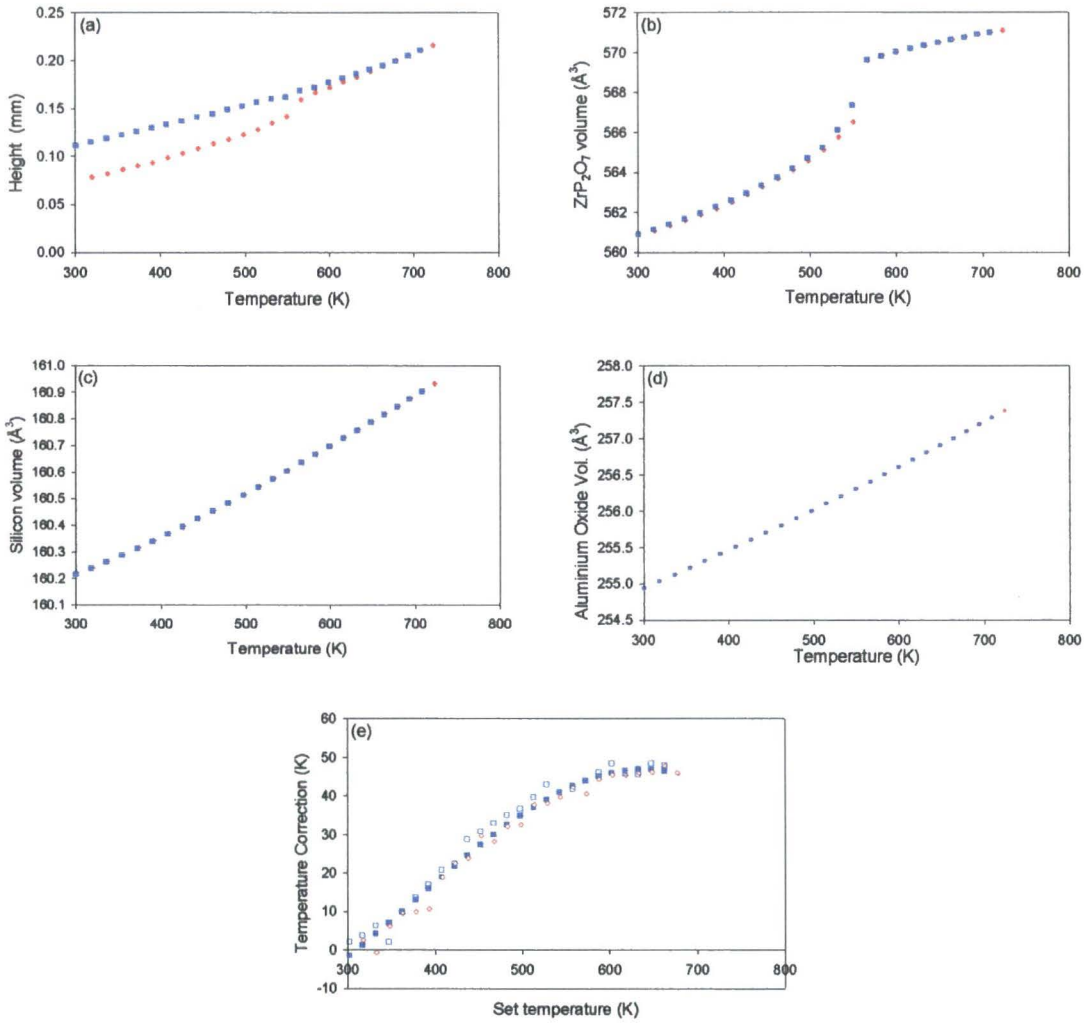

Figure 3-9: Results of simultaneous Rietveld refinement with a polynomial temperature correction and a 2θ correction applied. All data points during heating are shown as red diamonds, those during cooling as blue squares. (a) shows the height displacement in millimetres from the optimum position. (b), (c) and (d) show the volume with respect to temperature of ZrP_2O_7, Si and Al_2O_3 respectively. (e) shows the difference in temperature between the set temperature and the actual temperature determined from the silicon and aluminium oxide cell parameters. The results from this section are shown as filled points, with those from the previous section as open points for comparison.

3.2.8 Accurately Determination of the Phase Transition Using Small Temperature Steps

While surface fitting had been successfully applied to the variable temperature data set from ZrP_2O_7, the 15°C step between diffraction measurements obviously means that the temperature of the phase transition could only be determined to within a 15°C bracket. It was therefore decided to take a second set of VT diffraction measurements on the sample. This

consisted of taking measurements every 2°C from 30°C up to 900°C then down to 30°C. Each scan was taken for 4 minutes. This series of 871 data sets was designed to see how much information parametric Rietveld refinement could extract from very noisy data.

Both sequential and parametric Rietveld refinement was carried out by JSO Evans using the method described in section 3.2.5 and section 3.2.7 respectively. The main results are shown in Figure 3-10. Using a 3 GHz desktop PC with 2 Gb of RAM all 871 data sets could only be refined on a realistic timescale by rebinning the step size and we therefore chose to refine every second data set. The key results are shown in Figure 3-10 and Figure 3-11.

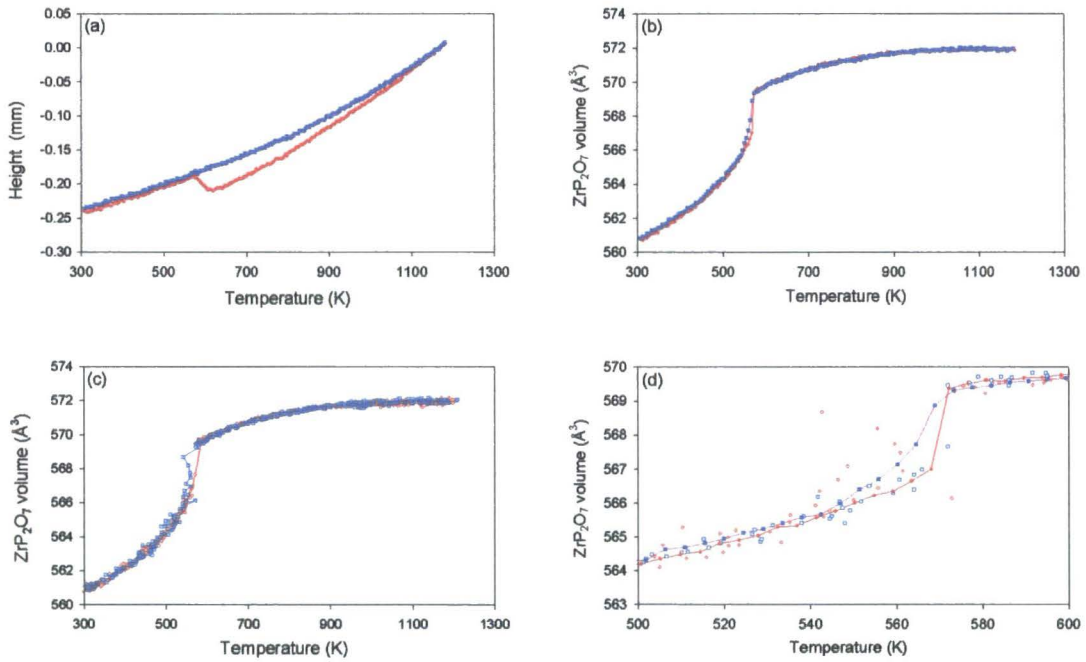

Figure 3-10: Plots of (a) sample, (b) volume from surface fitting, (c) volume from independent fitting; (d) superimposes parametric (joined closed points) & independent fitting (open points) close to the phase transition temperature.

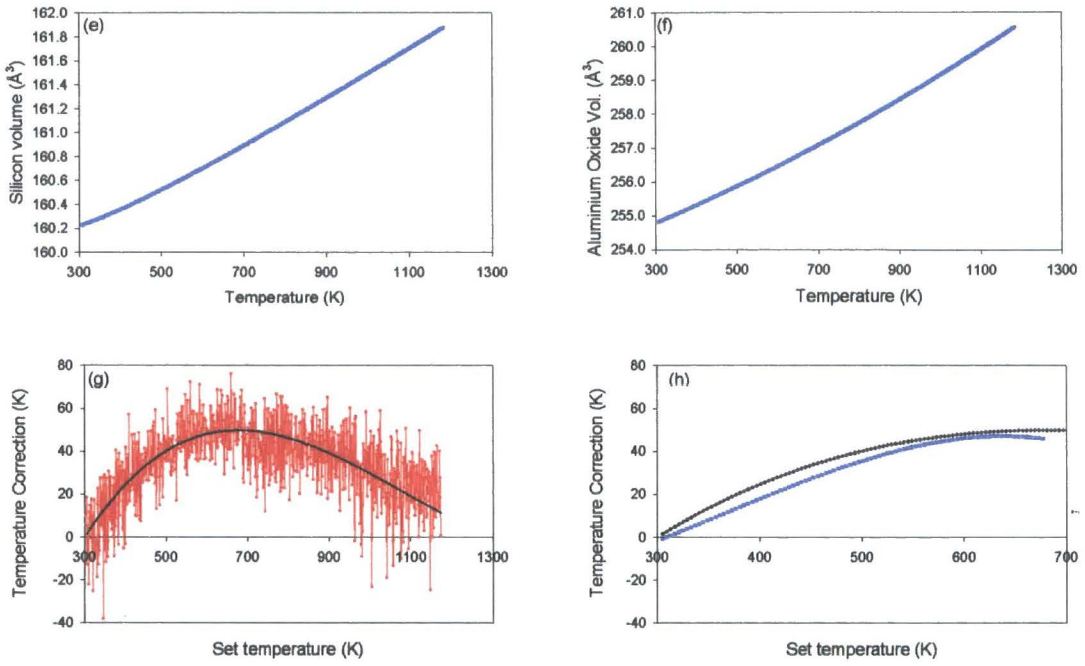

Figure 3-11: (e) and (f) show the unit cell volume calculated during surface fitting for silicon and aluminium oxide respectively. (g) shows the difference in temperature between the set temperature and the actual temperature determined from the silicon and aluminium oxide cell parameters. The results from surface fitting are shown as black, filled points, with those from the free refinement as red points. (h) shows the comparison between the temperature correction from 436 data sets (black) and from 50 data sets (blue).

The application of surface fitting to this data produces a much smoother variation in cell parameter than the sequential refinement. Much of the random scatter seen in Figure 3-10(c) is absent in Figure 3-10(b). This is particularly true of the points of greatest interest; those around the phase transition. The phase transition occurs between 295°C and 299°C on heating and between 292°C and 300°C on cooling. The application of the surface fitting also allows the hystersis of the phase transition to be clearly seen.

3.2.9 Parametric Fitting of ZrP_2O_7 - Conclusion

A new approach to the Rietveld refinement of variable temperature data has been demonstrated using a simultaneous rather than sequential process. This is potentially useful for all VT data, enabling better control over which parameters are refined from all of the data recorded and which from individual data sets. The ability to directly derive the temperature *via* Rietveld refinement using standard materials added to the sample has also been investigated and found to be achievable. It is therefore possible to refine 'non-crystallographic' parameters directly from diffraction data using this method.

3.3 Using Parametric Rietveld Refinement to Help Determine Rates of Reaction

3.3.1 Introduction

The aim of this section of work was to test the ability of surface fitting to assist in providing a solution to problems other than the change of cell parameter with temperature. It was therefore decided to analyse a series of kinetic X-ray diffraction measurements of $ZrWMoO_8$, which changes from a disordered, $Pa\bar{3}$, β phase to an ordered, $P2_13$ α phase over time, as discussed in section 1.3.1.

The data used were recorded by S Allen[7] and consisted of 97 measurements taken sequentially over a period of 29 hours at a constant temperature of 215 K on a sample of β-$ZrWMoO_8$ which had previously been quench cooled from 473 K. In the work by S Allen, this experiment was repeated at different temperatures to determine the activation energy of the phase transition.[8] The series of measurements at 215 K was chosen for this work due to the transition between the two phases at this temperature being sufficiently slow to occur across most of the time scale of the experiment. At higher temperatures complete conversion was achieved after only a few data sets had been collected.

Figure 3-12 shows the structure of α-$ZrWMoO_8$, consisting of ZrO_6 octahedra together with WO_4 and MoO_4 tetrahedra in a 50:50 ratio. During the conversion of β-$ZrWMoO_8$ into α-$ZrWMoO_8$ two changes which can be monitored by X-ray diffraction occur. The central $WMoO_8$ group changes from a disordered to an ordered arrangement. This is shown in more detail in Figure 3-13. During refinement sites W1, W2, O3 and O4 are defined as having identical occupancies, labelled 'frac' and W11, W21, O31 and O41 all have a fractional occupancy of '1 – frac'. The positions of W11, W21, O31 and O41 are linked to those of W1, W2, O3 and O4 respectively by a centre of symmetry at (0.5,0.5,0.5). The effect of this ordering on the diffraction pattern is the appearance of several peaks over time, for example those at ~29° and ~31°, as shown in Figure 3-14. The second change is an increase in cell parameter over time.

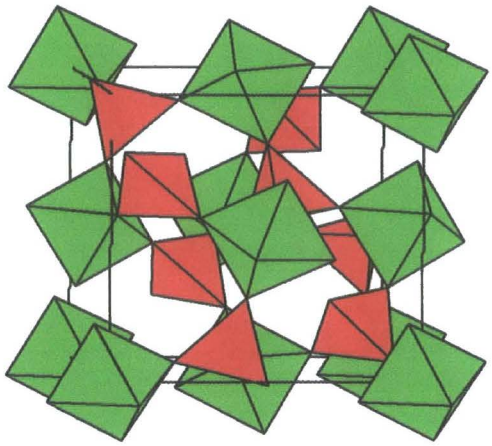

Figure 3-12: Structure of $ZrWMoO_8$. ZrO_6 octohedra are in green, MoO_4/WO_4 tetrahedra are shown in red.

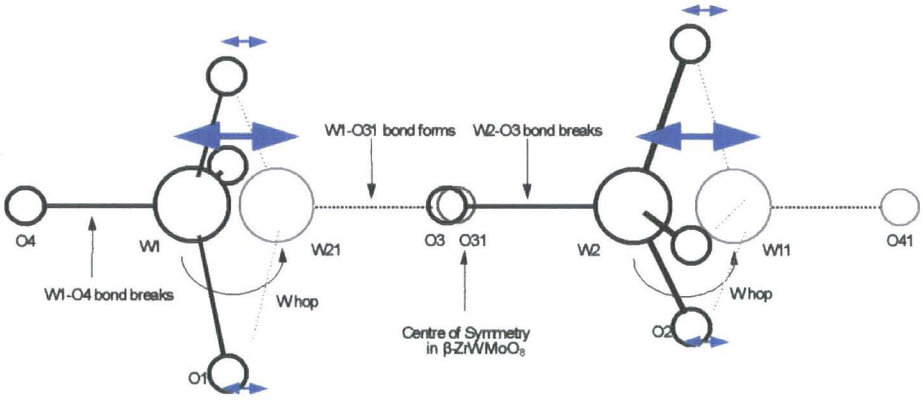

Figure 3-13: A schematic of the WO_4^{2-}/ MoO_4^{2-} group inversion in the order-disorder phase transition of $ZrWMoO_8$. In the α phase, W1, W2, O1, O2, O3 and O4 are fully occupied (bold bonds). In the β form W1, W11, W2, W21, O3, O31, O4 and O41 are all half occupied, with O1 and O2 remaining full occupied (bold and dashed bonds). Figure taken from Evans *et al.*.[9]

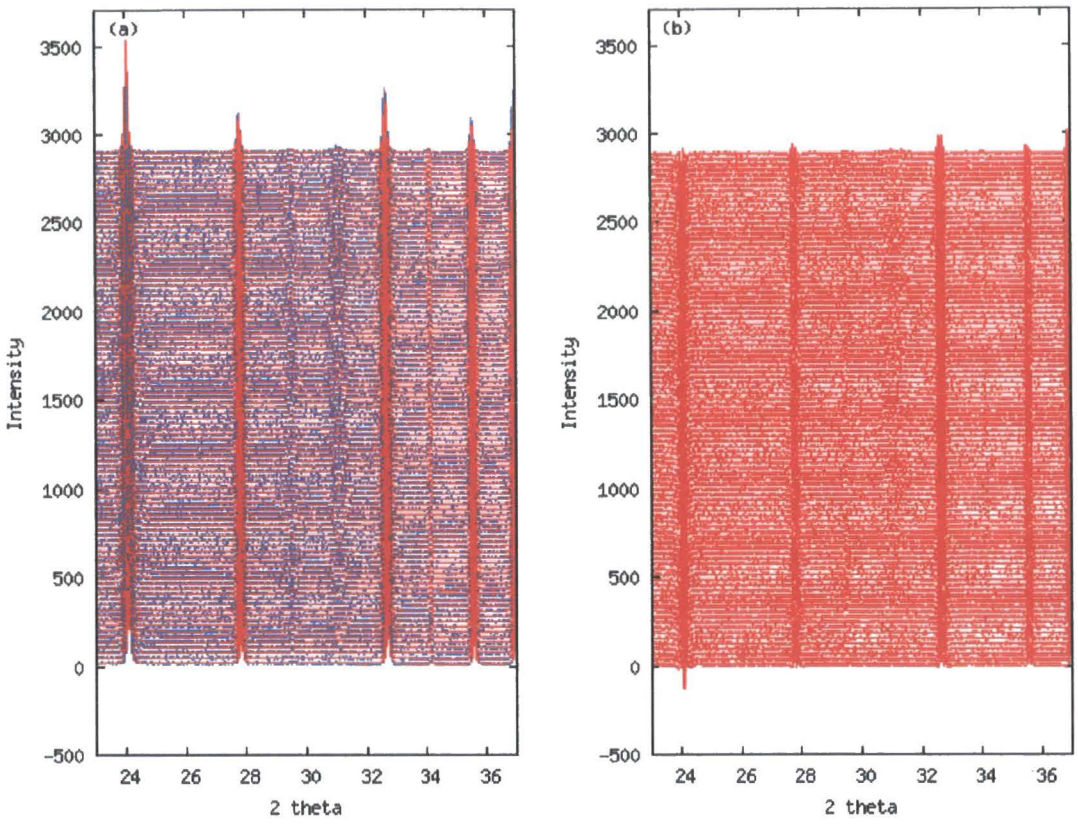

Figure 3-14: Rietveld plot of part of the parametric refinement. (a) shows the experimental data in blue and the theoretical fit in red. (b) shows the difference between the experimental and theoretical data. 2θ theta angle is on the x axis, intensity is on the y axis. The first scan is at the bottom of the plots; with later scans sequentially offset to higher values of y. Scans were taken every 18 minutes. Peaks appearing at ~29 and ~31° 2θ show the α to β transition.

3.3.2 Parametric Rietveld Analysis

Five sets of Rietveld refinement were carried out with the aim of extracting quantitative information about the time dependence of fractional occupancies and cell parameters. Simulated annealing was used in all cases to try and ensure that a true minimum had been found. This involved randomising cell parameters and fractional occupancies between solutions where these values were freely refining. If these values were controlled by kinetic equations, then the parameters in the equations were randomised.

Strategy 1: A sequential independent refinement of individual data sets. 32 parameters were refined for each data set – i.e. 3104 parameters in total. These were 1 cell length, 1 scale term, 1 height correction, 6 terms of a TCHz pseudo-Voigt function to model peak shape, 9 terms of a Chebychev polynomial to describe the background, 2 terms to model size broadening and 11 atomic position parameters. These consisted of x, y & z coordinates for O1 and O2; Zr, W1, W2, O3 and O4 lie on the 3-fold axis, therefore only required one parameter each. The average of the Rwp's of all of the refinements was 29.007 %.

From this series of Rietveld refinements 2 principal results files were obtained, one consisting of cell parameter versus time and the second of fractional occupancy of the sites of the alpha

form versus time. The first data set was fitted to the rate expression shown in Equation 3-7, using TOPAS.

In this formula B_{cell} is the initial unit cell length, theoretically this should be the unit cell length of the β phase but in practice some conversion between the two phases had occurred before the start of the diffraction measurements. A_{cell} is the difference between the initial and final unit cell lengths, again theoretically the difference between the α and β phases. k is the rate of transformation between the two phases. The second data set were fitted with same equation, only with all terms labelled cell replaced with terms labelled frac. The key results are included in Table 3-3.

$$a(t) = A_{cell} \times \left(\left[1 - e(-kt)\right] + B_{cell} / A_{cell}\right) \qquad \text{Equation 3-7}$$

Strategy 2: A simultaneous refinement of all data, with no overall parameters. This was designed to mimic the refinement in stage 1. This required 3104 parameters, consisting of 97 times the 32 parameters used for refinement 1. This gave an average Rwp of 28.989 %. It became clear that problems were occurring during simulated annealing, in that the first solution always had the lowest Rwp. When the cell parameters and fractional occupancies were randomised between structural solutions, some models for individual data sets refined to false minima. This led to a series of poor solutions. To prevent this occurring, the individual structural models for each data set were replaced by a single, overall structural model for all temperatures. This cut the number of parameters to 2048, with 97 sets of 11 atomic coordinates replaced by 11 overall atomic coordinates. The overall Rwp actually decreased, from 28.989 % to 28.842 %. This suggests that the problem of the structural model becoming stuck in false minima for some data sets had also occurred for some refinements in strategy 1.

Strategy 3: A simultaneous surface refinement of all data with the unit cell length parameterised by the rate expression shown in Equation 3-7. A_{cell}, B_{cell} and k_{cell} were freely refined parameters for the whole surface fit. This reduced the number of parameters to 1954, with 97 individual unit cell lengths replaced by the 3 overall parameters.

Strategy 4: A "mirror image" of run 3 was performed with the unit cell lengths freely refined but the fractional occupancies were parameterised using Equation 3-7. Again 1954 parameters were refined, with 97 individual fractional occupancies from refinement 2 replaced by 3 overall parameters (A_{frac}, B_{frac} and k_{frac}).

Strategy 5: Both the fractional occupancies and unit cell lengths were controlled by parametric Rietveld refinement. 1860 parameters were refined, with both the independent fractional occupancies and cell parameter replaced by the two equations, each with 3 overall parameters.

3.3.3 Results

The main results from the series of refinements in section 3.3.2 are shown in Table 3-3 and Figure 3-15. The quality of fit is slightly better for the refinements which use a single structural model for all data. There is essentially no decrease in the quality of fit by parameterising the cell lengths and occupancy; in fact there is very slight improvement in Rwp between refinements 2b and 4.

There is some variation between the values of k, A and B produced by the different refinement strategies but they generally lie within two E.S.D.s of the mean. The largest differences occur in the k_{frac} values. The differences between the different strategies are believed to be largely caused by the correlations between A, B and k, for example, the correlation between the values of A_{cell} and B_{cell} in refinement 5 is 92 %. The effect of this can be seen in Figure 3-15(c), where despite the differences in k_{frac}, A_{frac} and B_{frac} values for refinements 4 and 5, the fractional occupancy values calculated for both overlap very closely except at the extreme ends of the data.

Strategy	1.	2a.	2b.	3.	4.	5.
Method	Multitopas independent fits	Parametric Fit - no overall parameters	Parametric Fit - one structural model	Parametric Fitting of Cell	Parametric Fitting of Occupancy	Parametric Fitting of both Cell and Occupancy
k_{frac} (s^{-1})	$3.0(2)\times10^{-5}$	$3.5(2)\times10^{-5}$	$3.3(2)\times10^{-5}$	$3.3(2)\times10^{-5}$	$2.9(2)\times10^{-5}$	$3.9(2)\times10^{-5}$
A_{frac} (Å)	0.187(3)	0.180(4)	0.178(4)	0.176(4)	0.168 (4)	0.182(4)
B_{frac} (Å)	0.701(4)	0.705(5)	0.708(4)	0.710(4)	0.722 (4)	0.698(5)
k_{cell} (s^{-1})	$3.6(2)\times10^{-5}$	$4.0(2)\times10^{-5}$	$3.9(2)\times10^{-5}$	$4.2(2)\times10^{-5}$	$4.0(2)\times10^{-5}$	$3.7(2)\times10^{-5}$
A_{cell} (Å)	0.00428(7)	0.0046(1)	0.0045(1)	0.00431 (8)	0.0045(1)	0.00440(8)
B_{cell} (Å)	9.14791(7)	9.1475(1)	9.1476(1)	9.14772 (9)	9.1476(1)	9.14777(8)
Average Rwp (%)	29.007	28.985	28.825	28.827	28.823	28.833
Rwp (%)	N/A	28.989	28.831	28.833	28.828	28.838

Table 3-3: Main results from fitting $ZrWMoO_8$ phase transition data. Cell length errors for refinement 3, fractional occupancy errors for refinement 4 and all error in refinement 5 were obtained directly from parametric Rietveld refinement. All other errors were obtained from the least-squares fitting of the individual cell or frac results vs. time data using Equation 3-7.

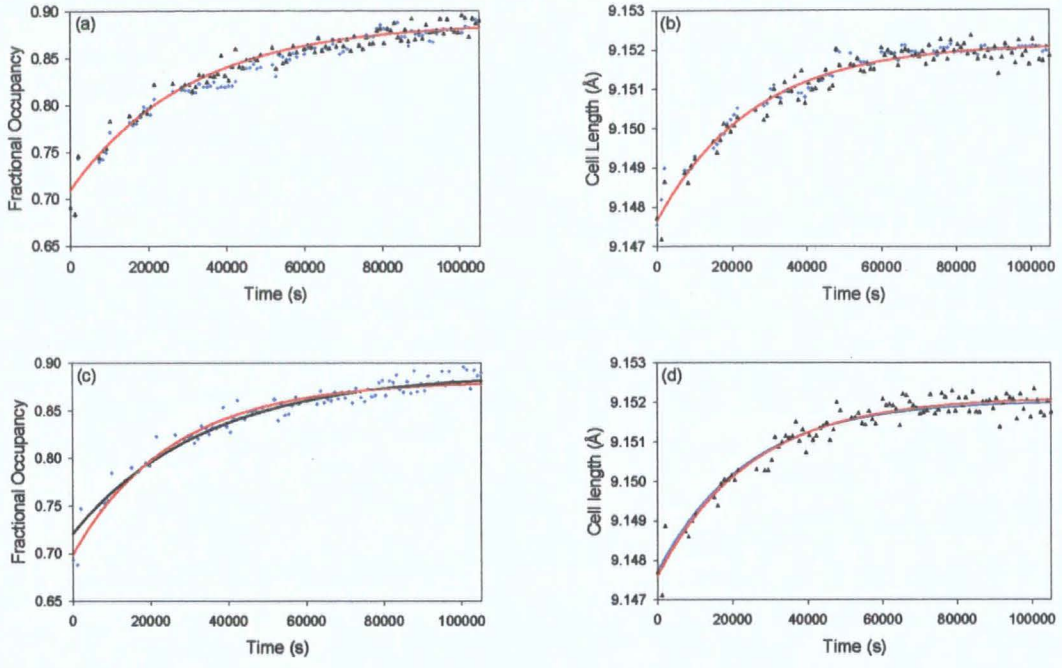

Figure 3-15: Fractional occupancies and cell parameters from the refinements. (a) and (b) show the values from the sequential refinement (strategy 1 – shown as blue squares), the parametric refinement with a single structural model (strategy 2b - black triangles) and the parametric refinement with both cell parameter and fractional occupancy parameterised (strategy 5 – solid red line). (c) and (d) show the values from parametric refinement with cell length parameterised (strategy 3 – shown as blue squares in c and a blue line in d), with fractional occupancy parameterised (strategy 4 – black line in c and black triangles in d) and both cell parameter and fractional occupancy parameterised (strategy 5 – red lines).

3.3.4 Conclusion

It is possible to use surface fitting to directly obtain kinetic information from refinements, rather than extracting crystallographic parameters from a series of refinements and determining the desired information from subsequent analysis of these parameters. The final values for the rate of reaction obtained *via* surface fitting were $3.9(2) \times 10^{-5}$ s^{-1} and $3.7(2) \times 10^{-5}$ s^{-1} from the change in fractional occupancy and the change in cell parameter respectively. Whilst it was possible that the two changes in the material occur at subtly different rates, the proximity of the two values, within one standard deviation, suggests that both processes reflect the same kinetic changes. The values found here are comparable to the previously found values of $3.8(2) \times 10^{-5}$ and 4.2×10^{-5} from fractional occupancies and cell parameters respectively.[8]

This analysis uses data at a single experimental temperature. In principle the data sets shown above could be combined with data sets from different temperatures to directly obtain the activation energy from Rietveld refinement, by simultaneous parametric fitting in both the time and temperature dimensions.

3.4 Using Surface Fitting to Obtain a Better Background Model for FePt Nanoparticle Data

3.4.1 Introduction

Co-workers have carried out variable temperature X-ray diffraction measurements on a series of FePt nanoparticles[10, 11] synthesised by various methods. The aim of this work is to convert the nanoparticles from a face centred cubic (FCC) phase to a magnetically and crystallographically face centred tetragonal (FCT) phase on heating without excessively increasing the particle size.

The refinement of data such as these is problematic. The small crystallite size of the nanoparticles means the Bragg peaks are extremely broad. Background intensity is also present primarily due to scattering from the windows of the furnace and from the sample holder in this example. The background contribution to the intensity occurs across the whole 2θ range and typically the peaks and troughs are shallow and very broad (~ 10° to 15° 2θ).

During Rietveld refinement the background is normally modelled using a Chebychev polynomial. This method works well where the Bragg peaks are sharp. For the initial data sets of this work, however, the crystallites are very small, leading to broad peaks. This causes the Bragg peaks to be partially fitted by the background polynomial and experimental background intensity to be fitted by the structural model. This leads to inaccurate determination of structural parameters.

The aim of this work was to investigate whether such correlations could be reduced using parametric Rietveld refinement. The background could be more accurately determined for the later data sets which had sharper Bragg peaks (see Figure 3-16). All temperatures could be refined simultaneously, with the background terms varying smoothly as a function of temperature. This could potentially help determine the background of the earlier scans using information from the later scans.

3.4.2 Visual Analysis of the Diffraction Data

Diffraction measurements were taken every 25 K from 308 K to 908 K and down to 308 K again. This gave a total of 49 data sets. This shows several things. The data in Figure 3-16 reveal two distinct phenomena that occur on heating. Firstly diffraction peaks sharpen, which is an indication of the growth of crystallite size. Secondly, extra peaks are observed to grow into the diffraction pattern (eg. at 2θ = 23° and 32°). These peaks indicate the onset of atomic ordering in the material as its structure changes (see Figure 3-17) from a face-centred cubic, disordered structure to a face-centre, tetragonal one.

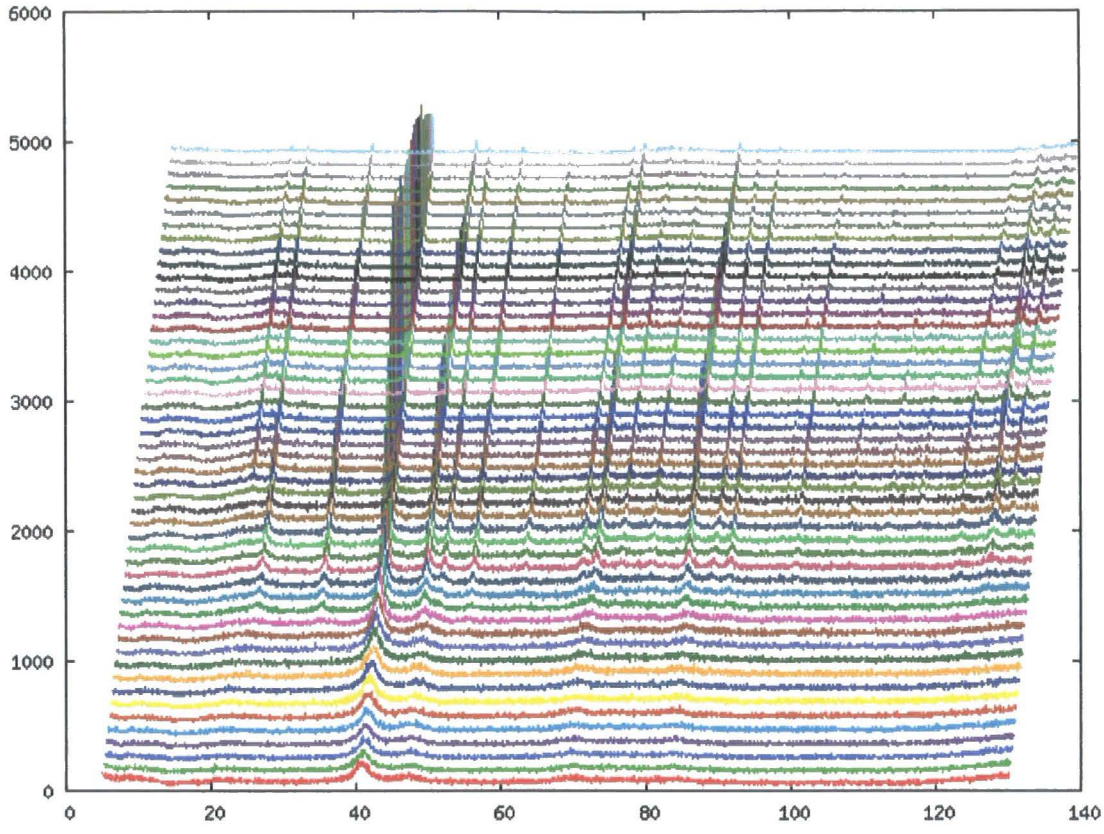

Figure 3-16: Raw data from variable temperature X-ray diffraction of FePt. The x axis shows 2θ angle and the y axis intensity. The first data set are at the bottom of the graph, with each subsequent data sets offset by x = 0.2° and y = 100. The first data set is at 308 K, with each subsequent data sets 25 K warmer until the middle pattern (908 K), after which each subsequent data sets is 25 K cooler.

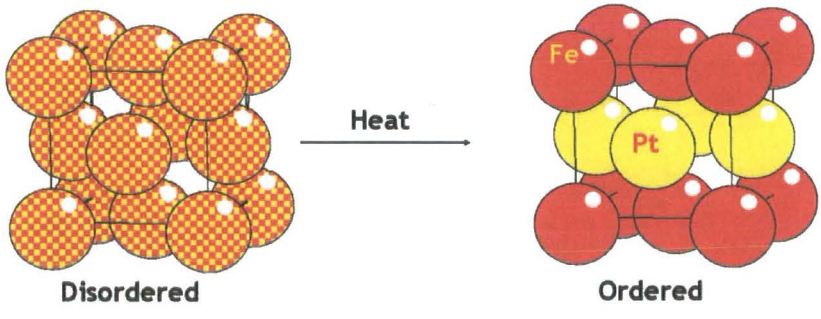

Figure 3-17: The phase transition from the disordered FCC phase to the ordered FCT phase.

All of the data collected were refined using the same starting structural model with P4/mmm symmetry. As the material orders, each site changes from having an equal amount of both elements to having one major component and one minor component. During refinement, all 3 sites shared one value for the fractional occupancy of the minor component. This was labelled 'frac'. The amount of ordering was measured as '1 - 2 * frac'. Therefore a fully disordered material had a 'frac' of 0.5 and an order parameter of 0, where as values of 0 and 1 respectively occur for a fully ordered material.

Closer examination of the data of Figure 3-16 shows that the background demonstrates

relatively complex behaviour, with several broad "humps" visible. This can be seen more clearly in Figure 3-18. Modelling these humps using a standard background polynomial would require the use of a large number of terms. It was therefore decided to exclude the region below 16°, as no diffraction peaks occurred here, in order to simplify the refinement. The region above 118° was also excluded. The regions between 18° to 27° and between 66° to 83° were kept in the refinement, as they are regions where peaks appear during the phase transition. To model the shape of the background in these two regions, 2 independent Gaussian peaks were added in the input file alongside the background polynomial. For both of the independent peaks three parameters were refined. These were a peak area, a fwhm and the centre point of the peak in 2θ.

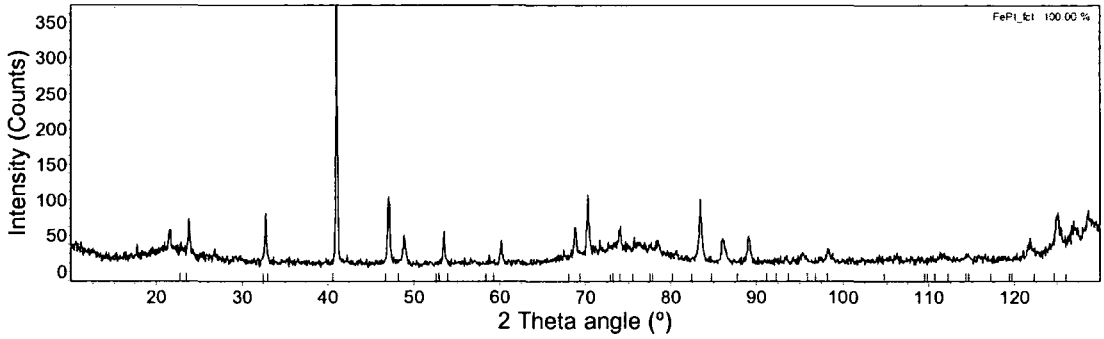

Figure 3-18: Final data set after cooling.

It is also clear from examining individual data sets that there are significant changes in background as a function of temperature. This is shown in Figure 3-19 which plots the average background counts over 3 narrow 2θ ranges of the data. Some of the processes leading to changes in the background are reversible on cooling and arise due to the changing sample height; others are due to irreversible changes in the sample caused by heating.

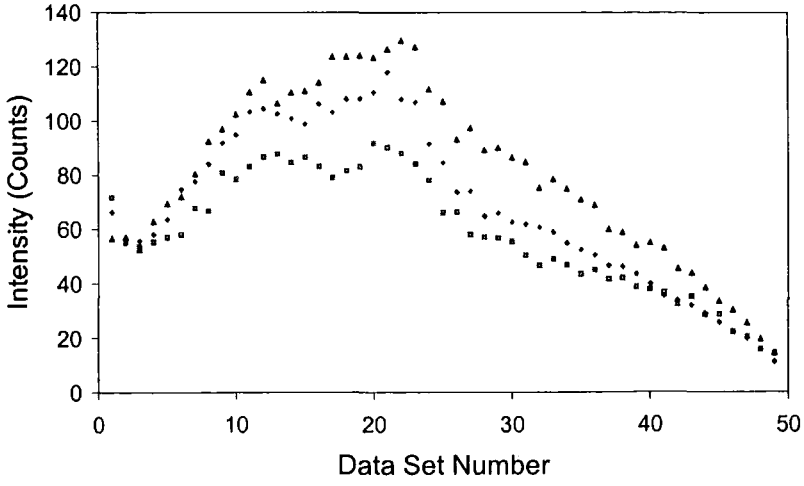

Figure 3-19: Graph of the variation in background intensity with data set. The number of the data set is shown on the x axis and the background intensity on the y axis. The averages of intensities between 30.03° and 30.57° 2θ are light grey squares, between 56.00° and 56.54° 2θ are dark grey diamonds and between 100.00° and 100.54° 2θ are black triangles.

3.4.3 Free Refinement

The first stage was to see what occurred with a completely free refinement of the data with no parameterising of the background. Data from 18° to 118° 2θ were used for all 49 data sets. 2 independent peaks were added, initially centred at 22° and 75°, to fit the background humps. The normal background function was replaced by the shifted Chebychev polynomial shown in Equation 3-8. X_{sh} is the shifted 2θ value in the refinement. This was calculated by subtracting the average 2θ value of the data (78°) from the real 2θ value and dividing by the length of the 2θ range (100°). This was designed to improve stability of the refinement in a similar manner to that shown in section 3.2.7. This function worked on a same principle as the standard background Chebychev polynomial, but allowed the terms in the model to be controlled by mathematical functions in the later stages of this work. For each individual temperature, the variable names bk0_t_0000 etc. were replaced by a name including that temperature. For this refinement the 4 background parameters per data set were allowed to freely refine.

$$(background) = fit\_obj = bk0\_t\_0000 + bk1\_t\_0000 * X_{sh} + bk2\_t\_0000 * X_{sh}^{\ 2} + bk3\_t\_0000 * X_{sh}^{\ 3}$$

Equation 3-8

A total of 833 parameters were refined, 17 for each of 49 data sets. These 17 parameters consisted of the 4 background terms; an area, a fwhm and a centre point for each of the two independent peaks used to fit the humps in the background; 2 cell lengths for the tetragonal unit cell, 1 fractional occupancy, 1 crystallite size, 1 scale, 1 atomic displacement parameter for all of the atomic sites and 1 height correction.

The main results are shown in Figure 3-20. The order parameter is significantly above the expected value of 0 for ranges 1 to 11. This is due to the background refining to too low a value in these ranges in various places e.g. from 23° to 33°. Additional theoretical intensity is therefore produced in this region by partially ordering of the FePt structural model. This leads to the 001 and the 110 peaks having non-zero intensity, which improves the fit but leads to theoretical peaks where no experimental peaks are visible. This can be seen in Figure 3-21. The average Rwp of the 49 refinements was 8.865 %.

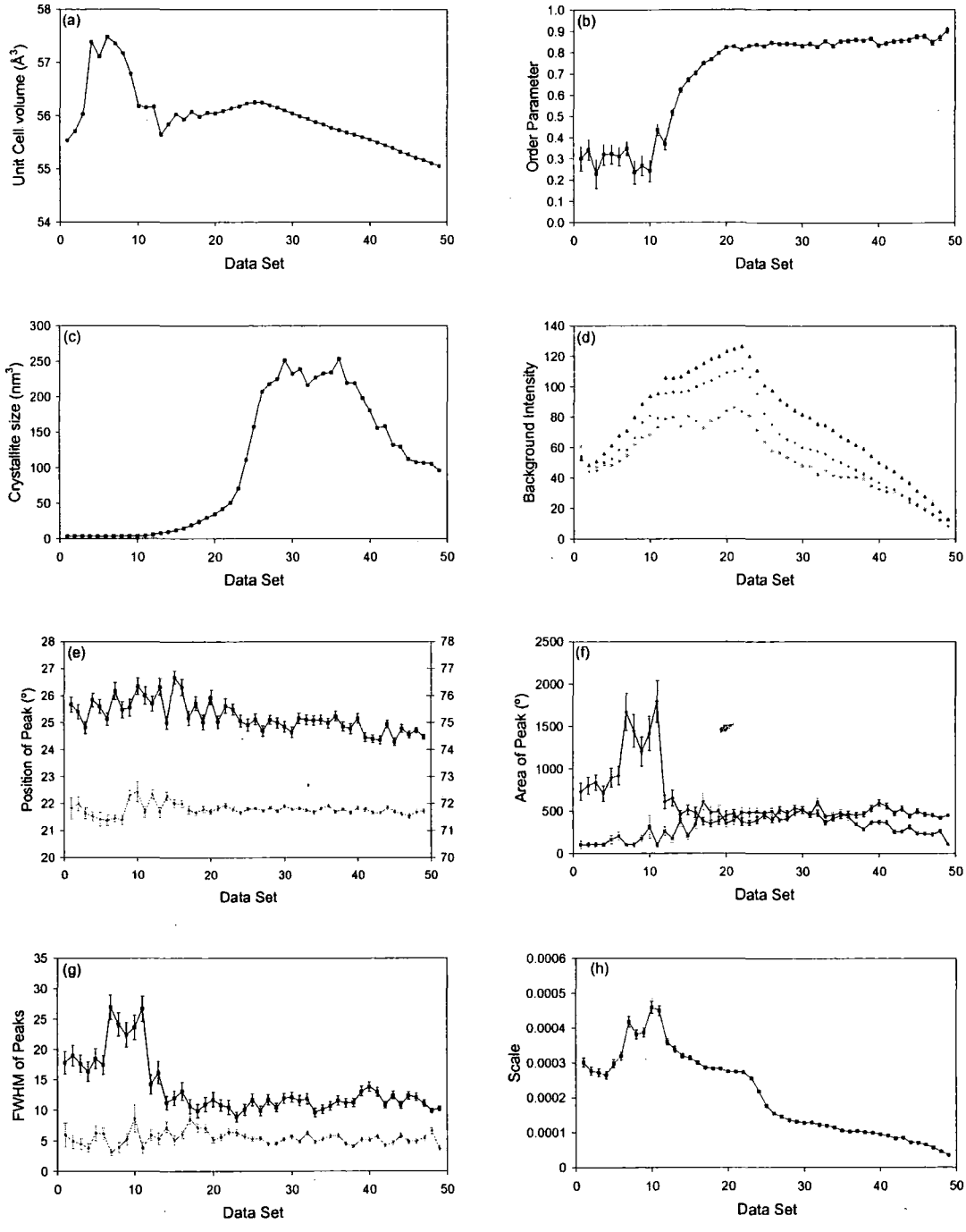

Figure 3-20: Variation in key parameters with changing data set, produced by a free refinement of the data. (a) shows the variation in unit cell volume. (b) shows the change in order parameter and (c) the crystallite size. (d) plots the variation in background at the points in the pattern analysed in Figure 3-19. The intensities at 30.3° ° 2θ are light grey squares, at 56.27 2θ are dark grey diamonds and between 100.27° 2θ are black triangles. (e) shows the centre position of two independent peaks, peak 1 as black squares with the scale on the right and peak 2 diamonds in grey with the scale on the left. (f) and (g) show the area and FWHM respectively of the two independent peaks (peak 1 as black squares and peak 2 as grey diamonds).

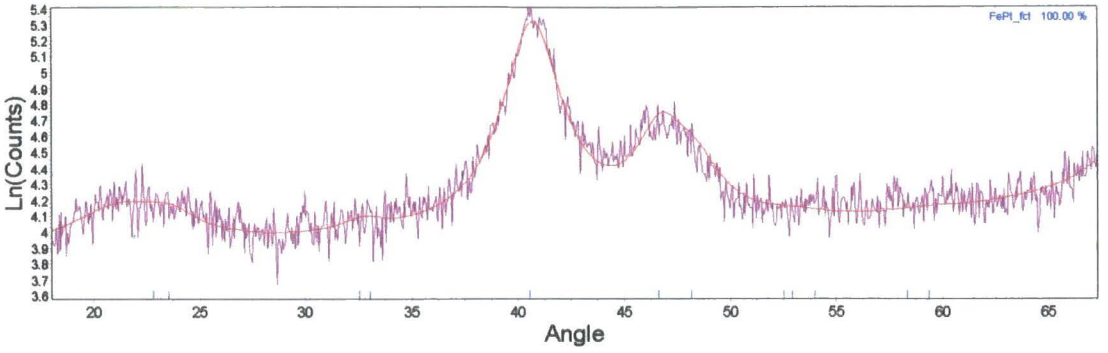

Figure 3-21: Detail of the 5th data set (408 K) of the free refinement. The experiment data is in dark purple, the fit is in red. The intensity is shown as on a logarithmic scale to highlight the smaller peaks.

For the independent Gaussian first peak there is strong correlation between the area and the fwhm. This leads to much broader peaks between ranges 7 and 11 than occurs for the other ranges. This can clearly be seen by the similarity of graphs (g) and (h) in Figure 3-20. This is probably due to the broad peaks caused by the FePt being located at 68.5° and 82° 2θ. These structural peaks are then partially fitted by the peak designed to fit the amorphous hump. This is one of the problems that surface fitting may be able to prevent; in the refinements during and after section 3.4.5 one value was refined for the fwhm of all ranges.

The area of the 2nd amorphous peaks, located around 22°, increases with increasing T. On cooling it decreases again, but more slowly. The peak centre and fwhm remained constant within experimental errors.

3.4.4 Determining the Background with Fixed Fractional Occupancy

It is clear from the refinements described above that the order parameter derived from Rietveld refinement is artificially high for early ranges due to correlations with the background function. To judge the improvement in order parameter potentially achievable from a better background treatment the following protocol was used:

1. The order parameter was fixed at zero; 2θ regions containing peaks indicative of the ordered fct phase were excluded and each data set refined.

2. Background functions were fixed at values from "order = 0" refinements.

3. Rietveld refinement was performed in which the order parameter was allowed to refine.

This process should potentially produce background functions in which contributions of ordering peaks to the background are minimised. 784 parameters were refined in the first stage, using all the 833 parameters from the free refinement except the 49 fractional occupancies. 637 parameters were refined in stage 3, with the 196 background terms being fixed. The shape of the background is shown in Figure 3-22, together with the results from the free refinement for comparison. The difference between the two background functions was very small.

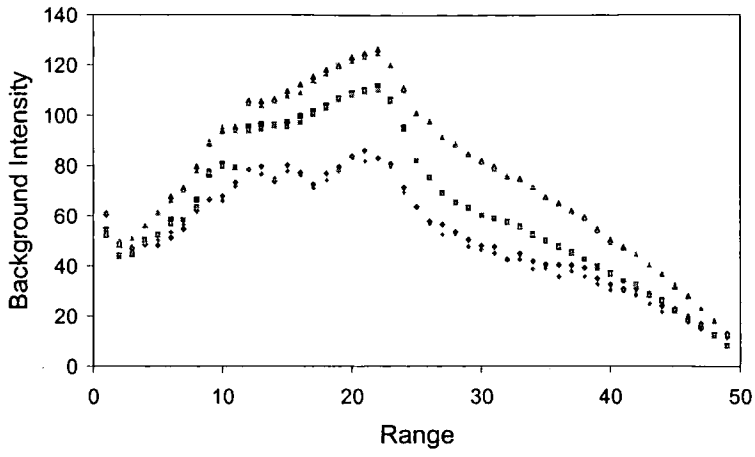

Figure 3-22: Comparison of the background between the free refinement (shown in black) and the background produced using fixed fractional occupancies (shown in grey) at 3 2θ values. The intensities at 30.3° ° 2θ are squares, at 56.27 2θ are diamonds and between 100.27° 2θ are triangles.

The resulting order parameter is shown in Figure 3-23. The order parameter is very similar after the phase transition. Before the phase transition, is lowered by around 0.1 units. This, combined with the large ESDs before the transition, suggests that obtaining the expected order parameters, regardless of the background model used, may prove difficult.

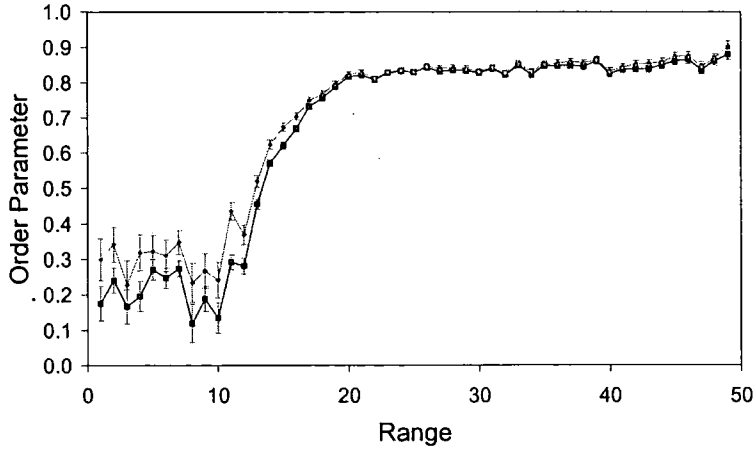

Figure 3-23: Difference in Order Parameter between the completely free refinement and the refinement with fixed background parameters. The former is shown as grey diamonds; the latter is shown as black squares.

3.4.5 Modelling the Background as a Smoothly Varying Function

The next stage was to control the background polynomials as smoothly varying functions. There were 2 main options for doing this. The first was to vary the background as a function of temperature; this should enable information about the background to be transferred from the later data sets, which had clearly defined backgrounds, to the earlier ones. The second option was modelling the background as a function of data set. This should enable any irreversible differences between the heating and cooling scans to be modelled.

3.4.6 Background as a Function of Temperature

Instead of freely refining each background term of Equation 3-8, the values were modelled as a function of T. The model is shown in Equation 3-9 for the zero order background term for the data set at 308 K, with the other terms controlled by identical equations. Bkg_0a, bkg_0b and bkg_0c are refinable parameters derived from the entire data set; t_{0308} is the temperature of the data set and t_{mid} is the average temperature (608 K). The addition of the t_{mid} terms improves the stability of the refinement.

$$bk0\_t\_0308 = bkg\_0a + bkg\_0b\left[\frac{(t_{0308} - t_{mid})}{t_{mid}}\right] + bkg\_0c\left[\frac{(t_{0308} - t_{mid})}{t_{mid}}\right]^2;$$

Equation 3-9

The 2 independent peaks used to model the background humps were also controlled as a function of temperature. The areas and fwhms used the same 2nd order polynomial as shown in Equation 3-9. For centres of the peaks, a single value was refined from every data set. By using every data set to determine a good shape for these background features, it should prove possible to avoid the correlations between the background shape at ~ 75° and the broad peaks at 68.5° and 82° 2θ which occurred during the early ranges in the free refinement. This gave 322 parameters which consisted of 28 overall parameters and 6 parameters for each of the 49 ranges. Each of the 4 2nd order polynomials modelling the background terms as a function of temperature required 3 parameters. There were also 3 terms for each of the polynomials which modelled the area & fwhm of the two independent peak shapes and 2 parameters for the peak positions. The height of the sample for each data set was modelled as a linear function of temperature, requiring 2 parameters. The six parameters for each data set were 1 scale factor, 1 fractional occupancy, 2 cell parameters, 1 atomic displacement parameter and 1 crystallite size term.

The overall rwp was 15.314 %. This was significantly worse than the free refinement. The background fitting was very poor, too low on warming and too high on cooling. Given the shape of the background in Figure 3-19, this is not very surprising. There are significant differences in the warming and cooling backgrounds; it was hoped that modelling the background as a function of the data set number would enable this problem to be eliminated.

3.4.7 Background as a Function of Data Set Number

The next stage was to see if the difference in background function between heating and cooling could be modelled. Instead of parameterising the background coefficients as a function of temperature, it was described as a function of range. The variation in the 4 background parameters and the area & fwhm for the two independent peaks were modelled using the polynomial shown in Equation 3-10. Bkg_0a, bkg_0b and bkg_0c are refinable

parameters for the entire refinement; r_t_{0308} is the number of the data set (1 in this example) and r_{mid} is the number of the central set (25). The number of parameters was again 322.

$$bk0\_t_{0308} = bkg\_0a + bkg\_0b\left[\frac{(r\_t_{0308} - r_{mid})}{r_{mid}}\right] + bkg\_0c\left[\frac{(r\_t_{0308} - r_{mid})}{r_{mid}}\right]^2;$$

Equation 3-10

The rwp improved from modelling the background as a function of temperature to 13.129 %. The fit was still fairly poor, particularly for the data sets towards either end of the run. This is highlighted by range 4 shown in Figure 3-24. It was clear that it was difficult to model the background as a simple polynomial. More attention needed to be paid to the sharp drop in background that can be seen after range 20 (783 K) in Figure 3-19.

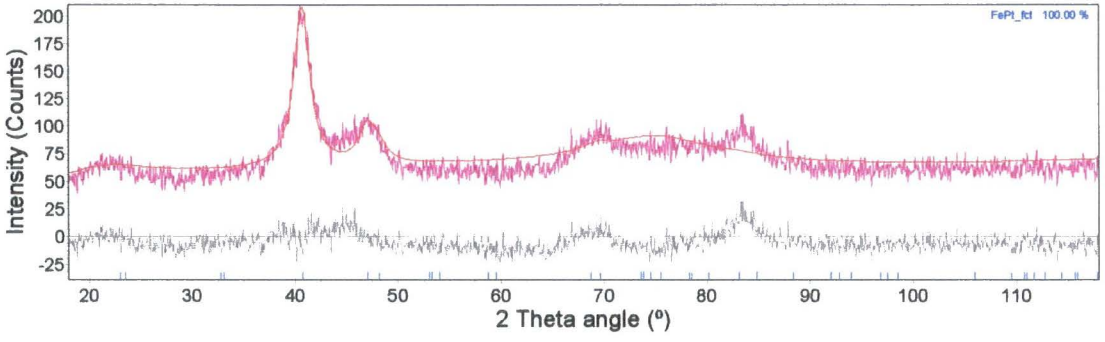

Figure 3-24: Rietveld fit of the 4th range with background modelled as a function of range. The data is in pink, the fit in red and the difference in grey. Position of hkl peaks are shown as blue tick marks.

3.4.8 Modelling the Rapid Drop in Background at High Temperature

The shape of the background intensities shown in Figure 3-19 resembles a smooth curve with a sudden drop around the middle ranges. It was therefore decided to model the variation in background parameter as a polynomial function of temperature with an additional step function to model this drop. The step function is shown in Equation 3-11. This was modelled as a function of data set to ensure the background was higher on heating than on cooling. The term r_t_middle was set to 25, the midpoint of the range and the centre of rapid drop in background. The term δ was started at 1 and refined. The value of δ = 1 meant that 96 % of the decrease in background occurred over the middle 8 ranges, which was concurrent with rapid drop in the data.

$$Step\_function = Stepsize \times \left[1 - \frac{1}{e^{(r\_t\_0000 - r\_t\_middle)/\delta} + 1}\right]$$

Equation 3-11

The function which controlled the variation of background parameters is shown in Equation 3-12. This leads to a total of 326 parameters which consisted of the 322 used in section 3.4.6 and a step size parameter for each of the four polynomials which modelled the background terms.

$$bk0\_t_{0308} = bkg\_0a + bkg\_0b\left[\frac{(t_{0308} - t_{mid})}{t_{mid}}\right] + bkg\_0c\left[\frac{(t_{0308} - t_{mid})}{t_{mid}}\right]^2 + step\_0;$$

Equation 3-12

The rwp of this refinement was 9.514 %. This was better than the 2 previous models for the background but the still significantly worse than the 8.865 % obtained for the free refinement. This can be seen from Figure 3-25(a), which compares the individual rwps from the free refinement to those from this modelled background work. The main difference between the qualities of fit is in the early data sets. This was probably due to the fact that, even with the step function, the function for varying background was insufficiently flexible for fitting the background. This lead to the order parameters behaving strangely, which is shown in Figure 3-25(b). This is most noticeable for the first two ranges, where the refined order parameter is very high. This is possibly due the sample being prepared in hexane. This causes additional background intensity, but evaporates off at low temperatures e.g. over the first three ranges.

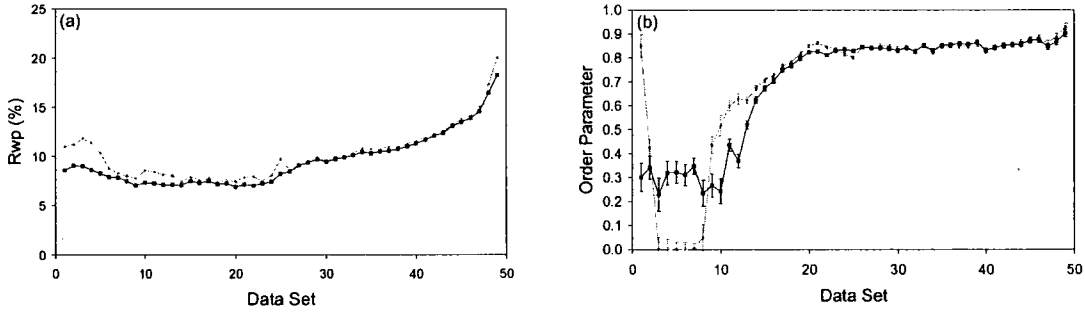

Figure 3-25: (a) shows a comparison between the quality of fit using a free refinement (black) and the surfacing fitting using a step in the data (grey). (b) shows the difference in order parameter for the same two refinements.

3.4.9 Correlation between the Background and the Scale Parameter of the Structure

The refinements in the earlier sections of this work all show a significant drop in scale at the same position as the drop in background, from ranges 22 to 28. It was therefore decided to investigate whether there was any correlation between the scale of the structure and the intensity of the background. Each background parameter was modelled as a function of range, before being multiplied by the scale. An example of this is shown in Equation 3-13.

$$bk0\_t_{0308} = scale_{0308}\left(bkg\_0a + bkg\_0b\left[\frac{(r\_t_{0308} - r_{mid})}{r_{mid}}\right] + bkg\_0c\left[\frac{(r\_t_{0308} - r_{mid})}{r_{mid}}\right]^2\right);$$

Equation 3-13

The quality of fit was slightly better than that produced using a step function, with an rwp of

9.321 %. The order parameter was also smaller for the first two ranges, as shown in Figure 3-26. While an improvement on previous models, this method was still not entirely satisfactory.

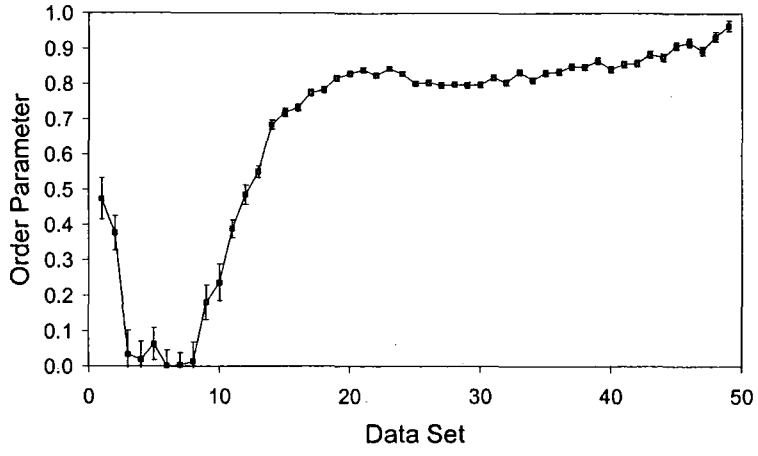

Figure 3-26: Changing order parameter with data set in a refinement where the background model is multiplied by scale.

3.4.10 Conclusion of Surface Fitting the Background of Variable Temperature Data of FePt Nanoparticles

This work has shown it is theoretically possible to fit the background using parametric Rietveld refinement. This offers the possibility of removing correlations between background and the structure. In practice, a system such as the one used here may have many different processes occurring which affect the background; such as volatiles evaporating, changing height of the sample holder and material crystallising. These different processes are difficult to model without risking biasing the model.

A background function to describe step changes has been developed, which leads to some improvement in the order parameter. Using the scale of the crystalline phase to help model the background also showed some promise as a technique. Although the technique shows some potential it was difficult to draw firm conclusions due to the variation in the background. More careful analysis of the averaged background parameters in Figure 3-19 is probably required to make further progress with this work.

3.5 Conclusion to the Development of Parametric Rietveld Refinement

The possibilities of using simultaneous refinement of diffraction data using the TOPAS academic suite have been demonstrated. It has helped provide greater insight into two diffraction problems, one with variable temperature data, the second with time-dependent kinetic data. As yet it has not been conclusively demonstrated that this technique could aid the study of FePt nanoparticles. It is a useful and flexible technique in situations where

understanding of the basic principles of the changes occurring in the system is understood. Additional examples of the technique are given in a research paper on this work; the paper is reproduced in the e-appendix.[12]

3.6 References

1 Coelho A. A., 'Topas - Academic', Karlsruhe, 2004.

2 Taylor D., *Brit. Ceram. Trans. J.*, 1988, **87**, 39.

3 Cline J. P., 'Standard Reference Material 676 - Alumina Internal Standard for Quantutative Analysis by X-ray Powder Diffraction', Gaithersburg, Maryland, USA, 1992.

4 Okada Y. and Tokumaru Y., *J. Appl. Phys.*, 1984, **56**, 314.

5 Lyon K. G., Salinger G. L., Swenson C. A., and White G. K., *J. Appl. Phys.*, 1977, **48**, 865.

6 Cline J. P., 'Standard Reference Material 640c - Silicon Powder Line Position and Line Shape Standard for Powder Difffraction', Gaithersburg, Maryland, USA, 2000.

7 Allen S., 'Thermoresponsive Behavior of AM_2O_8 Materials', University of Durham, Durham, 2003.

8 Evans J. S. O. and Allen S., *J. Mater. Chem.*, 2004, **14**, 151.

9 Evans J. S. O., Mary T. A., Vogt T., Subramanian M. A., and Sleight A. W., *Chem. Mat.*, 1996, **8**, 2809.

10 Howard L. E. M., Nguyen H. L., S. R. Giblin, Tanner B. K., Terry I., Hughes A. K., and Evans J. S. O., *J. Am. Chem. Soc.*, 2005, **127**, 10140.

11 Nguyen H. L., Howard L. E. M., Giblin S. R., Tanner B. K., Terry I., Hughes A. K., Ross I. M., Serres A., Burckstummer H., and Evans J. S. O., *J. Mater. Chem.*, 2005, **15**, 5136.

12 Stinton G. W. and E. J. S. O., *J. Appl. Cryst.*, 2007, **40**, 87.

4. The Structure of Pseudo-cubic Alpha ZrP_2O_7

4.1. Introduction

As discussed in section 1.3.2, alpha zirconium phosphate is part of the pseudo-cubic AM_2O_7 family of materials. This section describes a full structure solution of this material from powder diffraction data; performed in order to aid the understanding of the interesting thermal expansion properties of this family of materials. This structural solution has recently been published[1] and a reprint is available as an e-appendix.

The structure of ZrP_2O_7 contains of PO_4 tetrahedra and ZrO_6 octahedra. The structure can be thought of as analogous to the NaCl structure with ZrO_6 octahedra replacing the Na sites and P_2O_7 pyrophosphate groups, consisting of two linked PO_4 tetrahedra, replacing the Cl sites. Each oxygen atom of the ZrO_6 group is shared with a different P_2O_7 group. Each PO_4 tetrahedra shares three of its oxygen with different ZrO_6 groups and one with the second PO_4 tetrahedra. The ideal structure (Figure 4-1) is cubic with linear P_2O_7 groups and Z=4. This structure is found above a phase transition at 293°C.[2] Below this transition the structure distorts to form a 3 x 3 x 3 supercell, with an accompanying change to orthorhombic symmetry. It is this, lower temperature phase that will be discussed here. The symmetry of the room temperature has been demonstrated to be Pbca by 2-D double quantum ^{31}P NMR.[3]

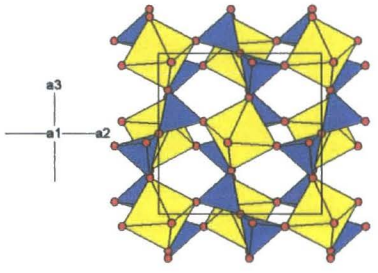

Figure 4-1: The ideal structure of ZrP_2O_7. ZrO_6 octahedra are in yellow, PO_4 tetrahedra in blue and oxygen atoms in red.

4.2. Experimental Details

TOPAS Academic[4] was used for all refinements as it provides a powerful platform to develop user-defined constraints and restraints alongside Rietveld refinement. TOPAS allows modified simulated annealing to be added to the refinement. This generates different solutions with a randomization of parameters after completing each solution as used. Instead of randomizing each parameter by a temperature regime, the user can define which parameters are randomized and by how much. It also allows Pawley fitting, as described in section 4.3.

4.2.1. Synthesis

Data were collected on a sample synthesised by JSO Evans (labelled JSOE_439), based on a method described by both Harrison *et al.*[5] and Huang *et al.*[6] A 2:1 molar ratio of $ZrOCl_2 \cdot 6.91H_2O$ (Alfa 99.985 %) and H_3PO_4 were mixed in a Pt crucible before standing for 2 hours. The sample was dried at 350°C for 1 hour, with a heating rate of 5°C per minute. The resulting white sample was crushed before being washed using distilled water and centrifuged four times. It was then dried at 180°C. A two stage annealing process was used, in the first stage the sample was heated to 850°C for 12 hours with a heating rate of 3°C per minute, then re-ground. For the second stage, the sample was heated to 1000°C for a further 12 hours with heating rate of 5°C per minute. Powder diffraction suggested the sample was pure.

4.2.2. X-ray Diffraction Data

Data were collected by Pat Woodward using beam line X7A of the National Synchrotron Light Source at Brookhaven National Laboratory. Data were collected from 2 to 67.06° 2θ using a wavelength of 0.8013 Å, selected using a Ge(111) channel cut crystal monochromator. The step size was 0.01°. A flat plate sample was used with a multiwire position sensitive detector.

4.2.3. Neutron Diffraction Data

Data were collected by JSO Evans, CJ Crossland and R Gover at the High-Resolution Powder Diffractometer (HRPD) station at the ISIS pulsed neutron source of the Rutherford Appleton Laboratory. Data were collected from an 11 g sample loaded into a 15 mm cylindrical vanadium can. Data from the backscattering bank of detectors were measured from 0.705 to 2.364 Å and were used for all the refinements in this section. The other banks of detectors gave significantly resolution and were not used.

4.3. Pawley Refinements

Neither the X-ray or neutron diffraction patterns showed any obvious peak splitting which would directly confirm the orthorhombic symmetry determined by NMR. To help determine the correct symmetry, Pawley fitting[7] was carried out in both $Pa\bar{3}$ and Pbca symmetry. Pawley fitting uses the same principle as Rietveld refinement; adjusting a model to produced a theoretical diffraction pattern as close to the experiment data as possible. Both use refinable unit cell dimensions and user-defined symmetry to calculate a series of hkl reflections. The difference is the intensity of these hkl reflections is refined freely in the former and is calculated from atomic positions in the latter. The model produced by Pawley fitting demonstrates the best possible fit that could be obtained for a given symmetry and unit cell dimensions. The aim of this approach is to see if all of the features of the data are modelled

by the suggested space group before proceeding to a full structure solution.

For these Pawley refinements, neutron data from 80000 to 130000 μs (1.59 to 2.58 Å) were used, however, the data between 103000 and 103500 μs were discarded for this and all subsequent refinements due to diffraction from the vanadium sample holder in this region. This gave Rwps of 6.828 % and 2.145 % for $Pa\bar{3}$ and Pbca symmetry respectively. For the X-ray refinement, data between 2 and 28° (1.67 and 5.81 Å) were used. This gave Rwps of 7.213 % and 5.743 % for $Pa\bar{3}$ and Pbca symmetry respectively. All of the fits of the data are shown in Figure 4-2.

These results suggest two things. Firstly, a better fit to the data can be obtained using Pbca rather than $Pa\bar{3}$ symmetry, although lack of visible splitting means that this is possibly due to the lower symmetry allowing a better fit of the experimental peak shape. There is also a large in increase in the number of parameters as the symmetry decreases; from 377 to 1127 and from 620 to 1998 for neutron and X-ray data respectively, so the decrease in Rwp may not be statistical significant. The second point of note is that the neutron data proved more sensitive to the lowering of the symmetry than the X-ray data. The whole data range for the 4 Pawley refinements is shown in Figure 4-2 with details of individual peaks in Figure 4-3.

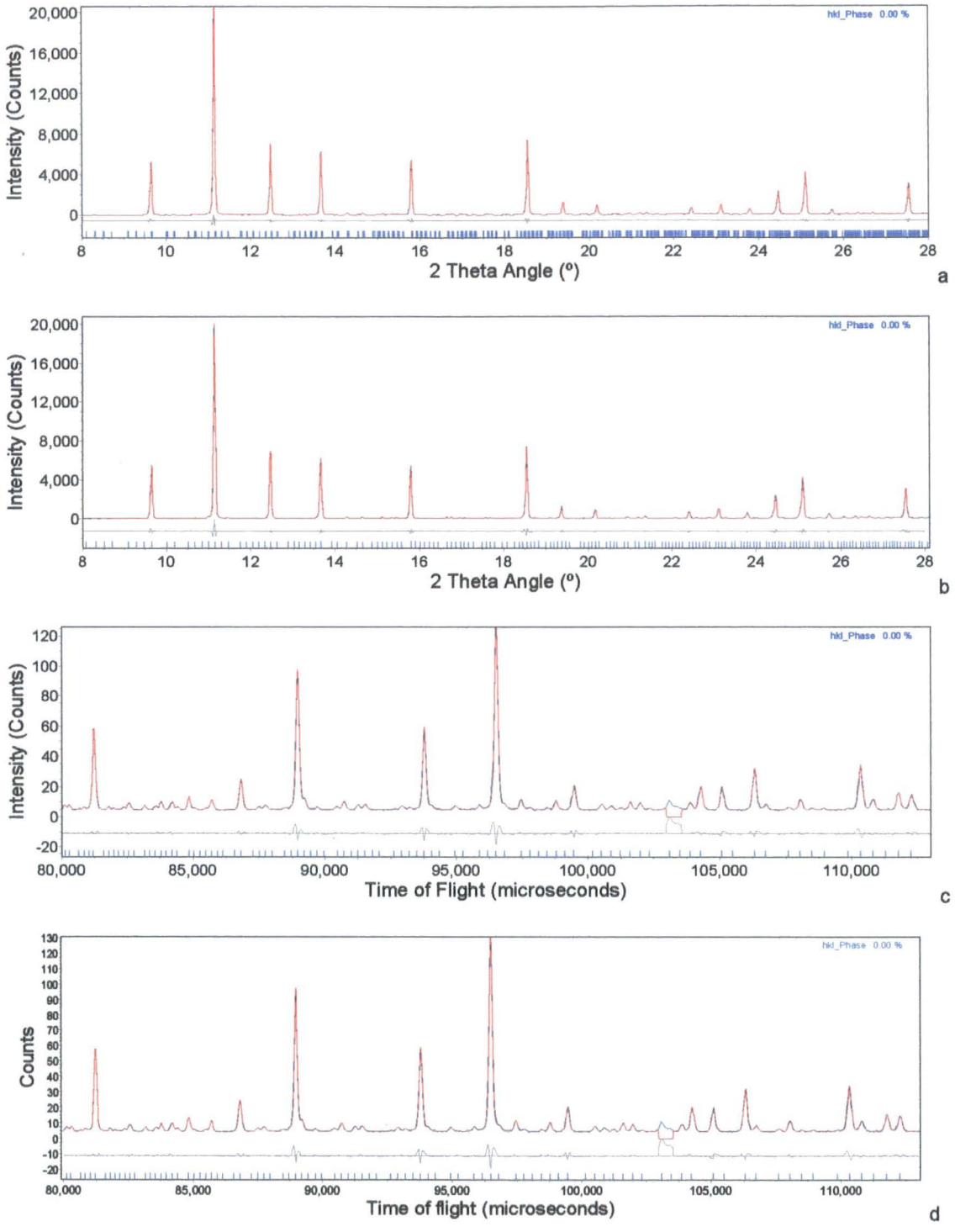

Figure 4-2: Plots showing Pawley fits of the data. (a) shows the fit of the X-ray data using Pbca symmetry. (b) shows the same data fitted using a model with $Pa\bar{3}$ symmetry. (c) and (d) show the neutron data in Pbca and $Pa\bar{3}$ respectively.

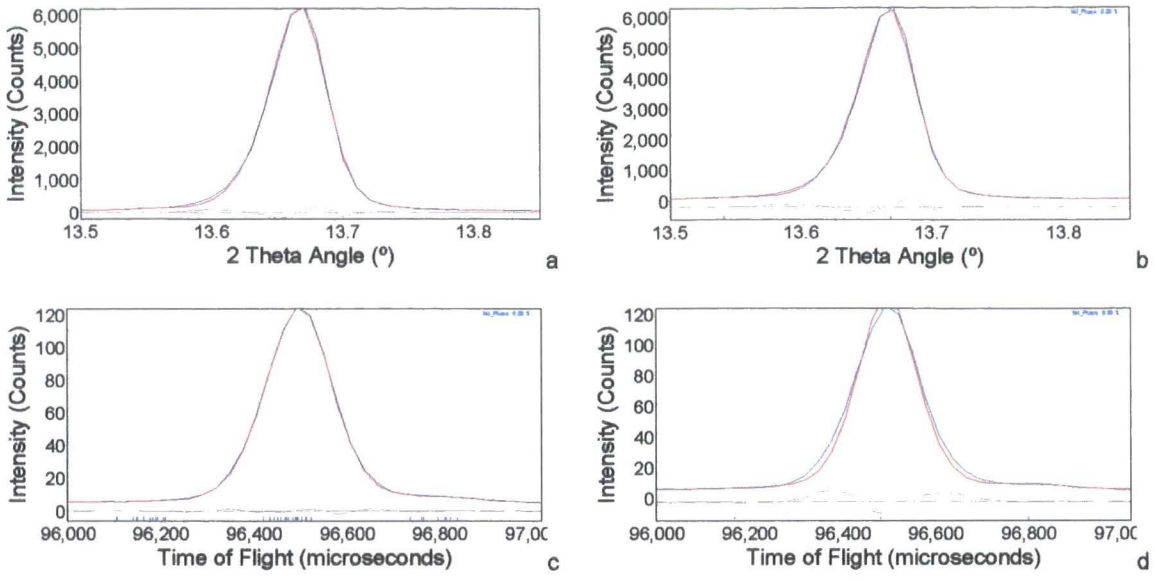

Figure 4-3: Details of the Pawley refinements. (a) and (b) show the (6,3,3) peak and its symmetry equivalents in the X-ray data for Pbca and $Pa\bar{3}$ respectively. (c) and (d) show details of the (0,3,12) peak and its symmetry equivalents for in the neutron data for Pbca and $Pa\bar{3}$ respectively.

The difference in the quality of fit produced by the 2 symmetries suggests it may be possible to determine the splitting of cell lengths from the asymmetry of the peaks even without any visible peak splitting. It is therefore worth attempting a full structural solution in Pbca, together with a solution in $Pa\bar{3}$ for comparison.

4.4. Structure Solution

4.4.1. Structure Solution Methodology

The supercell of ZrP_2O_7 contains 136 atoms in the asymmetric unit cell. With 2 atoms on inversion centres, this leaves 402 atomic position variables. The refinement of such a complex structure from powder diffraction data is clearly a significant challenge. Steps were therefore taken to prevent refinement to false minima.

A simulated annealing approach was used to find the best structure solution. Also, Rietveld refinement was combined with either constraints or restraints on bond angles and/or distances to help prevent implausible models. A schematic of the approach used to find the best structural solution is shown in Figure 4-4.

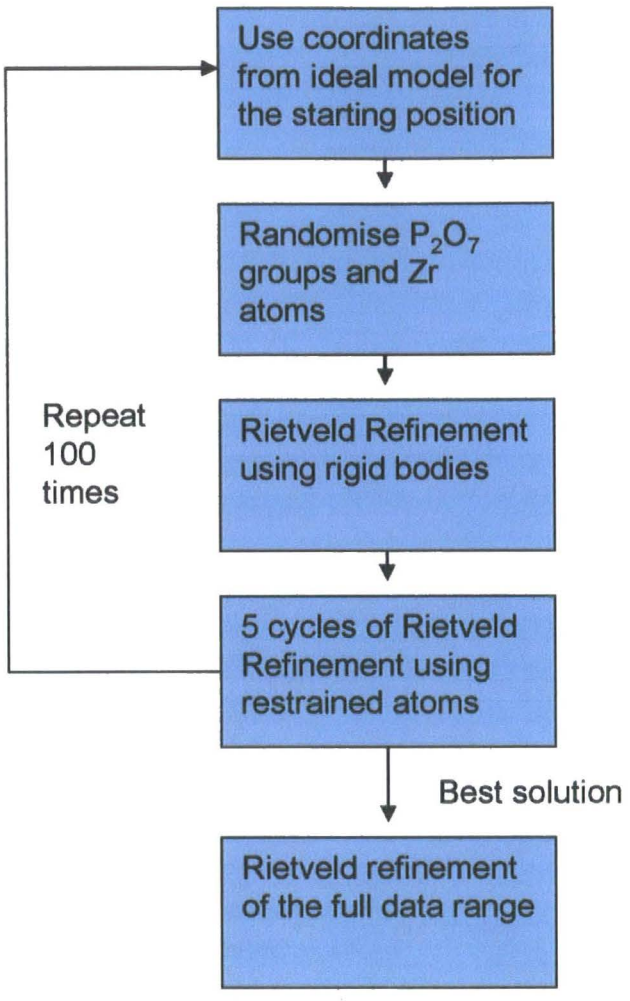

Figure 4-4: The basic strategy for structural solution.

Instead of refining all of the atoms individually, P_2O_7 groups were modeled together as two linked, rigid PO_4 tetrahedra, with all internal angles set to 109.47°. A study of P_2O_7 groups in the ICSD was carried out to determine the starting bond lengths. The bond lengths between the phosphorus atoms and those oxygen that are bonded to two phosphorus atoms, henceforth referred to as $O_{bridging}$, are significantly longer than P-O bonds for the oxygen that are bonded to one phosphorus and one metal atom (O_{AM}). Therefore the two distances were treated separately with the P-$O_{bridging}$ bond lengths initially constrained to 1.5775 Å and the P-O_{AM} bonds set to 1.5000 Å. The relationship between the two tetrahedra was defined by an O-P-O-P-O torsion angle and a P-O-P angle.

The starting values of the atomic coordinates are generated by Macro 4-1 in the form of a rigid body. All macros are defined using the TOPAS macro language which is described in the TOPAS manual.[8]

Each atom is defined by its relationship with the bridging oxygen, labeled s4, it also has the

dummy label s9. Sites s0 and s5 are phosphorus atoms and the rest of the sites are oxygen atoms linked to adjacent tin atoms. The terms r1 and r2 refer to the P-O_{AM} and the P-$O_{bridging}$ distance respectively. This produces the P_2O_7 group shown in Figure 4-5.

```
macro Pyrophosphate(s0, s1, s2, s3, s4, s5, s6, s7, s8, s9, r1, r2)
'p2o7 with s4 bridging
{
point_for_site s0 ux =  0.000000000000000  ; uy = 0.0000000000000000
;  uz= -r2;
point_for_site s1 ux = -0.816496580927726 r1; uy = 0.4714045207910317
r1;  uz = -r2-r1/3;
point_for_site s2 ux =  0.816496580927726 r1; uy = 0.4714045207910317
r1;  uz = -r2-r1/3;
point_for_site s3 uy = -0.942809041582063 r1; uz = -r2-r1/3;
point_for_site s4 uz = 0;
point_for_site s5 ux =  0.000000000000000  ; uy = 0.0000000000000000
;  uz=  r2;
point_for_site s6 ux = -0.816496580927726 r1; uy = 0.4714045207910317
r1;  uz =  r2+r1/3;
point_for_site s7 ux =  0.816496580927726 r1; uy = 0.4714045207910317
r1;  uz =  r2+r1/3;
point_for_site s8 uy = -0.942809041582063 r1; uz =  r2+r1/3;
}
```

Macro 4-1

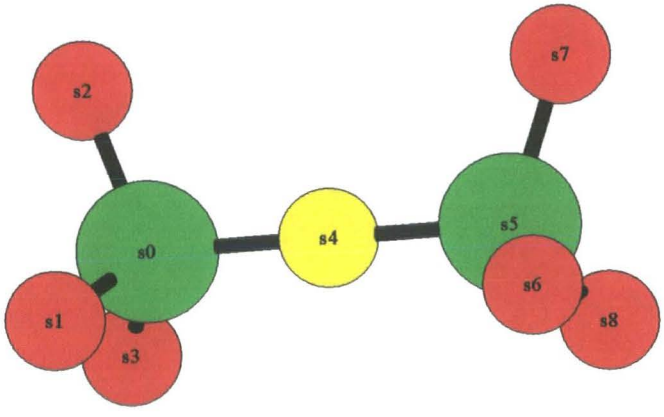

Figure 4-5: Diagram of the pyrophosphate group produced by the rigid body macro. O_{AM} atoms are shown in red, phosphorus atoms in green and the $O_{bridging}$ atom is in yellow.

Macro 4-1 defines initially starting positions of the atoms relative to one another. To allow this group to move, rotate and bend Macro 4-2 is required. As in Macro 4-1, terms s0 to s9 are used to define atomic sites. The next 8 terms are in 4 pairs. The first term of each pair defines a parameter name; the second defines the parameter value. These terms are, respectively, the P-O_{AM} distance, the P-$O_{bridging}$ distance, the O-P-O-P-O torsion angle and the P-O-P angle. The next nine parameters are in 3 groups of 3. These consist of a parameter name, a refined value and an ideal value for the each of the x, y and z atomic coordinates of the bridging oxygen. The final six parameters are again pairs of terms, giving the rotation of the P_2O_7 group in the three directions.

```
macro p2o7_group
(s0,s1,s2,s3,s4,s5,s6,s7,s8,s9,
p_dist1,v_dist1,p_dist2,v_dist2,p_tor,v_tor,p_ang,v_ang,
p_x1,v_x1,v_x2,p_y1,v_y1,v_y2,p_z1,v_z1,v_z2,
p_rotx,v_rotx,p_roty,v_roty,p_rotz,v_rotz)
```

Macro 4-2

Macro 4-2 then receives information from a series of lines, one for each individual P_2O_7 group. The information for one group is shown in Macro 4-3. This defines which atoms are present in each group, gives the parameter names and their starting values.

```
p2o7_group(P27,O35,O40,O28,S99,P119,O120,O121,O122,S99,
poz,1.50650,pop01,1.57750,tor_pop01, 66.50115,ang_pop01,-56.81429,
xS99, 0.30344,0.33333,yS99, 0.19001,0.16667,zS99,-0.01908,0.00000,
rotx_pop01,-16.30096,roty_pop01, 220.50914,rotz_pop01,-77.72981)
```

Macro 4-3

The final shape of the P_2O_7 group is generated by Macro 4-4, which takes the coordinates from Macro 4-1 and moves them according to the angles and distances defined by Macro 4-2. The first line in Macro 4-4 means that Topas will define the shape as a rigid body, preventing free refinement of the atoms and only allowing the group to move by the defined parameters. The 2nd line inserts the first 12 pieces of information from Macro 4-2 into Macro 4-1 to generate the starting atomic coordinates. Line 3 rotates O_{AM} atoms s6, s7 and s8 by the torsion angle (v_tor) around an axis defined by atoms s4 and s5. Line 4 inverts the second PO_3 group so the two phosphate atoms overlap. Line 5 then bends the P_2O_7 group at the bridging oxygen by the defined P-O-P angle (v_ang), before line 6 re-inverts the second PO_3 back to the correct side of the bridging oxygen. This process of inverting, bending and re-inverting was used as it was decided to define the parameter v_ang in terms of the angle between the P-O-P angle and a theoretical linear P-O-P group. Line 7 rotates the entire P_2O_7 group around each of three principal axes. As the group was always generated at the origin, the last 4 lines shift the group to the correct position. These positions were calculated by expanding the ideal, high temperature phase into a 3 x 3 x 3 supercell.

```
rigid
Pyrophosphate(s0,s1,s2,s3,s4,s5,s6,s7,s8,s9,p_dist1,p_dist2)
Rotate_about_points(p_tor v_tor min=0; max=120;,s4,s5," s6 s7 s8 ")
Translate_point_amount(s4,-) operate_on_points " s5 s6 s7 s8 !s9 "
rotate  p_ang v_ang qa 1 operate_on_points " s5 s6 s7 s8 !s9 "
Translate_point_amount(s4,+) operate_on_points " s5 s6 s7 s8 !s9 "
Rotate_about_axies(p_rotx v_rotx valcon , p_roty v_roty valcon,
p_rotz v_rotz valcon)
translate
      ta p_x1 v_x1 min = v_x2-0.05;  max = v_x2+0.05;
      tb p_y1 v_y1 min = v_y2-0.05;  max = v_y2+0.05;
      tc p_z1 v_z1 min = v_z2-0.05;  max = v_z2+0.05;
```

Macro 4-4

Before the start of each of the 100 structural solutions the positions of the 108 P_2O_7 groups was randomised, with the central bridging oxygen being moved up to 1.3 Å in each of the three directions parallel to the unit cell edge. The orientation, torsion angle and P-O-P angle of the group were also randomized. The torsion angle was defined using an O_{AM} atom, the adjoining P atom, the second P atom and one O_{AM} join to the second P atom. At the start of refinement these O_{AM}-P-P-O_{AM} torsions angles were randomized to between 0° and 120°, where 0° is the full eclipsed position defined by Macro 4-1. The P-O-P angles were randomized between 60° and 180°. The initial positions of the zirconium atoms were also derived from the expansion of the ideal structure. The atoms were prevented from refining more than 1.3 Å in any the three directions parallel to the unit cell edges. A full example of the input is included in the e-appendix.

4.4.2. Restrained bodies

While the constrained rigid bodies are useful to allow approximate refinement of the structure following randomization, it is chemically implausible that certain distances and angles in the structure would distort from their optimum values while other angles and distances remained exactly at prescribed ones. The simple process of randomizing, then refining with constraints was therefore replaced by randomizing, refining with constraints then refining using restraints. For these restraints, penalties were calculated for the distortion of each bond distance and each internal angle of the polyhedra away from the ideal values. The format of these penalties is shown in Equation 4-1. The P-$O_{bridging}$ refers to the distance between the phosphorus and bridging oxygen atoms. The ideal values for the P-O distances are those listed in section 4.4.1. The ideal Zr-O bond length was determined by using the valence bond concept.[9] For a r_{ij} values of 1.937 and 6 coordinate Zr, the expected Zr-O distance is 2.0695 Å. The ideal values of the O-Zr-O angles were set to 90°.

$$total\_penalty = weight_1 \sum (dist\_po_{bridging} - ideal\_po_{bridging})^2 + weight_2 \sum (dist\_po_{AM} - ideal\_po_{AM})^2 + weight_3 \sum (angle\_opo - ideal\_opo)^2 + weight_4 \sum (dist\_zro - ideal\_zro)^2 + weight_5 \sum (angle\_ozro - ideal\_ozro)^2$$

Equation 4-1

In order to ensure an appropriate balance between penalties assigned to the deviation of different types of bonds and angles, a series of distance least-squares calculations with no data were carried out. The aim of these purely geometric calculations was to ensure an approximately Gaussian distribution of angles and lengths, where the standard deviation divided by the average value was approximately equal for all of the parameters. The final parameters were 3, 3, 0.0005, 2.4 and 0.0003 for weights 1 to 5 sequentially. This produced

the spread of angles and lengths shown in Figure 4-6.

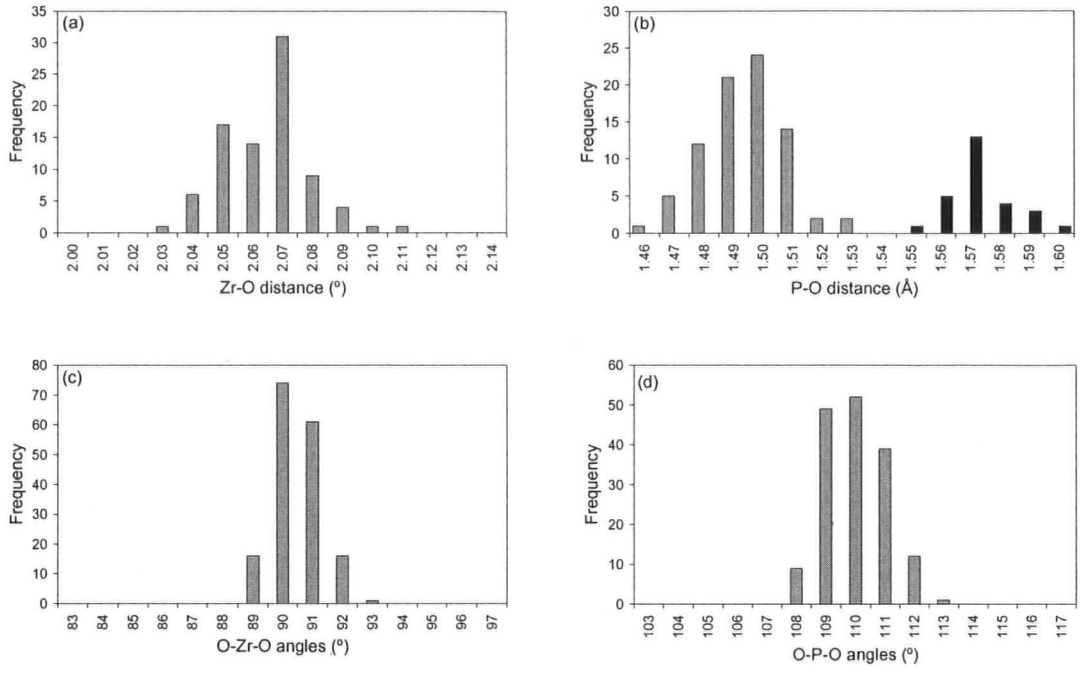

Figure 4-6: Histograms to show the spread of bond angles in the final distance least-squares calculations using restraint weights defined in the text. (a) shows the Zr-O distances. (b) shows P-O distances, with P-O_{AM} bonds in grey and P-$O_{bridging}$ bonds in black. (c) shows the internal angles of the ZrO_6 octahedra and (d) angles of PO_4 tetrahedra.

These restraints were then weighted against the data to ensure that a sensible spread of angles and distances was maintained. The X-ray and neutron data were weighted against each other so that the overall Rwp was approximately the midpoint between the individual Rwps of the two data sets. This ensures approximately equal contribution of both data sets to the model obtained.

4.4.3. Structure Models Produced

Three sets of refinements were carried out. One used only X-ray data, the second only neutron and the third combined both data sets. The process of randomization and refinement was carried out 100 times to find the best fit to the data for each set. All three unit cell lengths were initially started off at 24.7592 Å and allowed to refine freely. To increase the rate of refinement, only data above 0.829 Å were used. For the combined X-ray and neutron refinement, 437 parameters were used. 7 of these were for the neutron data, which were 6 terms of a Chebychev polynomial to describe the background and 1 scale factor. 21 of the parameters were used for the X-ray data; 12 terms of a Chebychev polynomial to describe the background, a $1/\theta$ background function , a TCHz pseudo-Voigt model for peak shape where 4 of the terms were refined (u, v, w and y), 1 zero-point error, 1 term to model axial divergence,

1 scale and 1 absorption correction. 409 structural parameters were refined, consisting of 3 cell lengths, 4 isotropic atomic displacement parameters, (1 each for Zr, P, O_{AM} and $O_{bridging}$ atoms) and x, y & z coordinates for 134 atoms. Figure 4-7 aims to summarise the results of the 3 simulated annealing processes, which each produced 100 structural models *via* the randomisation and refinement process described above. The scatter plots show the dimensions of the unit cell of each structural solution against its quality of fit.

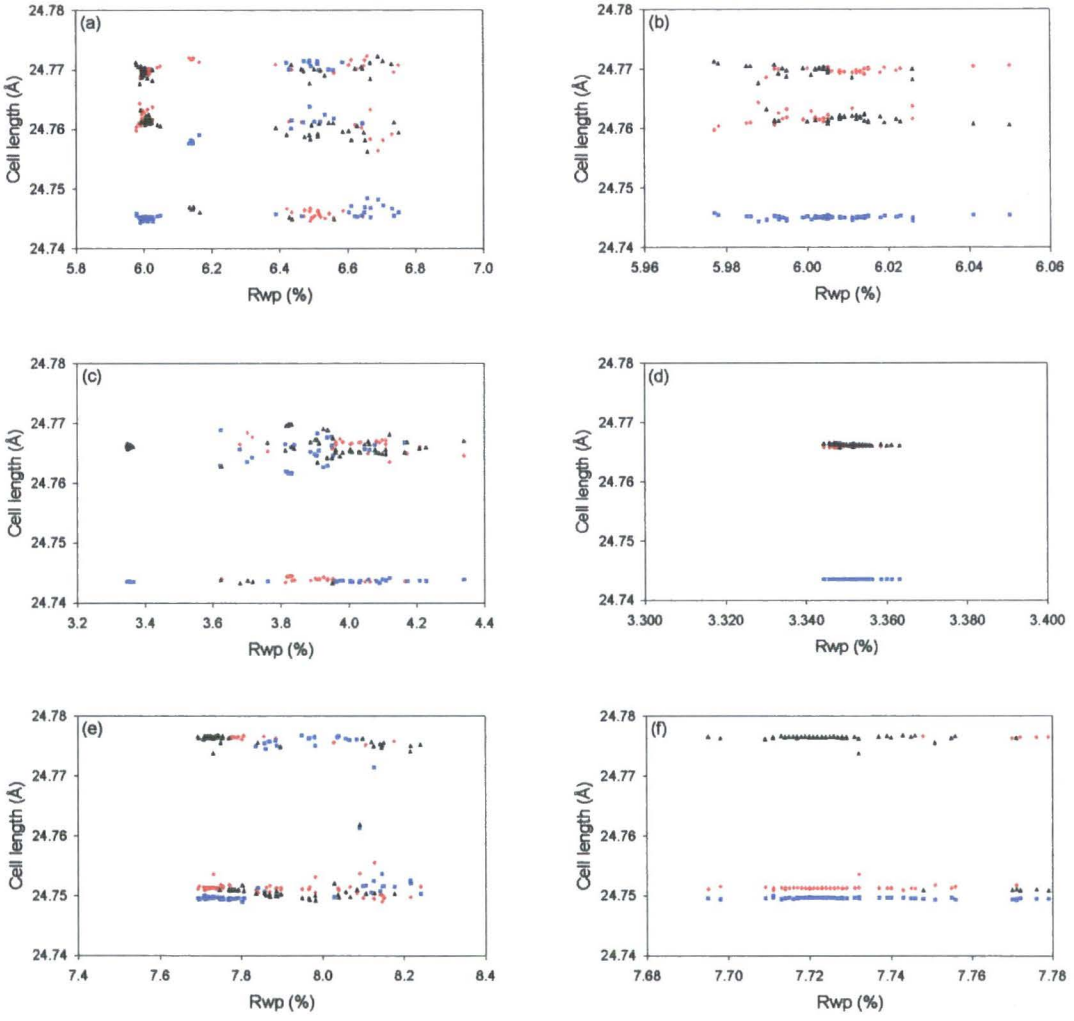

Figure 4-7: Scatter plots showing the cell parameters produced by 100 cycles of randomisation and refinement. (a) shows the combined X-ray and neutron refinement, with detail of the 57 best solutions in (b) for clarity. This shows in detail the cluster of solutions at the end of the series with the best quality of fit. (c) shows the results of refining the neutron data on its own, with the best 49 solutions shown in (d). (e) shows the results of refining the X-ray data on its own, with the best 49 solutions shown in (f). Cell lengths 'a' are shown as red diamonds, lengths 'b' are shown as blue squares and lengths 'c' are shown as black triangles.

Each of the three refinements shows significant numbers of very similar solutions at the low Rwp end of the series. They also show a selection of different possible cells with poorer quality of fits; this suggests the annealing process had the ability to find most of the possible

structural minima. These two factors suggested that the correct minima had been found, and further refinement of the model was possible.

All three refinements only achieved a good fit with splitting of the cell lengths. When the neutron and X-ray data were refined independently, different splitting patterns were produced. The best neutron results were achieved with two large and one small length, with the opposite splitting pattern fitting the X-ray data.

The 57 best results for the combined refinement, Figure 4-7 (b), were grouped in two very similar minima, with b always between 24.7444 to 24.7456 Å. One minimum had a > c and the other had c > a. The smaller value was between 24.75967 and 24.76431 Å, and the larger from 24.76767 to 24.7713 Å. To compare the atomic positions produced by the ten best solutions, an average model of the ten sets of coordinates was produced. The average model was then compared to each of the 10 individual result using the Fortran routine map_graham.[10] The furthest any atom was from this average position was 0.12 Å, with an average displacement of 0.022 Å. The ten best results are superimposed in Figure 4-8; this picture was generated using Atoms 6.[11] This suggests that same minimum in terms of atomic positions was being consistently found.

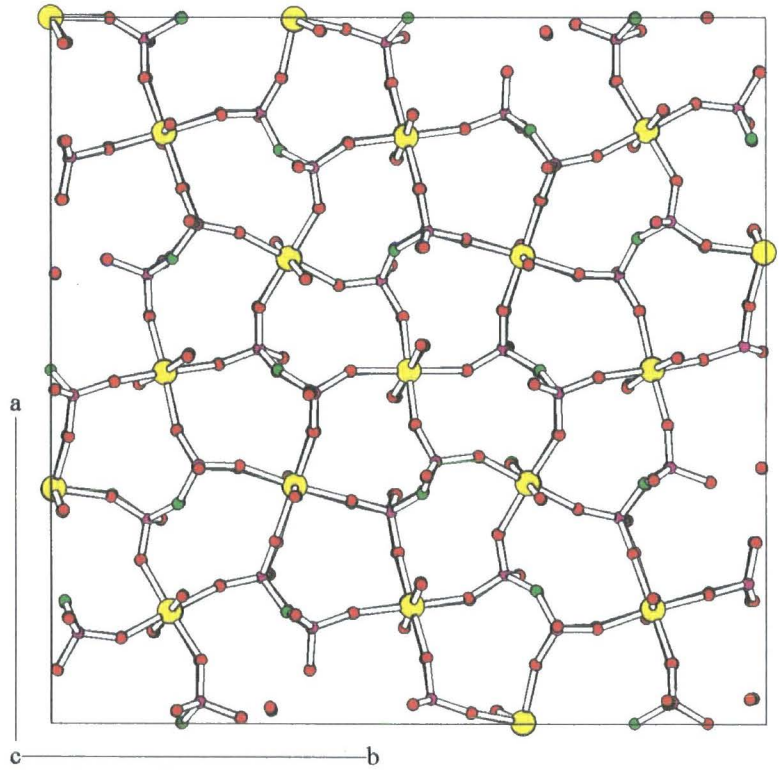

Figure 4-8: Atomic positions of the 10 best fits of the combined refinement. Zr atoms are in yellow, P in pink, O_{AM} in red and $O_{bridging}$ atoms in green. The entire unit cell is shown in the a and b direction but only a 5 Å slice in the c direction for clarity.

4.5. Structural Refinement

The best structure solution from section 4.4 was used as the starting point for a final Rietveld refinement. This used the entire data range of the neutron data, from 0.7258 Å to 2.4343 Å (21,195 hkl reflections), and from 0.7258 Å to 22.9739 Å for the X-ray data (22,015 hkl reflections). 446 parameters were refined, the 437 parameters listed in section 4.4.3 and 9 additional ones. 3 of these controlled the time-of-flight (TOF) x_axis calibration, 1 Lorentzian and 1 Gaussian term for the peak width of the TOF data, 2 terms for the TOF exponential and the 2 previously unrefined values for the TCHz peak shape for the X-ray data, neither of which changed significantly. This produced a final Rwp of 5.99 % and Rbragg values of 2.16 % and 3.11 % for the neutron and X-ray data respectively. The final cell parameters were a = 24.7437(4) Å, b = 24.7258(3) Å and c = 24.7507(4) Å. The Rietveld fits are shown in Figure 4-9.

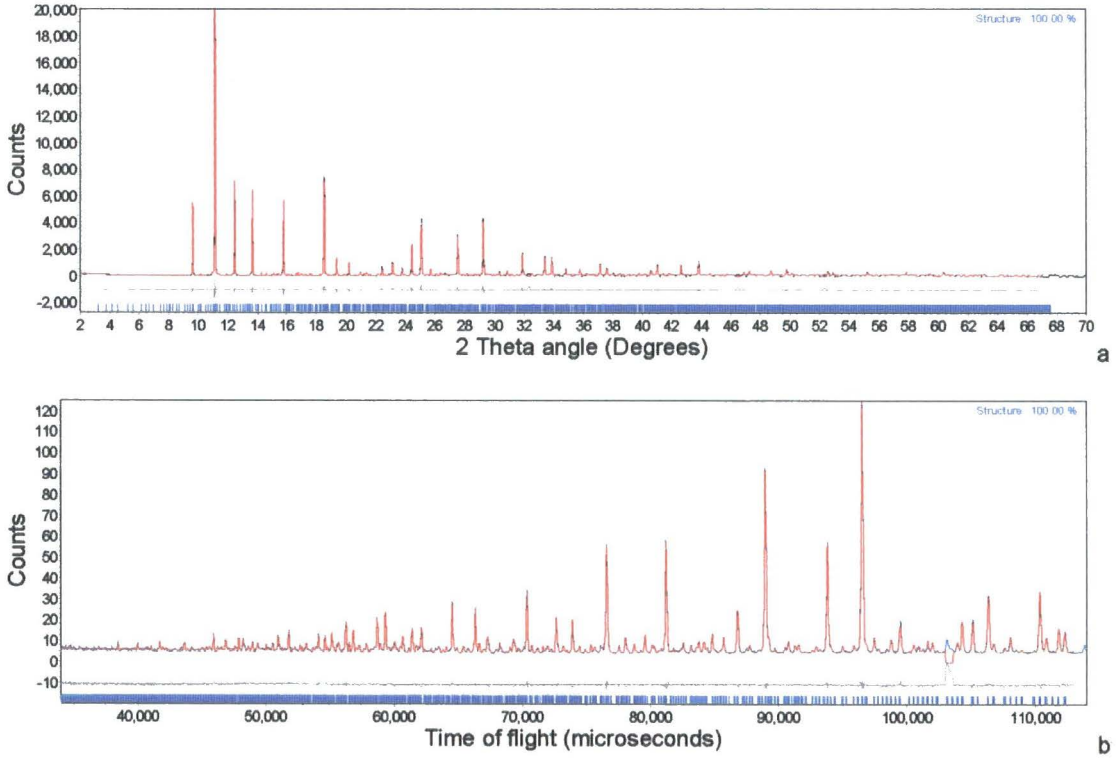

Figure 4-9: Final Rietveld refinement of X-ray (a) and neutron (b) data. Experimental data shown in blue, fit in red and the difference in grey. Tick marks below the data are positions of hkl peaks.

The bond angles and lengths of the structural model are shown in Figure 4-10, with full details of the refinement in Table 4-1. The average Zr-O bond length was 2.069(20) Å, with the maximum deviation from this being 0.061 Å. The average O-Zr-O angle was 90(2)°, with a maximum deviation of 6.5°. The average P-O_{AM} bond length was 1.503(16) Å and the average P-$O_{bridging}$ length was 1.557(16) Å, with maximum deviations of 0.049 and 0.053 Å

respectively. The average O-P-O angle was 109.4(2.6)° with a maximum deviation of 5.9°. All of these deviations are within the expect range.

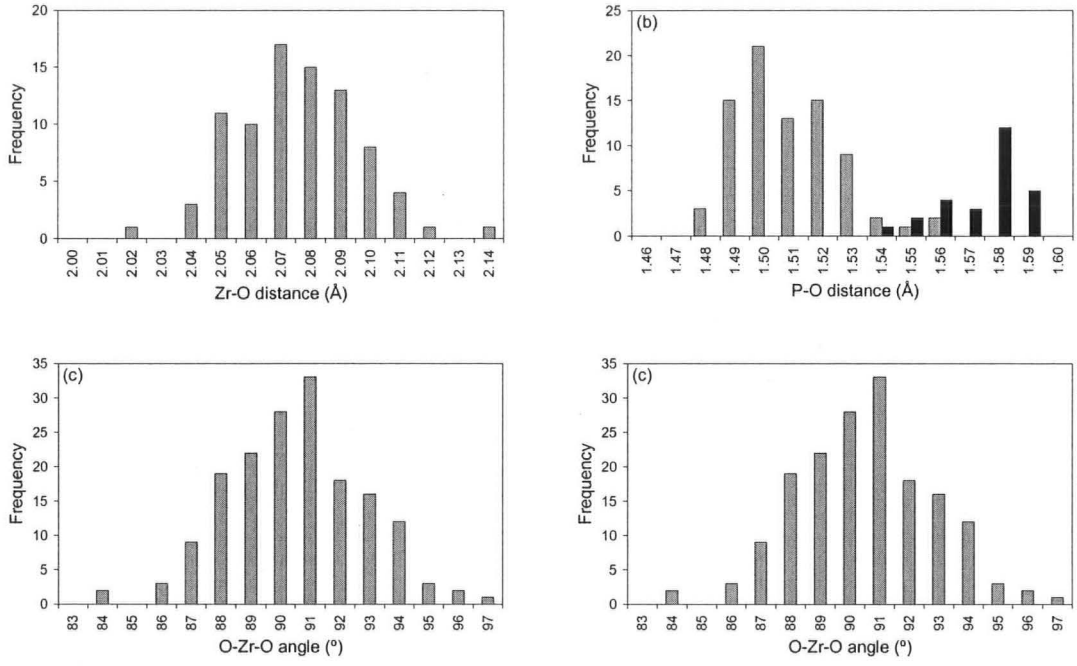

Figure 4-10: Histograms to show the spread of bond distances and angles in the final refinement. (a) shows the Zr-O distances, (b) shows P-O distances with P-O_{AM} bonds in grey and P-$O_{bridging}$ bonds in black. (c) shows the internal angles of ZrO_6 octahedra and (d) angles of PO_4 tetrahedra.

	α-ZrP_2O_7
a (Å)	24.7437(4)
b (Å)	24.7258(3)
c (Å)	24.7507(4)
V ($Å^3$)	15177.0(3)
wRp (all/neutron/x-ray)	5.99/ 3.83/ 7.80
R_{Bragg} (neutron/x-ray)	2.16/ 3.11
Goodness of Fit (all/neutron/x-ray)	0.470/ 0.370/ 0.535
N° Reflections (neutron/x-ray)	21195/ 22015
Structural Parameters	409
Total Parameters	446

Table 4-1: Details of the final refinement for ZrP_2O_7 in Pbca symmetry.

4.5.1. Structure refinement using rigid P_2O_7

The structure refinement was repeated using constrained rather than restrained P_2O_7 groups. Restraints were still used on the Zr-O distances and O-Zr-O angles. This led to a significant increase in the Rwp, for the neutron data the increase was from 3.83 to 7.77 % and for the X-ray from 7.80 and 10.25 %. The greater decrease in quality of fit for the neutron data, rather than the X-ray, is unsurprising given the greater sensitivity of the former to the position of light atoms. These results demonstrate the importance of switching from constraints to restraints during the structural solution process.

4.6. Refinement using cubic symmetry

In order to show the improvement in fitting by changing symmetry from $Pa\bar{3}$ to Pbca, the refinement process detailed in section 4.4 was also performed using the space group $Pa\bar{3}$. 100 separate refinements were carried out with Rwp's between 8.554 and 10.367 %. The best results had a comparably good fit to that achieved by Khosrovani *et al.*,[12] who also used a model in $Pa\bar{3}$. Structural refinement using the same extended data range as section 4.5 produced a Rwp of 8.636 %. The fit was visibly worse than that in Pbca, as shown in Figure 4-11, particularly for the supercell peaks. The restraints employed ensured that the polyhedra showed a similar level of distortion in $Pa\bar{3}$ as occurred using Pbca; both were considerably less distorted than the polyhedra in the model produced by Khosrovani *et al.* The distortion of

O-Zr-O angles is shown in Figure 4-12.

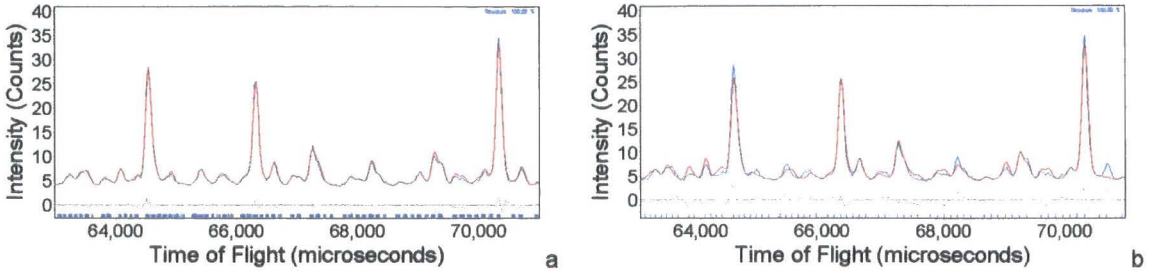

Figure 4-11: Detail of the final refinement of neutron data in Pbca (a) and $Pa\bar{3}$ (b). Data is shown in blue, fit in red and the difference in grey. Tick marks below the data are positions of hkl peaks.

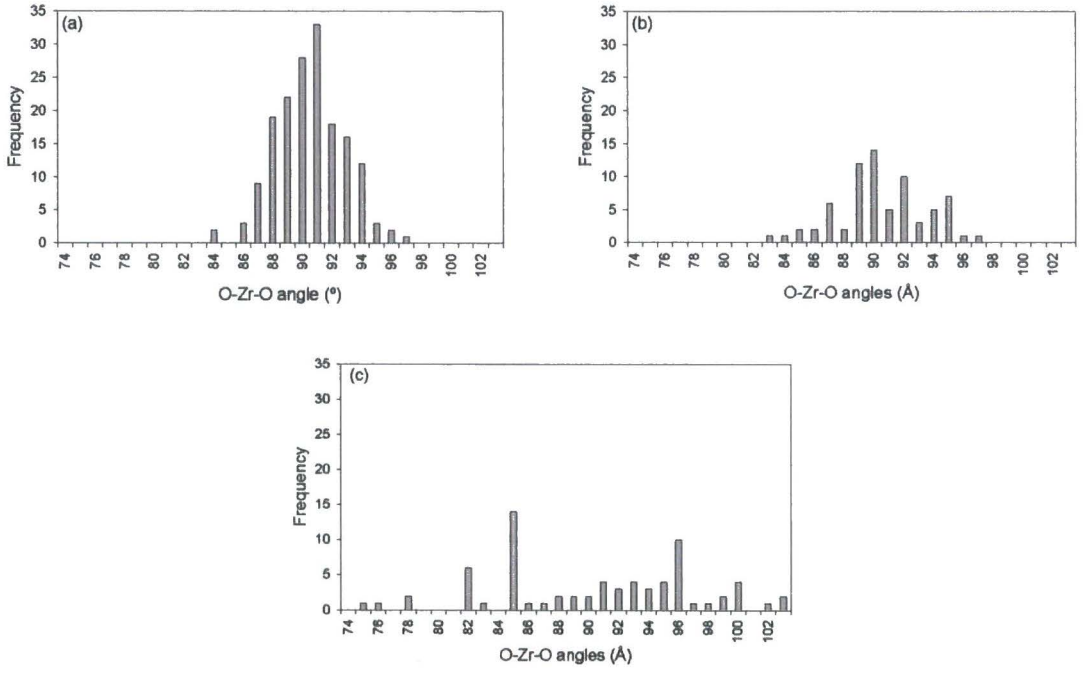

Figure 4-12: (a) shows the distribution of O-Zr-O angles for the final refinement in Pbca, (b) for the final refinement in $Pa\bar{3}$. The angle distribution of the refinement by Khosrovani *et al.* in $Pa\bar{3}$ is shown in (c).

4.7. Comparison with Single Crystal Data

Birkedal *et al.*[13] managed to synthesise single crystals of ZrP_2O_7. After the completion of this work, but prior to the publication of either, Birkedal *et al.* kindly supplied coordinates of the model determined from this single crystal data. This provided a valuable opportunity to test the validity of the method described in this chapter *via* comparison with the single crystal model. Both results were published back-to-back.

The two sets of cell parameters are shown in Table 4-2. Whilst the values produced by Birkedal et *al.* are slightly smaller, the pattern of splitting was very similar. This supports the conclusion that the cell length splitting of these pseudo-cubic materials can be obtained *via*

powder data, despite the lack of visible peak splitting.

Cell length	Birkedal *et al.* cell lengths	Distortion from the mean value in Birkedal *et al.*	Cell lengths from section 4.5 (Å)	Distortion from the mean value in section 4.5 (%)
a	24.7390(2)	0.022	24.7437(4)	0.015
b	24.7184(2)	-0.061	24.7258(3)	-0.058
c	24.7431(2)	0.039	24.7507(4)	0.043
mean	24.7335		24.7400	

Table 4-2: Comparison of absolute cell length and their relative shifts from metrically cubic symmetry between Birkedal *et al.* and this work.

The P-O-P bond angles obtained in the two models are shown in Table 4-3. Excluding the group on the inversion centre (group 14), all of the angles give good agreement between the two models. A slightly different model was used by Birkedal *et al.* for the bridging oxygen of the pyrophosphate group on the centre of inversion. It was modelled as being split over two sites either side of the inversion centre, compared to the single site on the inversion centre in this work.

POP group	POP angle single cryst.	POP angle (powder)	POP group	POP angle single cryst.	POP angle (powder)
1	146.4	143.4(5)	8	142	142.9(7)
2	145	143.7(9)	9	145.7	143.2(12)
3	145	147.3(12)	10	145.9	147.9(6)
4	143.1	142.3(12)	11	140.7	141.0(11)
5	143.3	142.3(12)	12	144.4	143.6(13)
6	147.2	146.8(12)	13	152.4	148.3(12)
7	147.8	148.2(13)	14	150.2	147.6*

Table 4-3: P-O-P bond angles (°) for the 14 crystallographically independent P_2O_7 groups. *Group 14 was modelled with a bond angle of 180° in this work. The value given in the table is estimated from the length of the P-O(-P) bond compared to those of the other groups.

The two sets of atomic coordinates were compared using the Fortran routine 'map_graham'.[10] This gave an average atomic shift between the two sets of coordinates of 0.056 Å if the bridging oxygen atom on the inversion centre was excluded. The spread of shifts is shown in Figure 4-13. The difference in average bond lengths between the two models is shown in

Table 4-4. Overall the two structural models are very similar; this supports the structure found using powder diffraction data and helps validate the methods used in this chapter.

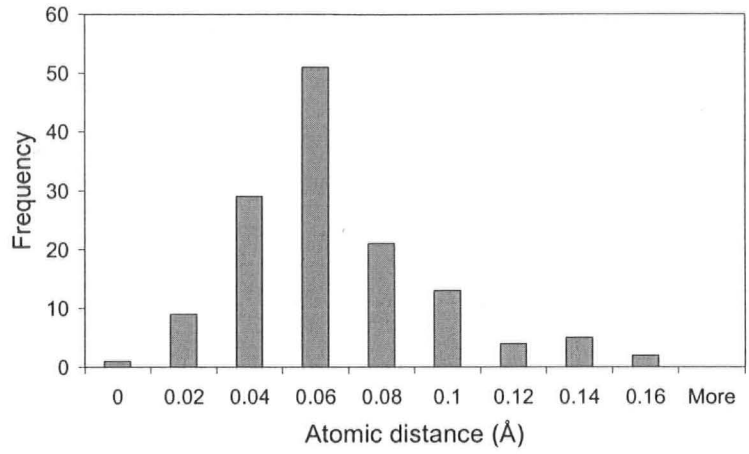

Figure 4-13: Histogram showing the distance between matching atomic position for this work and the structural model produced by Birkedal *et al.*

	Birkedal *et al.*	This work
Zr-O bonds (Å)	2.058(12)	2.069(20)
P-O(-Zr) bonds (Å)	1.504(6)	1.503(16)
P-O(-P) bonds (Å)	1.574(7)	1.567(16)

Table 4-4: Difference in average bond lengths between this work and the structural model produced by Birkedal *et al.*

4.8. Conclusion

It has been shown how Rietveld refinement and distance least-square calculations for polyhedra can be combined using TOPAS Academic software. This enables the solution of complex structures from powder data, providing the underlying network of polyhedra is known. The method's ability to find the same minimum was shown by 57 of the 100 structure solutions appearing in the same place, despite the initial randomisation.

This process enabled the structure of ZrP_2O_7 to be solved despite its complexity with 136 symmetry independent atoms due to the 3 x 3 x 3 superstructure. It also overcame the problem that its metric symmetry, at least with current data, is higher than its crystallographic symmetry. The space group Pbca provided a significantly improved fit of the data compared to attempts in $Pa\bar{3}$, both here and in other work. It also agrees with both the most recent NMR data by King *et al.* and the single crystal structure calculated by Birkedal *et al.* The agreement obtained between the models this work & from Birkedal *et al.* supported the use of this

method and enabled it to be applied to other AM_2O_7 materials in chapter 5.

Deriving the room temperature structure of ZrP_2O_7, with its subtle distortions away from cubic symmetry, should aid the understanding of its thermal expansion properties. It will also help understanding of the phase transitions caused by the opposing effects of P_2O_7 groups trying to achieve stable P-O-P configurations within the constraints of the overall connectivity.

4.9. References

1 Stinton G. W., Hampson M. R., and Evans J. S. O., *Inorgan. Chem.*, 2006, **45**, 4352.

2 Withers R. L., Tabira Y., Evans J. S. O., King I. J., and Sleight A. W., *J. Solid State Chem.*, 2001, **157**, 186.

3 King I. J., Fayon F., Massiot D., Harris R. K., and Evans J. S. O., *Chem.Commun.*, 2001, 1766.

4 Coelho A. A., 'Topas - Academic', Karlsruhe, 2004.

5 Harrison D. E., McKinstry H. A., and Hummel F. A., *J. Am. Ceram. Soc.*, 1954, **37**, 277.

6 Huang C. H., Knop O., Othen D. A., Woodhams F. W., and Howie R. A., *Can. J. Chem.-Rev. Can. Chim.*, 1975, **53**, 79.

7 Pawley G. S., *J. Appl. Crystallogr.*, 1981, **14**, 357.

8 Coelho A. A., 'TOPAS manual', 2000.

9 Brown I. D. and Altermatt D., *Acta Crystallogr., Sect. B: Struct. Sci.*, 1985, **B41**, 245.

10 Evans J. S. O., 'map_graham', Durham, 2005.

11 Shape Software, 'Atoms', Kingsport, TN, USA, 2002.

12 Khosrovani N., Korthuis V., Sleight A. W., and Vogt T., *Inorg. Chem.*, 1996, **35**, 485.

13 Birkedal H., Andersen A. M. K., Arakcheeva A., Chapius G., Norby P., and Pattison P., *Inorg. Chem.*, 2006, **45**, 4346.

5. The structure of pseudo-cubic SnP_2O_7 and GeP_2O_7

5.1. Introduction

This chapter describes investigations into the structures and thermal expansion of two AM_2O_7 species, pseudo-cubic SnP_2O_7 and GeP_2O_7. The structural investigation of both materials uses a similar strategy to that described in chapter 4 for ZrP_2O_7. This consists of a combination of simulated annealing and Rietveld refinement with bond length/angle restraints. Both SnP_2O_7 and GeP_2O_7 demonstrate lower symmetry at room temperature than ZrP_2O_7, making their structures significantly more complex.

As discussed in section 1.5.3, two polymorphs of SnP_2O_7 are found at RT.[1] The phase studied here is the ordered, type II phase. Two phase transitions have been shown to occur upon heating of the type II phase by Gover *et al.*[2] The aim was therefore to produce structural models for each phase using data collected at temperatures of 300 K, 400 K and 647 K. More extensive variable temperature studies were also carried out to support this work.

Only the γ phase of GeP_2O_7 was studied here, as this is the structural polymorph which is related to the other materials in this thesis. γ-GeP_2O_7 has been shown to have at least 35, and probably more, phosphorus environments by Losilla *et al.*[3] A full structure solution is attempted here together with variable temperature diffraction studies.

5.1.1. SnP_2O_7 diffraction data collection

Both neutron and X-ray diffraction data were collected at various temperatures on SnP_2O_7, using a sample synthesised by R Gover. The neutron data were collected at the High-Resolution Powder Diffractometer (HRPD) at the ISIS pulsed neutron source of the Rutherford Appleton Laboratory by JSO Evans and R Gover. Data were collected from an 11 g sample loaded into a 15 mm cylindrical vanadium can. Data from the backscattering bank of detectors were measured with a time-of-flight range of 40,000 to 130,000 μs (0.796 to 2.586 Å). This bank of detectors gives significantly better resolution than the 30° and 90° banks. Data sets were collected every 10 K from 373 K to 1243 K, with a collection time corresponding to a total charge of 9 μA h for each scan collected. Two longer data sets were recorded at 293 K and 1003 K with a time-of-flight range of 34,000 to 120,000 μs (0.676 to 2.387 Å) with a collection time corresponding to a total charge of 150 μA h.

X-ray data were collected by JSO Evans on station ID31 at the European Synchrotron Radiation Facility (ESRF), using a wavelength of 0.495754 Å, selected using a 111 silicon monochromater. 0.0157g of SnP_2O_7 was mounted in a 0.5 mm quartz capillary. 6 minute scans were taken every 12 K on cooling from 1003 K to 303 K, with 6 additional scans between 303 K and 298 K, and on heating every 6 K from 298 K to 910 K with 1 additional

scan at 1003 K. These data were collected between 0.062° and 31.05° (443.822 to 0.956 Å). 3 longer scans were collected at 295 K, 703 K and 1003 K with data collected between 0° and 63.05° (0.474 Å). These longer data sets consisted of 42, 37 and 22 data sets respectively of 6 minutes each, which were combined using ESRF software, Id31sum.

5.1.2. GeP_2O_7 diffraction data collection

Three separate sets of diffraction data were collected on a sample of γ-GeP_2O_7 produced by Franck Fayon. The first set was collected at HRPD at ISIS. Data were collected from a 2 g sample loaded into a 5 mm vanadium slab can. Data from the backscattering bank of detectors were measured from 30,000 to 205,000 μs (0.596 to 4.077 Å) and were used for all of the refinements in this section. A series of short measurements where taken at 2, 4, 10, and 15 K, with further measurements every 15K up to 630 K with a collection time corresponding to a total charge of 17 μA h for each scan collected. Three longer data sets were recorded at 15K (321.4 μA h), 400 K (166 μA h) and 647 K (161 μA h).

X-ray diffraction data were collected in two series. The data above room temperature were collected by R Gover using a Bruker d8 with an Anton Parr HTK1200 furnace to control the temperature. Measurements were taken every 10 K from 303 K to 1073 K and then to 303 K. The scan time for each data set was 42 minutes. Measurements were taken between 10 and 120° 2θ (8.834 and 0.889 Å).

The data below room temperature were collected using a Bruker d8 with a Phenix cryochamber. Measurements were taken for 12 minutes at a time as the sample was cooled from 297 K to 20 K over a period of 10.5 hours (d9_02001). This gave measurements approximately every 5 K. These were followed by a measurement at 18 K and 4 more at 17 K. At 17 K a single scan was taken for 3 hours 20 minutes (d9_02002) between 15° and 120° (5.899 and 0.889 Å).

5.2. SnP_2O_7 Variable Temperature Data

5.2.1. Method of refinement

The 172 short data sets collected at ESRF were refined using a subcell model due to the quick data collections making it difficult to accurately model the full supercell from these data. As the space-group had not been finally determined for this system and would vary across the phase transitions, the data were modelled with space group P1, with starting atomic coordinates derived from the $Pa\bar{3}$ subcell model. To prevent the atoms refining to unrealistic positions, bond angles and distances were restrained using the process described in section 4.4.2. The structural model is not the area of interest at this stage, only the unit cell parameters.

A simulated annealing approach was used to help ensure the correct minimum was found.

Cell parameters were repeatedly randomised and refined for each data set. Lengths were randomised between 7.95 and 8.03 Å, angles between 89.5 and 90.5°.

148 parameters were refined for each data set; these consisted of 117 atomic positions (one atom's position was fixed), 4 isotropic atomic displacement parameters (1 each for Sn, P, $O_{bridging}$ and O_{AM} atoms), 12 terms of a Chebychev polynomial to model the background, 1 zero point correction, 1 scale term, 1 term to model axial broadening, 6 terms of a TCHz peak shape and 6 unit cell parameters.

The variation in cell parameters is shown in Figure 5-1. The lack of symmetry elements in space group P1 means equivalent unit cells can be produced by changing which length is labelled a, b and c, with the concurrent change in labelling of the angles. Due to the simulated annealing this swapping over occurs between data sets, meaning it is the magnitude of the parameters which is important, not which is labelled a, b & c (or α, β & γ).

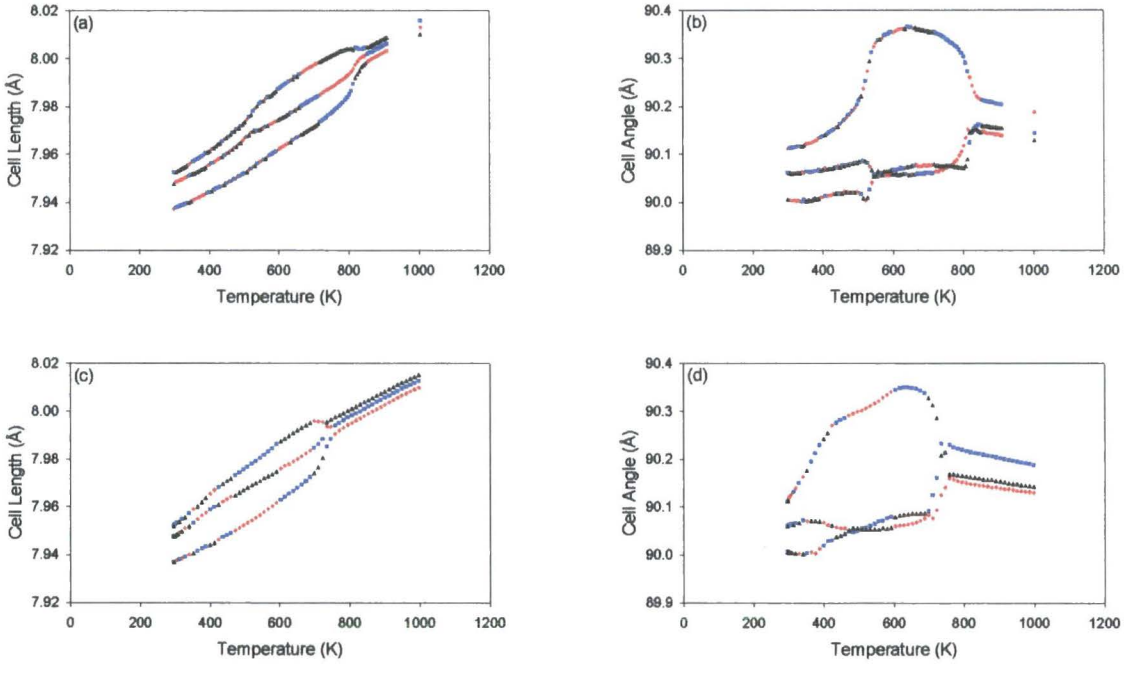

Figure 5-1: Plots showing the changing cell parameter for SnP_2O_7. (a) & (b) show the cell parameters on heating and (c) & (d) show the parameters on cooling. In (a) & (c), red diamonds show the cell length 'a', blue squares show 'b' and black triangles show 'c'. In (b) and (d), red diamonds equal alpha, blue squares show beta and black triangles show gamma.

There appear to be two clear phase transitions, both demonstrating substantial hysteresis. On heating the transitions occur at 525 and 820 K; on cooling they occur at 735 and 425 K. This agrees with the results found by Gover *et al.*[2] The room temperature phase appears to give three distinct cell lengths and angles; which would normally suggest triclinic symmetry. However all of the angles are very close to 90°, particularly the smallest two. This could therefore suggest that the non-90° bond angles are caused by minor deficiencies in precisely

describing the experimental peak shape. Therefore non-triclinic space groups remain feasible. The distortion of the cell lengths is approximately twice that shown for ZrP_2O_7 in chapter 4, which suggests the lengths are non-equivalent in SnP_2O_7 also. This is shown in Table 5-1.

	a	b	c	average	Δa %	Δb %	Δc %
SnP_2O_7 300 K	7.93715	7.95229	7.94764	7.94570	-0.108	0.083	0.024
SnP_2O_7 647 K	7.96654	7.99227	7.97852	7.97911	-0.158	0.165	-0.007
SnP_2O_7 900 K	8.00258	8.00547	8.00838	8.00548	-0.036	0.000	0.036
ZrP_2O_7 RT	8.24790	8.24193	8.25023	8.24669	0.015	-0.058	0.043

Table 5-1: The splitting patterns of the cell lengths of SnP_2O_7 for the three different phases on warming compared to ZrP_2O_7.

A similar situation exists for the intermediate phase. While all cell lengths are unequal and all angles are non 90°, it is possible that the 2 angles which refine to ~ 90.05° are really 90°. The largest angle clearly distorts away from 90°. This suggests monoclinic symmetry. At high temperature the cell lengths are similar and show similar thermal expansion. The cell angles are also similar to each other and show the same trend. This suggests that the differences between the cell lengths are artificial and the cell is possibly rhombohedral. The splitting of the angles shown by this probable rhombohedral phase suggests that the angles in other phases might also contain errors in the region of 0.05°, supporting the assumption of monoclinic phases at lower temperatures.

5.3. The Low Temperature Structure of SnP_2O_7

Fayon *et al.*[4] showed using ^{31}P NMR that at least 96 independent phosphorus environments existed for the room temperature structure of SnP_2O_7. This suggests it should have either $P2_1$ or Pc symmetry. Electron diffraction by Gover *et al.*[2] showed the presence of a 2_1 screw axis, which suggested $P2_1$ was the more likely of these two options.

Structure solution was therefore attempted in both these space groups in parallel. During all of the structural analyses which should have used Pc symmetry, the model was modified to use P 1 1 a symmetry. This allowed the initial atomic coordinates to be specified in the same manner as for P 1 2_1 1.

5.3.1. Pawley Refinement of the Data

The first step of structure solution was carrying out Pawley refinement for both of the data sets in each of the space groups. The results of this are shown in Table 5-2 and Figure 5-2. Table 5-2 gives a slight indication that $P2_1$ might be favoured over Pa. All of the refinements required splitting in terms of the cell length and non 90° angles to achieve a good fit. Given

the large number of reflections, this is far from conclusive, as the refinements could have reached a false minimum.

	X-ray $P2_1$	X-ray Pa	Neutron $P2_1$	Neutron Pa
Rwp (%)	3.785	3.901	1.781	1.852
a (Å)	23.81251	23.81193	23.84765	23.86714
b (Å)	23.82334	23.83244	23.83536	23.83089
c (Å)	23.83660	23.82221	23.84765	23.84117
Monoclinic angle (°)	90.33722	90.28468	89.69269	90.22960
Number of hkls	4572	4370	6600	6494
Zero Point	-0.00304	-0.00548	0.00051	-0.00660

Table 5-2: Results of the Pawley fitting.

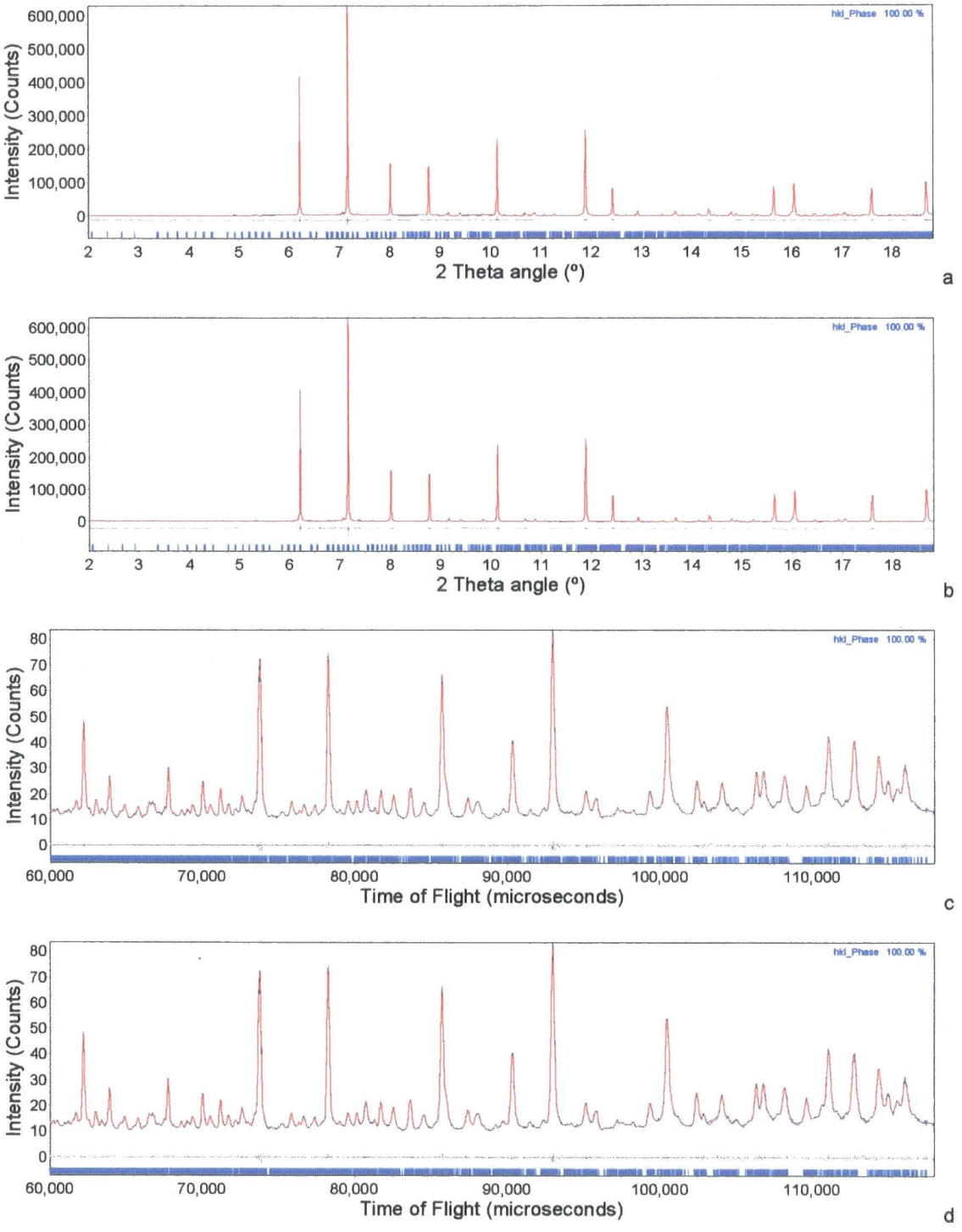

Figure 5-2: Individual Pawley refinement of X-ray and neutron data for SnP_2O_7. (a) and (b) show X-ray data fitted with $P2_1$ and Pa symmetry respectively; (c) and (d) show the neutron data.

5.3.2. Structural Solution Strategy

Structure solution for SnP_2O_7 was performed using the same strategy described in section 4.1.4 for ZrP_2O_7. This consisted of starting from a model derived from expanding a simple

subcell model into 3 x 3 x 3 supercell, randomly shifting the orientation and position of flexible P_2O_7 groups and Sn atoms, followed by Rietveld refinement. For the first stage of the Rietveld refinement, P_2O_7 groups were defined as two linked, rigid PO_4 tetrahedra. In the later stages, bond distances and the internal angles of the polyhedra were restrained. Refinements were carried out in both $P2_1$ and Pa symmetry to see which gave the better fit to the data.

P-O bond distances were constrained to 1.5775 Å for bridging and 1.5000 Å for non-bridging oxygen atoms for the initial stage. These values were the same as had been used in the solution of ZrP_2O_7. Sn-O bond distances were initially set to 2.05441 Å, as determined from the valence bond concept by Brown & Altomatt[5] using the constants of Brese and O'Keeffe.[6]

5.3.3. Distance Least-Squares Calculations

A series of DLS calculations were performed to ensure the correct balance between the different types of restraint. These were aimed at ensuring an approximately Gaussian distribution of angles and lengths, with a standard deviation divided by the average values approximately equal for all parameters. This required weightings of 2.4, 2.8, 0.0004 and 0.0003 for the Sn-O, P-O, O-P-O, and O-Sn-O penalties respectively, and produced the spread of angles and lengths shown in Figure 5-3.

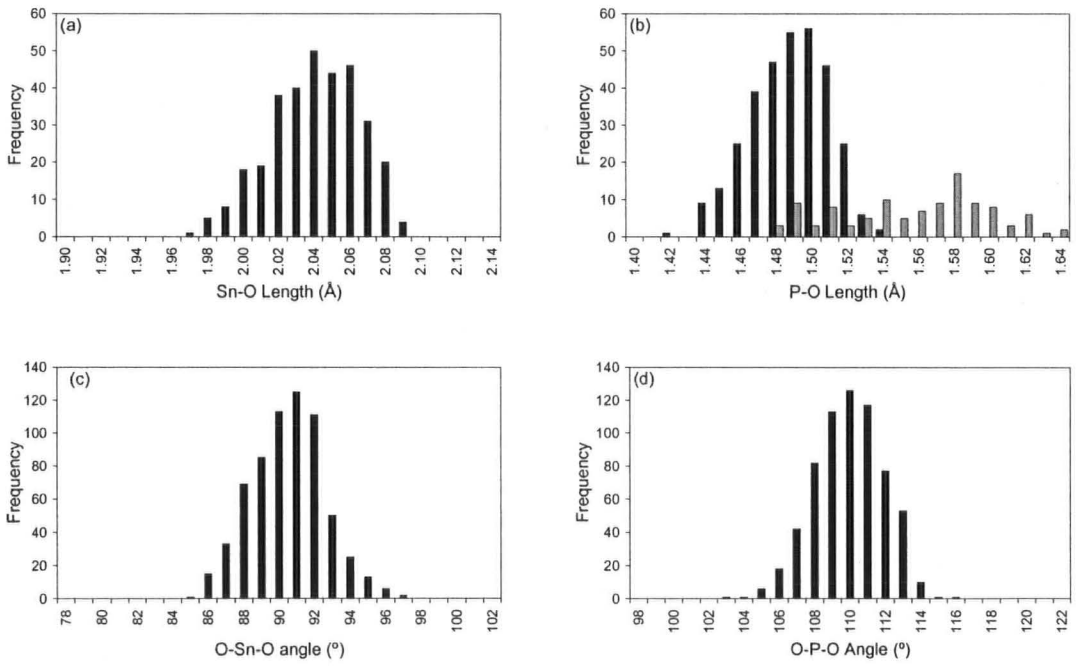

Figure 5-3: Histograms to show the spread of values in the final distance least-squares calculations. (a) and (b) show Sn-O and P-O distances respectively. In (b), the $P\text{-}O_{AM}$ distances are black and the $P\text{-}O_{bridging}$ grey. (c) and (d) show the O-Sn-O and O-P-O distances respectively.

5.3.4. Structural models produced for SnP_2O_7 using Rietveld refinement with constraints and restraints

Six sets of refinements were carried out. These consisted of refining the X-ray and neutron data separately and together in both $P2_1$ and Pa. Each set consisted of 100 solutions produced by the process of randomising, refining with constraints and refining with restraints. All cell lengths were initially set to 23.84 Å, with the monoclinic angle, β for $P2_1$ and γ for Pa, set to 90°. These cell parameters were then allowed to freely refine.

For the combined refinements there were 1662 and 1661 parameters for space groups $P2_1$ and Pa respectively. Both sets of refinement had 7 parameters for the neutron data, which consisted of 6 terms of a Chebychev polynomial to describe the background and 1 scale factor. 28 parameters were required for the X-ray data. These were 18 terms of a Chebychev polynomial to describe the background, 1 scale, 6 terms for a TCHz pseudo-Voigt model for peak shape, 1 monochromator term, 1 zero-point error term and 1 term to describe axial divergence. 4 cell parameters were refined (a, b, c and either β or γ depending on the symmetry) and 4 isotropic atomic displacement parameters, (1 each for Sn, P, $O_{bridging}$ and O_{AM} atoms).

With 540 crystallographically independent atoms, theoretically 1620 parameters should be refined for the x, y and z positions of each of the atoms. As the space group $P2_1$ has one axis (b) in which along which the origin can take any value; the whole structure can shift in this direction while providing an identical fit to the data. This might lead to the structure not converging, as the refinement would continuously shift the whole structure in the y direction. It might also make it difficult to compare different solutions, as very structural similar solutions might have very different sets of coordinates in this direction. Therefore the first tin atom had its y coordinate fixed at 0. This led to 1619 parameters for atom positions for the combined refinements in $P2_1$ symmetry. Similarly, to prevent this occurring in Pa, the x & y coordinates of the first tin atom were both fixed. The cell parameters produced for each of the 100 structural solutions are plotted against R-factor in Figure 5-4.

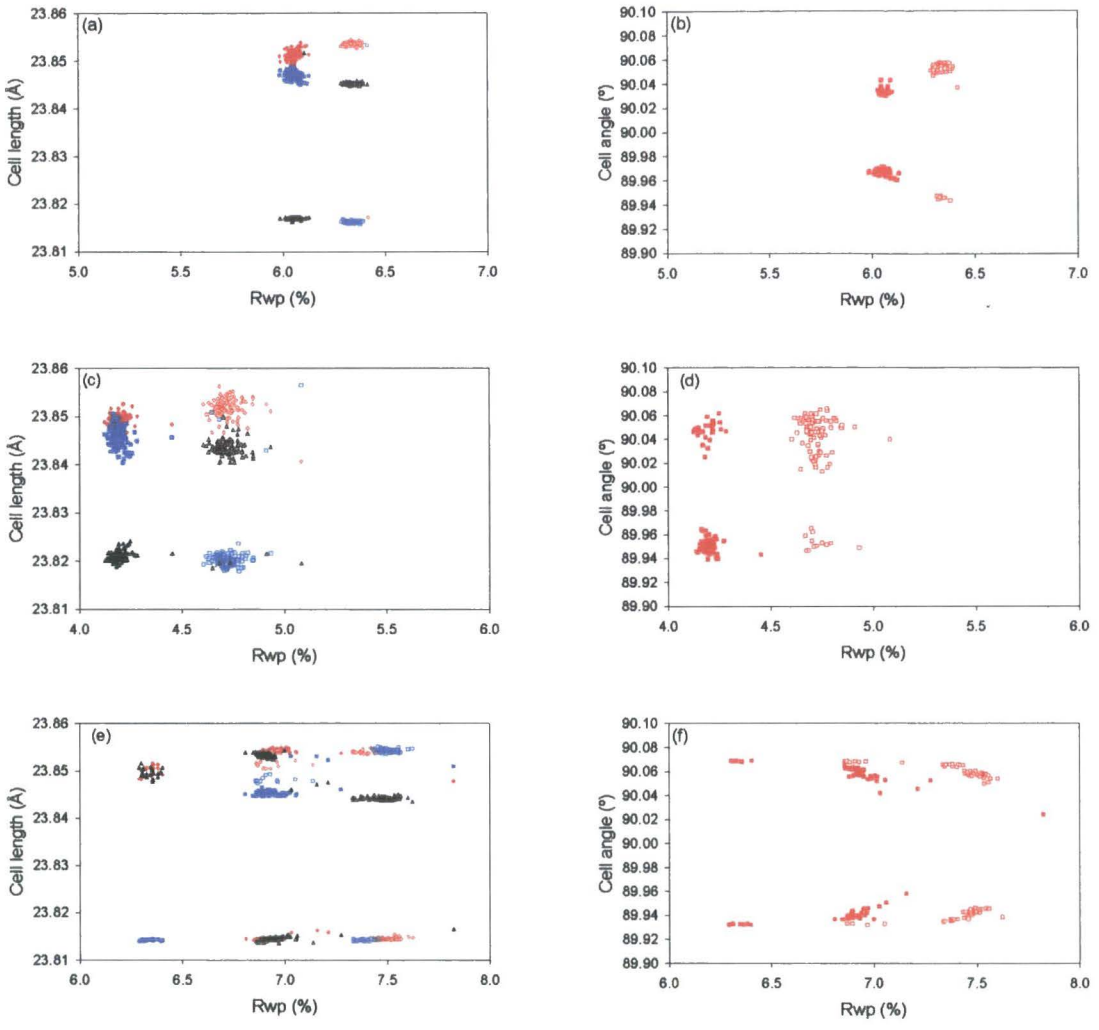

Figure 5-4: Plots showing the results of simulated annealing of the room temperature data of SnP_2O_7. Results of refinements using $P2_1$ symmetry are shown as closed symbols; those from refinements with Pa symmetry have open symbols. (a) & (b) show results of refinement of both neutron and X-ray data, (c) & (d) those from using only the neutron data and (e) & (f) only the X-ray; one result with a particularly high Rwp (23 %) is omitted. Cell lengths 'a' are red diamonds, 'b' are blue squares and 'c' are black triangles.

$P2_1$ showed significantly better fitting of the data than Pa for all of the refinements. All of the series produced two minima in terms of the monoclinic angle, these were always equidistant from 90° and were therefore equivalent. The distortion from away from 90° varied slightly, from ~ 0.033° for the combined refinement to 0.07° for the X-ray only refinement.

All refinement sets required one short cell length and two longer ones with distortions of 0.053 %, 0.036 % and –0.089 % for the best combined refinement. For the neutron only

refinements c is the shortest, for the X-ray data it is b. It seems that neutron data is more sensitive to the pattern of a, b & c as the combined data set echoes the neutron, this is unsurprising given that neutron data is more sensitive to the subtle oxygen distortions. The magnitude of the three cell lengths from the combined refinement are closer to the values from the X-ray data, probably due to the sharper X-ray peaks making this data more sensitive to absolute unit cell dimensions.

To compare the atomic positions produced by the ten best solutions from the combined refinement in $P2_1$, an average model of the ten sets of coordinates was produced. The average model was then compared to each individual result using the Fortran routine map_graham.[7] The atoms were on average 0.14 Å away from the mean position. A few of the atoms were quite far from the mean, 17 were at distances greater than 0.62 Å from the mean, up at 0.92 Å, although all of these occurred in three refinements. The distances from the mean are shown in Figure 5-5.

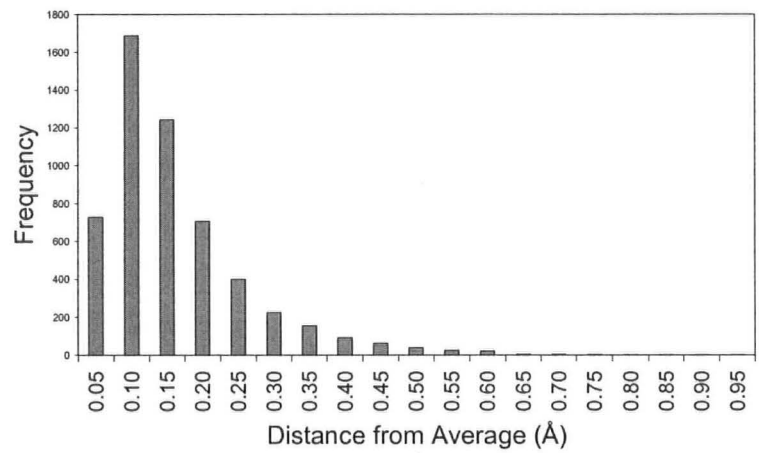

Figure 5-5: Distribution of individual atoms away from the mean position of the 10 best solutions.

The oxygen atoms showed the greatest variation in position, with an average error of 0.16 Å for non-bridging and 0.19 Å for bridging oxygen atoms. This was significantly greater than the average variation of 0.08 Å and 0.07 Å for P and Sn atoms respectively. This is probably due to the weak diffraction of X-rays from light atoms, which means only the neutron data is reliable for determining the position of the oxygen atoms. This leads to more uncertainty in their position than for the heavier atoms. The ten results are shown together in Figure 5-6, produced using Atoms 6.[8] The results show a wider spread than for ZrP_2O_7. Despite small coordinate shifts it is clear that each refinement has found the same structural minimum, giving confidence in the annealing process.

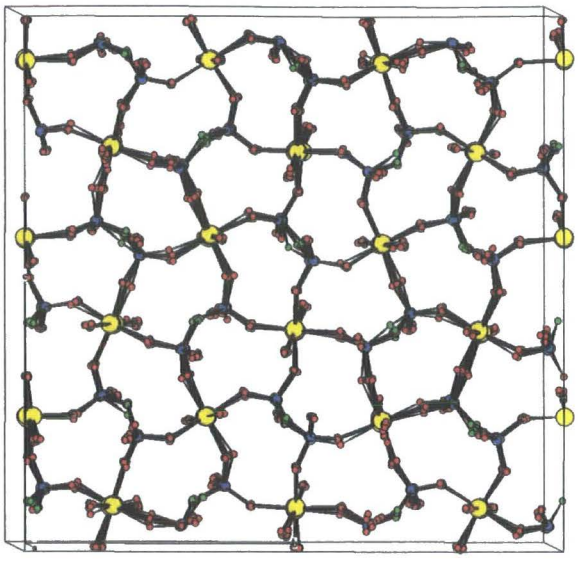

Figure 5-6: Atomic positions of the 10 best fits of the combined data. Tin atoms are in yellow, phosphorus in blue, oxygen in red and bridging oxygen atoms in green. The entire unit cell is shown in the b and c direction but only 5 Å in the a direction are displayed for clarity purposes. Compare with ZrP_2O_7 results in figure 4-7.

5.3.5. Structure Refinement

The best solution from section 5.3.4 was used as a starting point for full structure refinement. The entire neutron data range was used, from 34,000 to 119,990 μs (0.705 Å to 2.489 Å). This range contains 40383 predicted reflections. X-ray data were used from 2.2° to 41.17° 2θ (12.912 Å to 0.705 Å), giving 42839 predicted reflections. This produced a final Rwp of 6.433 % and an Rbragg of 2.53 %. The final Rietveld plots are shown in Figure 5-7.

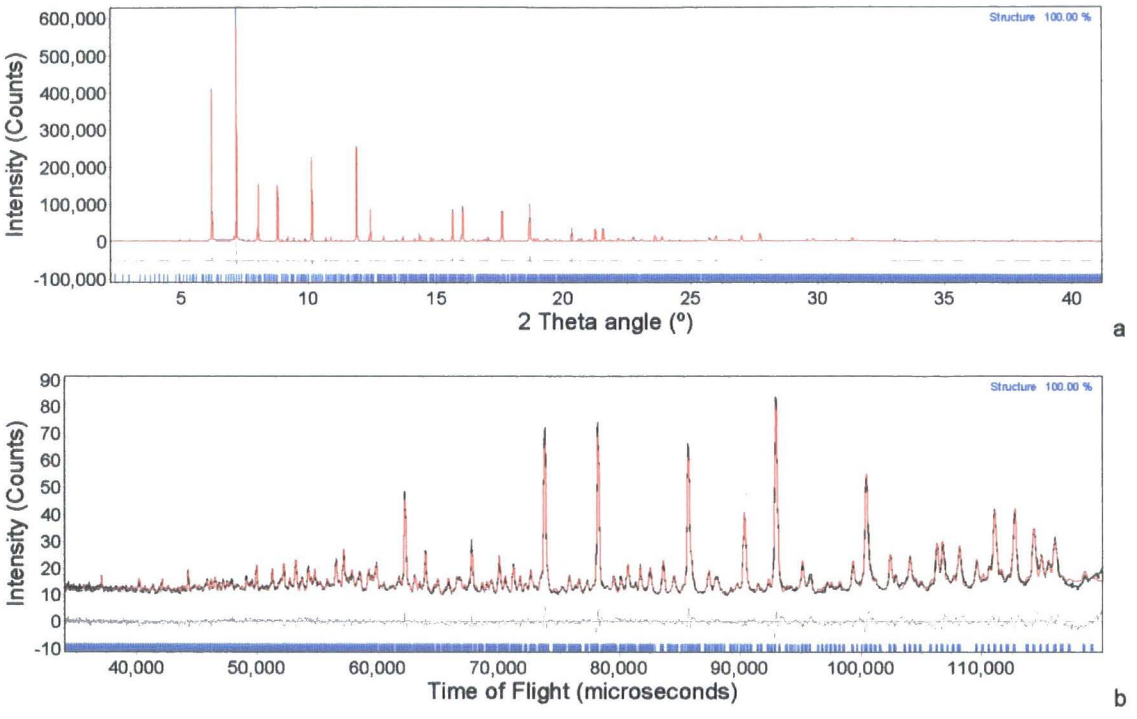

Figure 5-7: Fit of room temperature SnP_2O_7 data in TOPAS Academic of both X-ray (a) and neutron (b) data. Data are shown in blue, fit in red and the difference in grey. Tick marks below the data are positions of hkl peaks.

The bond lengths and angles of this model are shown in Figure 5-8, with full details of the refinement in Table 5-3. The average Sn-O bond length was 2.028(33) Å, with the maximum distortion from the average length being 0.109 Å. The average O-Sn-O angle was 90° (4), with a maximum distortion of 10.2°. The average P-O bond length was 1.49(3) Å for O_{AM} and 1.56(3) Å for $O_{bridging}$, with maximum deviations of 0.087 and 0.108 Å respectively. The average O-P-O angle was 109.4° (2.8) with a maximum deviation of 9.6°. All of these deviations were within the expected range. A Cif file of the structure is available in the e-appendix.

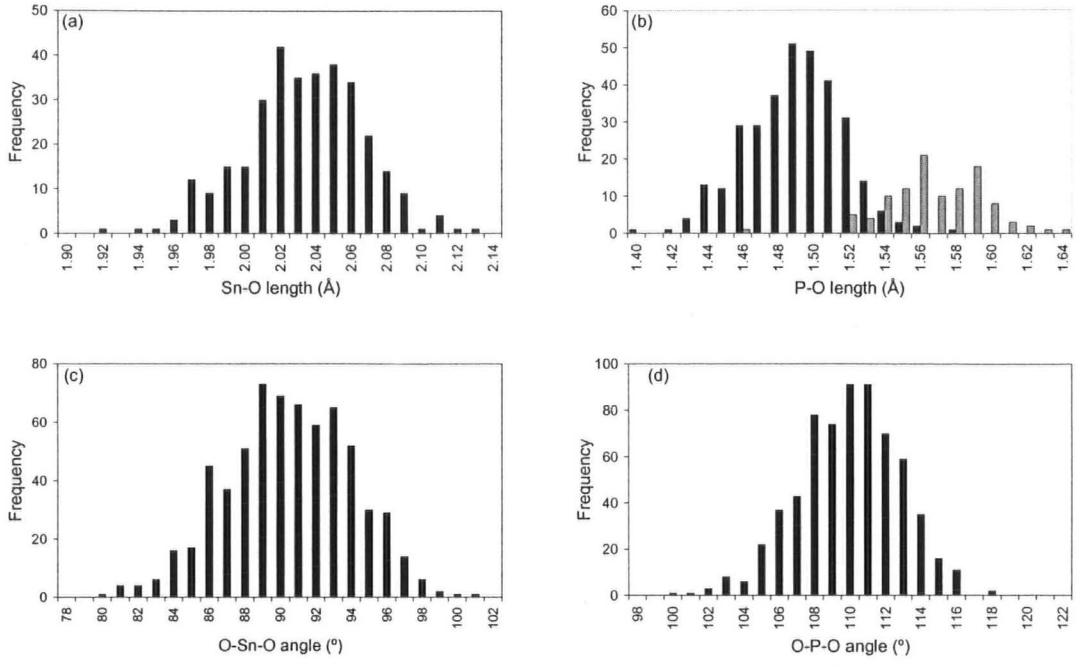

Figure 5-8: Histograms of (a) Sn-O distances, (b) P-O distances with P-O_{AM} in black and P-$O_{bridging}$ in grey, (c) O-Sn-O angles and (d) O-P-O angles.

	α-SnP_2O_7
a (Å)	23.850 (2)
b (Å)	23.847 (2)
c (Å)	23.8141(5)
Beta angle (°)	89.975 (9)
V ($Å^3$)	13544.3 (3)
wRp (all/neutron/x-ray)	6.433/ 5.515/ 6.924
R_{Bragg} (neutron/x-ray)	2.339/ 2.529
Goodness of Fit (all/neutron/x-ray)	0.894/ 1.154/ 0.891
N° Reflections (neutron/x-ray)	40383/ 42839
Structural Parameters	1619
Total Parameters	1662

Table 5-3: Details of the final refinement of SnP_2O_7 in $P2_1$.

5.3.6. Conclusion

By using a combination of distance least-squares calculations and Rietveld refinement it has been possible to produce a series of structural models for SnP_2O_7 in both $P2_1$ and Pa. The fitting of the data was significantly better in $P2_1$ than in Pa, suggesting this is the correct space group. This was supported by the electron diffraction by Gover *et al.* which suggested a screw axis. A final structure model for α-SnP_2O_7 has been produced, which gives a chemically plausible set of bond angles and lengths.

5.4. The Intermediate Phase of SnP_2O_7

5.4.1. Introduction

The aim of this section of work was to produce a structural model for the phase of SnP_2O_7 that exists on heating type II SnP_2O_7 to between 525 K and 820 K. This presented an additional challenge compared to the refinement of the room temperature data due to the fact that no ^{31}P NMR data could be obtained at this temperature and the space group could not be determined as easily. There were however, details in the diffraction pattern which assisted with the space group determination. As is shown in Figure 5-9, the X-ray diffraction pattern of the room temperature and intermediate phases are very similar. This suggested that the intermediate phase is a small structural modification of the room temperature phase. One major difference between the two is the broader peaks of the intermediate phase, this suggested possible size and/ or strain broadening.

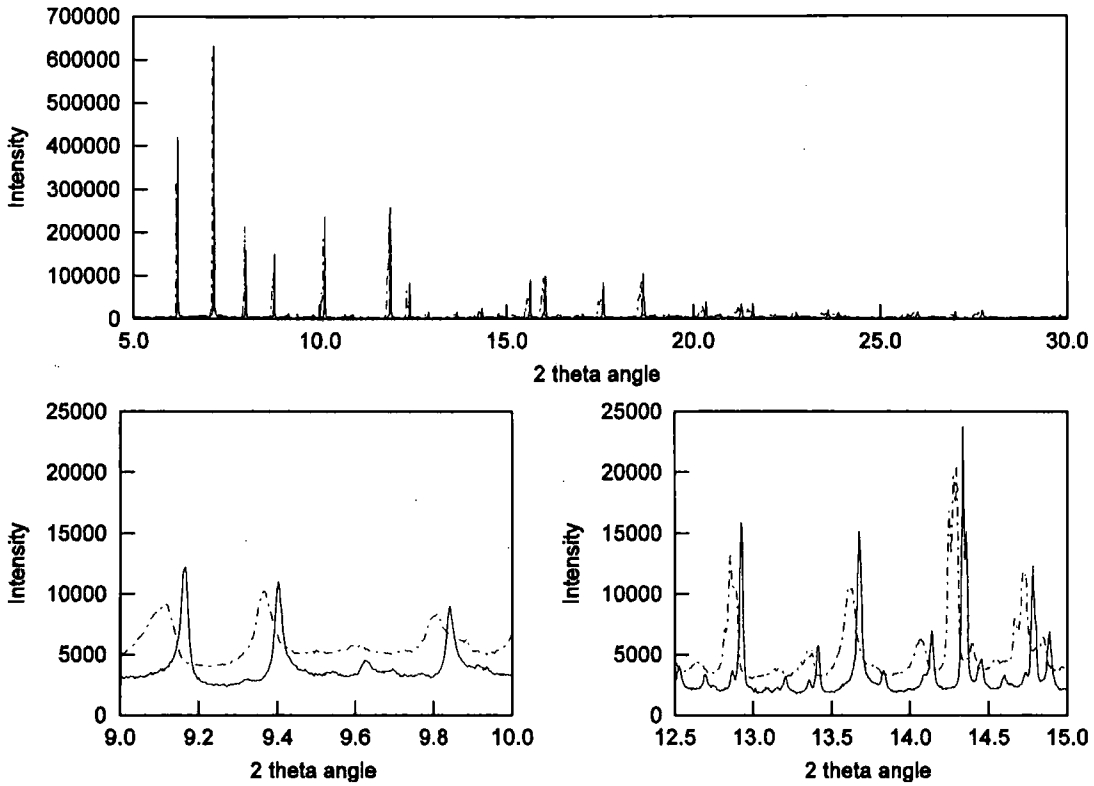

Figure 5-9: Comparisons of the raw X-ray data for the room temperature (solid line) and intermediate phase (dashed line) of SnP_2O_7. The top graph shows the main subcell peaks, the two lower graphs show details of the supercell peaks.

5.4.2. Modified Pawley Fitting

The first method employed to try and understand the structure was to carry out a series of Pawley refinements[9] in the different crystal systems. The simplest space group for each system that occurred as a possible isomorphic subgroup of $Pa\bar{3}$ was used to try and model the main subcell peaks of the data. Refinements were therefore carried out each of the available Laue groups,

As the vast majority of the structures of these AM_2O_7 materials can be thought of as modified versions of the original $Pa\bar{3}$ model, all of the subcell hkl reflections which have identical intensities in $Pa\bar{3}$ should have similar intensities in the lower symmetry structures. It was therefore decided to ensure that the intensities of these groups of reflections stayed within a certain range of each other.

Intensities of reflections that would be equivalent in the ideal cubic structure were therefore constrained to lie within a certain percentage of their average value. The percentage used were 0, 1, 5, 10, 20, 50 and 500 %, with the latter effectively a free refinement. For the R3 space group, all limits were corrected to account for the different multiplicities of reflections in a group. The results are shown in Figure 5-10.

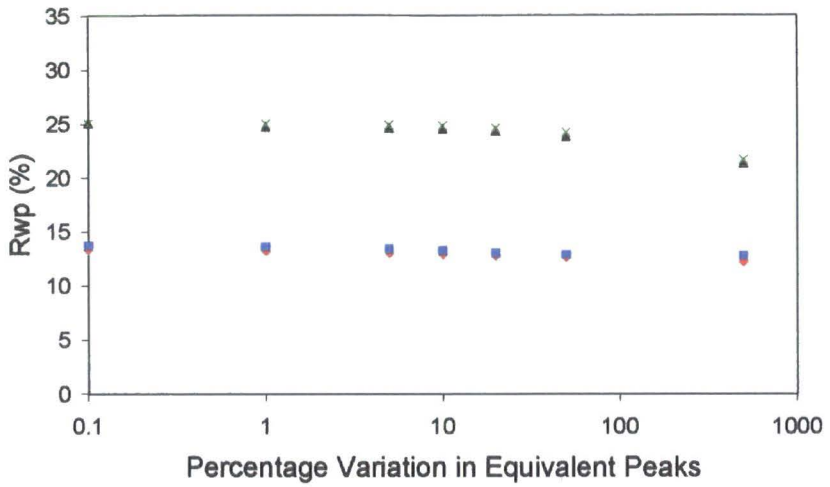

Figure 5-10: The results of Pawley fitting with controlled intensities for the intermediate temperature phase. Red diamonds show the fit in Laue class $\bar{1}$, blue squares the fit in 2/m, black triangles $\bar{3}$ and green crosses 2/m 2/m 2/m.

It is clear from this simple analysis that the material has a structure closely related to the ideal $Pa\bar{3}$ subcell structure in that excellent Pawley fits can be achieved with only small % changes between intensities of previously equivalent reflections. It is also clear that a significant improvement in fit is obtained on moving from an orthorhombic to monoclinic Laue symmetry, but that the further improvement on moving to triclinic is minimal.

5.4.3. Structure Solution

For each of the three plausible space groups (P1, $P2_1$ & $P2_1/a$, see Figure 1-13), 100 structural solutions were carried out based on randomising the unit cell and then using the Rietveld refinement mechanism discussed in chapter 4. Cell lengths were randomised between 23.89 & 23.99 Å and non-90° cell angles were randomised between 89.5 and 90.5°.

A total of 3288, 1665 and 850 parameters were refined for the structure solutions in P1, $P2_1$ and $P2_1/a$ respectively. Of these 3240, 1619 and 804 were for the x, y and z coordinates of atoms respectively. P1 has 6 refinable cell parameters; $P2_1$ and $P2_1/a$ have 4.

In addition, 42 parameters were refined for all of the data sets. These consisted of 4 atomic displacement factors (1 each for Sn, P, $O_{bridging}$ and O_{AM} atoms), 28 parameters for the X-ray data and 10 parameters for the neutron data. The X-ray data had an 18 term Chebychev polynomial to describe the background, 1 scale term, 6 terms of a TCHz pseudo-voigt function to describe peak shape, 1 term to describe axial broadening, 1 absorption correction and 1 zero point correction. The 10 neutron parameters were a 6 term Chebychev background polynomial, 1 scale, 2 terms to describe the peak width and one term of the time-of-flight peak shape function. Plots of Rwps vs. cell parameters are shown in Figure 5-11.

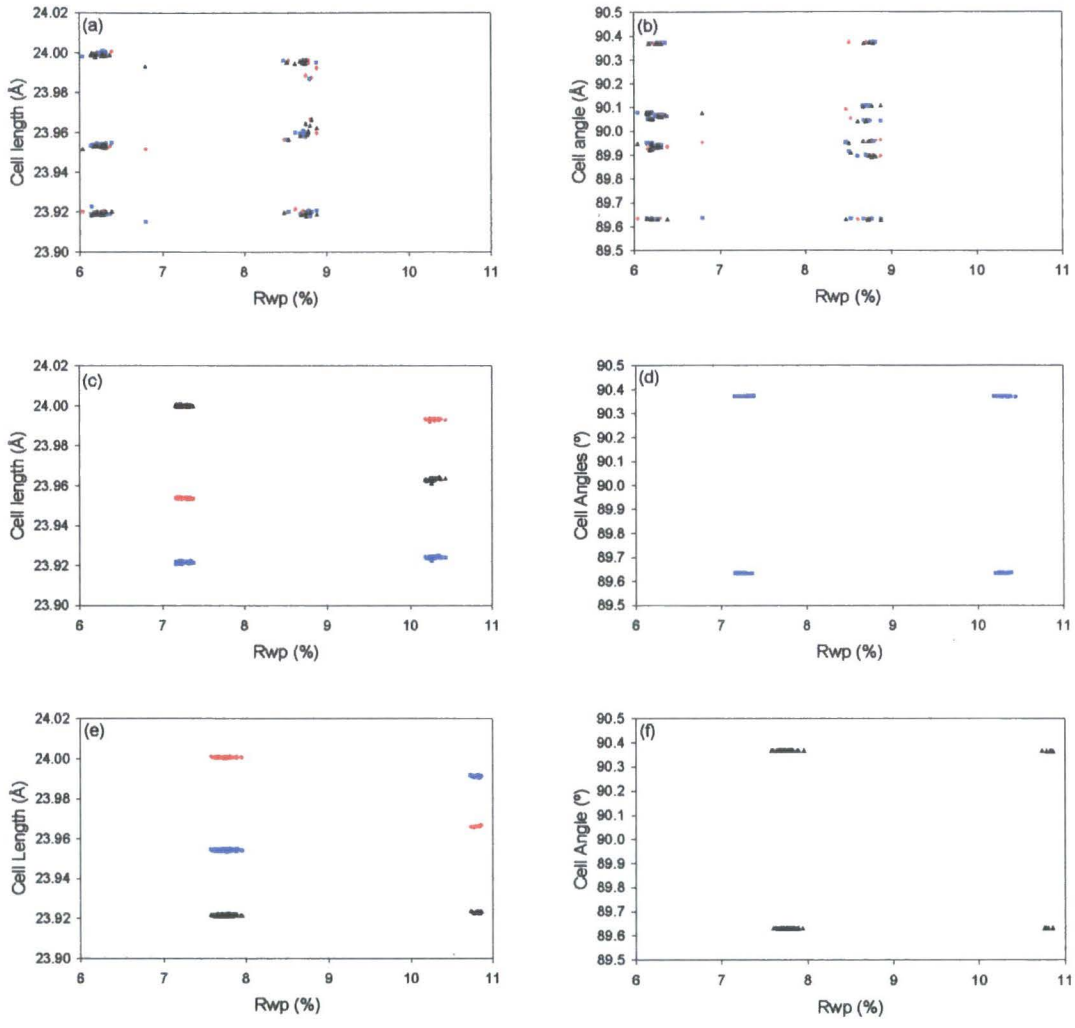

Figure 5-11: Scatter plots showing the results of simulated annealing of the intermediate temperature data of SnP_2O_7. (a) & (b) show the cell parameters for the refinements with P1 symmetry, (c) & (d) show the results with $P2_1$ symmetry and (e) & (f) show the results with $P2_1/a$ symmetry. Cell length 'a' & angle α are red diamonds, 'b' & β are blue squares and 'c' & γ are black triangles.

5.4.4. Comparison of the Results in Different Symmetries

The lowering of symmetry in section 5.4.3 produced superior models; however, increasing the number of parameters will always give an equal or better fit of the data, providing the smaller set of parameters is a subset of the larger parameter set. The statistical significance of the improvement in fitting was therefore investigated. The testing was based on the Hamilton's R-ratio test.[10] This applies an F test to determine whether the fit of an unconstrained model to a given set of data is better than that of a constrained one, given the additional number of parameters.

This test does require the number of observations to be calculated. For single crystal data this

is trivial, being the number of observed hkl reflections in the diffraction pattern. For powder diffraction data the situation is more complicated due to the overlapping of reflections and several theories for deriving the number of independent observations have been proposed.[11,12,13] This is particularly problematic in cases such as this, with a relatively large unit cell and subtle distortions away from cubic symmetry giving many overlapping hkl peaks. In fact for the 3 space groups used the number of predicted hkl reflections is actually larger than the number of data points, which is clearly unreasonable. The maximum number of independent observations is therefore the number of data points, rather than the number of hkls. In this case the structural model has to fit the restraints as well as the diffraction data, therefore these can be thought of as additional observations. The number of observations is important to the conclusion drawn; as it increases, the chance of the lower symmetry, more complex model passing the test increases.

Given that the number of observations is ambiguous, it was decided to carry out two sets of tests. The first used the maximum possible number of observations: the number of data points plus the number of restraints for a P1 model (11076). The second used only the number of data points (6648). This also serves as an intermediate figure if only some of the data points and some of the restraints were used. The results are shown in Table 5-4.

Observations	Data Points and Restraints			Data Points Only		
Comparison of model A vs. B	$P2_1/a$ vs. $P2_1$	$P2_1/a$ vs. P1	$P2_1$ vs. P1	$P2_1/a$ vs. $P2_1$	$P2_1/a$ vs. P1	$P2_1$ vs. P1
Rwp of constrained model (%)	7.5778	7.5578	7.1592	7.5778	7.5578	7.1592
Rwp of unconstrained model (%)	7.1592	6.0377	6.0377	7.1592	6.0377	6.0377
observations, n	11076	11076	11076	6648	6648	6648
constrained parameters q	850	850	1668	850	850	1668
unconstrained parameters p	1668	3288	3288	1668	3288	3288
μ_1 (p-q)	818	2438	1620	818	2438	1620
μ_2 (n-p)	9408	7788	7788	4980	3360	3360
F value for constrained model vs. unconstrained model	1.384278	1.810992	1.951817	0.732749	0.781322	0.842078
95% probability	1.09	1.06	1.07	1.09	1.06	1.07
B significantly better than A	True	True	True	Unproven	Unproven	Unproven

Table 5-4: Results of statistical analysis on the difference between the various structural models. If the F value is greater than 95 % probability, then the difference in the R-factor is greater than would be expected by chance.

The results of this analysis are, as might be anticipated, somewhat ambiguous. If it is assumed that there is 11076 reliable independent observations, it can be concluded that P1 gives a significantly better fit that either $P2_1$ or $P2_1/a$. If the more pessimistic view that there is only 6648 observations, then we accept $P2_1/a$ as the statistically best model. One firm conclusion can be drawn, which is that a $P2_1$ model would never be accepted by this test. $P2_1$ would only be accepted over $P2_1/a$ if there where > 9200 observations. However for > 7500 observations, P1 is accepted over $P2_1$. It is therefore concluded that the symmetry is either $P2_1/a$ or P1. The former is favoured for the reasons given below.

Due to the inconclusive nature of these F tests for the intermediate phase it was decided to repeat the process using the room temperature data. As the RT structure had been proven by NMR to be $P2_1$ (or Pc), it would be possible to see if the F tests produced the same result,

hopefully giving an indication of how much information could be extracted from the first set of tests.

Simulated annealing was performed on the combined neutron and X-ray data in both P1 and $P2_1/a$. This led to 3282 and 844 parameters respectively, instead of 1662 from section 5.3.2, due to the different number of atoms in the asymmetric unit and the 2 additional refinable cell angles in P1 symmetry. The results of annealing are shown in Figure 5-12, with the results of $P2_1$ repeated for clarity. Results of equivalent F-tests are shown in Table 5-5.

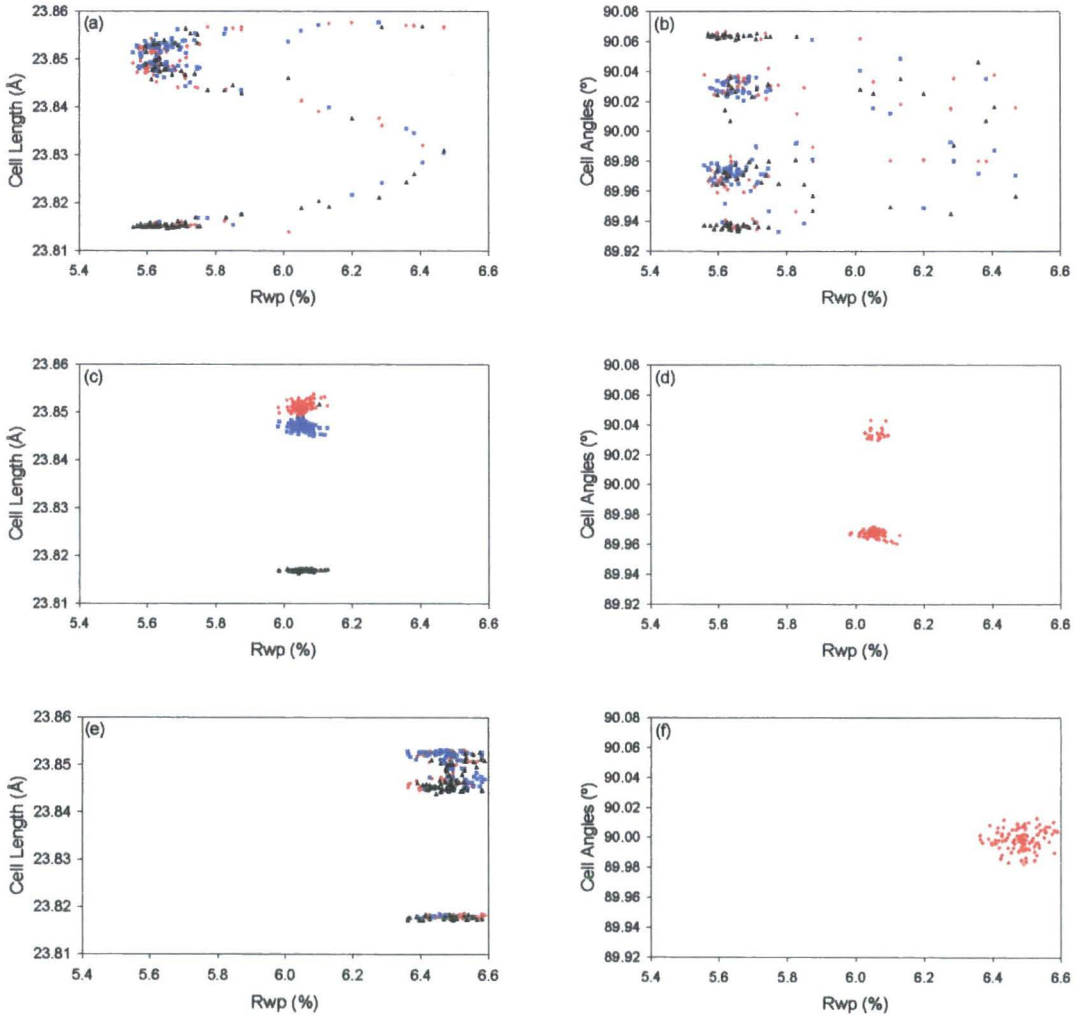

Figure 5-12: Plots showing the results of simulated annealing of the room temperature data of SnP_2O_7. (a) & (b) show results of refinements in P1 symmetry, (c) & (d) those in $P2_1$ and (e) & (f) those in $P2_1/a$. Cell length a & angle α are red diamonds, b & β are blue squares and c & γ are black triangles.

Observations	Data Points and Restraints			Data Points Only		
Comparison of model A vs. B	$P2_1/a$ vs. $P2_1$	$P2_1/a$ vs. P1	$P2_1$ vs. P1	$P2_1/a$ vs. $P2_1$	$P2_1/a$ vs. P1	$P2_1$ vs. P1
Rwp of constrained model (%)	6.3622	6.3622	5.984	6.3622	6.3622	5.984
Rwp of unconstrained model (%)	5.984	5.56	5.56	5.984	5.56	5.56
observations, n	10864	10864	10864	6576	6576	6576
constrained parameters q	847	847	1662	847	847	1662
unconstrained parameters p	1662	3278	3278	1662	3278	3278
μ_1 (p-q)	815	2431	1616	815	2431	1616
μ_2 (n-p)	9202	7586	7586	4914	3298	3298
F value for the constrained model vs. unconstrained model	1.4723	0.965422	0.743266	0.786229	0.419716	0.323133
95 % probability	1.1	1.09	1.07	1.1	1.09	1.07
B significantly better than A	TRUE	Unproven	Unproven	Unproven	Unproven	Unproven

Table 5-5: Results of statistical analysis on the difference between the various structural models. If the F value is greater than 95 % probability, then the difference in the R-factor is greater than would be expected by chance.

From Table 5-5 it can be seen that there are differences in conclusions of the F-test for the room temperature models compared to those for the intermediate phase. For the RT data P1 is never statistically better than $P2_1$ for any feasible number of observations. This is expected given the results of ^{31}P NMR. For the $P2_1$ model to be statistically better than the $P2_1/a$ model for the room temperature data, the number of observations must be assumed to be greater than 8600.

If the number of observations is assumed to be greater than 8600 for the intermediate phase data, then the P1 model should be accepted as significantly better than $P2_1/a$. However the situation is further complicated by the low quality of the 647 K neutron data and the significant strain at this temperature. This strain is discussed in section 5.4.5.

5.4.5. Strain Effects at 647 K

Peak by peak analysis of the difference in quality of fit between the $P2_1/a$ and P1 models revealed that most of the difference in Rwp was caused by a small number of subcell peaks being fitted significantly worse using the former symmetry than the latter. The two most noticeable sets of peaks were the 333 & $3\bar{3}\bar{3}$ and the 666 & $6\bar{6}\bar{6}$. The former pair of peaks is shown in Figure 5-13; the 666 & $6\bar{6}\bar{6}$ pair show similar behaviour. The difference between the sharper lower angle peak and the broader higher angle peak suggests either that the true symmetry is P1 or that there are different amounts of strain-broadening between the 2 peaks in $P2_1/a$ symmetry. The theory of strain broadening is supported by the greater peak width of the intermediate over the room temperature phase, as is shown in Figure 5-13. It was therefore decided to attempt to model this differing strain using spherical harmonics.

The best structural solutions from section 5.4.4 were used as the starting point of structural refinements in $P2_1/a$ and P1 with eighth-order hkl dependent spherical harmonics in addition to the previously refined peak shape parameters. This gave 25 additional parameters in $P2_1/a$ symmetry, which consisted of 23 values to describe the strain in each hkl direction and 2 terms to scale this for the neutron and the X-ray data. 45 additional parameters were used in the P1 refinements, 43 hkl strain terms and 2 scale terms. The results showed a great improvement in the quality of fit of the data, with the Rwp decreasing from 7.5578 % to 6.6623 % and from 6.0377 % to 5.6534 % for $P2_1/a$ and P1 respectively. The improvement in the $P2_1/a$ model was clearly seen in peaks like the 333 & $3\bar{3}\bar{3}$, as shown in Figure 5-13.

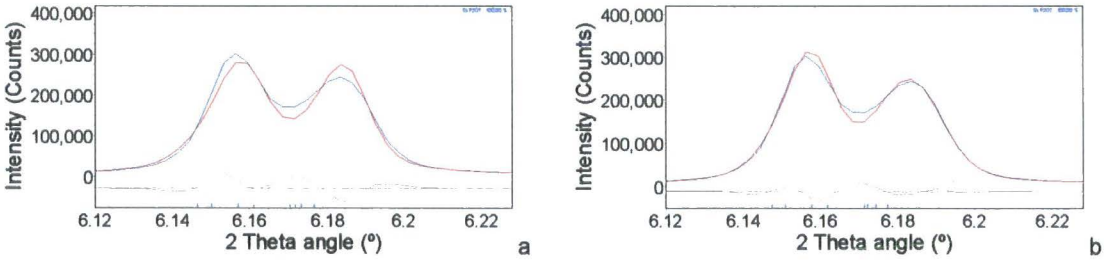

Figure 5-13: Rietveld fits of the 333 and $3\bar{3}\bar{3}$ peaks fitted using a model with $P2_1/a$ symmetry. (a) shows the results without and (b) with the spherical harmonics. The data are in blue, the theoretical fit is in red, the difference in grey and blue tick marks show the position of hkl peaks. Note that the intensity of hkl peaks due to the 511 family which occur at similar 2θ values do not contribute significantly to the overall intensity.

Despite the noticeably greater decrease in Rwp with spherical harmonics for $P2_1/a$ the results of the F-tests remained the same; the P1 model was statistically superior only if the restraints were included in the observations. The number of observations required for P1 to be accepted over $P2_1/a$ does increase from 7800 to 10300 with the addition of spherical harmonics, meaning the latter is more likely than previously. This means that if the number of observations is assumed to be ~ 8600 (the level required for the room temperature structure

to be $P2_1$) then P1 is not significantly better than $P2_1/a$.

5.4.6. Conclusion

Due to the lack of phosphorus NMR, the conclusions on the symmetry of the intermediate temperature phase are not as definitive as those for the room temperature phase. Neither of the $P2_1/a$ and P1 symmetry models could definitely be rejected based on these results. $P2_1/a$ seems the more likely due to the tendency for symmetry to increase with increasing temperature. This is supported by small magnitude of the difference in Rwp when spherical harmonics are applied to model strain broadening.

5.5. The High Temperature Phase of SnP_2O_7

As demonstrated in section 5.2, a further phase transition occurs at 820 K on heating. A full structural solution of this phase was therefore attempted using the same methodology as was used for the intermediate temperature phase.

5.5.1. Pawley Fitting of the Subcell

The first stage of data analysis was to carry out Pawley fitting of the ESRF X-ray data taken at 1003 K. The same style of limits on the minimum and maximum peak intensity that was demonstrated in section 5.4.2 was used here. The results are shown in Figure 5-14. Pbca and $P2_1$ symmetry gave a very poor fit and should be discounted. The similarly in quality of fit between Laue class $\bar{1}$ and $\bar{3}$ models suggested R3 (or possibly $R\bar{3}$) was the correct space group. The average cell length of the refinements in R3 symmetry was 8.0151(2) Å, with angles of 90.1522(7)°.

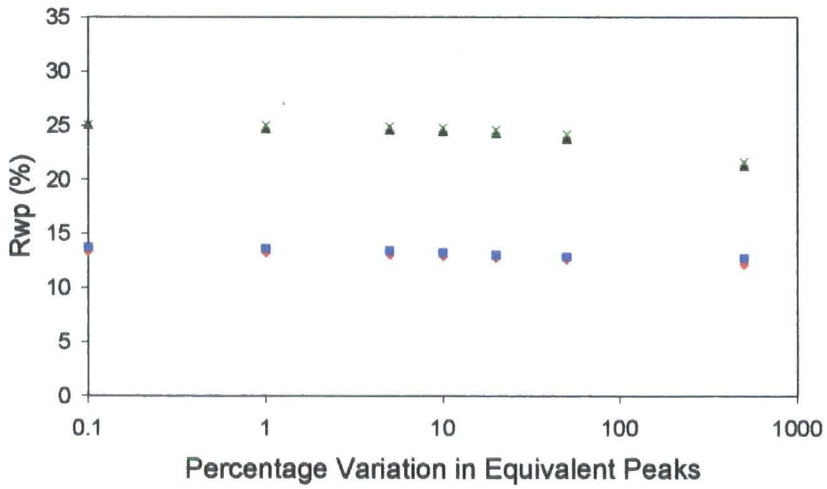

Figure 5-14: Results of Pawley fitting with controlled intensities for the high temperature phase. Red diamonds show the fit in Laue class $\bar{1}$, blue squares the fit in 2/m, black triangles $\bar{3}$ and green crosses 2/m 2/m 2/m.

5.5.2. Supercell Pawley Fitting

To check if all the supercell peaks were fitted by a 3 x 3 x 3 supercell of the subcell proposed in section 5.5.1, a Pawley refinement was carried out using a rhombohedral cell with lengths of 3 x 8.0151 Å and angles of 90.1522°. This fitted the majority of supercell peaks, but some remained unfitted. These peaks were typically one of a pair of peaks, where the other member of the pair was fitted. Closer investigation of the variable temperature data, shown in Figure 5-15, shows that many of the supercell peaks split into 2 at the phase transition. At first it was thought that these additional peaks might be due to an impurity, but this is discounted due to the fact they disappear at the phase transition on cooling.

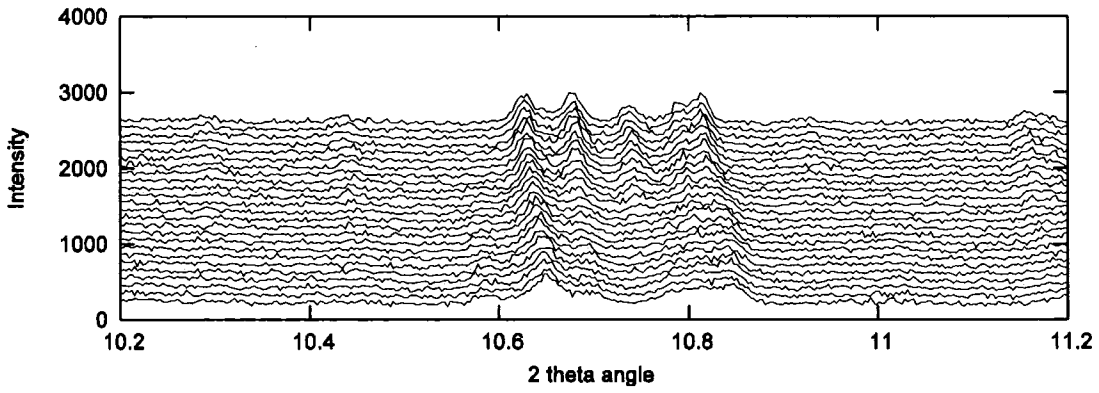

Figure 5-15: Plot showing detail of supercell peaks at the phase transition with increasing temperature in the y direction. Note the new peak at ~10.55°, which proved impossible to index with a 3 x 3 x 3 supercell.

These additional peaks meant that the method of deducing the subcell and expanding to 3 x 3 x 3 supercell failed. Attempts were made to index the data using both Svd-index[14] and Supercell.[15] Neither gave any solutions that fitted all of the peaks, unless the cells were sufficiently large that they would fit virtually any data pattern. A full structure solution was therefore not possible at this stage.

5.5.3. Fitting the subcell in R3

Although a model of the supercell could not be deduced, it was feasible to model the subcell using rhombohedral symmetry. Models were produced in both R3 and $R\bar{3}$. 75 parameters were refined for the R3 model. Of these 27 were used for the X-ray data, these consisted of 18 terms of a Chebychev polynomial to model the background, 1 zero point correction, 1 absorption correction, 1 term to model axial broadening, 1 scale and a TCHz peak shape with all 6 terms refined. 9 terms were used for the neutron data, these consisted of two peak shape terms, 6 background terms and 1 scale. 38 structural parameters were refined; these consisted of 4 isotropic atomic displacement parameters (1 each for Sn, P, $O_{bridging}$ and O_{AM} atoms), the cell angle and length and 32 fractional coordinates.

Both models fitted the subcell peaks reasonably well, with Rwp's of 10.882 and 11.032 % for R3 and $R\bar{3}$ respectively. The difference in Rwp was shown to be statistically significant using the method in described in section 5.4.4. The Rietveld plots are shown in Figure 5-16.

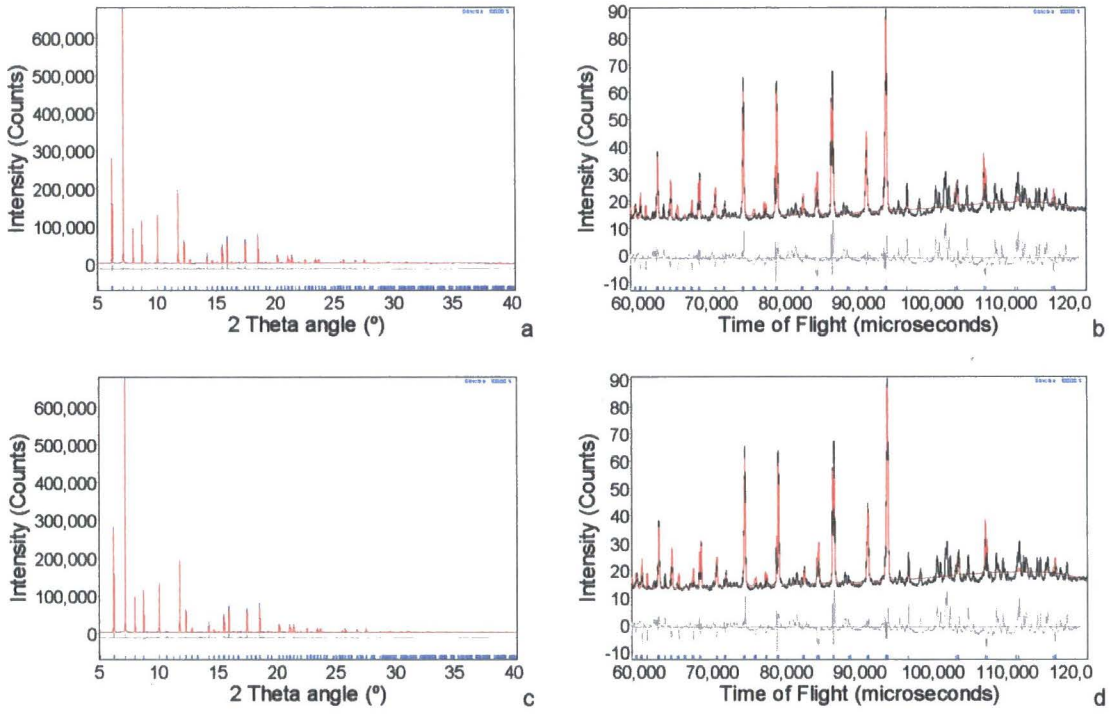

Figure 5-16: Results of Rietveld refinement using a subcell model in spacegroups R3, (a) & (b), and $R\bar{3}$, (c) & (d). (a) and (c) show the fits of the blue X-ray data, (b) and (d) the black neutron data. The fit is in red, the difference is in grey and the position of hkl peaks are shown as blue tickmarks.

The fit to the neutron data is quite poor due to the presence of large subcell peaks at the long time-of-flight end of the data. The possibility of the phase possessing rhombohedral symmetry does provide some evidence that the intermediate phase could have P1 symmetry, which would act as intermediate between the $P2_1$ room temperature phase and the high temperature phase.

5.6. Variable Temperature Refinements for GeP_2O_7

5.6.1. Method of refinement

The three sets of variable temperature measurements described in section 5.1.2 were refined using the same P1 subcell model. This was identical to the model used for SnP_2O_7 in section 5.2.1. Restraints on atomic bond lengths and angles were also used. The P-O distance restraints were the same as used in previous sections and the Ge-O distances were restrained at 1.8604 Å. This was again calculated using the valence bond concept.

These refinements used 127 structural parameters, consisting of 117 atomic coordinates, 4 ADP's (1 each for Ge, P, $O_{bridging}$ and O_{AM} atoms) and 6 cell parameters. For the two X-ray

data sets, 17 additional parameters were refined. These consisted of a 15 term Chebychev polynomial to model the background, 1 scale and 1 zero point error. For the neutron data, 8 additional parameters were refined. These consisted of a 6 term Chebychev polynomial to model the background, and 2 terms to model Gaussian and Lorentzian broadening. The results are shown twice; firstly in Figure 5-17 with varying temperature scales to show the details clearly; secondly in Figure 5-18 with all of the graphs using a single temperature scale to allow easier comparison of the different data sets.

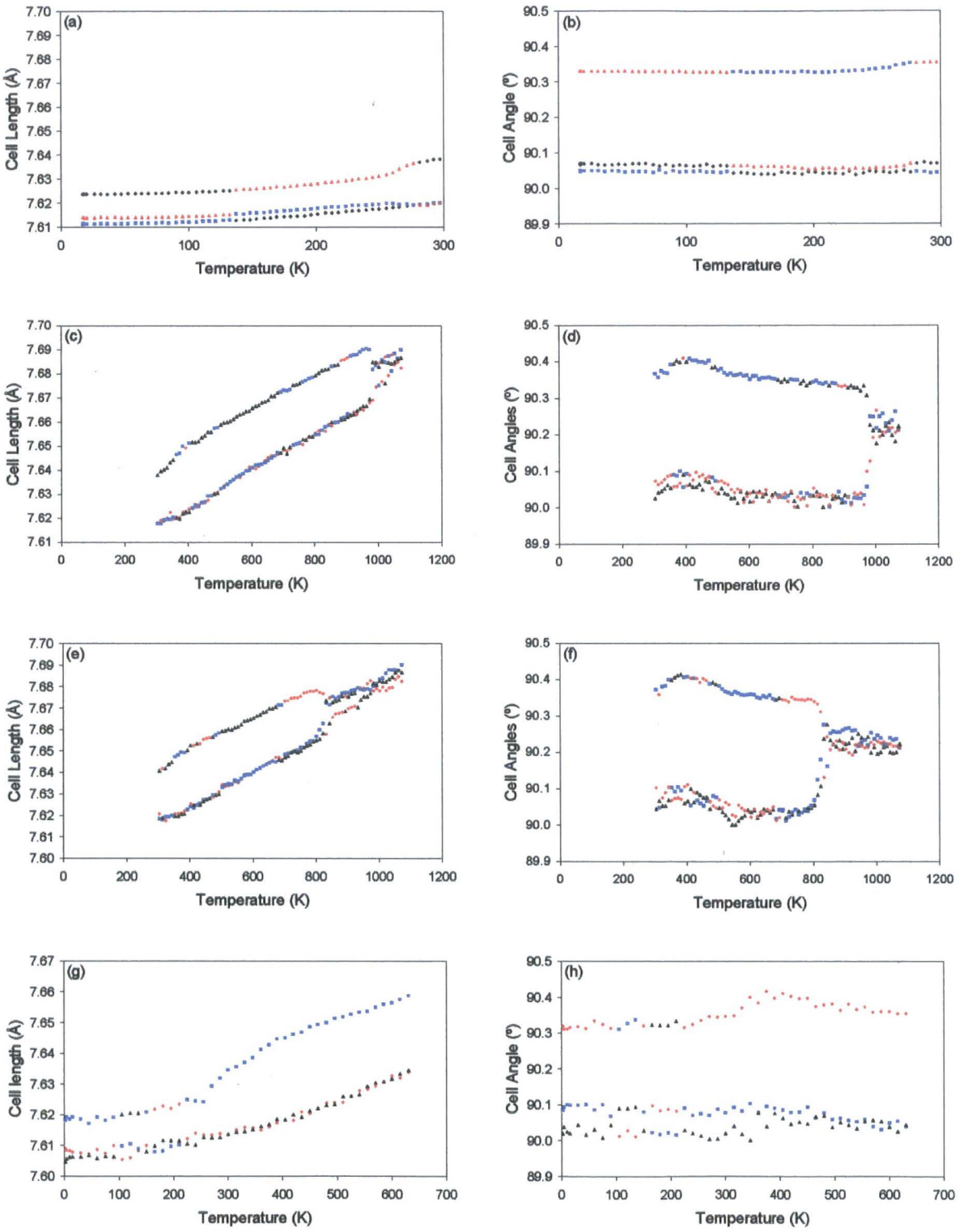

Figure 5-17: GeP_2O_7 subcell parameters. Low temperature X-ray data is shown in (a) & (b), the high temperature on warming (c) & (d) and on cooling (e) & (f) and neutron data (g) & (h). Cell length a & angle α are red diamonds, b & β are blue squares and c & γ are black triangles.

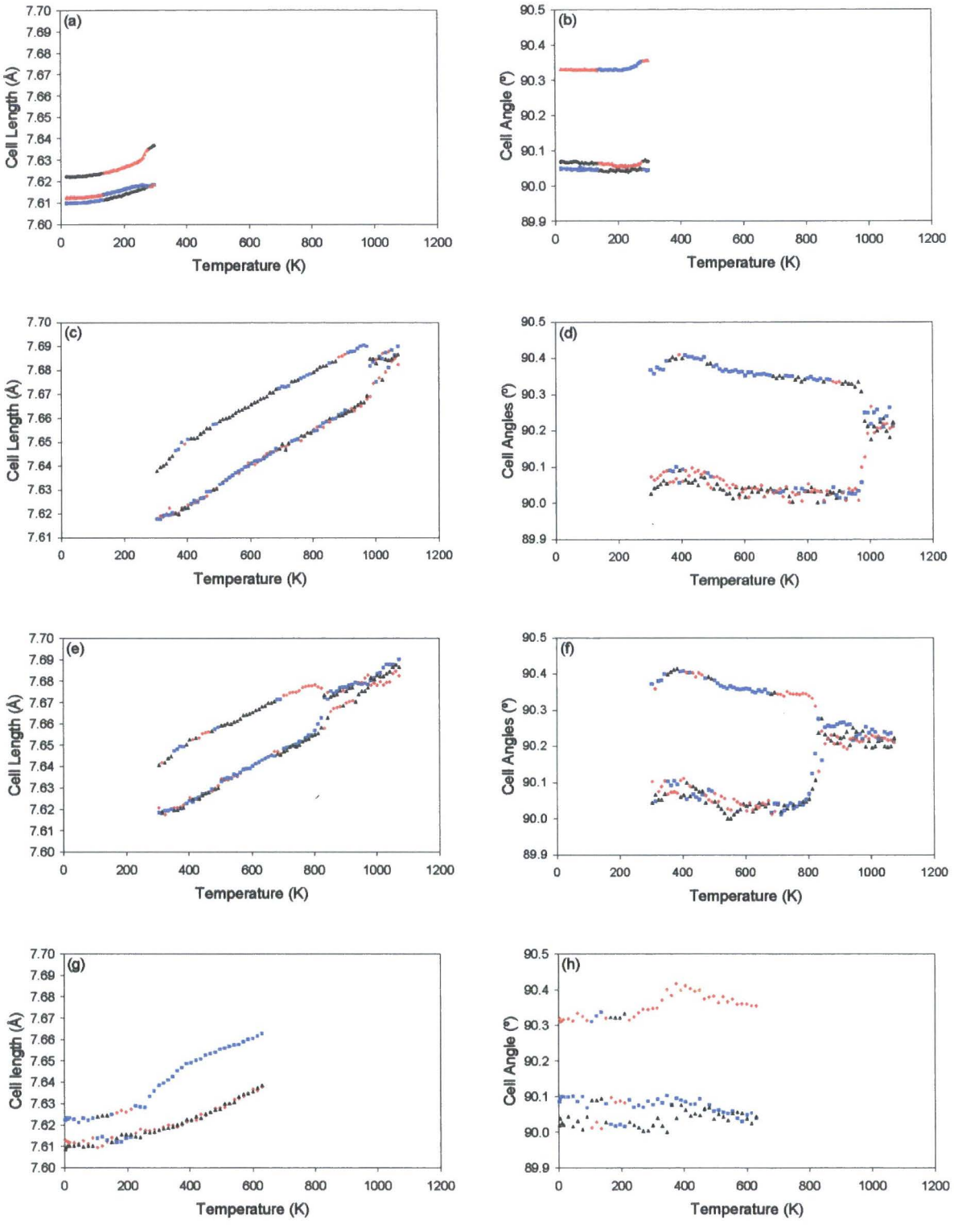

Figure 5-18: Repeat of the graphs shown in Figure 5-17, with all x axes on a 0 to 1200 K scale.

Three possible phase transitions appear in the data. The first occurs at approximately 265 K, with the largest cell parameter showing a significant increase in the rate of thermal expansion. There is also a more gradual increase in the thermal expansion of the other two axes. There is a second possible transition at approximately 550 K. This is the least clearly defined of the

transitions and can be most easily seen *via* the changing angles in graph d.

At 980 K there is clear transition on heating. Below this point the cell parameters suggest than all of the phases are either triclinic or monoclinic; all of the cells have non-90° angles, though two of the angles are always very close to 90°. Above this transition, all of the lengths and all of the angles become approximately equal, suggesting rhomobohedral symmetry. This is similar to the transition at 820 K for SnP_2O_7 in section 5.2. The transition shows substantial hysteresis, occurring at 850 K on cooling. None of the transitions show the substantial drop in thermal expansion associated with the supercell to subcell transitions found in other AM_2O_7 materials.

5.7. The Low Temperature Phase of GeP_2O_7

5.7.1. Symmetry Options

In order to better understand the GeP_2O_7 series of phases it was decided to model the lowest temperature phase first. Computational time constraints prevented serious attempts at producing structural models for the higher temperature phases. The methodology followed the same pattern as had been applied to the SnP_2O_7 work. No ^{31}P NMR had been published on this phase, Losilla *et al.* had however used NMR to deduce the RT structure had at least 35 phosphorus environments, suggesting either $P2_1$, Pc or $P2_1/a$ was the space group and unpublished work by Fayon suggests greater complexity than SnP_2O_7. The low temperature structure would probably be a lower symmetry distortion of the room temperature phase, suggesting either the space groups listed above or P1, since lower symmetry is not impossible. Pawley refinement was used to try and reach a conclusion on the space group.

5.7.2. Pawley Refinement

A series of controlled intensity Pawley refinements were carried out using the subcell peaks to help determine the correct symmetry of the long X-ray data set at 15 K. The results are shown in Figure 5-19. There is a smaller difference in the Rwp between best and worse results than was found for the two higher temperature phases of SnP_2O_7. This is due to the laboratory based diffraction equipment used giving broader peaks than the ESRF data. The refinements in P1 and $P2_1$ do give a better fit than the refinement in R3 and Pbca. This is confirms the 15 K phase has monoclinic or lower symmetry.

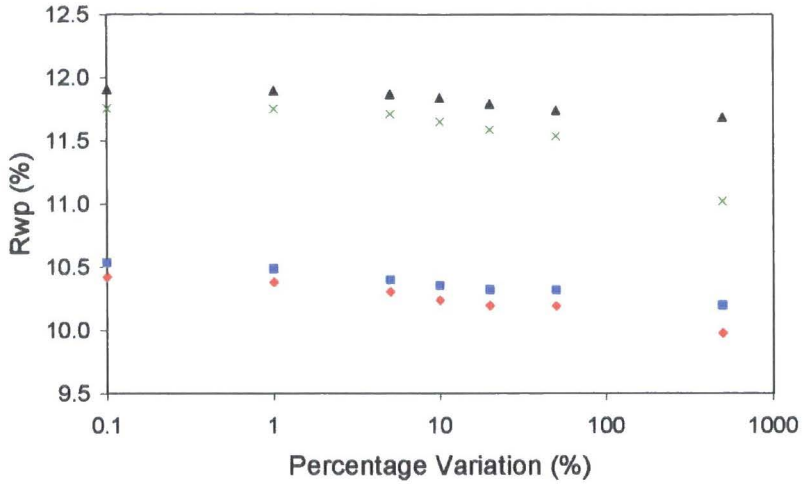

Figure 5-19: Plot to show the results of Pawley fitting with controlled intensities for the low temperature phase of GeP_2O_7. Red diamonds show the fit in Laue class $\bar{1}$, blue squares the fit in 2/m, black triangles $\bar{3}$ and green crosses 2/m 2/m 2/m.

5.7.3. Structure Solution

It was decided to attempt to solve the structure in P1 and all feasible monoclinic symmetries ($P2_1$, Pa and $P2_1/a$). The process of randomising, refining with constraints and then refining with restraints which had been used for SnP_2O_7 and ZrP_2O_7 was repeated here.

A total of 3282, 1659, 1658 and 844 parameters were refined for the structural solutions in P1, $P2_1$, Pa, and $P2_1/a$ respectively. Of these 3240, 1619, 1618 and 804 were for the x, y and z coordinates of atoms respectively. P1 has 6 refinable cell parameters, with the monoclinic symmetries only having one variable angle each, giving 4 refinable cell parameters.

In addition, 42 parameters were refined for all of the data sets. These consisted of 4 atomic displacement factors (1 each for all germanium and all phosphorus atoms, 1 for terminal and 1 for bridging oxygen atoms), 25 parameters for the X-ray data and 7 parameters for the neutron data. The X-ray data had an 15 term Chebychev polynomial to describe the background, 1 scale term, 6 terms of a TCHz pseudo-Voigt function to describe peak shape, 1 term to describe axial broadening, 1 absorption correction and 1 zero point correction. The 7 neutron parameters were a 6 term Chebychev background polynomial and 1 scale term. The results are shown in Figure 5-20. Of the 100 refinements carried out in P1, 27 had rwps under 8 % and are shown. The rest had not properly converged, with Rwps greater than 17 %.

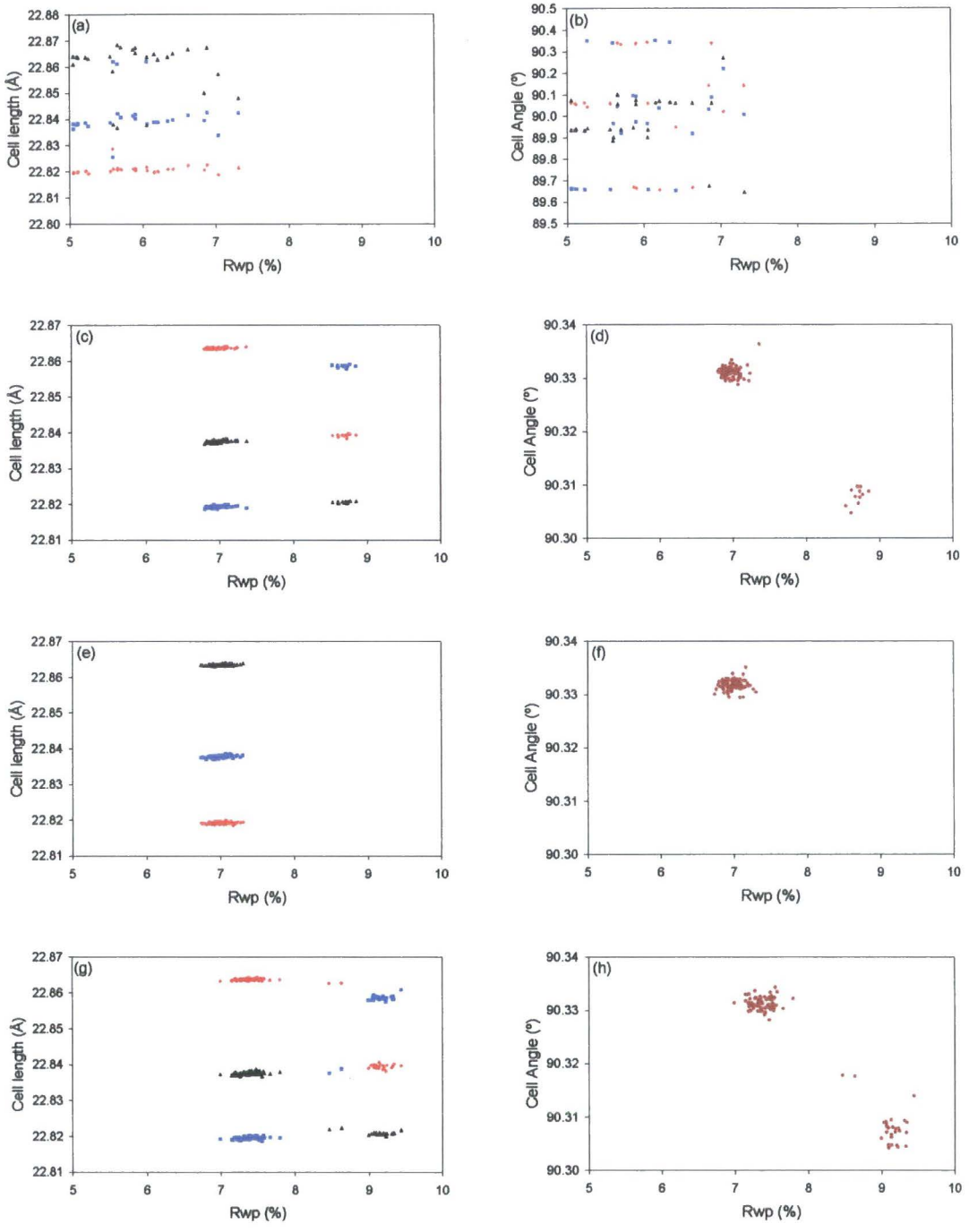

Figure 5-20: Plots showing the results of simulated annealing of the room temperature data of GeP_2O_7. (a) & (b) show refinements with P1 symmetry; (c) & (d) with Pa symmetry, (e) & (f) with $P2_1$ symmetry and (g) & (h) with $P2_1/a$ symmetry. Cell length a & angle α are red diamonds, b & β are blue squares and c & γ are black triangles. For the monoclinic cells, only the non-90° cell angles are shown.

The first point of note was that the best refinements in $P2_1$ were better than the refinements in Pa. As these two symmetries used effectively the same number of parameters, it could be stated that $P2_1$ definitely gave a better fit. To distinguish which of the other space groups were superior, statistical testing was required. The number of observations was still a matter

for some concern, but, unlike the SnP_2O_7 refinements, the number of hkl peaks was smaller than the number of data points. Therefore instead of using the number of data points and restraints, the number of hkl peaks was used instead. The results are shown in Table 5-6. It appears that the difference in Rwp between the P1 model and the monoclinic symmetries is significant.

Observations	Data Points			hkls		
Comparison of model A vs. B	$P2_1/a$ vs. $P2_1$	$P2_1/a$ vs. P1	$P2_1$ vs. P1	$P2_1/a$ vs. $P2_1$	$P2_1/a$ vs. P1	$P2_1$ vs. P1
Rwp of constrained model	6.98949	6.98949	6.736	6.98949	6.98949	6.736
Rwp of unconstrained model	6.736	5.05288	5.05288	6.736	5.05288	5.05288
observations, n	12389	12389	12389	10146	10146	10146
constrained parameters q	850	850	1668	850	850	1668
unconstrained parameters p	1668	3288	3288	1668	3288	3288
μ1 (p-q)	818	2438	1620	818	2438	1620
μ 2 (n-p)	10721	9101	9101	8478	6858	6858
F test value	1.005001	3.409821	4.366	0.794739	2.569449	3.289971
psi(F,nu1,nu2)=0.95 at	1.09	1.06	1.07	1.09	1.06	1.07
B significantly better than A	Unproven	TRUE	TRUE	Unproven	TRUE	TRUE

Table 5-6: Results of statistical analysis on the difference between the various structural models for GeP_2O_7. If the F value is greater than the column below, then the difference in the two models is greater than would be expected by chance.

5.8. Conclusion

The structures and phase transitions of SnP_2O_7 and GeP_2O_7 have been investigated. Two phase transitions were found in SnP_2O_7, at 525 and 820 K on heating and at 425 and 735 K on cooling. These matched the results found by Gover *et al.*[2] A full structure model has been produced for the room temperature phase of SnP_2O_7. This was shown to have $P2_1$ rather than Pa symmetry.

The results of the studies in to the higher temperature phases of SnP_2O_7 were less conclusive. The intermediate phase was shown to be either P1 or $P2_1/a$. It was not conclusive which of these two was correct, but the latter seemed more probable. The subcell peaks of the high temperature phase could be fitted with a R3 subcell model, but it proved impossible to index the supercell peaks. This suggests that the high temperature phase has some

differences from the 3 x 3 x 3 supercell normally found for these materials. Further investigation of these materials is required, probably *via* ^{31}P NMR

Two clear phase transitions were seen in GeP_2O_7, the first at 265 K, the second at 980 K on warming and 850 K on cooling. The lowest temperature phase of GeP_2O_7 appears to be P1 from the diffraction data; this is supported by the NMR work of Fayon. Both GeP_2O_7 and SnP_2O_7 have significantly lower symmetry for all their phases than the Pbca space group found for ZrP_2O_7. This, together with the difference in cation to unit cell size shown in section 1-11, suggests structural differences between the main group and transition metal pyrophosphates.

5.9. References

1 Huang C. H., Knop O., Othen D. A., Woodhams F. W., and Howie R. A., *Can. J. Chem.-Rev. Can. Chim.*, 1975, **53**, 79.

2 Gover R. K. B., Withers N. D., Allen S., Withers R. L., and Evans J. S. O., *J. Solid State Chem.*, 2002, **166**, 42.

3 Losilla E. R., Cabeza A., Bruque S., Aranda M. A. G., Sanz J., Iglesias J. E., and Alonso J. A., *J. Solid State Chem.*, 2001, **156**, 213.

4 Fayon F., King I. J., Harris R. K., Gover R. K. B., Evans J. S. O., and Massiot D., *Chem. Mat.*, 2003, **15**, 2234.

5 Brown I. D. and Altermatt D., *Acta Crystallogr., Sect. B: Struct. Sci.*, 1985, **B41**, 245.

6 Brese N.E. and O'Keefe M., *Acta Crystallogr., Sect. B: Struct. Sci.*, 1990, **B47**, 192.

7 Evans J. S. O., 'map_graham', Durham, 2005.

8 Shape Software, 'Atoms', Kingsport, TN, USA, 2002.

9 Pawley G. S., *J. Appl. Crystallogr.*, 1981, **14**, 357.

10 Wilson A. J. C., 'International Tables for Crystallography Volume C', Dordrecht/Boston/London, 1992.

11 Altomare A., Cascarano G., Giacovazzo C., Guagliardi A., Moliterni A. G. G., Burla M. C., and Polidori G., *J. Appl. Crystallogr.*, 1995, **28**, 738.

12 David W. I. F., *J. Appl. Crystallogr.*, 1999, **32**, 654.

13 Sivia D. S., *J. Appl. Crystallogr.*, 2000, **33**, 1295.

14 Coelho A. A., 'Topas - Academic', Karlsruhe, 2004.

15 Rodriguez-Carvajal J., 'Fullprof', Saclay, 2002.

6. Solid-State Solutions of Zirconium Tin Phosphate

The aim of this section of work was to synthesise and characterise a series of compounds of the general formal $Zr_xSn_{1-x}P_2O_7$. By studying the changing properties as the ratio of zirconium to tin varied, it was hoped to gain a greater understanding of the AM_2O_7 family. This mimicked other studies into mixed-cation AM_2O_7 materials, such as $Zr_xHf_{1-x}P_2O_7$[1] and $ZrV_xP_{1-x}O_7$.[2] Of particular interest was whether the change from the Pbca symmetry of ZrP_2O_7 to the $P2_1$ symmetry of SnP_2O_7 could be detected and if it could, whether it occurred *via* intermediate symmetries or as a single transition. Potential supercell to subcell transitions were also of interest.

6.1. Synthesis of $Zr_xSn_{1-x}P_2O_7$

The synthesis adopted was based on a method for making ZrP_2O_7 by King *et al.*[3] Compounds were synthesised from x = 0 to x = 1, with a step of x = 0.125. The amount of $SnCl_4 \cdot 5H_2O$ (Aldrich, 98 %) and $ZrOCl_2 \cdot 7.4H_2O$ shown in Table 6-1 were mixed with 1 cm^3 ($1.462*10^{-2}$ moles) of HP_3O_4. The water of crystallisation was determined *via* thermal gravimetric analysis. This method gave a 1:3 ratio of metal to phosphorus; an excess of phosphorus being used due to loss of phosphoric acid during heating.

The resulting material varied from a viscous liquid for the tin rich compounds to a tacky solid for the zirconium rich compounds. The mixture was either ground or stirred, depending on consistency, before being dried for 12 hours at 350°C. The resulting white solid was re-ground for 10 minute to ensure complete mixing. It was then heated twice, initially for 6 hours at 750°C (ramping at 5°C per minute to temperature), then for 12 hours at 1000°C (ramping at 10°C per minute). All of the compounds were fine, free flowing, white powders. X-ray diffraction showed no visible impurity peaks for any of the samples.

x	Mass of $SnCl_4 \cdot 5H_2O$	Moles of $SnCl_4 \cdot 5H_2O$	Mass of $ZrOCl_2 \cdot 7.4H_2O$	Moles of $ZrOCl_2 \cdot 7.4H_2O$
0	1.7064 g	$4.874*10^{-3}$	0 g	0 g
0.125	1.4931 g	$4.264*10^{-3}$	0.1897 g	$0.609*10^{-3}$
0.250	1.2798 g	$3.655*10^{-3}$	0.3794 g	$1.218*10^{-3}$
0.375	1.0665 g	$3.046*10^{-3}$	0.5691 g	$1.828*10^{-3}$
0.500	0.8532 g	$2.437*10^{-3}$	0.7587 g	$2.437*10^{-3}$
0.625	0.6399 g	$1.828*10^{-3}$	0.9485 g	$3.046*10^{-3}$
0.750	0.4266 g	$1.218*10^{-3}$	1.1382 g	$3.655*10^{-3}$
0.875	0.2133 g	$0.609*10^{-3}$	1.3279 g	$4.264*10^{-3}$
1.000	0 g	0 g	1.5174 g	$4.874*10^{-3}$

Table 6-1: Masses of $SnCl_4 \cdot 5H_2O$ and $ZrOCl_2 \cdot 7.4H_2O$ used for the desired $Zr_xSn_{1-x}P_2O_7$ materials.

6.2. Determining of Accurate Cell Parameters

The first stage of analysis was to determine accurate cell parameter at room temperature for the series. Silicon was added as a standard to the sample to increase the accuracy, as described in section 3.2.1. Due to the broad nature of the peaks (see section 6.3) and weak nature of the superstructure reflections, a simple cubic subcell model with spacegroup $Pa\bar{3}$ was used for the Rietveld refinement. The results are shown in Figure 6-1 and are tabulated in Table 6-2. The trendline is Length (Å) = 0.308 (Å/%) x Zr mole fraction (%) + 7.9445 (Å).

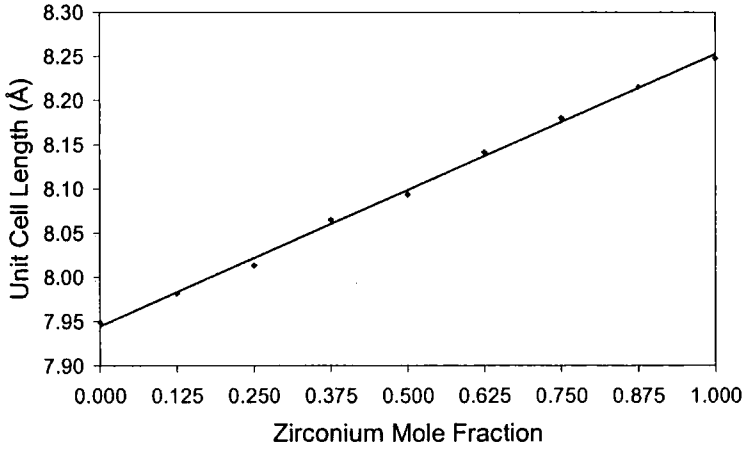

Figure 6-1: Graph to show the variation of cell parameter with changing zirconium/tin content at room temperature. The errors in cell parameters are plotted but are smaller than the point size.

Zr mole fraction (%)	Unit cell length (Å)
0.000	7.9487 (2)
0.125	7.9812 (3)
0.250	8.0132 (6)
0.375	8.0649 (8)
0.500	8.0932 (6)
0.625	8.1415 (4)
0.750	8.1802 (4)
0.875	8.2156 (2)
1.000	8.2478 (1)

Table 6-2: Unit cell parameters of the $Zr_xSn_{1-x}P_2O_7$ series.

The cell parameters found for SnP_2O_7 and ZrP_2O_7 were reasonably close to those found in the literature; which were 7.9444 (1)[4] and 8.2465 (3) Å[5] respectively. The general trend is a near-linear increase of subcell size with increasing zirconium content. Allowing for a small possible error in the Zr/Sn ratio for each of the samples, it is difficult to see any clear discontinuity in this pattern. Further investigation is required to determine whether structural changes occur across the series.

6.3. Variation in Size and Strain Broadening in the Zirconium Tin Phosphate Series

6.3.1. Introduction to Size/Strain Analysis

The diffraction patterns of the $Zr_xSn_{1-x}P_2O_7$ series have significantly broader peaks where x ~ 0.5, compared to x = 0 or 1. This is shown in Figure 6-2. The instrumental broadening effects should be the same for all samples, therefore broadening must be caused by either small crystallite size or significant microstrain in the samples. This also means that it is extremely difficult to determine any peak splitting caused by distortion of the unit cell away from cubic symmetry for the intermediate members.

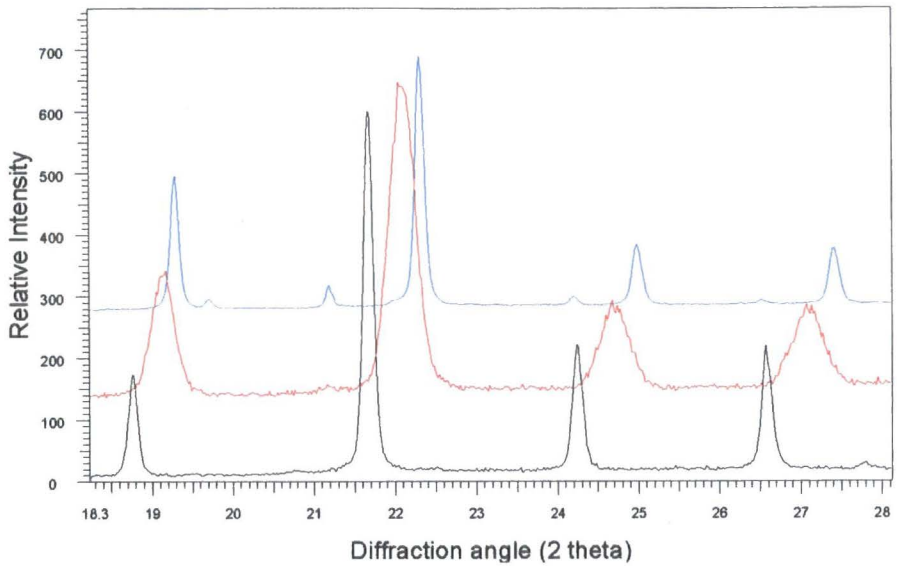

Figure 6-2: Plot showing the variation in peak width as a function of x in $Zr_xSn_{1-x}P_2O_7$. x = 1 is the lowest pattern in black, x = 0.5 is the central pattern in red and x = 0 is the highest pattern in blue. Note peaks have been scaled to give comparable peak heights.

The increase of peak width with decreasing crystallite size was first noted by Scherrer.[6] This led to the Scherrer equation, shown in Equation 6-1, where λ is the wavelength, θ the Bragg angle and β is the increase in FWHM of the peaks due to crystallite size. The term ε is an "apparent crystallite size", a function of the true crystallite size and hkl of the peak used for its determination

$$\beta = \lambda / \varepsilon \cos\theta \qquad \text{Equation 6-1}$$

A more useful version of the Scherrer equation is shown in Equation 6-2. The term k is the Scherrer constant which is dependent on the shape of the crystallite and normally set to 1, though it can be theoretical varied between 1 and 0.87. This allows the calculation of the mean column height, L_{vol}. A crystallite can be thought of as being divided into a series of columns perpendicular to the diffracting beam. The average of the lengths of these columns is the mean column height. As the scattering power of a column is dependent on its volume, the resulting mean column height is weighted by volume. Assuming a spherical particle shape, the diameter, L_o, can be calculated using Equation 6-3.

$$\beta = k\lambda / L_{vol} \cos\theta \qquad \text{Equation 6-2}$$

$$L_0 = 4L_{vol} / 3 \qquad \text{Equation 6-3}$$

Strain broadening occurs due to individual unit cells having slight differences, causing them to have subtly different sizes. These differences can be dislocations in the structure or, as in this case, different atoms occupying the same site in different unit cells. In this example, individual unit cells for the mixed metal phosphates will contain different ratios of the zirconium and tin ions. The two ions here have radii of 0.72 Å and 0.69 Å (+4, 6-coordinate Shannon & Prewitt

radii) for zirconium and tin respectively.[7] Therefore, individual unit cells containing more zirconium than average are likely to be larger than those which are tin rich.

The strain was modelled in terms of the microstrain, the maximum strain in the system between the largest and the smallest unit cells. The maximum strain can be calculated from peak broadening using Equation 6-4, where e is the microstrain and β_D is the increase in integral breadth of the peak due to microstrain. Equations 6-3 & 6-4 show it is possible to separate the effects of size and strain broadening due to their different dependence on diffraction angle.

$$\beta_D = 4e \tan\theta \qquad \text{Equation 6-4}$$

Rietveld refinements were carried out using TOPAS academic to determine the crystallite size and strain. TOPAS uses the double-Voigt method as described by Balzar *et al.*[8] amongst others. This is based on using a standard material, of theoretically infinite crystallite size and zero strain, to determine the instrumental peak shape. The peak shape parameters are then fixed at these values during Rietveld refinement, and additional terms introduced to account for sample size and strain broadening. The experimentally observed peaks are therefore fitted by a Voigt function which is a convolution of a Voigt function from the instrumental broadening and a second Voigt function from the size and strain broadening. The instrumental broadening of the diffractometer used in these experiments was determined by running a sample of CeO_2, carefully annealed to increase the crystallite size, to obtain a theoretically size and strain free peak shape. The diffractometer slit set-up for the standard measurements matched those used for the samples. As no material has an infinite crystallite size and some strain will always be present, the standard material will show some size and strain broadening, although size broadening is minimal for crystallites above 200nm. This will lead to a small overestimate crystallite size and an underestimate of strain in the actual sample.

Following the methodology of Balzar *et al.* the TOPAS academic macro 'e0_from_Strain' was used to calculate the strain. This calculates both the Gaussian and Lorentzian strain broadening and uses these two values to calculate the microstrain. Similarly the macro 'LVol_FWHM_CS_G_L' was used to calculate the crystallite size. This again refines the values of Gaussian and Lorentzian broadening and from them derives the volume weighted mean column height.[9] Tests[10] confirm that this method reproduces particle sizes and strains as published in the IUCR round robin.[11]

6.3.2. Rietveld Refinement of the Data

Four sets of Rietveld refinement were carried out. The first was with freely refining peak shapes with no size or strain terms. The second used a fixed peak shape from the standard and size broadening only. The third used strain broadening only and the fourth models both

size and strain broadening.

6.3.3. Free Refinement of the Peak Shape

All nine data sets with values of x = 0, 0.125, 0.25, 0.375, 0.5, 0.625, 0.75, 0.875 and 1 were refined independently. Due to the broad nature of the peaks and weak nature of the superstructure reflections, a simple cubic subcell model with $Pa\bar{3}$ symmetry was used. 32 parameters were refined, these consisted of 18 terms of a Chebychev polynomial to describe the background, a TCHz pseudo-Voigt model for peak shape with all 6 of the terms refined, one cell length, 4 isotropic atomic displacement parameters, (one for the Zr/Sn site, and 1 each for the P, $O_{bridging}$ & O_{AM} atoms), 1 term for the position of the P atom along the 3-fold axis, 1 scale and 1 sample height correction. This gave Rwps for the 9 refinements between 8.56 and 11.33 %, with an average of 10.26 %. An overview of the quality of fit for all the refinements is shown in Figure 6-6.

6.3.4. Refinement using a fixed peak shape with only size broadening

In the second series of refinements the peak shape values were fixed to those obtained from the CeO_2 standard, and the size broadening macro added. 28 parameters were refined, including all of those from section 6.3.3 except the 6 peak shape terms, with two additional terms for the Gaussian and Lorentzian contributions to size broadening.

The quality of fit was significantly worse than in the previous section, with Rwps between 9.87 % and 16.66 %, with an average of 13.59 %. This is exemplified in Figure 6-2. The low angle peaks are too broad and the high angle peaks are too narrow.

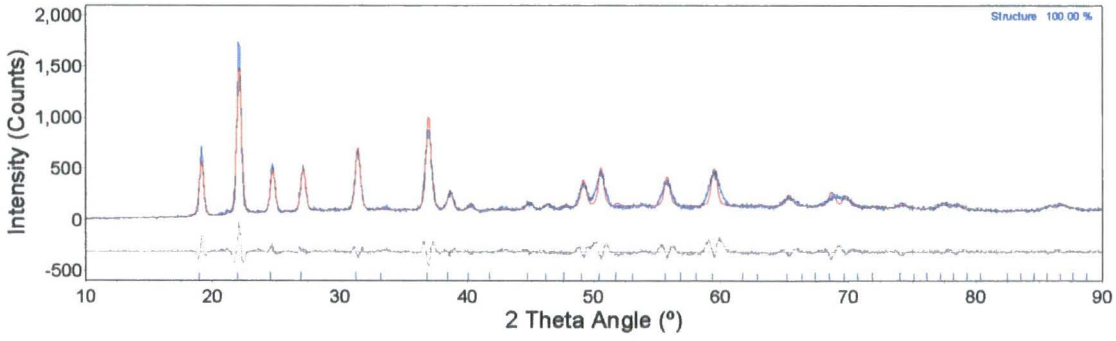

Figure 6-3: Fit of the data for $Zr_{0.5}Sn_{0.5}P_2O_7$ using only size broadening. The experimental data is in blue and the theoretical model is in red. The difference is in grey and the blue tick marks show hkl positions.

6.3.5. Refinement using a fixed peak shape with only strain broadening

The experiment from the previous section was repeated with the macro for size broadening replaced by the macro for strain broadening. Again 28 parameters were refined, with the two crystallite size terms being replaced by Gaussian and Lorentzian strain broadening

contributions. The quality of fit was significantly better than using only size broadening, with rwps between 9.01 % and 11.81 %, with an average of 10.48 %. The improvement can be seen in Figure 6-4. This was still slightly worse than a free peak shape refinement. The improved fit when using strain rather than size broadening suggests that most of the broadening is due to strain.

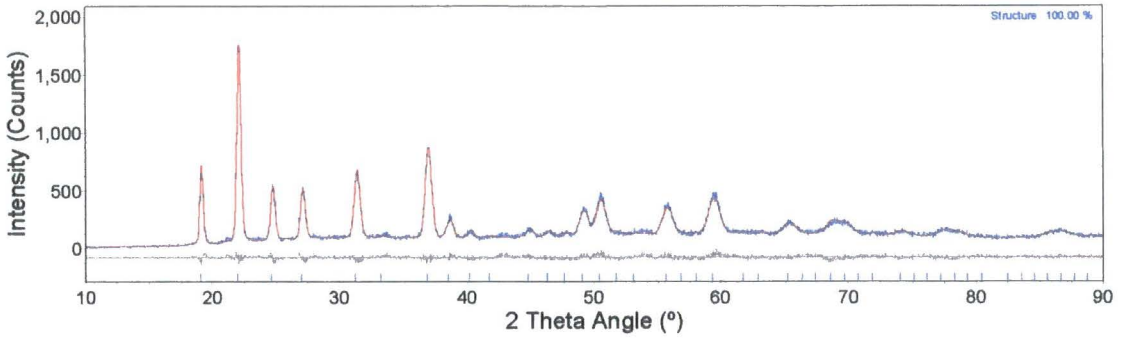

Figure 6-4: Fit of the data for $Zr_{0.5}Sn_{0.5}P_2O_7$ using only strain broadening. The experimental data is in blue and the theoretical model is in red. The difference is in grey and the blue tick marks show hkl positions.

6.3.6. Refinement using both size and strain broadening

The refinement was repeated using both size and strain contributions to broadening, giving a total of 30 parameters. The quality of fit was comparable to the free refinement, with Rwps between 8.86 % and 11.38 %, with an average of 10.36 %. The quality of fit for $Zr_{0.5}Sn_{0.5}P_2O_7$ is shown in Figure 6-5. The variation in crystallite size and strain with x is shown in Figure 6-7. The size proved difficult to determine accurately, as the relatively large crystallites gave a small amount of broadening, which was obscured by the more significant strain broadening. The microstrain was fairly low for the species at each end of the series, rising to a maximum at x = 0.375.

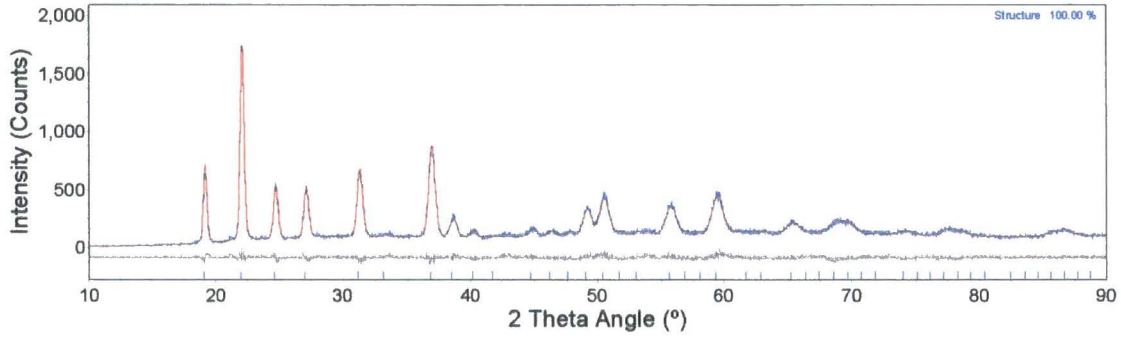

Figure 6-5: Fit of the data for $Zr_{0.5}Sn_{0.5}P_2O_7$ using size and strain broadening. The experimental data is in blue and the theoretical model is in red. The difference is in grey and the blue tick marks show hkl positions.

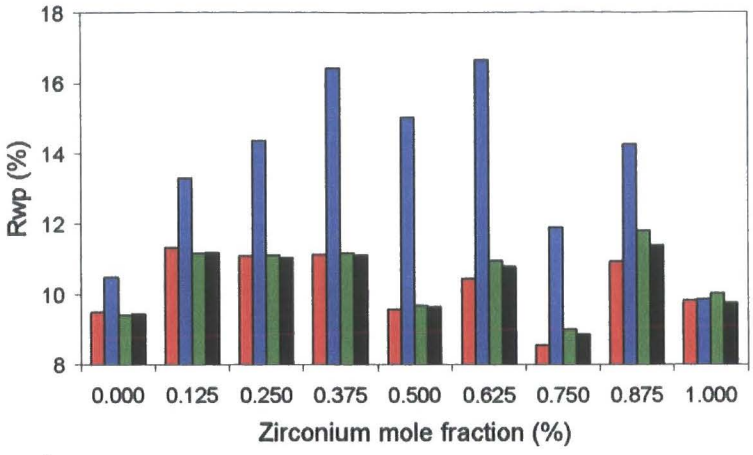

Figure 6-6: Plot showing the variation in Rwp between the various types of refinement. Data from the free refinement are in red, with size broadening only in blue, strain broadening only in green and size and strain broadening in black.

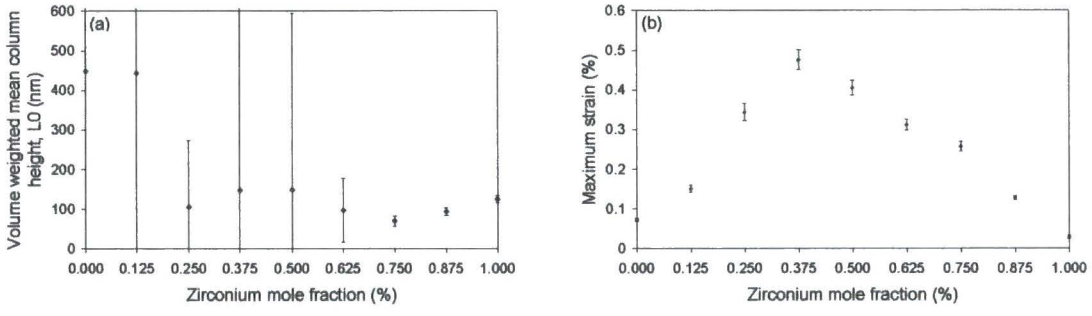

Figure 6-7: (a) shows the variation in crystallite size with composition and (b) shows the variation in microstrain with composition.

6.3.7. Conclusion

The particle size and microstrain has been calculated for the series of compounds $Zr_xSn_{1-x}P_2O_7$. As expected from the pattern of peak broadenings the microstrain increased for the compounds towards the centre of the range. There was also a possible minor decrease in crystallite size, but given the difficulties in determining these values when the particle size is relatively large and the strain high, no firm conclusions can be drawn. There was an improvement in fit when only strain broadening was used compared to using only size broadening. This suggested that strain has far more effect on peak shape than size for these materials.

6.4. Variable Temperature Measurements of $Zr_xSn_{1-x}P_2O_7$

One of the main objectives in this work was to see whether any phase transitions occurred to the series upon heating, particularly if any of the materials changed to a low thermal expansion phase like the high temperature phase of ZrP_2O_7. To do this a series of VT X-ray diffraction measurements were carried out. It would also enable the rate of thermal expansion to be determined for this series of compounds, showing whether the solid solutions varied

significantly in this respect from the parent compounds.

6.4.1. Variable Temperature Data collection

Data were collected using a Bruker d8, fitted with a HTK1200 furnace, as discussed in section 2.3.3. The first three compounds to be synthesised (x = 0.25, 0.50 and 0.75) were scanned every 15 K on warming from 303 K to 1173 K and then on cooling back to 303 K, with 20 minute data collections. On measuring the second batch of compounds, the first two tested (x = 0.875 and 0.625) decomposed at high temperature into ZrP_2O_7 and some other minor products (presumably tin containing) which could not be identified. The reason why these two compounds broke down at high temperature whilst the first set of materials, particularly x = 0.75, could not be determined. Therefore these compounds were only measured up to 1003 K.

6.4.2. Data Analysis

The lack of clear splitting, together with the broadening effects caused by strain, made it unlikely that accurate details of the distortion of cell parameters away from cubic could be obtained for these materials. It was therefore decided to use the $Pa\bar{3}$ subcell model for the refinement of the VT data, with the addition of size and strain terms to describe peak broadening. This methpd would hopefully enable the determination of temperatures where there were changes in the peak splitting pattern, or apparent size and strain, highlighting any phase transitions. In order to use a single peak shape for all of the data sets from a single compound, the parametric Rietveld refinement technique developed in chapter 3 was adopted. This method of refinement was initially tested using the data collected in section 3.2 (scan d8_02968), which consisted of measurements on ZrP_2O_7 mixed with Si and Al_2O_3. The results are shown in Figure 6-8.

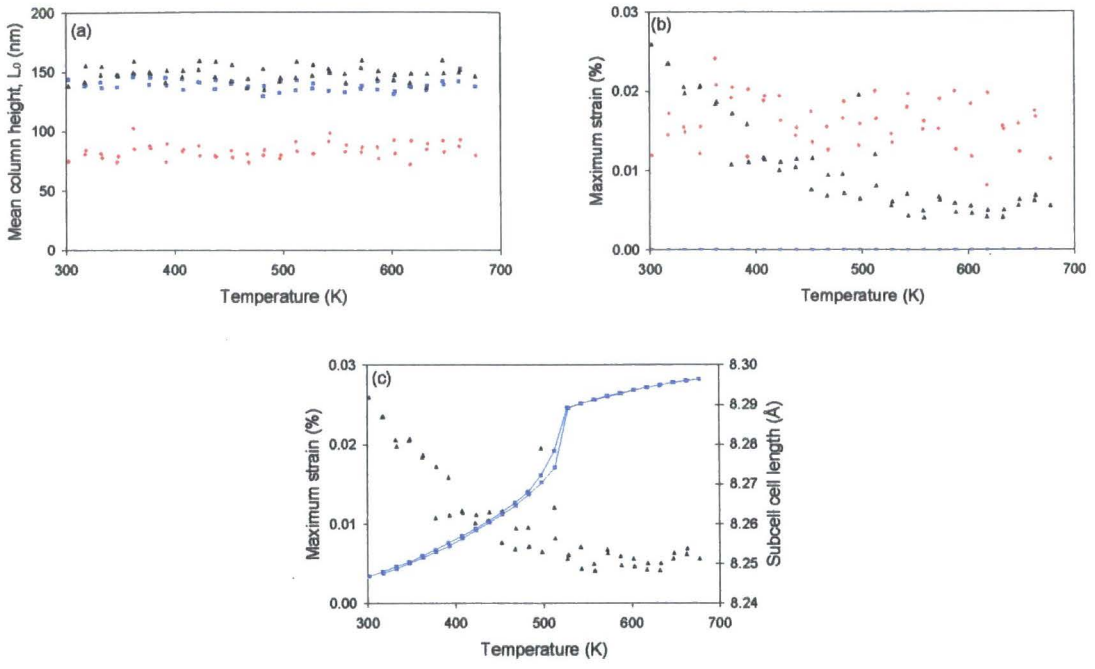

Figure 6-8: Plots showing the results of size/strain analysis of variable temperature data of a mixture of ZrP_2O_7, Si and Al_2O_3. (a) shows the variation in crystallite size with Si as blue squares, Al_2O_3 as red diamonds and ZrP_2O_7 as black triangles. (b) shows the variation in strain, with the same symbols as (a). (c) shows the variation in strain for ZrP_2O_7 (black triangles), alongside the cell length to highlight the phase transition.

Data of Figure 6-8 (a) & (b) show two important effects. Firstly there are no significant changes in refined crystallite size with temperature. This suggests that the peak shape changes due to sample height movement are insignificant. It also suggests that when using parametric Rietveld refinement a single overall sample size can be refined. Secondly the microstrain for Si and Al_2O_3 standards are essentially temperature independent, though the latter demonstrated some scatter. This suggested that there was no significant correlation between strain and the variation of instrumental parameters with temperature. Therefore the change in strain in ZrP_2O_7 can be assumed to be reflecting changes in the sample.

The apparent strain in ZrP_2O_7 decreases up to the orthorhombic supercell to cubic subcell phase transition. As the structure moves towards cubic symmetry, the difference in cell lengths decreases and numerically equivalent hkl peaks move closer together. This has the effect of narrowing the peaks in the diffraction pattern, which consist of several overlapping hkls. This narrowing of the peaks means that the strain term fitting this broadening decreases. Once the structure becomes cubic, the numerically equivalent hkls become crystallographically equivalent and therefore this narrowing effect stops. The two anomalously high points at the phase transition are both from the cooling data. This corresponds to the region where hysteresis occurs and is probably due to both high and low temperature structures being present at the same time or the incommensurate phase as reported Withers *et al.*[12]

For surface fitting VT data on each member of the series, 7 overall parameters were used. These were 1 term to model axial broadening, 4 terms of TCHz pseudo-Voigt function to model peak shape, (the x and z parameters were fixed) and 1 term each for the Gaussian and Lorentzian peak broadening due to crystallite size. 28 parameters were refined for each data set; these were 18 terms of a Chebychev polynomial to model the background, 1 scale, 1 cell length, 4 isotropic atomic displacement parameters (one for the Zr/Sn site, and 1 each for the P, $O_{bridging}$ & O_{AM} atoms), 1 sample displacement parameter and 2 terms to model the Gaussian and Lorentzian broadening caused by strain. The two strain terms in the first range were fixed to those values calculated in section 6.3. This reduces correlations between strain terms and coefficients of the peak shape function. In essence this procedure transfers the well determined room temperature strain information from the d9 measurements in section 6.3 to the d8 VT data. This gave 2693 parameters for x = 0.125, 0.375, 0.625 and 0.875 (which had 96 ranges), 3364 parameters for x = 0.25, 0.50 and 0.75 (120 ranges), 4931 parameters for SnP_2O_7 (176 ranges) and 1405 parameters for ZrP_2O_7 (50 ranges).

For materials showing second-order phase transitions the temperature dependence of thermal expansion data can provide a clearer indication of structural changes than looking directly at cell length changes (cell vs. T showing a change of slope, α vs. T a discontinuity). For these data, standard deviations of individual cell parameters made it difficult to calculate the rate of thermal expansion without smoothing the data. The raw cell parameters where therefore fitted with a Bezier function using gnuplot[13], as shown in Figure 6-10. For the middle members of the series, a single function provided a believable smoothing pattern. For x = 1, 0.875 and 0, the Bezier curves departed significantly from the data at the phase transitions. A more realistic smoothing was achieved by modelling with different functions either side of the phase transition, requiring 2, 2 and 3 Bezier functions respectively. This is demonstrated for $Zr_{0.875}Sn_{0.125}P_2O_7$ in Figure 6-9. The two lines overlapped, but the overlapping points were removed from the final analysis. These smoothed cell parameters from gnuplot were then differentiated numerically to obtain the rate of thermal expansion using the Fortran program alpha.[14]

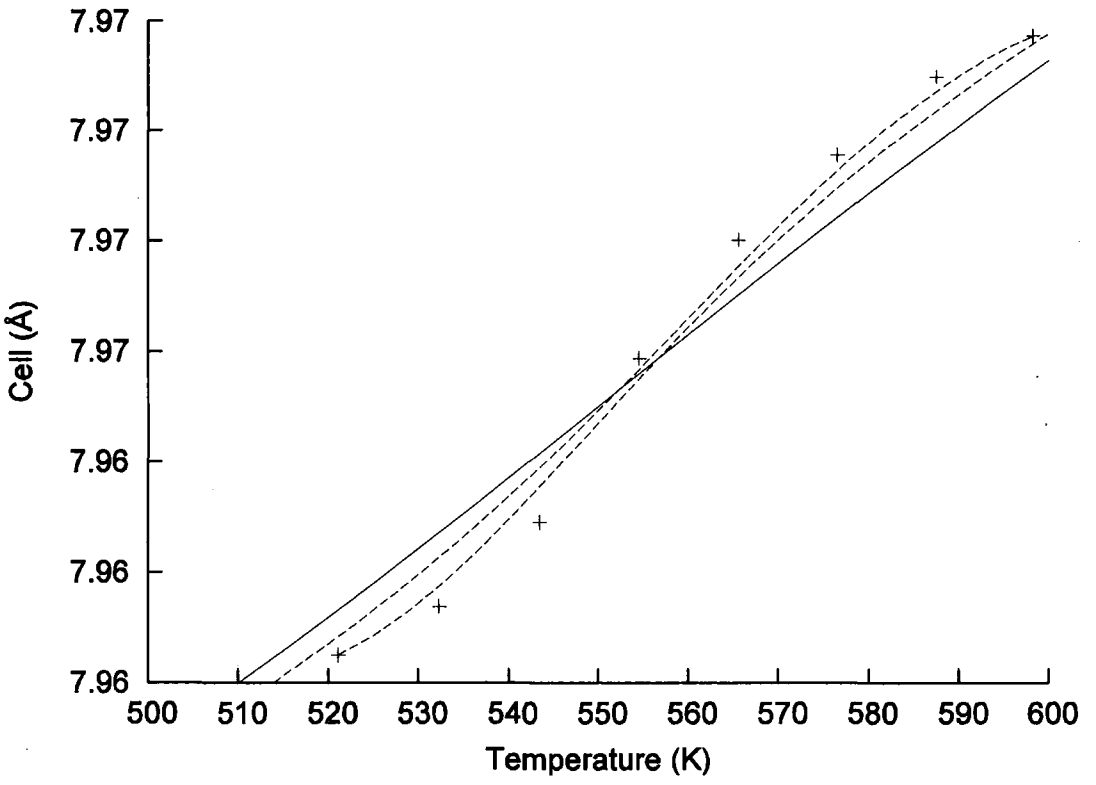

Figure 6-9: Graph showing the need for using more than one Bezier curve where clear phase transitions are present. Crosses show actual data points, the solid line is the result of fitting a single Bezier curve and the dotted lines the result of using two Bezier curves.

6.4.3. Graphical Results

Since this series of experiments involves a large number of data sets (969 Rietveld refinements), involving 28250 parameters in total, key experimental quantities (cell, relative expansion, alpha and apparent strain) are presented graphically over the next 4 pages. The cubic subcell lengths are shown in Figure 6-10; the cell lengths divided by the room temperature lengths are shown in Figure 6-11; the rates of thermal expansion are shown in Figure 6-12 and the variation of strain is shown in Figure 6-13. For the graphs which show all of the series members together the symbols are; '+' for x = 1, 'x' for x = 0.875, '*' for x = 0.75, '□' for x = 0.625, '■' for x = 0.5, '○' for x = 0.375, '●' for x = 0.25, 'Δ' for x = 0.125 and '▲' for x = 0. Although size and strain analysis was only carried out on a relatively short temperature range of ZrP_2O_7, the very short data sets from section 3.2.8 could be used for thermal expansion calculations.

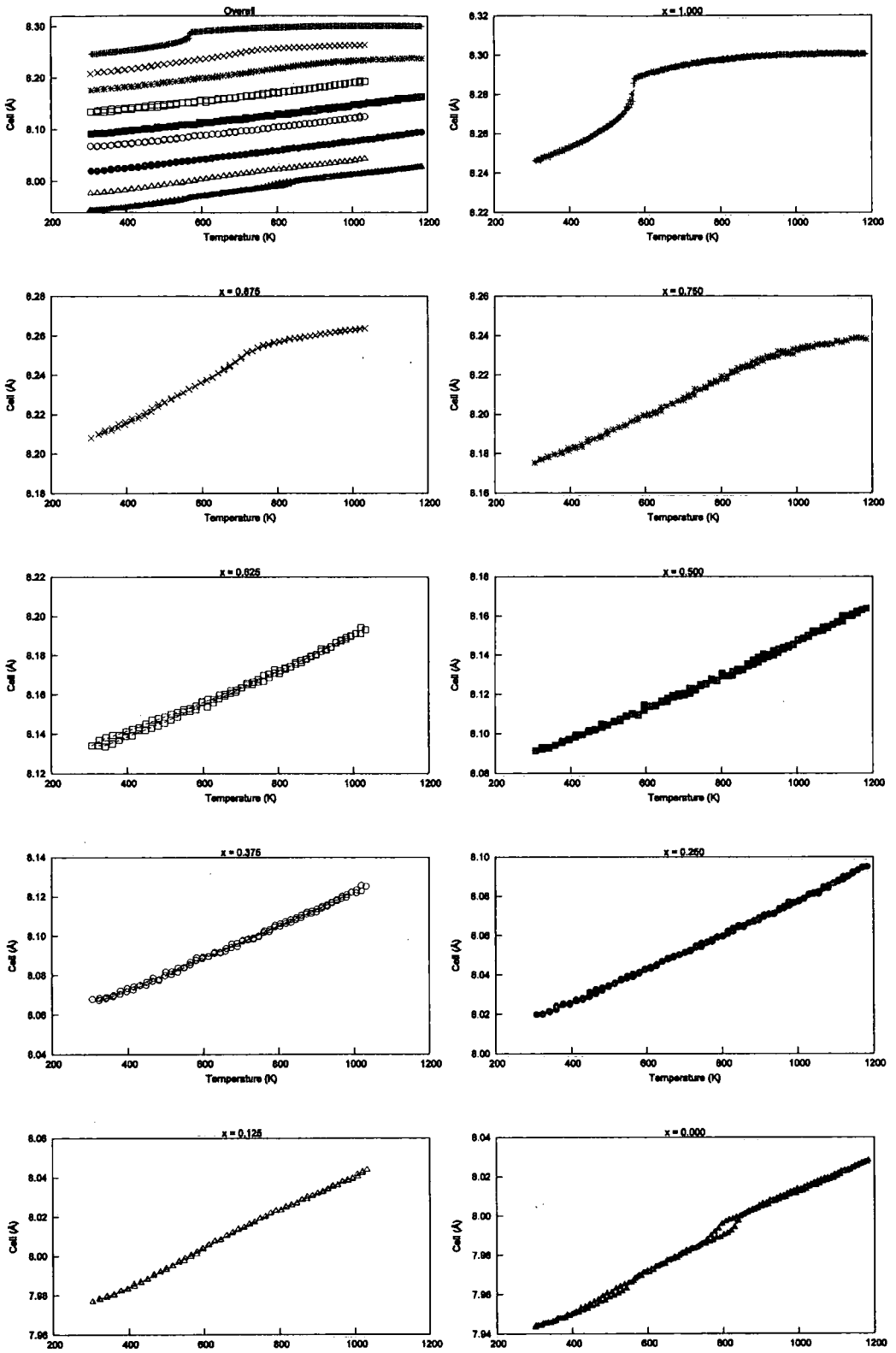

Figure 6-10: Graphs showing the variation in cell parameters with temperature for the $Zr_xSn_{1-x}P_2O_7$ series. Crosses show the cell parameters from Rietveld refinement and dotted lines show Bezier curves fitted through the data. The overall graph shows the results of x = 0 at the bottom, sequentially increasing to x = 1 at the top.

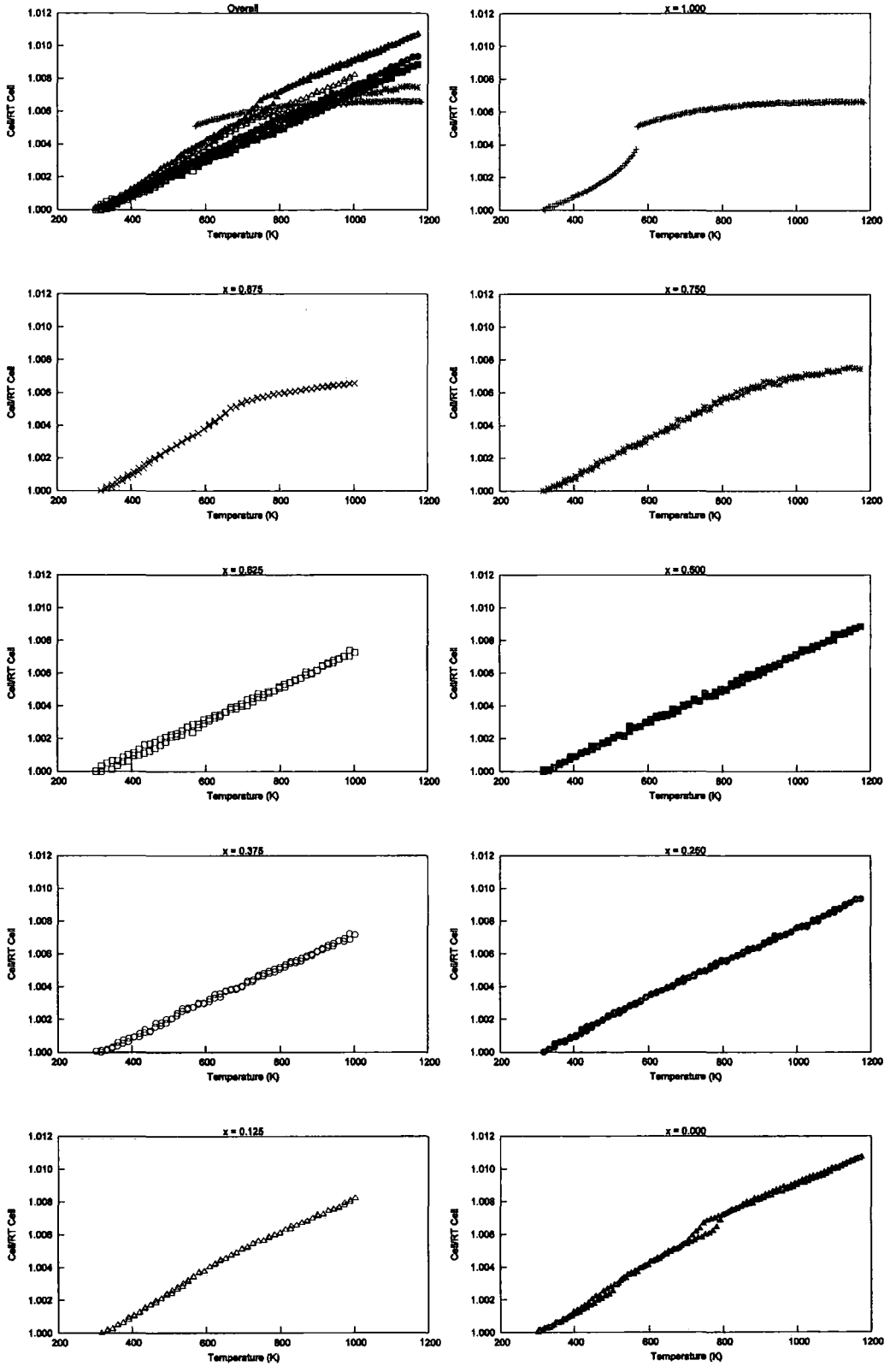

Figure 6-11: Graphs showing the relative expansion $a/a_{293\,K}$ for the $Zr_xSn_{1-x}P_2O_7$ series. Crosses show the cell parameters from Rietveld refinement divided by the RT cell. The overall graph is intended to show the similarly in thermal expansion between all members of the series, excluding the high temperature phases of x = 1, 0.875 and 0.75.

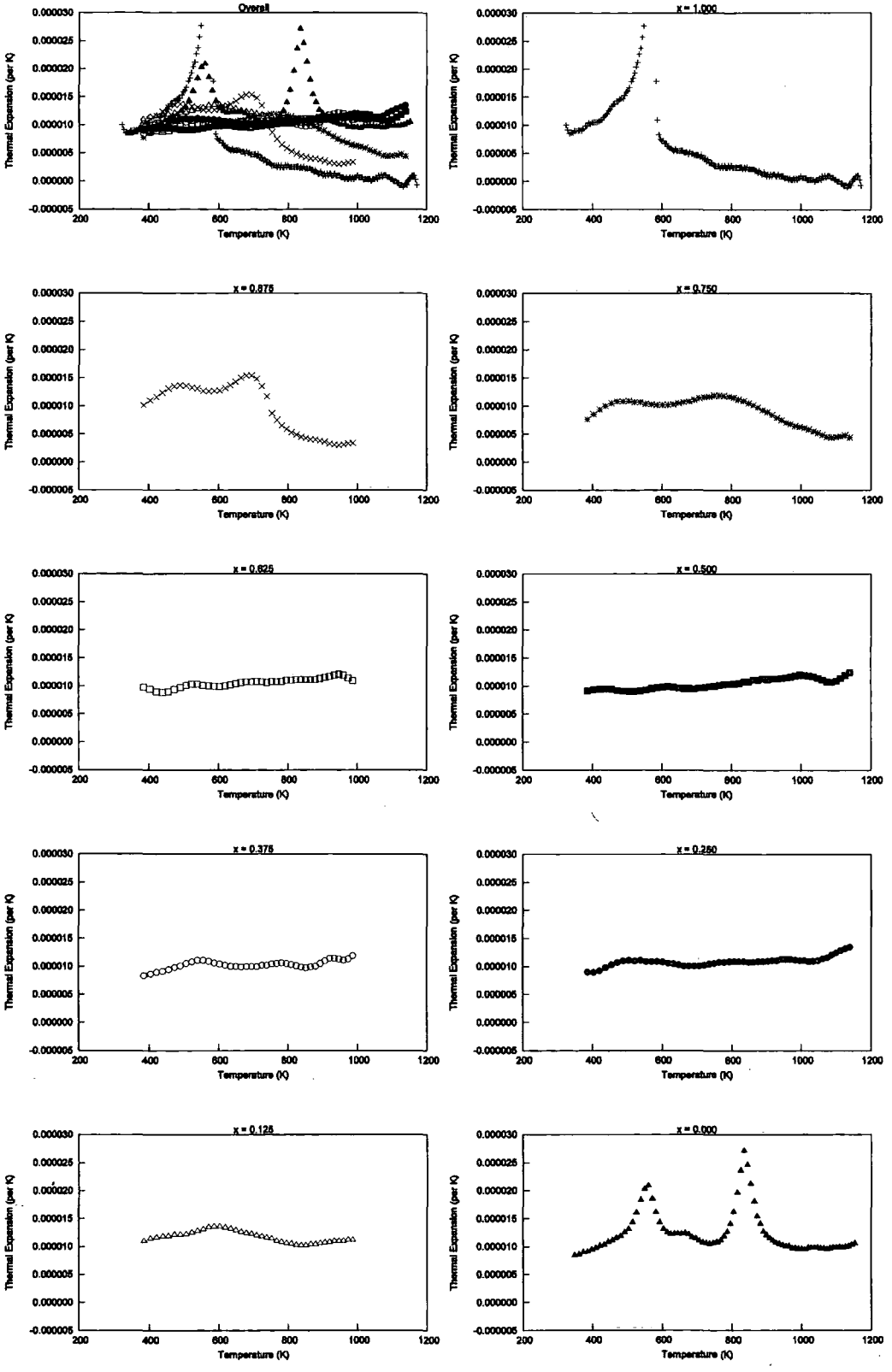

Figure 6-12: Graphs showing the rate of thermal expansion for the $Zr_xSn_{1-x}P_2O_7$ series. Note the thermal expansion of ZrP_2O_7 and SnP_2O_7 jump to high values at the phase transitions as expected for first-order transitions ($\infty$for an ideal system/ experiment). Data are shown for warming only.

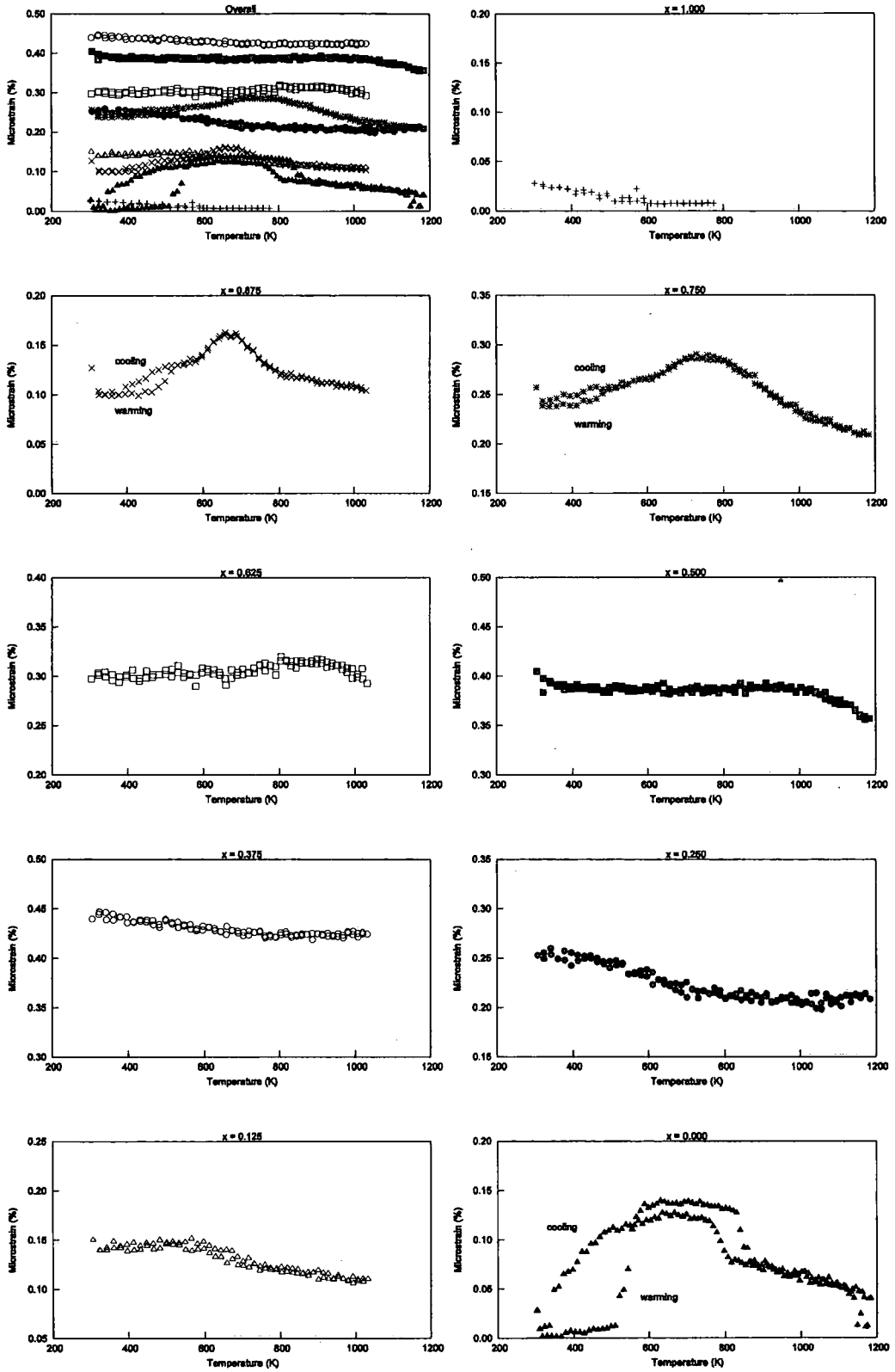

Figure 6-13: Graphs to show the variation in microstrain with temperature and composition. All plots have an identical range on x-axis.

6.4.4. Overall results

The series $Zr_xSn_{1-x}P_2O_7$ appeared to show three different regions according to the variation of cell parameter with temperature. The discussion of the results shown in section 6.4.3 has therefore been broken into three sections, x = 1.000 to 0.750, x = 0.625 to 0.250 and x = 0.125 to 0.000. All of the compounds showed very similar rates of thermal expansion, between 1 x 10^{-5} and 1.5 x 10^{-5} K^{-1}, except for the high temperature phase of the three most zirconium rich compounds and during the phase transitions of the SnP_2O_7. An overview of the results is given in Figure 6-14.

6.4.5. x = 1.0 to 0.75 – Zirconium Rich Phases

The cell parameter data for the three compounds from x = 1 to 0.75 all show a transition from a region with thermal expansion of approximately 1 x 10^{-5} K^{-1} to a significantly lower value. This transition occurs at lower temperature with increasing zirconium content, occurring at 951 K (x = 0.75), 747 K (x = 0.875) and 568 K (x = 1). For ZrP_2O_7 this has been identified as a transition from a 3 x 3 x 3 supercell with Pbca symmetry to a $Pa\bar{3}$ subcell.[2] Given the similarly of the thermal expansion data it is hypothesised that the transitions occurring in the x = 0.875 and 0.75 data are also supercell to subcell transitions. The transition also becomes sharper with increasing zirconium content. ZrP_2O_7 shows a sudden, first-order style change from the low to the high temperature phase, with more gradual changes for the tin containing compounds.

As discussed in section 6.4.2, ZrP_2O_7 shows a steady decrease in strain with increasing temperature, until the phase transition, where it becomes approximately constant. Both x = 0.875 and 0.75 members show similar behaviour in strain with temperature. Both appear to show two plateaus on warming from ~ 300 to ~ 450 then from ~ 500 – 600 K. It is possible that this is indicative of further phase transitions around these temperature regions (see discussion for SnP_2O_7 in section 6.4.7). Significant differences are observed between heating and cooling experiments, again suggestive of hysteresis. These changes are not seen in the pure zirconium compound, but it is possible that they mimic changes occurring below room temperature due to the general shift in phase transitions to lower temperature with increasing zirconium content. Above this temperature the two mixed compounds mimic the pure zirconium compound with a steady decrease in strain up to the probable supercell-subcell transition, followed by a region of more slowly decreasing strain.

6.4.6. x = 0.625 to 0.25 – Intermediate Phases

There is significantly less variation in thermal expansion and strain of the compounds in the middle of the series. The rate of thermal expansion for all members is around 10^{-5} K^{-1} at room temperature, rising slightly with temperature. There is some evidence of phase transitions, shown by variation strain at ~ 700 K and ~ 650 K for x = 0.25 and 0.375 respectively. Given

the broadening of the phase transition caused by the mixture of cations in the x = 0.875 and 0.75 compounds, it is possible that several changes are occurring in this region which are undetectable by analysis of the subcell peaks. Better data, clearly showing the supercell peaks, might contain more information.

6.4.7. x = 0.125 to 0 – Tin Rich Phases

Both of these tin-rich compounds show three distinct regions in the temperature range analysed. SnP_2O_7 shows clear phase transitions at 550 K and 840 K. The strain pattern clearly mimics the pattern for the largest cell angle; this can be seen by the comparison of Figure 6-13 and Figure 5-1. This indicates that the strain is fitting the peak broadening caused by distortion of the angles away from 90°. For $Zr_{0.125}Sn_{0.875}P_2O_7$ the transitions can be seen in the thermal expansion and the strain parameters, occurring at ~ 600 K and ~ 800 K. Both of the latter phase transitions have no clear shift in cell parameters, suggesting second order or higher transitions. It is hypothesised that $Zr_{0.125}Sn_{0.875}P_2O_7$ may demonstrate the rhombohedral symmetry above 800 K, which is found in the high temperature phase of SnP_2O_7, but due to peak broadening it was not possible to determine this decisively.

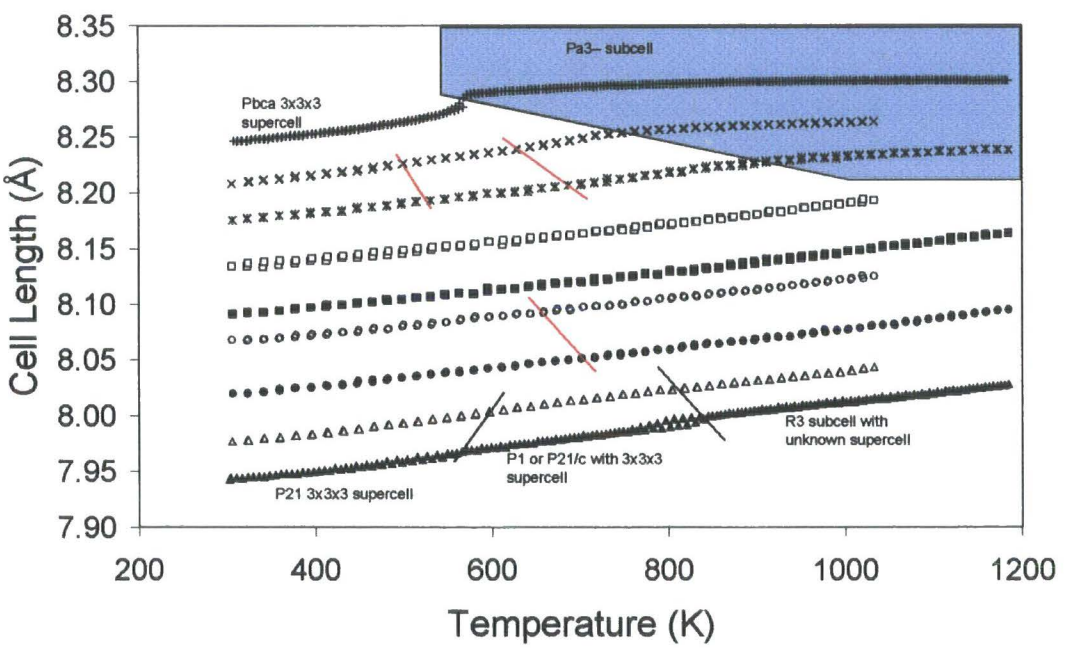

Figure 6-14 : Overview of results from VT refinement of $Zr_xSn_{1-x}P_2O_7$. Black lines show phase transitions, red lines possible phase transitions and the blue region the area above the supercell to subcell phase transition.

6.5. NMR and DSC

Additional information can usually be extracted about these metal pyrophosphate using solid-state ^{31}P NMR. Therefore 2D COSY experiments were carried out on the compound x = 0.5 by A Solielhavoup. The results were unclear, giving a single large peak noticeably broader

than would be expected for a single signal. This prevented any clear determination of the space group. It was hypothesised either low symmetry, combined the subtle differences in the local environment caused by the mix of tin and zirconium atoms, gave a very large number of phosphorus sites, or that the structure was incommensurate. It was decided not to continue with the entire series due to machine time restraints.

Differential scanning calorimetery was carried out on all compounds. ZrP_2O_7 showed the well established phase transition at 293°C but no other material did. This suggests that all possible phase transitions in the other members of the series must be second order or higher.

6.6. Conclusion

Compounds of the series $Zr_xSn_{1-x}P_2O_7$ have been synthesised. Their thermal expansion has been derived from X-ray diffraction data and several phase transition found. Size/strain analysis has also been performed upon the samples, demonstrating the variation of strain within the series. For further investigation of these compounds, better data is required at the higher temperatures.

6.7. References

1 Yamamura Y., Tsuji T., Yamaguchi T., and Hisashige T., *J. Ceram. Soc. Jpn.*, 2006, **114**, 607.

2 Korthuis V., Khosrovani N., Sleight A. W., Roberts N., Dupree R., and Warren W. W., *Chem. Mat.*, 1995, **7**, 412.

3 King I. J., Fayon F., Massiot D., Harris R. K., and Evans J. S. O., *Chem.Commun.*, 2001, 1766.

4 Gover R. K. B., Withers N. D., Allen S., Withers R. L., and Evans J. S. O., *J. Solid State Chem.*, 2002, **166**, 42.

5 Stinton G. W., Hampson M. R., and Evans J. S. O., *Inorgan. Chem.*, 2006, **45**, 4352.

6 Scherrer P., *Gott. Nachr.*, 1918, **2**, 98.

7 Shannon R. D. and Prewitt C. T., *Acta Crystallogr., Sect. B: Struct. Sci.*, 1969, **B25**, 925.

8 D. Balzar and H. Ledbetter, *Journal of Applied Crystallography*, 1993, **26**, 97.

9 Coelho A. A., 'TOPAS manual', 2000.

10 Evans J. S. O., *Unpublished work.*

11 Balzar D., Audebrand N., Daymond M. R., Fitch A., Hewat A., Langford J. I., Le Bail A., Louer D., Masson O., McCowan C. N., Popa N. C., Stephens P. W., and Toby B. H., *J. Appl. Crystallogr.*, 2004, **37**, 911.

12 Withers R. L., Tabira Y., Evans J. S. O., King I. J., and Sleight A. W., *J. Solid State Chem.*, 2001, **157**, 186.

13 Williams T. and Kelley C., 'wgnuplot', Alberta, 2004.

14 Evans J. S. O., 'Alpha.exe', Durham, 2003.

7. Guide to the E-Appendices

All of the main TOPAS input and results files are in the CD-R attached to this thesis. Results are divided by the section of thesis to which they relate.

Section	Name	Files
3	"Parametric Rietveld Refinement"	- Paper accepted for the Journal of Applied Crystallography (sendproof.pdf)
3.2.4	Sequential Rietveld Refinement of VT ZrP_2O_7.	- Seed input file used for the first range of sequential refinement (d8_02968_03.inp).
3.2.5	Rietveld refinement using 16 hour scan of RT ZrP_2O_7 to determine 2θ correction.	- Input file (d8_02967_05.inp). - Rietveld plot in xyd format (d8_02967_05.xyd)
3.2.5	Sequential Rietveld Refinement of VT ZrP_2O_7, with 2θ correction and T calibration.	- Seed input file used for the first range of sequential refinement (d8_02968_02.inp).
3.2.6	Simultaneous Rietveld Refinement of VT ZrP_2O_7, with 2θ correction and T calibration.	- Input file (d8_02967_07.inp).
3.2.7	Simultaneous Rietveld Refinement of VT ZrP_2O_7, with 2θ correction and T calibration controlled by a polynomial.	- Input file (d8_02968_08.inp). - 50 Rietveld plots in xyd format labelled by temperature in K (riet_t_0***.xyd)
3.2.8	Simultaneous Rietveld Refinement of VT ZrP_2O_7, with 423 data sets.	- Input file (d8_02999_29_01.inp). - 423 Rietveld plots in xyd format (riet_t_0***.xyd)
3.3.2	Fitting kinetic $ZrWMoO_8$ data. Strategy 1 - Multitopas independent fits.	- Seed input file (d8_01790_GWS_01.inp).
3.3.2	Fitting kinetic $ZrWMoO_8$ data. Strategy 2a - Parametric fit with no overall parameters.	- Input file (d8_01790_GWS_02a.inp).
3.3.2	Fitting kinetic $ZrWMoO_8$ data. Strategy 2b -	- Input file (d8_01790_GWS_02b.inp).

	Parametric fit with one structural model.	
3.3.2	Fitting kinetic $ZrWMoO_8$ data. Strategy 3 - Parametric fitting of cell parameters.	- Input file (d8_01790_GWS_03.inp).
3.3.2	Fitting kinetic $ZrWMoO_8$ data. Strategy 4 - Parametric fitting of occupancy.	- Input file (d8_01790_GWS_04.inp).
3.3.2	Fitting kinetic $ZrWMoO_8$ data. Strategy 5 - Parametric fitting of both cell and occupancy.	- Input file (d8_01790_GWS_05.inp).
3.4.3	Free refinement of FePt nanoparticle data.	- Input file (d8_02642_01.inp)
3.4.4	Determining the background of FePt nanoparticles with fixed fraction occupancy.	- Input file with occupancy fixed at zero (d8_02642_02.inp). -Subsequent refinement with fixed background parameters (d8_02642_03.inp).
3.4.6	Modelling FePt nanoparticle background as a function of temperature.	- Input file (d8_02642_04.inp)
3.4.7	Modelling FePt nanoparticle background as a function of data set.	- Input file (d8_02642_05.inp)
3.4.8	Applying a step function to the background of FePt nanoparticle data	- Input file (d8_02642_07.inp)
3.4.9	Correlation between the background and the scale parameter of FePt.	- Input file (d8_02642_scale_07.inp)
4	"The 136-atom structure of ZrP_2O_7 and HfP_2O_7 from Powder Diffraction data."	Paper from Inorganic Chemistry
4.5	Final structural model of ZrP_2O_7 in Pbca.	- Input file (structural_refinement_05.inp) - CIF file (structural_refinement_05.cif) - Rietveld plot, X-ray (structural_refinement_05_xray.riet)

		- Rietveld plot, neutron (structural_refinement_05_neutron.riet) - Position of hkls, X-ray (structural_refinement_05_xray.tic) - Position of hkls, Neutron (structural_refinement_05_neutron.tic)
4.6	Final structural model of ZrP_2O_7 in $Pa\bar{3}$.	- Input file (cubic_extended_range_05.inp) - CIF file (cubic_extended_range_05.cif) - Rietveld plot, X-ray (cubic_extended_range_xray.riet) - Rietveld plot, neutron (cubic_extended_range_neutron.riet) - Position of hkls, X-ray (cubic_extended_range_xray.tic) - Position of hkls, Neutron (cubic_extended_range_neutron.tic)
5.3.4	Best structure solution of RT SnP_2O_7 in $P2_1$.	- Input file as originally used (run_23_old.inp). This no longer runs due to changes in TOPAS Academic. The same file is included, without re-refinement, but with the position of restraints moved and the MVW lines removed (run_23.inp) - CIF file (run_23.cif) - Rietveld plot X-ray (run_23_xray.riet) - Rietveld plot neutron (run_23_neutron.riet) - Position of hkls, X-ray (run_23_xray.tics) - Position of hkls, Neutron (run_23_neutron.tics)
5.3.4	Best structure solution of RT SnP_2O_7 in Pa.	- Input file as originally used (run_83_old.inp). Replacement (run_83.inp) - CIF file (run_83.cif)

		- Rietveld plot X-ray (run_83_xray.riet) - Rietveld plot neutron (run_83_neutron.riet) - Position of hkls, X-ray (run_83_xray.tics) - Position of hkls, Neutron (run_83_neutron.tics)
5.3.5	Structure refinement of RT SnP_2O_7 in $P2_1$.	- Input file (structural_refinement_05.inp) - CIF file (structural_refinement_05.cif) - Rietveld plot X-ray (structural_refinement_05_xray.riet) - Rietveld plot neutron (structural_refinement_05_neutron.riet) - Position of hkls, X-ray (structural_refinement_05_xray.tics) - Position of hkls, Neutron (structural_refinement_05_neutron.tics)
5.4.4	Best structure solution of RT SnP_2O_7 in P1.	- Input file (run_00.inp) - CIF file (run_00.cif) - Rietveld plot X-ray (run_00_xray.riet) - Rietveld plot neutron (run_00_neutron.riet) - Position of hkls, X-ray (run_00_xray.tics) - Position of hkls, Neutron (run_00_neutron.tics)
5.4.4	Best structure solution of RT SnP_2O_7 in $P2_1/c$	- Input file (run_23.inp) - CIF file (run_23.cif) - Rietveld plot X-ray (run_23_xray.riet) - Rietveld plot neutron (run_23_neutron.riet) - Position of hkls, X-ray (run_23_xray.tics) - Position of hkls, Neutron (run_23_neutron.tics)

5.7.3	Best structure solution of low temperature GeP_2O_7 in P1	- Input file (run_10.inp) - CIF file (run_10.cif) - Rietveld plot X-ray (run_10_xray.riet) - Rietveld plot neutron (run_10_neutron.riet) - Position of hkls, X-ray (run_10_xray.tics) - Position of hkls, Neutron (run_10_neutron.tics)
5.7.3	Best structure solution of low temperature GeP_2O_7 in $P2_1$	- Input file (run_74.inp) - CIF file (run_74.cif) - Rietveld plot X-ray (run_74_xray.riet) - Rietveld plot neutron (run_74_neutron.riet) - Position of hkls, X-ray (run_74_xray.tics) - Position of hkls, Neutron (run_74_neutron.tics)
5.7.3	Best structure solution of low temperature GeP_2O_7 in Pa	- Input file (run_69.inp) - CIF file (run_69.cif) - Rietveld plot X-ray (run_69_xray.riet) - Rietveld plot neutron (run_69_neutron.riet) - Position of hkls, X-ray (run_69_xray.tics) - Position of hkls, Neutron (run_69_neutron.tics)
5.7.3	Best structure solution of low temperature GeP_2O_7 in $P2_1/c$	- Input file (run_21.inp) - CIF file (run_21.cif) - Rietveld plot X-ray (run_21_xray.riet) - Rietveld plot neutron (run_21_neutron.riet) - Position of hkls, X-ray (run_21_xray.tics) - Position of hkls, Neutron (run_21_neutron.tics)

6.3.3	Refinement of $Zr_xSn_{1-x}P_2O_7$ data with freely refining peak shape.	- Input file (multitopas_input.inp) - Batch file (multitopas.bat) - Individual input (Zr_content_****.inp)
6.3.4	Refinement of $Zr_xSn_{1-x}P_2O_7$ data with fixed peak shape and size broadening.	- Input file (multitopas_input.inp) - Batch file (multitopas.bat) - Individual input (Zr_content_****.inp)
6.3.5	Refinement of $Zr_xSn_{1-x}P_2O_7$ data with fixed peak shape and strain broadening.	- Input file (multitopas_input.inp) - Batch file (multitopas.bat) - Individual input (Zr_content_****.inp)
6.3.6	Refinement of $Zr_xSn_{1-x}P_2O_7$ data with fixed peak shape and size & strain broadening.	- Input file (multitopas_input.inp) - Batch file (multitopas.bat) - Individual input (Zr_content_****.inp)
6.4.2	Variable temperature refinement of $Zr_xSn_{1-x}P_2O_7$ data	- Input files x = 0.000 (d8_02978_Zr_0000.inp) x = 0.125 (d8_03181_Zr_0125.inp) x = 0.250 (d8_02797_Zr_0250.inp) x = 0.375 (d8_03161_Zr_0375.inp) x = 0.500 (d8_02978_Zr_0500.inp) x = 0.625 (d8_03182_Zr_0625.inp) x = 0.750 (d8_02988_Zr_0750.inp) x = 0.875 (d8_03185_Zr_0875.inp) x = 1.000 (d8_02968_Zr_1000.inp)